

**Notice 1**

*Under the Copyright Act 1968, this thesis must be used only under the normal conditions of scholarly fair dealing. In particular no results or conclusions should be extracted from it, nor should it be copied or closely paraphrased in whole or in part without the written consent of the author. Proper written acknowledgement should be made for any assistance obtained from this thesis.*

A thesis submitted to the Faculty of Science, Monash University, in fulfilment  
of requirement for the degree of Doctor of Philosophy

October 2012

**Mesoporous Silica SBA-15 Supported  
Cobalt Oxide: An Investigation Of The  
Structure, Morphology And Catalytic  
Activity Of Various Composites**

**Jamileh Taghavi Moghaddam**



**MONASH** University

# Declaration

Monash University

Monash Research Graduate School

**Declaration for thesis based or partially based on conjointly published or unpublished work**

## General Declaration

In accordance with Monash University Doctorate Regulation 17/ Doctor of Philosophy and Master of Philosophy (MPhil) regulations the following declarations are made:

I hereby declare that this thesis contains no material which has been accepted for the award of any other degree or diploma at any university or equivalent institution and that, to the best of my knowledge and belief, this thesis contains no material previously published or written by another person, except where due reference is made in the text of the thesis.

This thesis includes two original papers published in peer reviewed journals and six unpublished publications. The core theme of the thesis is “Mesoporous silica SBA-15 supported cobalt oxide: an investigation of the structure, morphology and catalytic activity of various composites”. The ideas, development and writing up of all the papers in the thesis were the principal responsibility of myself, the candidate, working within the School of Chemistry under the supervision of Prof. Alan L. Chaffee and Prof. Douglas Macfarlane. The inclusion of co-authors reflects the fact that the work came from active collaboration between researchers and acknowledges input into team-based research

In the case of 3 - 5 my contribution to the work involved the following:

Thesis chapter	Publication title	Publication status*	Nature and extent of candidate's contribution
3.2	Preparation and characterization of mesoporous silica supported cobalt oxide as a catalyst for the oxidation of cyclohexanol	Published in <i>Journal of Molecular Catalysis A: Chemical</i>	Proposed original idea; prepared and analysed samples; identified major issues; developed interpretations; fully drafted papers and conclusions (80%)
3.3	Mesoporous silica SBA-15 supported $\text{Co}_3\text{O}_4$ nanorods as efficient liquid phase oxidative catalyst	Published in <i>Topics in Catalysis</i>	
3.4	Impact of low cobalt loading on the morphology and dispersion of crystalline $\text{Co}_3\text{O}_4$ patches supported on SBA-15	Submitted to <i>ACS Catalysis</i>	

4.2	Cobalt precursor impact on the dispersion and morphological development of SBA-15 supported cobalt oxide species	Submitted to <i>Microporous and Mesoporous Materials</i>	Proposed original idea; prepared and analysed samples; identified major issues; developed interpretations; fully drafted papers and conclusions (80%)
4.3	SBA-15 supported cobalt oxide species: preparation, morphology and catalytic activity	To be adjusted for submission to <i>Applied Catalysis A: General</i>	
5.4	Effect of Ce-doping on the dispersion of $\text{Co}_3\text{O}_4$ nanorods supported on SBA-15	To be adjusted for submission to <i>Journal of Catalysis</i>	Proposed original idea; prepared and analysed samples; identified major issues; developed interpretations; fully drafted papers and conclusions (80%)
5.5	Effect of Ce-doping on the structure and redox properties and SBA-15 supported cobalt oxide species in catalytic oxidation reactions	To be adjusted for submission to <i>Journal of Molecular Catalysis A: Chemical</i>	
5.6	The impact of Co:Ce ratio on the dispersion and catalytic activity of cobalt-cerium oxides supported on SBA-15	To be adjusted for submission to <i>Topics in Catalysis</i>	

I ~~have~~/ have not (circle that which applies) renumbered sections of submitted or published papers in order to generate a consistent presentation within the thesis.

J.Taghavi

## **Acknowledgment**

During the period I have been working for this thesis, a lot of people helped me and supported me in a variety of ways. I am indebted to all of them. Here, I would like to distinguish and express my special thanks.

First of all I would like to express my gratitude to my supervisor Prof. Alan L. Chaffee for his support, guidance, advice and valuable discussions during the course of this whole research work presented here. He always has a lot of insightful ideas, many of which nobody else has ever thought of. I really appreciate his patience in reading my articles and reports, especially those written in very early stages of my PhD. I especially thank him for teaching me how to interpret and present my work to be scientifically acceptable. Above all I appreciate the way he has taught me to be independent and solve problems without panicking.

I thank Prof. Douglas Macfarlane for his advice. He was always available for all kinds of questions related to my project.

I am grateful to Greg Knowles who patiently trained me on most of the instruments I used to characterise my samples. The training and productive discussions helped me to have clear idea about what I was doing and in which direction to go. He has always been available and encouraging even when some of my experiments did not work.

I would like to extend my deepest gratitude to Dr. Marc Marshall for kindly editing my thesis and providing me productive feedback on my work.

I am indebted to Dr. Tim Williams for his training in TEM and STEM. If it was not for his confidence in me I would have never gone back to work with microscopes after the first session of training. The techniques I have learnt from him gave better direction and understanding in my project.

I thank Dr. Laure Bourgeois and Ellen Lovie at The Monash Centre for Electron Microscopy (MCEM) for assisting me in TEM and STEM training. Many thanks also to Dr. Xi-ya Fang for assisting me in acquiring SEM images.

I am very thankful for the training and guidance for ICP-MS analyses that was provided by Dr. Massimo Raveggi. I also thank Mr Victor DeGuzman for all the time and effort he put into assisting the development of GC and GC-MS methods.

The XPS analyses in this work were carried out at the Australian Synchrotron under the supervision of Drs. Bruce Cowie and Anton Tadich. I'm grateful I was able to experience the fun of discovery that follows long hours of work.

I am also thankful to Mr. Bruce Dobney and Ms. Maria Triantis for their technical support.

I would like to acknowledge my colleagues in Alan Chaffee's group especially, Brad Wells, Lachlan Ciddor, Christian Vogt and Christin Patzscke, who have always been with me. They were all supportive and helped me in various ways both professionally and personally. I made some of my best friends during this period.

This work was supported by financially by the Australia Research Council Discovery program. The scholarships provided by the Monash Research Graduate School and the Faculty of Science, Monash University are very gratefully acknowledged.

## **Dedication**

This present work is dedicated to my mother, Mahereh Nasiri, for her guidance, unconditional love and support. I am what I am today because of her selfless love and encouragements. Sometimes words cannot express appreciations and feelings. Thanks for being such an angel.

I would also like to dedicate this work to Mr Faramarz Pedram who supported me in everything when I first came to Australia. He has always been a like a loving father to me. I wish you were still with me when I wanted to submit this thesis. I am also deeply thankful to Pedram's family for all their emotional support.

I would also like to thank my partner, Hossein Shiringoo and my family members, my grandmother, uncles and cousins for their support and love.

I take this opportunity to convey my heart-felt admiration to all my teachers, from my school days to my post-graduate education.

## Abstract

Mesoporous silica supported cobalt oxide composites have attracted enormous attention due to their wide range of applications, especially in the catalysis field. The focus of this thesis concerns the preparation of mesoporous silica SBA-15 supported cobalt oxide species and the evaluation of their catalytic activities for liquid phase oxidation of various alcohols and olefins. The impact of different variables such as preparation method, metal precursor, metal loading and dopant was investigated on the morphology and dispersion of the active particles, the overall structure of the resulting composite materials and their catalytic activity.

The first section of the thesis concerns the use of  $\text{Co}(\text{NO}_3)_2 \cdot 6\text{H}_2\text{O}$  as a precursor. Various amounts of  $\text{Co}(\text{NO}_3)_2 \cdot 6\text{H}_2\text{O}$  were deposited on SBA-15 using the “two-solvent” method. This method accommodates cobalt oxide species exclusively inside the pores of SBA-15. Analogous composite materials were also prepared using the more conventional methods of impregnation and adsorption. Irrespective of preparation method, all the composite materials were black. The two-solvent method resulted in the formation of crystalline cobalt oxide ( $\text{Co}_3\text{O}_4$ ) nanorods which filled adjacent mesopores to form patches incorporating all the cobalt available. In the case of composites prepared via impregnation cobalt oxide particles formed both on the external and internal surfaces of the SBA-15, also incorporating all the available cobalt. When adsorption was used as a preparation method, cobalt oxide species were predominantly formed inside the pores of SBA-15, however not all the cobalt available in solution was incorporated. All the composites were characterised by  $\text{N}_2$  adsorption-desorption, XRD, XPS, TPR, ICP-MS, FTIR, DR UV-vis, SEM, TEM, STEM and elemental mapping. The size of the crystalline  $\text{Co}_3\text{O}_4$  patches was measured using the XRD diffraction patterns and Scherrer equation. The lattice fringes of  $\text{Co}_3\text{O}_4$  were also observed in HRTEM images. The catalytic activity of the composite materials in liquid phase oxidation of various substrates was determined by GC and GC-MS. It was found that for the composite materials prepared by the “two-solvent” method, the catalytic activity varied in reverse proportion to the cobalt loading and that the composite with the lowest amount of cobalt exhibited the highest catalytic activity. This was attributed to the morphology of the cobalt oxide species and the way they were dispersed throughout the SBA-15. As the cobalt loading increased, more pores became blocked due to the elongation of the  $\text{Co}_3\text{O}_4$  nanorods inside the pores and, thus, a lower proportion of the cobalt was accessible by the reactants. The composite prepared via adsorption also demonstrated high catalytic activity as a result of the relatively

good dispersion of  $\text{Co}_3\text{O}_4$  and, hence, its accessibility by the reactants. The composite prepared via impregnation exhibited the lowest catalytic activity compared to the analogue composites with the same cobalt loading prepared either by the two-solvent method or adsorption. This is attributed to the formation of large cobalt clusters (poor dispersion) mostly on the external surfaces of SBA-15 on the aperture of the pores. The composites prepared via the two-solvent method could be reused up to at least three times without significant changes in their catalytic activities.

In the second section of the thesis SBA-15 was loaded with various amounts of  $\text{CoCl}_2 \cdot 6\text{H}_2\text{O}$  via the two-solvent method, impregnation and adsorption. Regardless of the preparation method a blue coloration with intensity proportional to the cobalt loading was observed for the composites. The suite of characterisation techniques (see above) was applied to investigate the morphology, dispersion and chemistry of the incorporated cobalt as well as the structure of the composites. The cobalt oxide species were found to exist as an amorphous phase which was highly dispersed throughout the SBA-15, presumably due to the interaction between  $\text{Co}^{2+}$  ions and the silica surface. A comparison of composites shows that the micropores became progressively more blocked as the cobalt loading was increased, but the mesopore volume was reduced only marginally. For the series of composites prepared via the two-solvent method, an unexpected morphological transformation was observed when the cobalt loading was 30 wt% or beyond. This transformation happened during the calcination step of the preparation and resulted in the collapse of the highly ordered mesoporous channels of SBA-15. It is suggested that the interaction between incorporated  $\text{Co}^{2+}$  ions and the oxygen of the silica walls at high cobalt loadings, is what leads to this transformation during calcination. The catalytic activity of these composite materials was evaluated for liquid phase oxidation of cyclohexanol. For the series prepared by the two-solvent method, it was found that the composite with lowest cobalt loading again showed the highest catalytic activity. However, the composite which experienced the morphological transformation (Co 30 wt%) showed only slightly lower catalytic activity compared to other composites. This suggests that although the surface area decreased substantially, the catalytically active species remained accessible to the reactants. It was confirmed that the oxidation reaction did not occur in the absence of either cobalt or oxidant tert-butylhydroperoxide, TBHP. With this series of catalysts, it was found that a small amount of cobalt could 'leak' into solution, indicating that the catalytic activity for this series of composites might best be thought of as a mixed 'heterogeneous-homogeneous' system.

Since ceria has been widely employed as a dopant, both for bulk and supported metal oxides with promising results on their catalytic activity, the main objective of the third section was to investigate the effect of ceria as a promoter on the morphology, dispersion, crystallinity, leakage and catalytic activity of the SBA-15 supported cobalt oxide species. Two series of composites were prepared via the two-solvent method using  $\text{Co}(\text{NO}_3)_2 \cdot 6\text{H}_2\text{O}$  and  $\text{CoCl}_2 \cdot 6\text{H}_2\text{O}$  with 5 wt% loading as cobalt precursors and  $\text{Ce}(\text{NO}_3)_3 \cdot 6\text{H}_2\text{O}$  with 0.5 wt% loading as a dopant. It was found that the ceria-doped composite prepared from  $\text{Co}(\text{NO}_3)_2 \cdot 6\text{H}_2\text{O}$  exhibited better dispersion of cobalt oxide species, with both  $\text{Co}_3\text{O}_4$  single nanorods and less extensive  $\text{Co}_3\text{O}_4$  patches, than its non-doped analogue. Here the better dispersion of the  $\text{Co}_3\text{O}_4$  nanorods, the synergistic effect between cobalt oxide and ceria and the improvement in redox properties result in higher catalytic activity of the composite in liquid phase oxidation of various alcohols and olefins. Ceria-doped composites prepared from  $\text{Co}(\text{NO}_3)_2 \cdot 6\text{H}_2\text{O}$  was reusable up to four times without significant change in its catalytic activity. However for the composites prepared from  $\text{CoCl}_2 \cdot 6\text{H}_2\text{O}$  (5 wt%) and  $\text{Ce}(\text{NO}_3)_3 \cdot 6\text{H}_2\text{O}$  (0.5 wt%), the addition of the dopant did not improve the crystallinity of the cobalt oxide phase. The XRD patterns did not indicate any trace of phase separated cobalt-cerium mixed metal oxide. The dispersion of the cobalt oxide species in this specific case appeared to be the same as for the undoped analogue. However the ceria-doped composites demonstrated better catalytic activity. This can be attributed to the improvement in the redox properties of  $\text{Co}^{2+}/\text{Co}^{3+}$  due to the presence of ceria. Ceria-doped composites prepared from  $\text{CoCl}_2 \cdot 6\text{H}_2\text{O}$  still exhibited some slight 'leakage'. The effect of the Co:Ce ratio on the morphology and catalytic activity of the composites was also investigated. These composites were prepared via the two-solvent method using  $\text{CoCl}_2 \cdot 6\text{H}_2\text{O}$  (5 wt%) and  $\text{Ce}(\text{NO}_3)_3 \cdot 6\text{H}_2\text{O}$  (0.5-2 wt%) as metal precursors. The highest catalytic activity was obtained from composites with 0.5 wt% and 1.5 wt% cerium loadings. It is speculated that these two compositions facilitate better synergy between cobalt oxide species and ceria.

An in-depth study on the liquid phase oxidation of benzyl alcohol was carried out to investigate the mechanism of the oxidation reaction. The amount of TBHP added was not stoichiometrically sufficient to facilitate the 'double oxidation' of the substrate through benzaldehyde and then to benzoic acid. Moreover, after the completion of the reaction TBHP was still observed (by GC) to be present. This suggests that aerial oxygen was also behaving as an oxidant and that TBHP behaved more as an initiator to the catalytic reaction. This was

confirmed by carrying out the reaction under an inert atmosphere ( $N_2$ ) and also in the absence of the TBHP with negligible conversion in both cases.

In summary, it was found that various preparation methods result in the formation of cobalt oxide species with different morphology and dispersion. The two-solvent method clearly facilitates the formation of the cobalt oxide species inside the pores of the SBA-15 and prevents their aggregation into inactive clusters on the external surface of the support. The nature of the cobalt precursor, more specifically the nature of the counter ion, determines the nature of the cobalt oxide species, its crystallinity and its interaction with the support. This, in turn, impacts the overall structure of the composite. The amount of cobalt loading also affects the morphology of the active species, the overall structure of the composite, the degree of pore blockage and thus the availability of the active sites. Ceria, as a dopant, was found to improve the dispersion of the  $Co_3O_4$  nanorods prepared from  $Co(NO_3)_2 \cdot 6H_2O$  and the redox properties of the cobalt oxide species (prepared using either  $Co(NO_3)_2 \cdot 6H_2O$  or  $CoCl_2 \cdot 6H_2O$  as cobalt precursor) supported on SBA-15. The Co:Ce ratio was also shown to be important in improving the catalytic activity and is attributed to a synergistic effect between the cobalt oxide species and ceria. It is suggested that the extent to which ceria covered the surface of cobalt oxide species and the boundary between these two phases are important in determining the catalytic activity. In conclusion there are many factors that were shown to play critical roles in determining the catalytic activity of the composites prepared in this study.

# Table of Contents

<b>1 Chapter 1</b> .....	<b>18</b>
1.1 Catalysts .....	19
1.2 Importance of catalysts.....	20
1.3 Heterogeneous and homogeneous catalysts .....	21
1.3.1 Heterogeneous catalysts .....	22
1.4 Catalytic oxidation reactions .....	24
1.5 Metal oxides .....	26
1.5.1 Surface co-ordination in metal oxides .....	27
1.5.2 Types of adsorption on the surface .....	27
1.5.3 Oxidation reactions on metal oxides surfaces.....	28
1.5.4 Type of oxidation reactions .....	28
1.5.5 Oxidation mechanism on the surface of metal oxides .....	29
1.6 Different types of supports .....	31
1.6.1 Zeolites.....	32
1.6.1.1 Zeolite X and Y .....	33
1.6.1.2 Zeolite A.....	33
1.6.1.3 Erionite .....	33
1.6.2 Carbon nanotubes.....	34
1.6.3 Mesoporous metal oxides .....	34
1.6.4 Ordered mesoporous silica (OMS) .....	36
1.6.4.1 Hexagonal mesoporous silicas (HMS).....	38
1.6.4.2 MCM-41.....	38
1.6.4.3 SBA-15.....	39
1.6.5 Supported metal oxides.....	44
1.6.5.1 Impregnation .....	45
1.6.5.2 Ion exchange .....	47
1.6.5.3 Adsorption.....	47
1.6.5.4 Ammonia method.....	47
1.6.5.5 Solvent-free deposition .....	48
1.6.5.6 Molecular design dispersion (MDD).....	48
1.6.5.7 Supercritical fluid deposition .....	49

1.6.5.8	Functionalized supports.....	50
1.6.5.9	Two-solvent method.....	51
1.6.5.10	Framework incorporation .....	52
1.7	Cobalt chemistry .....	52
1.7.1	Cobalt oxides .....	54
1.7.2	Catalytic performance of cobalt oxide species, bulk or supported .....	56
1.8	Scope of the present study.....	65
1.9	Thesis overview.....	66
<b>2</b>	<b>Chapter 2.....</b>	<b>69</b>
2.1	Catalysis synthesis.....	70
2.1.1	Synthesis of mesoporous silica SBA-15 .....	70
2.1.2	Supported cobalt oxide catalyst preparation .....	70
2.1.2.1	Two-solvent method.....	70
2.1.2.2	Impregnation .....	71
2.1.2.3	Adsorption.....	71
2.1.3	Supported Ce-doped Co-composites.....	71
2.2	Characterization techniques .....	72
2.2.1	Adsorption.....	72
2.2.1.1	N <sub>2</sub> adsorption-desorption.....	72
2.2.1.2	Temperature programmed reduction (TPR).....	76
2.2.2	X-ray diffraction (XRD) .....	78
2.2.2.1	Formation of diffraction pattern.....	79
2.2.3	X-ray photoelectron spectroscopy (XPS) .....	81
2.2.4	<sup>29</sup> Si magnetic angle spinning nuclear magnetic resonance spectroscopy (MAS NMR) 83	
2.2.5	Electron microscopy .....	85
2.2.5.1	Electron gun .....	86
2.2.5.2	Transmission electron microscopy (TEM).....	87
2.2.5.3	Scanning electron microscopy (SEM).....	88
2.2.5.4	Energy dispersive X-ray (EDX) spectroscopy.....	90
2.2.5.5	Scanning transmission electron microscopy (STEM).....	90
2.2.5.6	Elemental Mapping .....	92
2.2.6	Fourier-transform infrared spectroscopy (FTIR).....	93
2.2.7	Diffuse reflectance ultraviolet-visible spectroscopy (DR UV-vis).....	95

2.2.8	Inductively coupled plasma mass spectrometry (ICP-MS) .....	95
2.3	Catalytic performance .....	97
2.3.1	Gas chromatography (GC).....	97
2.3.1.1	Selected stationary phases.....	98
2.3.2	Gas chromatography-mass spectrometry (GC-MS).....	99
2.4	References .....	102
<b>3</b>	<b>Chapter 3.....</b>	<b>117</b>
3.1	General overview .....	118
3.2	Preparation and characterization of mesoporous silica supported cobalt oxide as a catalyst for the oxidation of cyclohexanol .....	121
3.3	Mesoporous silica SBA-15 supported Co <sub>3</sub> O <sub>4</sub> nanorods as efficient liquid phase oxidative catalyst.....	132
3.4	Impact of low cobalt loading on the morphology and dispersion of the crystalline Co <sub>3</sub> O <sub>4</sub> patches supported on SBA-15.....	142
3.4.1	Introduction.....	142
3.4.2	Experimental .....	145
3.4.2.1	Preparation of SBA-15 and Co-composites .....	145
3.4.2.2	Characterization techniques .....	145
3.4.3	Catalytic tests .....	146
3.4.4	Results and discussion .....	146
3.4.5	Conclusion .....	157
3.4.6	REFERENCES .....	158
3.5	Appendix .....	161
3.5.1	Wide-angle XRD .....	161
3.5.2	Scanning transmission electron microscopy and elemental mapping.....	161
3.5.3	Reference .....	162
<b>4</b>	<b>Chapter 4.....</b>	<b>163</b>
4.1	General overview .....	164
4.2	Cobalt precursor impact on the dispersion and morphological development of SBA-15 supported cobalt oxide species.....	167
4.2.1	Introduction.....	167
4.2.2	Experimental.....	168
4.2.2.1	Material preparation .....	168
4.2.3	Characterization methods.....	169

4.2.4	Results and discussion .....	169
4.2.5	Conclusion .....	173
4.2.6	References.....	174
4.3	SBA-15 supported cobalt oxide species: preparation, morphology and catalytic activity.....	177
4.3.1	Introduction.....	178
4.3.2	Experimental.....	180
4.3.2.1	Preparation of SBA-15 and Co-composites .....	180
4.3.2.2	Characterization techniques .....	180
4.3.2.3	Catalytic tests .....	181
4.3.3	Results and discussion .....	182
4.3.3.1	Composites characterization .....	182
	Fig. 9. FTIR spectra of (a) SBA-15, .....	191
	(b) SCo(Cl)5-A, (c) SCo(Cl)5-I,.....	191
	(d) SCo(Cl)5 and (e) SCo(Cl)10.....	191
4.3.4	Catalytic evaluation .....	194
4.3.5	Conclusion .....	197
4.3.6	References.....	198
4.4	Appendix .....	201
4.4.1	<sup>29</sup> Si Magnetic angle spinning nuclear magnetic resonance spectroscopy.....	201
4.4.2	References.....	202
<b>5</b>	<b>Chapter 5.....</b>	<b>203</b>
5.1	Literature review .....	204
5.1.1	Ceria applications.....	205
5.1.1.1	Ceria in the glass industry .....	205
5.1.1.2	Ceria in catalysis .....	205
5.2	General overview .....	209
5.3	References .....	210
5.4	Effect of Ce-doping on the dispersion of Co <sub>3</sub> O <sub>4</sub> nanorods supported on SBA-15..	213
5.4.1	Introduction.....	213
5.4.2	Experimental.....	215
5.4.2.1	Catalyst preparation.....	215
5.4.2.2	Characterization of materials structural morphology/chemsitry.....	216
5.4.2.3	Catalytic tests .....	217

5.4.3	Results and discussion .....	217
5.4.3.1	Characterization of supported catalysts.....	217
5.4.4	Conclusion .....	228
5.4.5	References.....	228
5.5	Effect of Ce-doping on the structure and redox properties of the SBA-15 supported cobalt oxide species in catalytic oxidation reactions .....	232
5.5.1	Introduction.....	232
5.5.2	Experimental .....	235
5.5.2.1	Synthesis of the SBA-15 support .....	235
5.5.2.2	Characterization techniques .....	235
5.5.2.3	Catalytic tests .....	236
5.5.3	Results and discussion .....	236
5.5.3.1	Characterization of supported catalysts.....	236
5.5.4	Conclusion .....	245
5.5.5	References.....	245
5.5.6	Supportin information.....	249
5.6	The impact Co:Ce ratio on the dispersion and catalytic activity of cobalt-cerium oxide supported on SBA-15 .....	251
5.6.1	Introduction.....	251
5.6.2	Experimental.....	252
5.6.2.1	Synthesis of the SBA-15 and supported mixed oxide catalyst support .....	252
5.6.2.2	Characterization techniques .....	253
5.6.2.3	Catalytic tests .....	254
5.6.3	Results and discussion .....	254
5.6.3.1	Characterization of supported mixed oxides catalysts .....	254
5.6.4	Conclusion .....	264
5.6.5	References.....	264
<b>6</b>	<b>Chapter 6.....</b>	<b>267</b>
6.1	Concluding remarks .....	268
6.1.1	SBA-15 supported Co <sub>3</sub> O <sub>4</sub> nanorods.....	268
6.1.2	SBA-15 supported highly dispersed cobalt oxide species .....	270
6.1.3	Ce-doped Co-composites .....	272
6.2	Future work .....	274



---

# Chapter 1

## General Introduction

---

## 1.1 Catalysts

Catalysis has been used for thousands of years e.g. in the production of ethanol using yeast, but the concept of catalysis was discovered and rationalized only about two hundred years ago. In 1835, the Swedish scientist Jöns Jakob Berzelius pointed out that some reactions were initialized in the presence of certain substances which were not themselves changed by the reaction; he called such substances catalysts. In the light of his discovery, he could elucidate previous work of other researchers such as Faraday and Döbereiner [1].

Catalysis can be simply described as an initiation or acceleration of chemical reactions by substances (catalysts), which participate in the preliminary steps of the reactions but after each reaction cycle are, in an ideal situation, left in a chemically unchanged state. The intermediate interactions between reagents and catalyst result in the formation of active complexes in a series of elementary steps. These steps in turn provide a new reaction pathway more advantageous compared to the noncatalytic pathway [2]. Catalysis is important in many chemical transformations in nature and different sectors of industry. There are no stoichiometric relationships between the amount of catalysts and the amount of reagents converted as catalysts are not incorporated in the final products. However, in the course of catalysis, the catalyst is influenced by the reaction mixture and thus the ideal situation of a chemically unchanged catalyst may not be found in practice; the catalyst composition or structure may change. These changes might inactivate the catalysts during the course of the reaction.

In the catalytic process, the free energy of the catalyst does not change, which means the catalyst does not change the equilibrium constant of the chemical reaction. What the catalyst usually does is to lower the energy barrier to reaction (Figure 1.1). Thus it permits the chemical reaction to reach the final equilibrium state in a shorter time. In a chemical reaction, the mass of the reactants does not have an essential role in attaining equilibrium rapidly. However, the orientation of the reaction components and catalyst in the media in which the reaction proceeds, affects the reaction rate. An appropriate space configuration facilitates attaining equilibrium rapidly.

In many cases, catalysts accelerate reactions which are thermodynamically possible but cannot proceed at a significant rate due to kinetic difficulties. Every catalyst is optimally active for specific reaction(s). However, the rate of different even closely related reactions on the same catalyst can vary [3]. If several reaction pathways are possible thermodynamically

and all the paths lead to the same reaction, what is the advantage from the selectivity point of view of a catalyst? Surely a catalyst, by its selectivity, tends to suppress side-reactions. A catalyst might selectively accelerate some or even one of the pathways preferentially, so that the catalysts are often useful if a specific reaction is desirable.

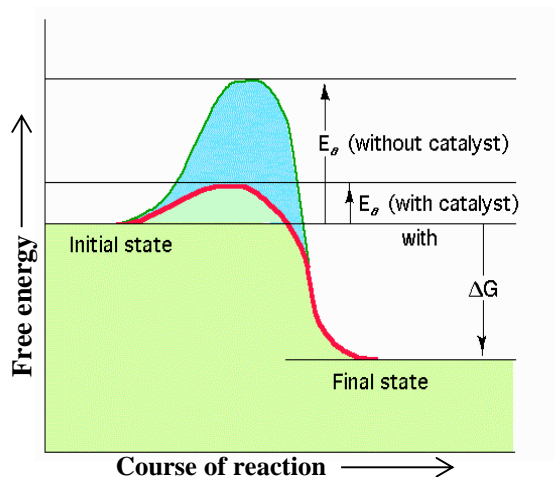


**Figure 1.1.** Energy profile for the reaction with/without catalyst

## 1.2 Importance of catalysts

Since most industrial processes utilise catalysts to increase economical profitability, catalysis is an intensively investigated field of applied chemistry and engineering [4, 5]. The most important industrial reactions relying on catalysts include cracking of long-chain hydrocarbons, synthesis of ammonia used in fertilizers, production of gasoline from naphtha, the water-gas shift reaction, epoxidation of ethylene, oxidation of carbon monoxide (CO) emitted in engine exhaust and oxidation of alcohols and olefins to valuable intermediates for further use in the pharmaceutical and agricultural and food industry [6-11].

In some cases, the chemical reactions do not take place at all in the absence of the catalysts, whereas in other cases the catalysts simply enhance the effectiveness of the process. The improvement of the effectiveness of industrial processes can be beneficial both economically and environmentally by reducing waste or undesirable by-products, using lower pressure or temperature and utilizing the reactants more efficiently [12].

A survey of catalytic technologies that have been introduced into the USA market in the 1990s reported over 130 examples of new catalysts which are in an advanced stage of scale up or have been commercialized [13]. This demonstrates the undeniable role of catalytic technology in many industrial processes. It is noteworthy that in 1997, world catalysts sales reached \$ 7.4 billion and increased to \$ 13 billion in 2004 [14].

### 1.3 Heterogeneous and homogeneous catalysts

Catalytic reactions may take place in heterogeneous or homogeneous systems. In heterogeneous systems the catalyst and the reactants are not in the same phase, for example the catalyst may be solid whereas the reactants are gases or liquids [15]. In the homogeneous system, however, the catalyst and the reactants are in the same phase and both uniformly distributed in the system. In principle there is no limitation to the phase of a homogeneous system. The first industrial catalytic reaction developed, the oxidation  $\text{SO}_2$  to  $\text{SO}_3$  with  $\text{NO}$  as catalyst, was carried out in a homogeneous gas phase system in 1750 by J. Roebuck. However most of the processes using homogeneous catalysts utilize a liquid phase [16].

In homogeneous systems, the catalyst operates as single molecules, which are distributed among the molecules of the reactants with the same mobility. This makes homogeneous catalysts by nature more active and selective compared to heterogeneous catalysts [17]. In these systems the concentration of the catalyst plays a significant role in the rate of the catalytic reaction. In homogeneous systems the concentration, mobility and reactivity of the molecules are different at the boundary of the reactants and catalyst compared to the bulk of each component [18].

In heterogeneous catalysis, where the catalyst is usually solid the rate of the reaction depends on the diffusion rates of the reactants to the surface of the catalyst and of the product(s) from the surface of the catalyst [19]. This indicates that the rate of a heterogeneous reaction is directly proportional to the surface area of the catalyst, whereas for homogeneous catalysts the concentration of the catalyst is the key factor.

In terms of total tonnage and dollar value, the contribution of heterogeneous catalytic processes in the chemical industry is significantly greater than that of homogeneous catalytic reactions. Nearly 85 % of catalytic processes are based on heterogeneous catalysts. There are also some limitations in using homogeneous catalysts operating in a liquid phase industrially [20], such as relatively low boiling point of solvents, low thermal stability of the catalysts and limited catalyst life time. Thus homogeneous catalysts cannot be in practice at above about  $250\text{ }^\circ\text{C}$ . In contrast, heterogeneous systems do not have the temperature restrictions and can be operated at much higher temperature. In addition, homogeneous catalysts are known to have, in general, a shorter life time compared to heterogeneous catalysts and it is more difficult to recover them; both these factors increase the cost of recovery compared to that of heterogeneous catalysts. This is of particular importance when expensive metals such as Rh,

Pt or Pd are used as catalysts. The major advantages and disadvantages of homogeneous vs. heterogeneous catalysts are summarized in Table 1.1.

**Table 1.1** Advantages and disadvantages of heterogeneous catalysts vs. homogeneous catalysts [20]

<b>Properties</b>	<b>Heterogeneous</b>	<b>Homogeneous</b>
<b>Catalyst recovery</b>	Cheap & easy	Expensive & difficult
<b>Selectivity</b>	Good/poor – multiple active sites	Excellent/good-single active site
<b>Thermal stability</b>	Good	Poor

### 1.3.1 Heterogeneous catalysts

Since a large amount of waste is produced per kg of product in various segments of the chemical industry (Table 1.2) [9], legislation is being increasingly used to lower the amounts of dangerous compounds released into the environment. Catalysts are expected to be more environmentally friendly by effectively reducing the amount of undesirable by-products. Therefore the utilization of heterogeneous catalytic systems, known to be green and environmentally friendly is growing rapidly [19]. Heterogeneous catalysts are greener, because their simple recovery process and high reusability [21] reduces waste during recovery and regeneration stages. They are also efficient because their long life-time minimizes environmental problems and reduces plant maintenance. A good example of introducing a heterogeneous catalyst is introduction of silver (Ag) as a catalyst in the oxidation of ethylene in the petrochemical industry. The new catalyst, combined with O<sub>2</sub> as oxidant, improved the atom utilization<sup>1</sup> from 25% (using Cl<sub>2</sub>, H<sub>2</sub>O and Ca(OH)<sub>2</sub>) to 100% and the E-factor, kg waste per kg product, decreased from 3 to zero.

Most heterogeneous catalysts being used in industry are metal-based catalysts, mainly transition metals or metal oxides [22]. This makes transition metal/metal oxide of great importance technologically, which motivates extensive investigations in this specific catalysis field. These catalyst materials are either used as bulk materials or supported on mesoporous metal oxides such as alumina [23-25], titania [25, 26], zirconia [27, 28], CeO<sub>2</sub> [28-30], clays [31-33] zeolites [34, 35], carbon nanotubes [36], amorphous silica [37] or highly ordered mesoporous silica [38-41]. The catalytic activity is due to specific active sites, so that, in order to optimize the catalytic activity, it is crucial to maximize the accessibility of the active sites to the reactants. This highlights the importance of high dispersion of the active sites on a

<sup>1</sup> **Atom utilization** = molecular weight of the desired product / molecular weight of all the products

high surface area support with porous structure large enough to facilitate the diffusion of the reactants to the active sites [42].

**Table 1.2** Industrial waste [9]

<b>Industry</b>	<b>Product (tonnage)</b>	<b>kg waste/kg product (E-factor)</b>
<b>Pharmaceuticals</b>	10-10 <sup>3</sup>	< 1-5
<b>Fine chemicals</b>	10 <sup>2</sup> -10 <sup>4</sup>	5 - > 50
<b>Bulk chemicals</b>	10 <sup>4</sup> -10 <sup>6</sup>	25 - > 100
<b>Oil refinery</b>	10 <sup>6</sup> -10 <sup>8</sup>	Ca.0.1

Generally speaking the rate of the catalytic reaction in heterogeneous systems in which the active sites are dispersed on the support depends on the following rates: (i) diffusion rate of the reactants through the porous network to the active sites (ii) diffusion rate of the reactants to the surface of the catalysts, (iii) chemisorption rate of the reactants to the surface of the active sites, (iv) formation rate of the active intermediates, (v) rates of transformation to the product(s) (vi) desorption rate of the product(s) from the surface of the active sites, (vii) diffusion rate through the porous structure and (viii) diffusion rate of the product(s) into the bulk solution [19, 21].

Different factors could affect each step of the above mentioned catalytic process; the molecular size of the reactants and the pore size of the catalyst/support could have impact on step (i) and (vii) whereas the chemical nature of the reactants and product(s) together with their chemical compatibility with the active sites could influence steps (iii) and (vi). The accessibility and dispersion of the active sites and the catalyst particle size, as well as, the concentration of the reactants/product(s), control steps (ii) and (viii).

The slowest of the eight steps determines the rate of the reaction. Hence, it is of utmost importance to determine which step controls the reaction rate, in order to be able to optimize the reaction conditions and thereby obtain the best catalytic performance. It is generally accepted that due to the large number of diffusion steps, heterogeneous catalytic reactions are often slower than their homogeneous analogues [43].

Despite the advantages of heterogeneous catalysts, they are susceptible to loss of activity. The factors responsible for this include poisoning, fouling, aggregation of active sites leading to a reduction in surface area, pore blockage and, last but not least, loss of active species by leaching [44].

## 1.4 Catalytic oxidation reactions

There is an intimate relationship between the petroleum and chemical industries since large scale of the primary organic chemicals are derived from petroleum and natural gas sources [45]. Selective oxidation of alcohols and olefins is a class of exquisite atom-efficient molecular transformations (Figure 1.2). The resulting aldehyde, ketone, ester and acid products are valuable intermediates for the fine chemical, pharmaceutical, food and agrochemical industries [23, 46-55]. For example, allylic aldehydes are valuable components used in the perfume and flavourings industries [49, 50].

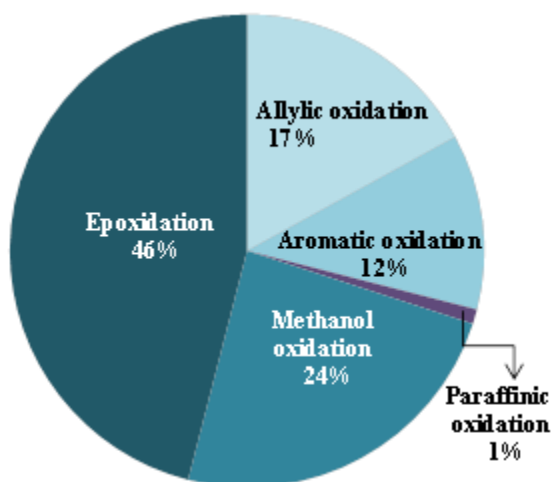


**Figure 1.2.** Heterogeneous oxidation reactions in industry

Generally catalytic oxidation reactions represent one of the most important challenges in green chemistry, since commercial oxidation reactions often utilize non-catalytic procedures to oxidize alcohol and olefins [56]. These often rely on hazardous/toxic stoichiometric oxidants such as chromates, permanganates and peroxides in the presence of mineral acids [57]. In addition to safety considerations, these technologies are also atom inefficient due to the poor selectivity and difficulty in separation of the products. Furthermore, large amounts of wastes such as toxic metal salts are produced due to the additional treatment steps required to purify and isolate the products. These additional purification steps are also economically disadvantageous. Such problems make it a matter of urgency to replace conventional homogeneous systems with oxidation reactions catalysed by solid materials.

It is generally accepted that oxidation reactions in the bulk and fine chemical industries are quite different. Fine chemicals are multifunctional molecules, in which regio, chemo and stereoselectivity may be required in producing the desired products [10]. Additionally the catalytic process has to be designed to take into account the high boiling point and limited thermal stability of the initial reactants and products and also the impact of the various

oxidants on them. There are several different oxidants ( $\text{H}_2\text{O}_2$ ,  $\text{O}_2$ ,  $\text{O}_3$ , tert-butylhydroperoxide (TBHP), sodium hypochlorite ( $\text{NaClO}$ ) and iodobenzene diacetate (PhIO) that can be utilized in oxidation reactions. The choice of oxidants is influenced by (i) their price, (ii) simplicity of the operation, (iii) the nature of the by-products and (iv) the percentage available oxygen.

While oxygen is the most environmentally friendly oxidant, there are few selective catalytic oxidation reactions that use  $\text{O}_2$  as an oxidant [58].  $\text{H}_2\text{O}_2$  is known to be the cleanest oxidant since the generated by-product is water. TBHP is also relatively clean, because it produces t-butanol as a by-product, which can be simply recycled to TBHP through oxidation using  $\text{H}_2\text{O}_2$ . TBHP and  $\text{H}_2\text{O}_2$  can be utilized in liquid phase oxidation reactions via an oxygen transfer mechanism [59, 60].

One of the first heterogeneous oxidative catalysts used to catalyze olefin epoxidation and alcohol oxidation in the presence of  $\text{H}_2\text{O}_2$  was titanium silicate (TS-1) [61, 62]. Platinum and palladium on charcoal were used for aerobic oxidation of gluconate to 2-ketogluconate [63]. Zeolite titanium beta (Ti-beta) was utilized for epoxidation of various alkenes in the presence of  $\text{H}_2\text{O}_2$  [64]. While this catalyst showed effective results for small alkenes, for large alkenes steric hindrance limited the effectiveness of the catalyst.

Vanadium was intercalated on montmorillonite, a mineral clay, and used as an effective heterogeneous catalyst to epoxidize/oxidize olefins and benzyl alcohol [65]. Chromia-montmorillonite was also reported to catalyze the oxidation of alcohols to their corresponding aldehydes and ketones in the presence of TBHP [66]. Zeolite NaX with encapsulated  $\text{Co}^{2+}$  catalysed the oxidation of 2,6-dialkylphenols by TBHP [67]. It was also reported that due to the steric hindrance inside the zeolite cage dimerization decreased drastically and the selective product was 1,4-benzoquinone. Iron-modified ZSM-5 zeolite (FeZSM-5) was used as a heterogeneous catalyst to oxidize benzene to phenol in the presence of nitrous oxide ( $\text{N}_2\text{O}$ ) as an oxidant [68]. It was shown that Bronsted acid centres (BAC) did not play a key role in the oxidation mechanism and that it was governed by a redox mechanism. Through this mechanism  $\text{O}_2$  was formed on the Fe active sites via the decomposition of  $\text{N}_2\text{O}$ . Vanadium silicate molecular sieves have been shown to catalyze alkane oxidation with  $\text{H}_2\text{O}_2$  [69]. Nafion K was impregnated with  $\text{Cr}^{3+}$  and  $\text{Ce}^{4+}$  to catalyze the chemoselective oxidation of a variety of unsaturated alcohols using TBHP as oxidant [70].

## 1.5 Metal oxides

Metal oxides, more specifically transition metal oxides, are technologically and industrially important compounds in material science, physics and chemistry [71-74]. Metal oxides can be used as heterogeneous catalysts, either bulk or supported [75, 76]. Transition metal oxides can be used in a wide range of applications, as electrodes in electrochemical processes [77], in fabrication of fuel cells and microelectronics circuits, as anti-corrosion coating, and as semiconductors and sensors in various sectors of industry [72, 78-82].

In the fine chemical and petroleum industries metals and metal oxides are used as catalysts to generate valuable intermediates and products, which are worth billions of dollars each year. It is noteworthy that many transition metal oxides are cheaper than noble metals. Due to environmental legislation, the amount of pollutants produced by industry has to be more strictly controlled than in the past and metal oxides are promising candidates to remove heavy metals from industrial and other wastewater [83-85] and CO, NO<sub>x</sub> and SO<sub>x</sub> species from the flue gas, generated during fossil-derived fuel combustion [86-88].

In catalysis applications some key properties of metal oxides are very crucial:

- (i) The surface chemistry of the metal oxide. This indicates the co-ordination environment. The interaction of various reactants (adsorbates) with the surface, the possibility of lattice oxygen mobility, the oxygen mobility energy, the acidity or basicity of the metal oxide surface, the occurrence of any vacancies on the surface and the likelihood of adsorbing charged species on the surface of the metal oxides are important properties of the surface of the metal oxide for catalytic applications. Due to the critical impact of the metal oxide surface on catalytic properties, an enormous effort has been made to investigate and understand the surface of the metal oxides [75, 89-97].
- (ii) Redox properties of metal oxides. These are important characteristic of the transition metal oxides and are due to the multiple possible oxidation state of many transition metal cations. Thus the metal ions can undergo oxidation and subsequent reduction. As a result of the redox cycle in metal oxides some vacancies are formed inside the crystal lattice, which in turn facilitate catalytic reactions, more specifically oxidation reactions [98-100]. The redox property of metal oxides is related to their acid-base properties. Cations in the metal oxides are Lewis acids whereas the lattice oxygen anions are Lewis bases. The oxidation state of cations affects their acidity and size.

(iii) Oxidation state of the metal oxide surface. The oxidation state of the metal cations on the surface indicates their electronic properties, which in turn determine how adsorbates may bond with the surface.

(iv) The geometric structure of the oxide. Metal oxides commonly suggested as catalytic materials come from many structural classes including corundum, rocksalt, wurtzite, spinel, perovskite, rutile and layer structure [101]. One general structural property of transition metal oxides is that the cation radius is smaller than the  $O^{2-}$  radius. As a result oxygen ions are close packed, with the cations located in the tetrahedral or octahedral holes in the  $O^{2-}$  lattice.

### 1.5.1 Surface co-ordination in metal oxides

One of the most important features in metal oxide surface chemistry, as discussed previously, is the surface co-ordination. This has a crucial impact on the catalytic activity of the metal oxide. Generally, it is an accepted concept in co-ordination chemistry that only a certain number of ligands can be present within the co-ordination sphere of a metal ion, due to steric and electronic reasons [102, 103].

In the bulk the  $O^{2-}$  anions have a saturated co-ordination sphere via  $M^{n+}$  cations. This is attributed to the cations occupying the holes in the anion lattice (See 1.5, iv). On the surface, however surface cations and anions have unsaturated co-ordination spheres. This normally occurs during calcination of the metal precursor solution at elevated temperature, where condensation of monomeric units results in the formation of a 3D network. The dehydrogenation between two or more adjacent hydroxyl groups on the surface at high temperature results in the existence of unsaturated cations and anions [104].

At ambient temperature these metal oxide surface sites are fully covered by water and hydroxyl anions due to exposure to atmospheric moisture. At temperatures less than 100 °C, the surface of the metal oxide is activated through the loss of weakly adsorbed water molecules which are held to the surface via hydrogen bonding. As the temperature increases to 200-300 °C, the metal oxide surface undergoes dehydroxylation. Finally at higher temperatures above, 400 °C, the isolated hydroxyl groups are lost [105].

### 1.5.2 Types of adsorption on the surface

Generally there are four main types of adsorption on the surface of the metal oxide [21];

(i) Nondissociative adsorption in which the adsorbate molecule does not dissociate. The adsorbate bonds with the surface mainly through  $\pi$  or lone pair orbitals.

(ii) Dissociative adsorption where the adsorbate molecule dissociates on adsorption on the surface. For this process to occur, co-ordinatively-unsaturated cations and anions must exist in pairs on the surface of the metal oxide. These are needed to accommodate the anions and cations of the adsorbate, which are formed via heterolytic dissociation.

(iii) Absorptive adsorption, where species on the metal oxide surface, typically protons, are abstracted by the adsorbate. As a consequence, the adsorbate interacts with the surface electrostatically.

(iv) Reductive adsorption associated with the oxidation of the adsorbate molecules by the lattice oxygen and subsequent reduction of the cations. This is a consequence of the multiple possible oxidation states of the cations in the transition metal oxide. This type of adsorption normally occurs on the surface of transition metal oxides. This phenomenon has been observed for methanol [106], ethanol [105] and propanol [107] oxidation on the surface of metal oxides.

### **1.5.3 Oxidation reactions on metal oxides surfaces**

Selective hydrocarbon oxidation on the surface of metal oxides acting as heterogeneous catalysts has received pronounced attention in the last three decades [108, 109]. In industry, it is of utmost importance to produce desirable products such as alcohols, aldehydes, ketones and carboxylic acids more selectively. Hence, it is essential to comprehensively understand the nature of the catalyst, such as availability of the active sites, kinetics of the redox cycle and nature of the intermediates generating during the catalytic reaction to aid the development of a catalytic system with high activity and selectivity [110, 111]. It is also important to have an in-depth insight into the physical properties of the catalyst such as thermal, hydrothermal and mechanical stability, the degree of porosity, pore size, pore shape and surface area so as to be able to optimize the kinetics of the reaction. This knowledge also facilitates to investigate the impact of these variables on the catalytic activity of the catalyst.

Currently various metal oxides are used as oxidation catalysts in industry, for instance; magnesium oxide (MgO) doped with lithium (Li) is a useful catalyst for oxidative coupling of methane [112]. Titania supported vanadium oxide is also used for catalytic oxidation of O-xylene to phthalic anhydrous [113-116].

### **1.5.4 Type of oxidation reactions**

Basically there two main types of oxidation reactions;

- (i) Dehydrogenation reactions, where a saturated hydrocarbon molecule becomes unsaturated [117]. This occurs through losing one or more hydrogen atoms. The by-product of this catalytic reaction is water, if oxygen or hydrogen peroxide is used as an oxidant.
- (ii) Oxygen insertion into the hydrocarbon [118], followed by dehydrogenation. Various types of oxygen can be used for these reactions such as the environmentally friendly molecular oxygen and hydrogen peroxide. Alkoxy peroxides, which are converted to the corresponding alcohols, can also be used.

### 1.5.5 Oxidation mechanism on the surface of metal oxides

In the presence of gaseous oxygen, the metal oxide surface is oxidised by adsorbing oxygen as  $O^-$ ,  $O_2^-$  or as lattice oxygen,  $O^{2-}$  (Eq. 1.1). Subsequently the oxygen atom transfers and incorporates into the products, which desorb from the surface in the next step. Upon desorption of the oxidized products the surface acquires electron(s), which in turn reduce the cations on the surface (Eq. 1.2). In other words, in one catalytic cycle a surface cation is oxidized and then reduced over many cycles, facilitating the transfer of oxygen from one entity to another. This phenomenon is known as a “redox cycle”[119]. The redox cycle may be expressed by the following chemical equations: where Ox-O refers to the oxidant, Catal-O indicates the surface of the catalyst and Red denotes reductant which is the substrate in most oxidative reactions.



Figure 1.3 demonstrates the catalytic redox mechanism on the surface of the metal oxide. This mechanism was first suggested by Mars and van Krevelen [100]. According to the Mars and van Krevelen mechanism the oxidant does not directly oxidize the substrate, but generates the oxygen which fills anion vacancies on the surface of the metal oxide lattice [120]. The lattice oxygen, however, is responsible for the substrate oxidation. In order to facilitate such a mechanism the existence of a cation with multiple oxidation states and high lattice oxygen mobility is necessary [117]. The kinetics of the redox process depend on various factors such as the reactivity of the substrates with oxygen, the concentration of the substrate, electron transfer efficiency and the partial pressure of oxygen. However, it is generally accepted that the redox process is faster than the oxidation of the substrate.

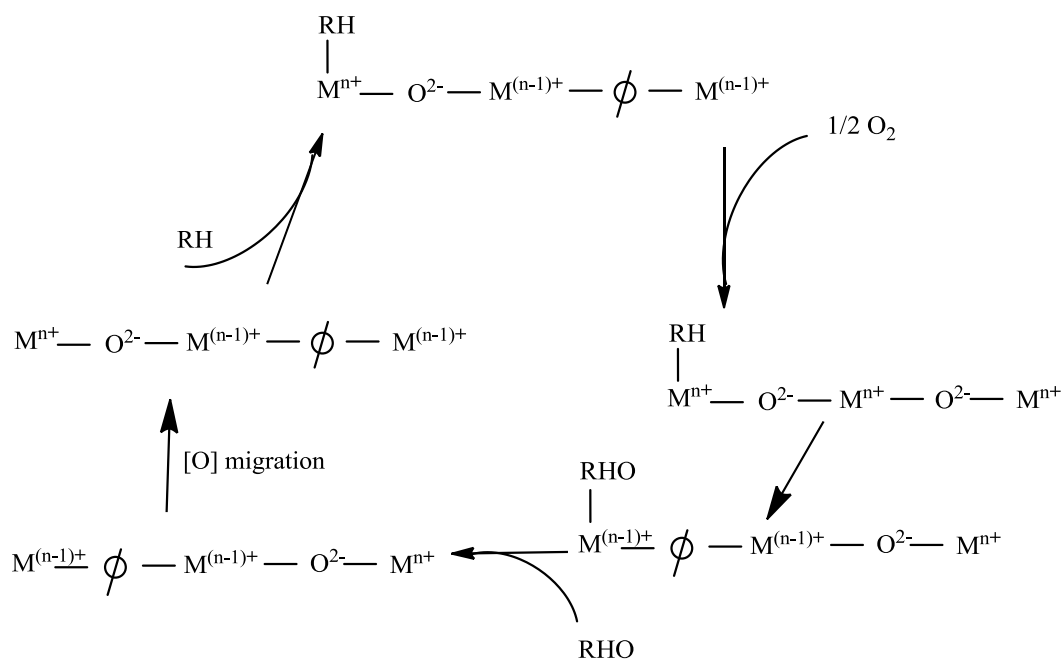


**Figure 1.3.** Schematic redox cycle, Mars and van Krevelen mechanism, on the surface of the metal oxide [100]

In oxidative catalysis some factors are known to play important roles in both catalytic activity and selectivity;

- (i) metal-oxygen (M-O) bond strength,

As discussed above it is the lattice oxygen which contributes the oxygen incorporated in the product. As a result the strength of the M-O bond affects the catalytic performance. The stronger the M-O bond, the less active the catalyst is expected to be [121].

- (ii) availability of the active oxygen,

The availability of a moderate amount of oxygen for the oxidative reaction is important in performance and selectivity of the catalyst. If there is too much active oxygen, the surface may be over-oxidized. If the amount of active oxygen is insufficient, the oxidation reaction may not proceed to completion [122].

- (iii) acid-base properties of the metal oxide surface,

The surface of the metal oxide contains a number of Lewis acid and base sites, which interact with the reactants to activate them through adsorption [102]. However, once the product is formed on the surface of the metal oxide it should be desorbed promptly. As a result the strength of the acid-base sites is important in determining the rate of reactant adsorption/activation the rate of product desorption.

- (iv) type of oxygen available on the surface of the metal oxide,

As noted above several different oxygen species can occur on the metal oxide surface or in the bulk [123]. Depending on the oxidation state and co-ordination environment of the metal ion, the metal-oxygen (M-O) bond can be polarized to some extent, so that the oxygen can possess electrophilic or nucleophilic properties.

Adsorbed oxygen species  $O^-$ ,  $O_2^-$  are classified as electrophilic. These are known to be very active and participate in extrafacial reactions, in which only adsorbed surface oxygen involves in the catalytic reaction. The lattice oxygen,  $O^{2-}$ , however, is classified as nucleophilic, and participates in interfacial reactions, which tend to be slower and give partial rather than complete oxidation.

## 1.6 Different types of supports

Various type of supports, more preferably of high surface area, have been used to either heterogenized the homogeneous catalysts or highly disperse bulk metal, metal oxides or organometallic complexes [11, 124]. Supported systems also improve poison resistance, therefore tending to increase the life-time of the catalyst. There are advantages in depositing catalytically active metal/metal oxides on supports with high surface area. Through this process the active sites can be highly dispersed, possibly as small particles throughout the porous system of the support [125]. Consequently, a large active metal surface is produced relative to the volume of the active catalyst due to its high dispersion [126].

Porous materials such as zeolites and mesoporous silicas are favourable as supports for depositing catalytically active materials due to their high surface area [127]. The advantages of mesoporous silicas over zeolites are attributed to their larger and adjustable pore size [128, 129], various pore shapes [130] and highly ordered and uniform pore structure [131, 132].

There are basically two types of pores: (i) open pores with a connection to the surface of the material and (ii) closed pores which are isolated and have no connection to external surface of the particle. The first group of porous materials are more useful in catalysis, adsorption, filtration, membranes and sensing applications [133]. Various shapes have been suggested for pores, such as cylindrical, spherical and slit-like and also more complicated structures, for instance, cage-like and cubic [130].

The International Union of Pure and Applied Chemistry (IUPAC) has classified pores into three classes based on the pore diameter [134]:

- (i) Micropores, with pore diameter smaller than 2 nm
- (ii) Mesopores, with pore diameter in the range 2-50 nm and

(iii) Macropores, with pore diameters more than 50 nm.

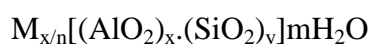
In addition to the advantage of large surface area discussed above, metal/metal oxide catalysts supported on porous materials, compared to their bulk analogues have the additional advantage of having the individual catalyst particles isolated from each other in the pores. This hinders the sintering of active particles into larger particles of reduced active surface area during calcination at high temperature [39, 135-138].

This property of supported active catalyst is also important because the size of the particles plays a key role in their catalytic activity. Particles with a size range of 1-50 nm exhibit physical and chemical properties that are intermediate between those of the single molecules and those of the bulk material [139]. Catalytic performance can be sensitive to the particle size as the surface structure and electronic properties can alter greatly in this size range. Gold (Au) nanoparticles supported on titania are reported to show the highest catalytic activity for oxidation of CO to CO<sub>2</sub> where the Au particle size is 2-3 nm [140].

Various approaches have been investigated for depositing the metal ions (active sites) onto a solid material, support, (see section 1.6.5). However, it is noteworthy that the support should be chosen after careful consideration, since the nature of the support (pore size, pore shape, surface area and surface properties) plays a crucial role in the catalytic performance of the final catalysts.

### 1.6.1 Zeolites

The term zeolite describes the family of crystalline aluminosilicates, with the structure based on an infinitely extending, 3D, network of AlO<sub>4</sub> and SiO<sub>4</sub> tetrahedrons linked together via shared oxygens [141]. The structural formula of a crystallographic unit cell of zeolite is expressed in terms of the oxides.



where M is a cation of valence n, m is the number of water molecules and the sum of x and y is the total number of tetrahedrons in the unit cell.

The framework contains channels and interconnected voids, which are occupied by cations and water molecules. In addition, having micropores of diameter in the range of molecular dimension, zeolites are known to possess valuable properties of shape selectivity [142]. The cations in zeolite can be replaced to a varying degree through exchanging them with other cations [143]. The intracrystalline water can be removed but doing this may affect the channel system, since many zeolites after dehydration contain very small channels. These

small channels may contain a diffusion block, which means they are not interpenetrating. The structure of many zeolites is collapsed after complete dehydration as a result of disturbance of the metal cations [144].

Few zeolites have been studied scientifically in enough detail to be employed in industry [145]. The main criterion for suitability for commercial application has been structural stability [146, 147].

The size of the zeolite pore has been used to classified zeolites [148];

- large-pore zeolites: X, Y and L
- small-pore zeolites: A and erionite

Industrially, the first group is used in hydrocarbon conversion catalysis whereas the second group is of interest in shape selective catalysis [127].

#### **1.6.1.1 Zeolite X and Y**

The framework structure of types X and Y is related to that of the mineral faujasite. These types of zeolites have a cubic unit cell, with the very large lattice parameter of 25 Å, which contains a total of 192 SiO<sub>2</sub> and AlO<sub>4</sub> tetrahedra [149]. Their framework structure leads to the presence of largest void space among zeolites, 50 vol % of the crystal. The SiO<sub>2</sub>/Al<sub>2</sub>O<sub>3</sub> molar ratio is between 2 and 3 for type X and between 3 and 6 for type Y. The unit cell contains eight large cavities with diameter of 13 Å, which are interconnected by apertures of twelve-membered oxygen rings with 7.4 Å free diameter [150].

#### **1.6.1.2 Zeolite A**

The unit cell of type A is formed by truncated octahedra joined by double four-membered rings. The three-dimensional channel system includes large cavities with a free dimension of 11 Å, which are separated by apertures formed by eight-membered oxygen rings, with free dimension of 4.2 Å. Some of the cations in type A are located close to the apertures and thus any change in the nature of these cations is likely to change the adsorption characteristics of the zeolite [151].

#### **1.6.1.3 Erionite**

The framework of this zeolite consists of repeat units of two six-membered rings and a single six-membered ring in parallel planes, which are perpendicular to the hexagonal axis. This arrangement produces a 3D pore system containing cavities of 15.5×6.3 Å in dimension.

The SiO<sub>2</sub>/Al<sub>2</sub>O<sub>3</sub> molar ratio of 6 makes it one of the most siliceous zeolites. This zeolite is thermally very stable [151].

### **1.6.2 Carbon nanotubes**

Graphite is a carbon allotrope with a two-dimensional (2D) structure, in which sp<sup>2</sup>-bonded carbon sheets interact with each other by Van-der-Waals interactions. As a result of this weak inter-layer interaction, graphite is a mechanically soft material which is used among other places in pencil. Due to its high melting point [152] and good electrical conductivity [153-155] it is also used in the electrodes of arc lamps and arc furnaces. A simple way to describe carbon nanotubes (CNT) is by imagining that a small sheet of a graphite monolayer is isolated and rolled into a nanometer-scale diameter tube [156]. The CNTs are among the most resilient and strongest materials known to exist in nature. The electronic properties of the CNT are completely determined by the tube geometry, resulting in semiconducting or metallic character [157].

Generally, due to their favourable mechanical properties, large surface area and high electrical conductivities CNTs have tremendous potential for a wide range of applications such as composite materials [158], hydrogen storage [159], and as catalyst supports [160]. Ceria nanoparticles were supported on CNTs and reported to show high adsorption capacity for Cr(VI) from drinking water [161]. Zeng et al. demonstrated that CNT can be used as a primary support to prepare binary, ternary and even more complex metal oxide nanocomposites. In these nanocomposites the particle shape, size and distribution can be controlled by varying processing time and the ratio of metal oxide nanoparticles/CNT [162].

CNT supported metallic cobalt was prepared using Co(NO<sub>3</sub>)<sub>2</sub>.6H<sub>2</sub>O as the metal precursor. The resulting materials were used as a catalyst for FTs [163]. It was reported that the cobalt particle size played a key role in the activity and selectivity of the catalyst. The optimum size of the cobalt nanoparticles was determined to be 6-8 nm since smaller particles showed lower activity and selectivity, whereas larger particles demonstrated lower activity.

### **1.6.3 Mesoporous metal oxides**

Ordered mesoporous metal oxides have been the basis of extensive research efforts over the last decade [41, 164, 165]. In this respect mesoporous transition metal oxides, specifically those with crystalline frameworks have unique physicochemical properties [166]. These can be attributed to their high surface area, porous structure as well as optical and electronic properties compared to bulk transition metal oxides. The porous structure facilitates the mass

transfer of the reactants whereas the high surface area provides a large number of accessible active sites with which the reactants can interact. In addition, transition metal oxides are capable of existing in various oxidation states due to availability of empty d orbitals, which facilitates electron transfer between reactants and active sites [167, 168]. All the above mentioned factors have a crucial impact on catalytic performance of the mesoporous metal oxides.

These materials have an immense number of applications in catalysis, molecular sorption, sensors, electrode materials and nanodevices [169-173]. It was shown that transition metal oxides with highly crystalline walls are more efficient in photocatalysis and this is attributed to the more efficient charge transfer in crystalline materials [174]. This is an important incentive to produce crystalline mesoporous metal oxides.

A common method to fabricate a mesoporous metal oxide is as follows:

- (i) Preparation of any type of mesoporous silica such as MCM-41, SBA-15 or SBA-16 as a hard template.
- (ii) Nanocasting of the metal oxide inside the pores of the mesoporous silica via various methods such as the multiple impregnation solid-liquid method for specific metal precursors [175], the “two-solvent” method [176] and the evaporation method [177]. Finally calcination at high temperature facilitates oxide formation through decomposition of the metal precursor, during which crystallization of the metal oxide takes place to some extent.
- (iii) Removal of the hard template by using HF (10 % aqueous solution) at room temperature.(RT) or NaOH (2M) at 70-90 °C [178].

Mesoporous metal oxides can also be fabricated using an organic template, but these mesoporous oxides are either amorphous or semicrystalline [179]. This is attributed to the fact that if the temperature exceeds 400 °C, the organic template decomposes, which leads to the collapse of the structure of the mesoporous silica.

Mesoporous  $\text{Co}_3\text{O}_4$  was prepared using KIT-6 silica as a hard template via the two-solvent method and exploited to catalyse CO oxidation. The catalytic performance was reported to depend on the texture of the mesoporous  $\text{Co}_3\text{O}_4$ . The samples with higher surface area and a more open porous system showed higher activity due to the accessibility of more active sites for the reactants [178].

Xia et al. fabricated 3D mesoporous  $\text{Co}_3\text{O}_4$  using KIT-6 and SBA-16 as a hard template. It was shown by low-angle XRD that the structure of the resulting  $\text{Co}_3\text{O}_4$  resembled the

mesoporous structure of KIT-6 and SBA-16. In addition, it was demonstrated that mesoporous  $\text{Co}_3\text{O}_4$  had higher catalytic activity than bulk  $\text{Co}_3\text{O}_4$  for toluene and methanol oxidation even at low temperature. It was suggested that, due to higher surface area, there are more active sites on the surface with adsorbed oxygen ( $\text{O}_2^-$ ,  $\text{O}^-$ ), which can accordingly facilitate the catalytic reaction [180].

Mesoporous  $\text{CeO}_2$  was prepared using KIT-6 as a hard template via impregnation. This  $\text{CeO}_2$  was used as a catalyst for CO oxidation, where it demonstrated higher catalytic activity than  $\text{CeO}_2$  prepared simply via direct decomposition. It was also shown that CuO can be homogeneously dispersed on the mesoporous  $\text{CeO}_2$ , which increased the catalytic performance in comparison with neat mesoporous  $\text{CeO}_2$  [181].

Recently, a simple method for fabricating highly crystalline mesoporous titania ( $\text{TiO}_2$ ) and niobium oxide ( $\text{Nb}_2\text{O}_5$ ) was reported [182]. These methods use polystyrene block-poly(ethylene oxides)s, PS-b-PEOs, as a structure directing agent. It was shown that various mesoporous  $\text{TiO}_2$  and  $\text{Nb}_2\text{O}_5$  samples, all with highly crystalline structure and a range of average pore sizes could be successfully synthesized. This was attributed to the template characteristics. Using PS-b-PEOs as a template provides the possibility of tuning the pore size of the final materials by varying polystyrene chain length. This in turn increases the hydrophobicity differences inside each block, which affects micelle formation [183]. The template was reported to decompose during heat treatment to amorphous carbon, which in turn acted as a hard template to prevent structural collapse of the mesoporous material at high temperature and also facilitated crystallization [82].

There are some potential disadvantages in using metal oxides as supports. For instance, there might be a strong interaction between the support and the active site, which could decrease the catalytic performance [184, 185]. Additionally the formation of mesoporous metal oxides as a support is a multistep process and might result in either the formation of materials with less crystallinity or a complete collapse of the mesoporous structure.

#### **1.6.4 Ordered mesoporous silica (OMS)**

There are some severe limitations involved in using zeolites as supports, mainly due to the small pore diameter of less than 2 nm [186]. This is especially problematic when large molecules need to be immobilized inside the pores. This is often the case in liquid phase reactions due to limitations in mass transfer inside the micropores [187]. Because of these shortcomings of zeolites, there is a requirement for supports with larger pore size, which will

allow larger molecules to enter the pores, process there and leave the porous system afterwards.

Ordered mesoporous silicas with high surface area and adjustable pore size were first described by scientists in the Mobil Oil Corporation in 1992. They discovered a family of materials (M41S) with highly ordered hexagonal arrays of mono-dispersed pores with a very narrow pore size distribution (PSD). The first ordered mesoporous material synthesized was MCM-41 which stands for Mobil Composition of Matter No. 41 [41, 128]. Over the next few years more robust materials were synthesized. In 1998, researchers at UC Santa Barbara, discovered a new family of mesoporous silicas SBA-X, where SBA stands for Santa-Barbara Amorphous Material and X refers to the material code [40, 129].

The formation of mesoporous materials is generally based on a liquid-crystal template (LCT) mechanism [128], by which the organic templates, effectively surfactants, form micelles. Upon adding a silicate precursor, the amorphous walls are generated on the micelles through hydrolysis and polymerization of the silicate precursor. The elongation of the micelles and polymerization of the silicate precursor continue during the hydrothermal treatment process and finally the as-synthesized mesoporous silica is recovered by filtration. To obtain the final mesoporous silica the template should be removed from the pores, which can be done in several ways (see section 1.6.4.3.2).

The organic templates (surfactants) are mostly cationic, such as cetyltrimethylammonium bromide in basic environment for the formation of M41S families. In contrast to this, non-ionic triblock copolymers, amphiphilic templates, are used to synthesize SBA-X families in a highly acidic environment.

Non-ionic triblock copolymers were patented in 1973 [188] and contain both hydrophilic (polyethylene oxide, PEO) and hydrophobic (polypropylene oxide, PPO) chains with various PEO/PPO ratios and different molecular weights. The commercial names of these polymers start with a letter followed by two or three numbers. The letters describe the polymer appearance, for instance, F (flake), P (paste) and L (liquid). The first one or two numbers multiplied by 300 give the PPO block molecular weight, whereas the last number refers to the PEO weight fraction [189]. Since the hydrolysis of methyl groups in both PEO and PPO blocks is temperature dependent, the properties of the PEO and PPO blocks are highly dependent on the applied temperature [190, 191].

Generally, for the ordered mesoporous silica to be formed, the interaction between the organic surfactant and the inorganic silicate (S/I interaction) is critical. This interaction is

summarized in Table 1.3. These chemical interactions are referred to as electrostatic ( $S^+I^-$ ) or ( $S^+XI^-$ ) [192, 193], hydrogen bonding ( $S^0I^0$ ) [194-196] and hydrogen-bonding electrostatic interactions ( $(S^0H^+)(XI^-)$ ) [129, 197].

**Table 1.3** Organic surfactant/inorganic silicate precursor interaction type for various mesoporous silicas

S/I Interaction	Type of mesoporous silica	S:I precursor	Reaction environment
$S^+I^-$	MCM-41	CTAB <sup>1</sup> : Sodium silicate	Basic
$S^+XI^-$	SBA-3	CTAB : TEOS <sup>2</sup>	Acidic
$S^0I^0$	HMS	Dodecylamine : TEOS	Neutral
$(S^0H^+)(XI^-)$	SBA-15	Pluronic P123 <sup>3</sup> : TEOS	Acidic

<sup>1</sup>cetyltrimethylammonium, or hexadecyltrimethylammonium bromide

<sup>2</sup> tetraethylorthosilicate

<sup>3</sup> HO-poly(ethylene oxide)<sub>20</sub>-poly(propylene oxide)<sub>70</sub>-poly(ethylene oxide)<sub>20</sub>

#### 1.6.4.1 Hexagonal mesoporous silicas (HMS)

Hexagonal mesoporous silicas (HMS) are prepared by a neutral  $S^0I^0$  templating route in which the neutral organic surfactants ( $S^0$ ) are primary amines [132]. In the course of synthesis hydrogen-bonding interactions between  $S^0$  and a neutral inorganic precursor ( $I^0$ ) take place in the self-assembly step [194, 198]. The organic phase can be easily removed from the HMS by solvent extraction due to the absence of strong electrostatic interactions. This prevents the partial degradation of the HMS structure which would otherwise occur during the calcination process. HMS exhibits a wormhole-like pore structure and compared to MCM-41 is less ordered. However it also shows more thermal stability and faster diffusion rate of the reactants due to shorter length mesopores [41]. These materials have strong potential for applications in catalysis due to their high surface area and uniform mesoporous structure [132].

#### 1.6.4.2 MCM-41

As mentioned previously in section 1.6.4, MCM-41 belongs to the first group of ordered mesoporous silicas, which was invented by Beck et al [128]. This material has a high surface area of up to  $1400 \text{ m}^2 \text{ g}^{-1}$  [199] and hexagonal arrays of cylindrical pores with narrow PSD. The pore diameter and the wall thickness of MCM-41 can be varied between 3-4 nm and 1-2 nm respectively, and so can be tailored to the specific application required (Figure 1.4) [200].

MCM-48 is another mesoporous silica reported by the same group with cubic mesostructures structure [41]. It has a 3D channel network [201], interwoven cubic pore structure [202, 203], a pore volume of  $1.2 \text{ cm}^3 \text{ g}^{-1}$  [204]. This favours mass transfer and high accessibility of the active sites when the material is used as a support for larger guest molecules. However the complexity of MCM-48 preparation process makes it less favourable as a support than MCM-41.

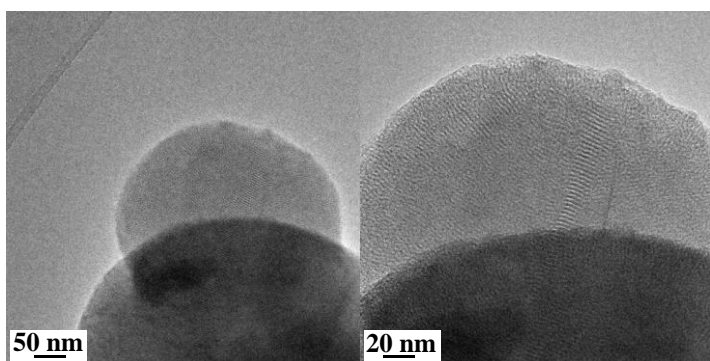


**Figure 1.4.** TEM images of MCM-41[205]

#### 1.6.4.3 SBA-15

The development of the OMS family SBA-X was another breakthrough in the mesoporous silicas field [40, 129]. This family of mesoporous silicas is prepared mainly by using non-ionic triblock copolymer surfactants (Pluronics) comprising of poly (ethylene oxide)<sub>x</sub>-poly(propylene oxide)<sub>y</sub>-poly(ethylene oxide)<sub>x</sub>, (PEO)<sub>x</sub>(PPO)<sub>y</sub>(PEO)<sub>x</sub>, in an acidic environment. Various triblock copolymers have been employed to synthesize different SBA-X frameworks such as SBA-11 using C<sub>16</sub>EO<sub>10</sub>, SBA-12 and SBA-14 using C<sub>16</sub>EO<sub>10</sub> and C<sub>12</sub>EO<sub>4</sub> respectively and finally SBA-15 and SBA-16 from EO<sub>20</sub>PO<sub>70</sub>EO<sub>20</sub> and EO<sub>106</sub>PO<sub>70</sub>EO<sub>106</sub> respectively [129, 206, 207].

Among these mesoporous silicas, SBA-15, with its highly regular mesoporous structure, has been the subject of many studies, due to its simple preparation procedures and various applications in drug delivery and heterogeneous catalysis. SBA-15 has a high surface area of  $600\text{-}1000 \text{ m}^2 \text{ g}^{-1}$ , It has thicker pore walls (3-7 nm), higher thermal and hydrothermal stability and also larger tuneable pore sizes, in the range 6-30 nm than the M41S families. The pore size of SBA-15 can be tuned by changing the time and temperature of the hydrothermal process [208], using a swelling agent [209], using co-surfactant [210] or by using alkenes [211].

The triblock copolymer which has been used as an organic template for SBA-15 synthesis is relatively inexpensive and nontoxic [208, 212-214]. Another interesting feature of SBA-15

is the presence of micropores, small mesopores, in the mesopores walls. These are formed randomly and interconnect the cylindrical mesopores. Lukens et al. first demonstrated the presence of micropores inside the walls of mesopores using quartz as a reference [215]. Subsequently systematic investigations using N<sub>2</sub> adsorption-desorption, inversion platinum replicas and high resolution transmission electron microscopy (HRTEM) studies [216] have proved that SBA-15 is composed of uniform hexagonal arrays of primary pores, which are interconnected by a number of smaller pores with a broad PSD. These secondary pores are in the range of micropores or smaller mesopores (1-3 nm) and are sometimes referred to as complementary pores.

Imperor-Clerc suggested that a “corona” region (see section 1.6.4.3.1) is formed during the formation of spherical micelles. In the next step silicate precursor is added and deposited on the corona region. Upon hydrolysis and polymerization of the silicate the corona is trapped in the walls and forms micropores when the template is removed [217].

Presence of these micropores in SBA-15 walls enhances the mass transfer, typically in gas phase catalytic reactions. The presence of micropores in the SBA-15 thick walls also makes it more thermally and hydrothermally stable than MCM-41. The surface of the micropores inside the walls is covered with numerous  $\equiv\text{Si-OH}$  groups. During thermal treatment at high temperature  $\equiv\text{Si-OH}$  groups are cross-linked and dehydrolyze to  $\equiv\text{Si-O-Si}\equiv$  groups [212]. This process consequently results in formation of thicker and more robust walls. Since SBA-15 has been widely used in various applications it is essential to fully understand the mechanism of its synthesis and also the formation of the micropores.

Although both MCM-41 and SBA-15 have highly ordered honeycomb mesopores, the pore size and moreover the wall structure makes for marked differences between these two materials [218]. In addition, micropores contribute a substantial proportion of the surface area to SBA-15 overall surface area. The microporous surface area can be varied based on the synthesis route [219].

#### **1.6.4.3.1 Micelles/Corona formation**

As the template (surfactant) made up of cationic or non-ionic triblock copolymers dissolves in a basic or acidic aqueous solution, aggregation of the surfactant into micelles occurs due to the amphiphilic nature of the surfactant. Different concentrations of the surfactant result in various forms of the micelles. Low surfactant concentration results in spherical micelles. The largest concentration giving spherical micelles is referred to as the

“critical micelles concentration” (CMC). By increasing the concentration of the surfactant to 10 times more than the CMC, rod-shaped micelles form and finally by further increasing the surfactant concentration close-packed cylinders result [220].

The micelles are stable due to electrostatic interaction of charges or hydrophilic-hydrophobic interactions. It is noteworthy that when spherical micelles are forming hydrophobic moieties of the surfactant aggregate in the centre and form the core of the micelles. Hydrophilic polar moieties move towards the outside and form the corona, where they can interact with aqueous solution [221].

Figure 1.5 demonstrates the spherical micelles of SBA-15. It can be clearly seen that the surfactant chains are arranged into a spherical shape such that the polar groups can easily interact with the aqueous solution. Since SBA-15 is made up of the amphiphilic surfactant, a “V” shaped structure is required to be formed with hydrophobic moieties (PPO) towards the centre and hydrophilic ends (PEO) towards the outside. This is because at low pH the surfactant folds to expose its hydrophilic moieties to the aqueous surroundings [40]. Several of these V-shaped molecules aggregate to form spherical micelles. The external, hydrophilic is referred to as the “corona”.

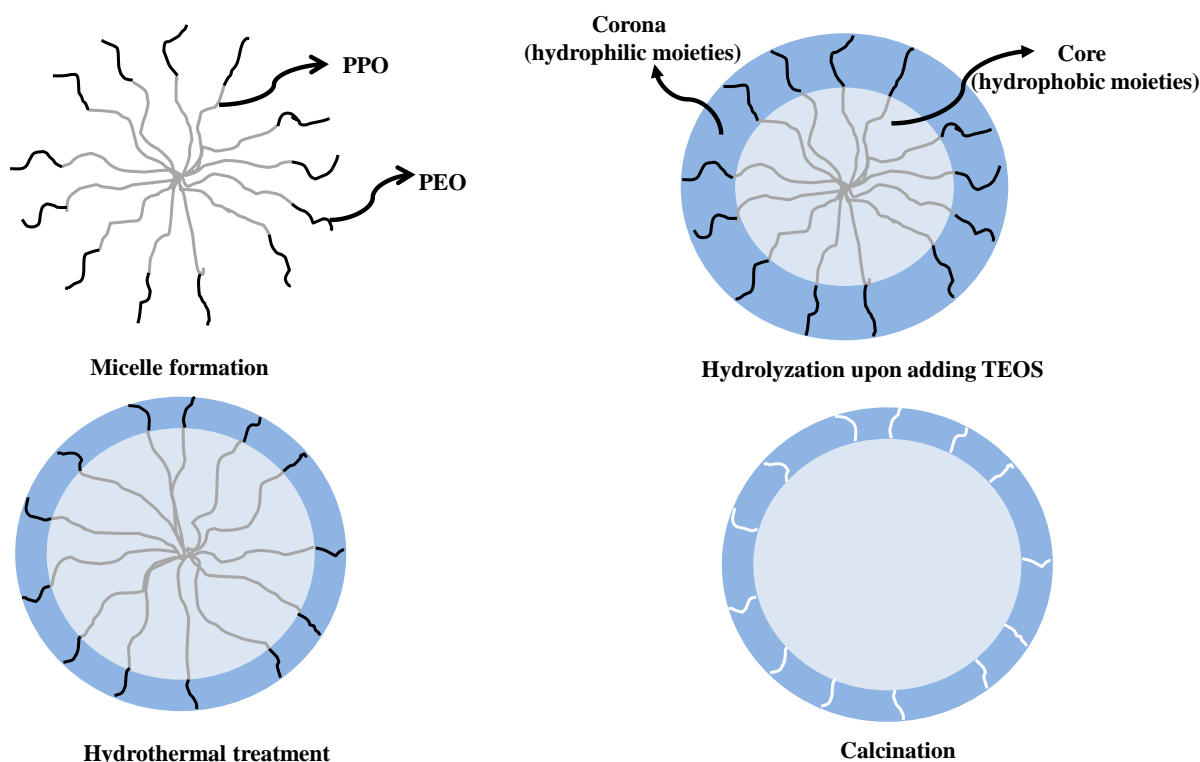


**Figure 1.5.** Micelles formation mechanism

Upon adding the silicate precursor such as tetraethyl orthosilicate (TEOS) or tetramethyl orthosilicate (TMOS) to the surfactant solution, the precursor hydrolyses and deposits on the

micelles to form a silica network. This will form the amorphous silica walls during the preparation process. The hydrolysis and polymerization of the silicate precursor on the micelles occurs in various steps based on the precursor's hydrophobicity and the degree of hydrolysis. In the first step, the silicate precursor penetrates to the core of the micelles. This is because the silicate precursor, like the micelles' cores, is hydrophobic and this facilitates the hydrolysis process [222]. As the hydrolysis of the silicate precursor progresses the silicate precursor becomes more hydrophilic. In the next step the precursors diffuse into the corona, where PEO groups are present. At this stage polymerization of the silicate precursor begins, at the interface of hydrophobic core and hydrophilic corona of the micelles, and simultaneously the micelles elongate. While the hydrolysis process is in progress, the polymerization of the silicate only occurs in the corona. Through this polymerization and condensation the PEO moieties are entrapped in the silica walls and as the reaction proceeds precipitation of the flocculents begins to occur [223].

After the formation of SBA-15, the hydrothermal process begins by increasing the temperature. Since the properties of PPO and PEO are temperature dependent (section 1.6.4) by increasing the temperature the hydrophilicity of the PEO chains, which have already been trapped in the silica walls, will change. As a result they retract from silica walls to the core of the micelles, resulting in pore size expansion and at the same time a reduction in the microporosity.

By increasing the hydrothermal process temperature from 35 °C to 130 °C the microporosity and consequently the surface area noticeably decreased. The pore size however, increases by several nanometers and the silica walls become more condensed [217, 224]. The micropores remain intact during calcination up to 900 °C, but they probably disappear at 1000 °C and as a result a structure similar to that of MCM-41 is obtained [225].

#### **1.6.4.3.2 Template (surfactant) removal**

Several different methods have been suggested in the literature to remove the template (surfactant) after the formation of the mesoporous silica. These are listed below:

(i) Calcination

Calcination is the most common way to remove the template (surfactant) from as-synthesized OMS. Conventionally calcination is performed in air starting with slow heating rate ( $1-2\text{ }^{\circ}\text{C min}^{-1}$ ) from RT up to 550 °C. The sample is then held at this temperature for 5-6 h after which it is cooled down to RT at the same rate at which it was heated. The initial

decomposition of the surfactant occurs at 150-250 °C [226, 227]. It has been reported that the organic surfactant moieties (PPO) within the mesopores are decomposed before the PEO chains inside the intrawall micropores [226]. The shrinkage of the framework due to condensation and water release occurs at above 300 °C. During this shrinkage the mesoporous volume decreases but the microporous volume remains intact. This is indicative of continuous decomposition of the surfactants from micropores during framework shrinkage [228].

(ii) Ethanol extraction

Ethanol can be used as an alternative to calcination for removing template (surfactant) from the OMS pores. This method, in which mesoporous silica is refluxed in ethanol for 24 h [40], has advantages and disadvantages over calcination. Advantages are that the surfactant can be recovered and reused and, furthermore the surface of the OMS becomes highly hydroxylated. The disadvantage of this method is that it generates large amounts of waste (ethanol) and also a small amount of the surfactant usually remains in the micropores [229].

(iii) Hydrogen peroxide

Hydrogen peroxide, which is known to be an environmentally friendly oxidant, can be used to completely remove the template (surfactant) from as-synthesised SBA-15. This is done by treating the SBA-15 in H<sub>2</sub>O<sub>2</sub> for 24 h at 100 °C. The resulting mesoporous material will have slightly larger mesopores and higher micropore volume, which results in a correspondingly higher surface area. One of the advantages of this method is the high number of silanol groups formed in the silica walls, which benefits any subsequent functionalization process [230].

(iv) Sulphuric acid

Sulphuric acid can also be used to remove template (surfactant) from the pores in as-synthesized SBA-15. Sulphuric acid removes the surfactant selectively by decomposing the PPO moieties but not PEO [231]. It is known that the cleavage of PPO and PEO moieties by sulphuric acid proceeds at a similar rate in the absence of spatial constraints. This suggests that the selective decomposition of PPO over PEO using sulphuric acid is attributed to the fact that the PEO moieties are trapped in the silica walls. And so the interaction between PEO units and sulphuric acid is hindered. Sulphuric acid surfactant removal, like that using hydrogen peroxide, results in mesopores expansion [231]. Since the PEO units remain in the micropores, the surface area of the resulting mesoporous material is not as high as the cases in which calcination or H<sub>2</sub>O<sub>2</sub> was used to remove the surfactant.

(v) Microwave

Microwaves have been suggested as a way to speed up the removal of the template (surfactant) from as-synthesized SBA-15 by ethanol or H<sub>2</sub>O<sub>2</sub>. The mesoporous silica (SBA-15) can be mixed with H<sub>2</sub>O<sub>2</sub> or ethanol and exposed to microwave radiation for 2 minutes. This results in the complete removal of the surfactant. With this method no shrinkage of the framework has been reported and the pore size is reported to be larger than those from the calcination method. Another advantage of this method is the high concentration of silanol groups on the mesoporous walls [232].

### 1.6.5 Supported metal oxides

Metals/metal oxides are among the most significant catalysts in industry. They are used on a large scale in various sectors of industry such as petroleum, hydrogenation of CO [233], hydrogenation of fat [234], selective oxidation reactions [235, 236] and many other processes. Most metal/metal oxide catalysts are expensive, suggesting that using smaller amounts of the catalyst would be economically and industrially favourable.

Bulk metal/metal oxides are not very active as catalysts due to their low surface area and low availability of active sites for the reactants. Moreover at high temperature they tend to aggregate and form large particles which are not catalytically active. As discussed previously (see section 1.6) to circumvent these disadvantages the active sites can be deposited on a support preferably of high surface area. The porous framework of mesoporous materials with uniform pore size and narrow PSD are appropriate for deposition of nanoparticles with high dispersion [237].

The degree of dispersion of the active sites is of great importance for the catalytic performance. It has been accepted as a general concept that once the particles are confined inside the pores, their aggregation at high temperature will be hindered due to the barrier set up by the pore walls.

Catalytically active metals can be deposited on various supports such as metal oxides, zeolites, clays or various mesoporous silicas [28, 238-240]. The nature of the support [241, 242], preparation method by which the active metal particle is deposited on the support [176, 243] and the nature of the metal precursor [37, 243] all affect the catalytic performance of the supported metal/metal oxide. This is discussed in section 1.7.2.

According to IUPAC, deposition is defined as “the application of the catalytic component on to a separately prepared support.” It is important to mention that the properties of the

solution in the pores of a support are different from those of the solute in bulk. There are several different methods of deposition which are listed below:

#### **1.6.5.1 Impregnation**

Impregnation is a conventional and the most common method of depositing active metal particles on a support [244]. In impregnation the porous solid support is brought into contact with a metal precursor solution. Metal species from these solutions are then deposited onto the surface of the support. Generally, the impregnation method consists of three steps: (i) contacting the metal precursor solution with the support over certain period of time, (ii) a drying process to remove the adsorbed solvent and (iii) catalyst activation through calcination, reduction or other appropriate methods [245].

Several processes take place during the impregnation with various rates:

- (i) Adsorption of the metal species from the solution onto the surface of the support through dispersion, hydrogen-bonding or electrostatic forces.
- (ii) Partial dissolution of the support surface in the solution [246].
- (iii) Hydrolysis, polymerization or depolymerisation of the species attached to the surface.
- (iv) Ion exchange between the support surface and the cations or anions of the solution.

The type of product obtained after the impregnation process is affected by the nature of the metal precursor solution [37], support and also the reaction conditions [247, 248]. The nature of the metal precursor solution depends on various factors such as the pH of the solution, the nature of the solvent and finally the nature and concentration of the metal precursor, which affect the solvation of the metal precursor in the solvent [249]. The pH of the solution has a large impact on the ionisation and the nature of the cations and anions.

As for supports, the texture of the support such as the degree of porosity, size of the pores [250] and the specific surface area, the properties of the functional groups such as their concentration [138], the strength of acidic and basic centres [251], the isoelectric point and the presence of accessible exchangeable ions and also the reactivity of the surface [137] are influential elements in the impregnation process. They also help to determine the composition of the final product.

Impregnating the support with metal precursor solution can be achieved through different methods;

#### **1.6.5.1.1 Impregnation with an excess amount of the metal precursor solution, soaking**

The desired amount of metal precursor is dissolved in an excess amount of a solvent [246]. This solution is added to the support and the mixture is stirred from several hours to several days based on the rate of the deposition process. After stirring the extra solvent is evaporated under reduced pressure. The advantage of this method is the possibility of controlling the distribution of the active sites by controlling the contacting time of the support with the solution. However, the disadvantage of the method is that a fraction of the support can be dissolved in the solution over the long contact period.

#### **1.6.5.1.2 Dry impregnation**

In dry impregnation the volume of the solvent used to dissolve the metal precursor equals the pore volume of the support. This can be determined via N<sub>2</sub> adsorption-desorption in the case of porous supports. This method is known to result in a better distribution of the metal precursor on the support and is also highly recommended for species which might have weak interaction with the support [252].

#### **1.6.5.1.3 Wet impregnation**

The principle of wet impregnation is very similar to that of dry impregnation except that the volume of the solution is slightly higher than the exact pore volume. On adding the metal precursor solution the support looks wet. This is followed by drying and activation processes.

#### **1.6.5.1.4 Successive impregnation**

Two or more metal precursor solutions are introduced to the support successively [253, 254]. After each impregnation the support may be dried and activated. It is important to bear in mind that in the second and the following impregnations, the surface chemical and physical properties are not the same as that of the support in the first impregnation due to the presence of either metal or metal oxide particles. Sometimes successive impregnation is used for a single metal precursor solution to ensure the optimum uptake of the active particle.

#### **1.6.5.1.5 Solid-solid / solid-liquid impregnation**

This specific method is known either as the solid-solid and or the solid-liquid method, because the desired amount of the metal precursor is added to the support and together they are heated to the melting point of the metal precursor [246, 255]. At the melting point of the

metal precursor it liquefies and moves into the pore by capillary action. This method has some limitations. For instance, it cannot be used for metal precursors with melting points equal to or higher than decomposition temperature of the support. Another drawback of this method is the poor distribution of the metal precursor.

#### **1.6.5.2 Ion exchange**

Ion exchange is a specific type of impregnation, which involves mixing the support with an aqueous solution of the desired amount of metal precursor [244]. In this technique the surface of the support is charged due to the pH of the metal precursor aqueous solution. This suggests that if the point of zero charge (PZC) of the support occurs at a lower pH than that of the aqueous solution, then the hydroxyl groups of the surface will be deprotonated such that the surface of the support becomes negatively charged [249]. This increases the ability of the support to adsorb the cations of the metal solution electrostatically. Conversely, if PZC occurs at a higher pH than that of the solution the hydroxyl groups of the support surface will become protonated. As a result the surface becomes positively charged and tends to adsorb the anions of the metal solution.

#### **1.6.5.3 Adsorption**

Adsorption from an aqueous solution of the metal precursor is another conventional method of depositing metal/metal oxides onto various supports. In this method the support is mixed with the aqueous solution of metal precursor with a certain concentration for a known period of time after which the support with its adsorbed metal is recovered by filtration [176]. This method is very similar in many respects to impregnation except for the recovery process of the solid product. The composite then dries and goes through calcination process in air to form a supported metal oxide. This method results in poor uptake of the metal precursor, since only a proportion of the metal cations from the solution are deposited on the support. The rest is 'lost' (washed out) upon filtration. This is attributed to the weak interaction between the support and metal precursor.

#### **1.6.5.4 Ammonia method**

This method was first reported by Barbier et al. to highly disperse  $\text{Co}(\text{NO}_3)_2 \cdot 6\text{H}_2\text{O}$  on a silica surface [256]. It was reported that the desired amount of  $\text{Co}(\text{NO}_3)_2 \cdot 6\text{H}_2\text{O}$  was dissolved in water. To prevent  $\text{Co}^{2+}$  oxidation, the system was protected from air by using an Ar blanket. A solution of ammonia (28 wt%) was added to the cobalt aqueous solution, which

resulted in precipitation of  $\text{Co}(\text{OH})_2$ . In the next step the precipitate was dissolved in a large excess of ammonia. Next, silica was added to this solution, which decreased the pH of the solution to 11.6. After constant stirring the mixture reached equilibrium with a pH of 12. Then mixture was stirred for a further 1 h and centrifuged and washed repeatedly with water. The solid product was dried under vacuum at 80 °C overnight. Finally to obtain metallic cobalt, the dried solid was reduced under hydrogen flow to 650 °C at a very slow rate of temperature increase.

#### **1.6.5.5 Solvent-free deposition**

It is important in catalytic applications of supported metal oxides to obtain aggregation-free particles with high dispersion, which results in high active surface area. Tang et al. reported a solvent-free method in which the pre-calculated amount of metal precursor was added to SBA-15 in the absence of any solvent. In the next step, the two solids were ground manually in a mortar for 10 min and then calcined in air at 450 °C for 4 h after being heated to temperature at 1°C min<sup>-1</sup>. It was demonstrated that compared to the conventional impregnation method the solvent-free method results in highly-dispersed metal oxides on the interior surface of the SBA-15 without any aggregation on the external surface [136]. These composites are reported to be thermally stable and catalytically active by virtue of the high dispersion and small particle size of the active sites.

#### **1.6.5.6 Molecular design dispersion (MDD)**

Among new techniques recently reported for depositing metal precursors on the support, MDD is known to result in extensive formation of the active particles inside the pores of the mesoporous silica. This method requires two steps. In the first step an organometallic complex of the desired metal is added to the support, typically mesoporous silica with a sufficient amount of hydroxyl groups on the surface. In this step the silanol groups of the support interact with the metal complex, which facilitates the adsorption of the metal on the surface. In the next step, the adsorbed complex is thermally decomposed through calcination at high temperature in air and as a result the metal oxide species deposit on the surface of the support [257].

Metal acetylacetonates are known to be very efficient organometallic complexes for this purpose. This is attributed to the small size of the complex, which facilitates its migration to the pores of the mesoporous silica supports. These complexes also have planar geometry

which enables them to interact with the surface without steric hindrance [257]. Another advantage of metal acetylacetonate complexes is their high reactivity towards silanol groups on the surface of the support [251].

Two possible interaction mechanisms between metal acetylacetonate molecules and the silanol groups of the support have been reported in the literature [257]. One possible mechanism is a hydrogen bonding mechanism, through which the proton of the silanol groups interacts with the  $\pi$ -electrons of the acetylacetonate ligand. Another possible mechanism is a ligand exchange mechanism, whereby the deprotonated silanol groups of the surface interact with the metal ions of the acetylacetonate complex and form a covalent bond (Figure 1.6).

The preparation of silica/alumina supported copper, vanadium and molybdenum oxides by the MDD method has been reported. It was demonstrated that the geometry of the metal precursor had a great impact on the interaction of the metal complex with the support and in turn on the final deposition of the active metal particles on the support [257].

It has also been reported that aluminium and titanium modified SBA-15 have been used as supports for the deposition of copper and iron oxide via the MDD method [251]. It was claimed that modification of silica with Al and Ti increased the catalytic performance of the final catalysts for the DeNO<sub>x</sub> process, because the MDD method generated strong Lewis acid sites.

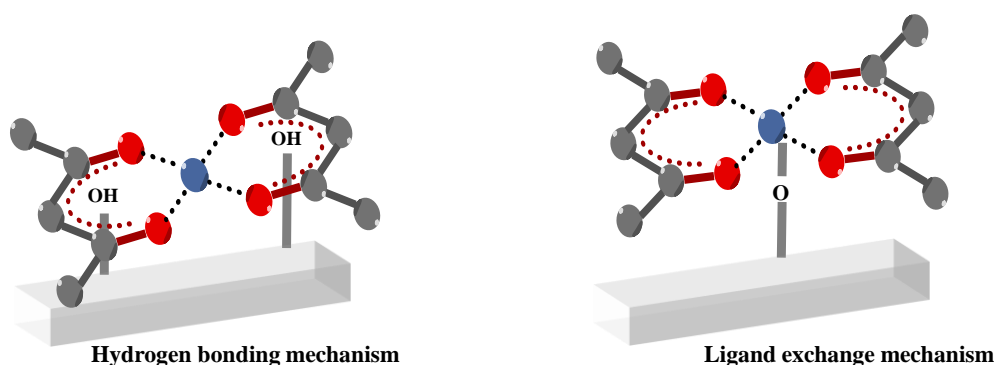


**Figure 1.6.** Schemes of interaction mechanisms between silanol groups and metal precursor

#### 1.6.5.7 Supercritical fluid deposition

Supercritical fluids have been successfully used to deposit metal/metal oxide nanoparticles on porous supports [258-260] and carbon nanotubes [261]. This method includes the dissolution of an organometallic precursor in the supercritical fluid (SCF) to make the metal precursor solution. This solution is then used to impregnate the support with the

organometallic precursor. A subsequent decomposition of the metal precursor in air results in formation of the metal oxide or with a further reduction at elevated temperature metallic nanoparticles.

Supercritical CO<sub>2</sub> (scCO<sub>2</sub>) is most commonly used as a supercritical fluid since it is non-flammable, non-toxic, non-reactive and financially affordable [139]. scCO<sub>2</sub> has intermediate properties between those of a gas and liquid. The gaseous properties of high diffusivity and low viscosity of scCO<sub>2</sub> facilitate its rapid diffusion into the porous network of the support. However, due to its liquid-like density a wide range of organometallic precursors are soluble in it.

The morphology and dispersion of the nanoparticles can be easily controlled by small changes in either the pressure or temperature. In addition, scCO<sub>2</sub> has zero surface tension, suggesting that it can easily penetrate the pores and increase the degree of support wetness. It can also be easily removed from the reaction media by controlled decompression.

Deposition of cobalt, copper and iron oxide in the pores of mesoporous silica using scCO<sub>2</sub> has been reported [262]. Aspromonte et al. reported deposition of cobalt oxide nanoparticles on MCM-41 and Al-MCM-41. They demonstrated that the concentration of the metal precursor had a large impact on the morphology of the metal oxide particles. If the concentration of metal precursor was higher than the solubility of the oxide in scCO<sub>2</sub>, large metal oxide particles formed on the external surface of the support with low catalytic activity [263].

The disadvantages of using this technique are the complexity and the cost of the metal complexes which are normally used as metal precursors, as well as the high temperature and pressure needed to apply in this process.

#### **1.6.5.8 Functionalized supports**

Selective functionalization of the mesoporous silicas has been used for deposition of both metal and metal oxides inside the pores of the support. Chao et al. reported synthesis of highly dispersed platinum and gold on the internal surface of the aminofunctionalized SBA-15. They demonstrated that the nature of the metal nanoparticles was a crucial element in determining the size and the shape of the particles. The process resulted in formation of spherical (5 nm) gold nanoparticles as opposed to disk-like (1.2-3 nm) platinum nanoparticles [264].

Escalera et al. reported formation of highly dispersed cobalt and cobalt oxide nanoparticles inside the pores of aminofunctionalized SBA-15. They selectively functionalized internal hydroxyl groups by silylation of the external hydroxyl groups before adding the metal precursor. Highly dispersed cobalt and cobalt oxide were formed inside the pores after heat treatment in an N<sub>2</sub> atmosphere or air, respectively [138].

#### **1.6.5.9 Two-solvent method**

The two-solvent technique is another new method which seems to disperse metal oxide nanoparticles exclusively inside the pores of mesoporous silica [176]. This method consists of three steps: (i) the desired amount of a metal precursor is dissolved in water of volume equal to the pore volume of the support determined by N<sub>2</sub> adsorption-desorption, (ii) mesoporous silica, typically SBA-15, is dispersed in an alkane such as n-hexane to form a hydrophobic solution, (iii) the aqueous solution of metal precursor is added to the hydrophobic solution dropwise and the mixture stirred for 2 h. The support is calcined in air after being filtered and dried at room temperature (Figure 1.7).

It has been reported that several factors can affect the dispersion of the metal oxide nanoparticles inside the pores of the support, including the type of hydrophobic alkane solvent used [265]. It is known that the interfacial tension between water and n-hexane, water and cyclohexane and water and heptane is 50.4 mN m<sup>-1</sup>, 50.3 mN m<sup>-1</sup> and 50.7 mN m<sup>-1</sup>, respectively [265]. This suggests that smaller droplets of the aqueous solution of metal precursor form on the surface of the n-hexane compared to heptane, which in turn results in formation of smaller particles. Another important factor is the adsorption enthalpy of various alkanes on the surface of the mesoporous silica. These are reported to be 27.4 J g<sup>-1</sup> [266] and 25.9 J g<sup>-1</sup> [267] for n-hexane and cyclohexane, respectively. In addition the evaporation temperatures (boiling points) for the n-hexane, cyclohexane and heptane are 68 °C, 80.7 °C and 98 °C respectively. These have been all reported to have an impact on the preparation procedures as well as the size of the final particles.

The mechanisms by which these properties act have been postulated to be as follows. It has been suggested that as the mesoporous silica SBA-15 is dispersed in the alkane the trace of water which is present in the system adheres to the silica walls due to their hydrophilic nature created by the presence of hydroxyl groups. This phenomenon makes the silica walls even more hydrophilic and increases their affinity for the metal aqueous solution upon its addition to the mixture. At this stage, the interfacial tension comes into account such that

smaller droplets are formed when using alkanes with a smaller interfacial tension with water. During the drying process alkanes with lower adsorption enthalpy and lower evaporation temperature are removed from the pores at lower temperature. As a result highly dispersed small metal oxide particles form inside the pores of the support after calcination [265].

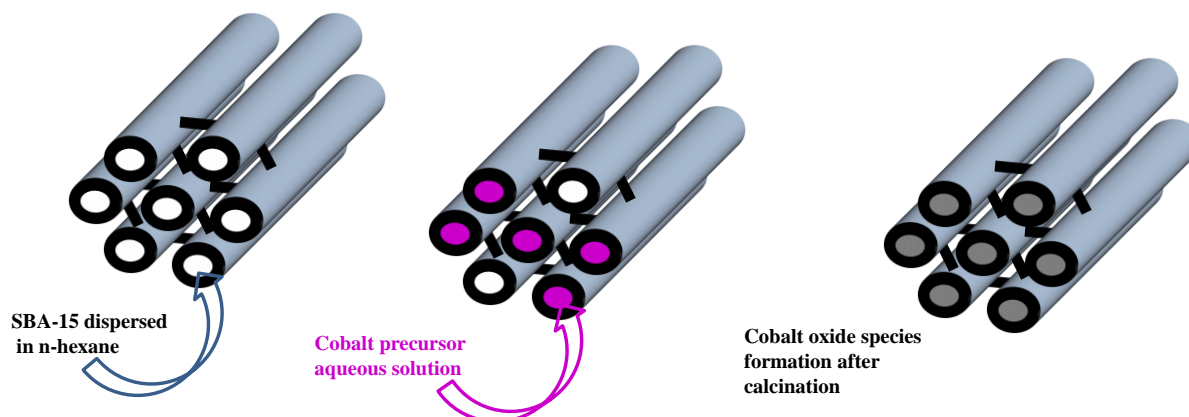


**Figure 1.7.** Schematic diagram of two-solvent method technique for cobalt oxide nanoparticles formation inside the pores of SBA-15

#### 1.6.5.10 Framework incorporation

The previous methods are associated with the post-synthesis procedure in which the mesoporous silica is first prepared followed by preparation of active metal or metal oxides inside the pores. However, transition metals can be incorporated in the framework of the mesoporous silica by introducing the metal precursor into the initial synthesis mixture [132, 268]. The advantage of this method is that the active particles are highly dispersed throughout the support. However, the disadvantage of this method is that the transition metal centre is buried in the framework and therefore is inaccessible for the reactants for any catalytic activity [269].

### 1.7 Cobalt chemistry

The history of cobalt goes back four thousand years to Persia and Egypt. Here it was used as a component in blue dyes. They called the cobalt compound something, presumably. Cobalt was first isolated by Brandt in 1735, but it was not confirmed as an element until 1780, when it was recognised by Bergman. Later on, in the early 1900s, Elwood Haynes patented the use of metallic cobalt [270]. Even nowadays, nearly 30 % of the cobalt produced is used in the paint and ceramic industries [271]. Cobalt is a brittle, hard, silvery transition metal with magnetic properties similar to that of iron and a close packed hexagonal crystal

structure. It is also not highly reactive and quite stable in air at normal temperature. However upon heating, it oxidises to  $\text{Co}_3\text{O}_4$  which breaks down to  $\text{CoO}$  at  $900\text{ }^\circ\text{C}$  [272].

Various formulation of cobalt with other oxides or sulphates is used in producing pigments industrially [273]. This mixture is then calcined at  $1100\text{-}1300\text{ }^\circ\text{C}$  and finally ground to a fine powder. Cobalt is also added to glass as a colour [274] or decoloriser [275]. In the former application cobalt at low levels (2 ppm) gives a blue tint and by increasing its concentration a dark blue colour is obtained. As a decoloriser, it suppresses the yellow tint from iron contamination.

Cobalt is used as a constituent in various metal alloys along with nickel, iron and vanadium. There are several factors that make cobalt-based alloys a favourable material in industry. Some of these factors are (i) their increased high temperature strength, through the mechanism by which this occurs is not fully understood [276], (ii) their higher melting point compared to that of nickel or iron based alloys [277], (iii) their superior hot corrosion resistance to gas turbine atmospheres, which is attributed to their high Cr content [278] as well as (iv) their superior thermal fatigue resistance [279] including their weldability compared to nickel based alloys. Cobalt-based alloys are used in various industries. For instance, Co-Cr-Mo alloys are used in dental prosthetics [280] and the cobalt-based alloy HS21 is used in gas turbine applications [281].

In the field of catalysis, there is a wide range of applications for cobalt both as a homogeneous and heterogeneous catalyst for example cobalt is used, in the plastics [282], sensors [283] and petrochemical industries [284]. Hydrodesulphurisation is a common process in petroleum refining; the crude oil fraction and hydrogen are passed over catalysts, typically cobalt (Co)-molybdenum (Mo) supported on alumina, at high temperature and pressure, to transform organic sulphur to hydrogen sulphide [284].

Cobalt salts are also known as promising homogeneous catalysts for oxidising p-xylene to terephthalic acid [285] and dimethyl terephthalate [282], which are used to manufacture resins for plastic bottles. In 2005 nearly 3000 tonnes of cobalt were used for this purpose. Various cobalt complexes and cobalt oxides, more specifically  $\text{Co}_3\text{O}_4$  have been used as both homogeneous and heterogeneous catalysts for the oxidation of alcohols and olefins to their corresponding aldehydes, epoxides and carboxylic acids (discussed in section 1.7.2). Furthermore, metallic cobalt is known as a promising catalyst for Fischer-Tropsch synthesis (FTs) [286].

In the human body cobalt is a vital trace element. It is found in the core of vitamin B12 and some other co-enzymes [287]. Although the body contains only 2-5mg of vitamin B12, its contribution in the formation of the red blood cells makes it essential to life [288].

All the above mentioned applications of cobalt demonstrate its importance to various segments of industry and also to human life.

### 1.7.1 Cobalt oxides

Five cobalt oxide species have been reported in the literature,  $\text{CoO}_2$ ,  $\text{Co}_2\text{O}_3$ ,  $\text{CoO(OH)}$ ,  $\text{Co}_3\text{O}_4$  and  $\text{CoO}$  [283, 289]. Since their discovery, they have been the subject of interest both in academia and industry due to their unique electric, magnetic and catalytic properties [290, 291]. Cobalt oxides contain two cations,  $\text{Co}^{2+}$  and/or  $\text{Co}^{3+}$ , which are thermodynamically competitive under ambient conditions [272]. Cobalt oxide with a cobalt oxidation state higher than three is unstable and readily decomposes with liberation of oxygen.  $\text{CoO}_2$  is reportedly formed during the preparation of  $\text{Co}_2\text{O}_3$  [292].

Cobalt hydroxide,  $\text{CoO(OH)}$ , has a hexagonal structure, in which  $\text{Co}^{2+}$  is located at an octahedral site and coordinated to six hydroxyl groups [293].

The two main cobalt oxide species,  $\text{CoO}$  and  $\text{Co}_3\text{O}_4$ , are generally stable and therefore found in nature [294, 295]. Generally  $\text{CoO}$  is stable at higher temperatures, but the  $\text{CoO}$  particles can exist under ambient temperature and oxygen partial pressure, while  $\text{Co}_3\text{O}_4$  is stable at lower temperature. It is known that it is difficult to obtain pure  $\text{CoO}$ , with small amounts of  $\text{Co}_3\text{O}_4$  and metallic cobalt always present as impurities [296].

$\text{CoO}$  is an antiferromagnetic material and is metal deficient. It has been suggested that the cation deficiency is due to cation vacancies in the crystal lattice.  $\text{CoO}$  exhibits p-type semi-conducting properties due to its 1.4-1.8eV energy band gap [297]. The oxygen partial pressure governs the concentration of cationic vacancies [298]. As a low valence transition metal oxide,  $\text{CoO}$  can form a rocksalt faced-centred cubic structure, where the  $\text{Co}^{2+}$  is in an octahedral co-ordination environment (Figure 1.8a) [272]. The unit cell length of the rocksalt structure is 4.267 Å and the unit cell contains four atoms [294].  $\text{CoO}$  can also form a hexagonal wurtzite structure with the  $\text{Co}^{2+}$  in a tetrahedral co-ordination environment [299, 300]. Wurtzite  $\text{CoO}$  was reported to be less stable than rocksalt [300].

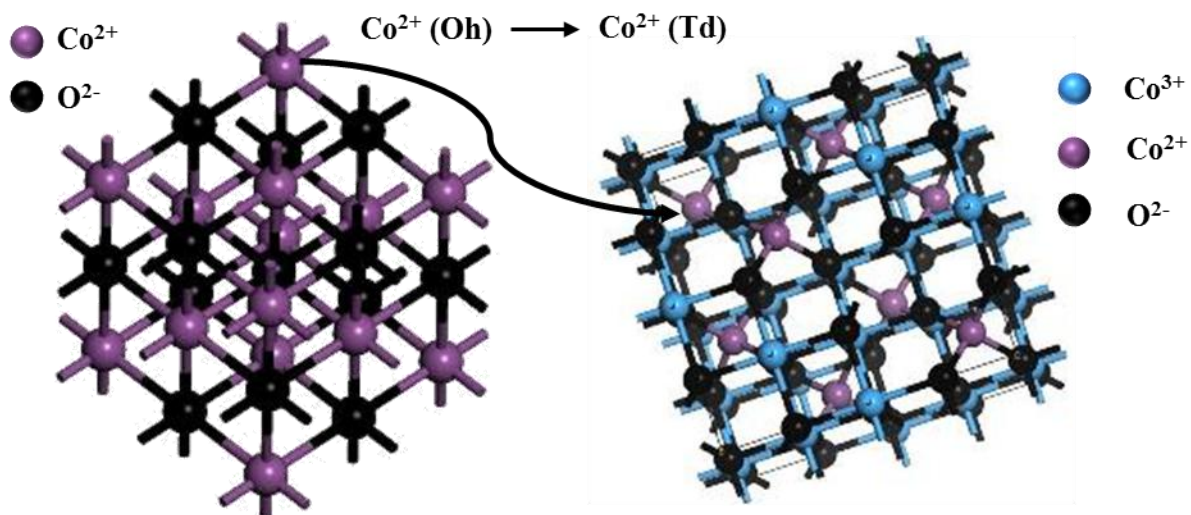


**Figure 1.8.** (a) Unit cell of rocksalt-structure CoO, with  $\text{Co}^{2+}$  in octahedral sites and (b) unit cell of spinel  $\text{Co}_3\text{O}_4$ , with  $\text{Co}^{2+}$  in tetrahedral and  $\text{Co}^{3+}$  in octahedral sites.

$\text{Co}_3\text{O}_4$  has a normal spinel structure, with a cation distribution known to be  $\text{Co}^{2+}[\text{Co}_2^{3+}]\text{O}_4^{2-}$ . Generally the spinel structure contains two metal oxidation states in different co-ordination environments. The cation sites are only partially occupied such that the unit cell of length 8.084 Å contains 56 cations and anions. In the unit cell of spinel half of the octahedral sites are occupied with  $\text{Co}^{3+}$  and one eighth of the tetrahedral sites are populated with  $\text{Co}^{2+}$  in a well-ordered manner (Figure 1.8b). In this structure  $\text{Co}^{3+}$  ( $3d^6$ ) is diamagnetic in the octahedral crystal field whereas  $\text{Co}^{2+}$  ( $3d^7$ ) at the tetrahedral sites form an antiferromagnetic sublattice, with the diamond structure below the Neel temperature [301].

Spinel  $\text{Co}_3\text{O}_4$  is stable up to 800 °C, decomposing to CoO above this temperature [302, 303]. Structurally, rocksalt CoO and spinel  $\text{Co}_3\text{O}_4$  both have oxygen atoms in a face centre cubic arrangement (Figure 1.8b). The closest  $\text{O}^{2-}$ -  $\text{O}^{2-}$  packing distance in rocksalt is ~ 5 % larger than that in spinel. Thus the complexity of the spinel structure of course is not due to its anions ( $\text{O}^{2-}$ ) but to the distribution of its cations ( $\text{Co}^{2+}$  and  $\text{Co}^{3+}$ ) [304].

In an oxidising environment, cobalt cations in the near surface region are mobile. This suggests that the cations which undergo oxidation will remain in their octahedral positions. However,  $\text{Co}^{2+}$  cations transfer to tetrahedral sites. This is considered to be the main reason for the spontaneous transformation of CoO to spinel  $\text{Co}_3\text{O}_4$  even at relatively low oxygen partial pressure (Figure 1.8).

Cobalt oxides have wide range of applications, such as in rechargeable batteries [305], lithium ion batteries [306], as a magnetic material [290], as a CO sensor [283], as an oxygen evolution catalyst [307], and, due to its low oxygen mobility energy, it can also be used as

oxidising catalyst [28, 308]. In addition,  $\text{Co}_3\text{O}_4$  is chemically stable over a wide range of temperatures and has a high mechanical strength, with a Young's modulus of 116-160 GPa which makes  $\text{Co}_3\text{O}_4$  a potential field emitter [309, 310].

The range of possible uses for cobalt and its oxides make it easy to see why an enormous amount of attention and effort have been devoted to investigate the properties of cobalt for different applications.

### **1.7.2 Catalytic performance of cobalt oxide species, bulk or supported**

Bulk or supported cobalt oxide species have been used in a wide range of catalytic applications, such as treating aqueous wastewater containing acetic acid and acrylic acid [311, 312], methane combustion [313], propane oxidation [314], phenolic contamination removal from wastewater [37, 315], CO oxidation [11], styrene epoxidation [238], ammonia oxidation [316], ethylbenzene oxidation [317], NO oxidation [87], water oxidation [239] and toluene oxidation [318].

Bulk cobalt oxide catalysts have shown lower catalytic activity than their supported analogues. This is generally attributed to their low surface area. It is also accepted that the shape and size of the metal/metal oxide particles in either bulk or supported materials are critical for improving their catalytic activity [319-322].

As noted above in section 1.6.4 and 1.6.5, OMSs are considered to be promising supports for metal/metal oxide particles. Their particular advantages can be explained in terms of their structure (see section 1.6.4). These advantages include: (i) their high surface area which facilitates the dispersion of the active sites, (ii) the presence of the silica walls which hinders the aggregation of the supported particles during calcination at high temperature as well as (iii) a large concentration of surface silanol groups (-OH) which expedites the introduction of the metal precursor onto the surface of the support.

Supported cobalt oxides can be synthesized via different techniques using various supports and different cobalt precursors, as discussed in section 1.6.5. A wide range of factors can influence the catalytic activity of the supported cobalt oxide species. These includes preparation methods [238], the nature of the support such as the metal-support interaction, surface area, pore size and surface acidity/basicity [247, 248], the presence and type of a dopant [323-325], nature of the metal precursor [37], nature of the solvent, calcination temperature [185, 326], the degree of dispersion and also the particle size [327-329].

Zhou et al. investigated the catalytic performance of  $\text{Co}_3\text{O}_4$  nanocrystals for the aerobic oxidation of cyclohexane. In their study, the catalyst was prepared by a precipitation method using  $\text{Co}(\text{NO}_3)_2 \cdot 6\text{H}_2\text{O}$  as the metal precursor and N-cetyl-N,N,N-tri-methyl ammonium bromide (CTAB) as a stabilizer. It was shown that the  $\text{Co}_3\text{O}_4$  nanocrystals were more catalytically active than nanocrystals prepared by more conventional methods or alumina supported cobalt oxide ( $\text{Co}_3\text{O}_4/\text{Al}_2\text{O}_3$ ) under the same reaction conditions [330]. The new catalyst was also reported to be easily recovered and could be reused up to five times with only a small decline in its catalytic performance.

Several groups have investigated the preparation, morphology and catalytic performance of mesoporous  $\text{Co}_3\text{O}_4$ . They have studied in detail the impact of the various mesoporous silicas as hard templates on the morphology and the catalytic performance of the resulting mesoporous  $\text{Co}_3\text{O}_4$  [177, 331]. The mesoporous system was demonstrated to play a major role on the morphology and the crystal growth of  $\text{Co}_3\text{O}_4$ . This was attributed to the confinement effect of the mesoporous silica on the decomposition of the cobalt precursor, thus leading to the formation of various intermediate phases [177].

Garcia et al. reported the synthesis of a range of mesoporous silicas KIT-6 obtained by varying the aging and calcination temperatures and incorporated cobalt oxide into them. It was demonstrated that the various KIT-6 templates influenced the degree of crystallinity and the morphology of the final mesoporous  $\text{Co}_3\text{O}_4$  [331]. These mesoporous  $\text{Co}_3\text{O}_4$  (prepared at aging and calcination temperature 100 °C and 500 °C, respectively) were catalysed propane and toluene oxidation with high catalytic performance. This was mostly attributed to the high concentration of  $\text{Co}^{2+}$  on the catalyst surface.

Mesoporous  $\text{Co}_3\text{O}_4$  replicated from KIT-6 and SBA-16 was demonstrated to catalyse low temperature toluene and methanol oxidation. These catalysts showed better catalytic performance than non-porous  $\text{Co}_3\text{O}_4$ . This was attributed to the higher active surface area and high concentration of adsorbed oxygen species [180]. Jaio et al. reported the synthesis and the catalytic performance of mesoporous  $\text{Co}_3\text{O}_4$  replicated from SBA-15 in the water oxidation reaction. It was demonstrated that the catalytic activity was inversely proportional to the cobalt content. This was because as the cobalt content increased, large patches of  $\text{Co}_3\text{O}_4$  were formed with less active surface area [239].

Cobalt oxide species supported on  $\text{Al}_2\text{O}_3$  were synthesized via wet impregnation (see section 1.6.5.1.3) using  $\text{Co}(\text{NO}_3)_2 \cdot 6\text{H}_2\text{O}$  as a metal precursor. They were then used as a catalyst for the aerobic oxidation of benzene. In addition, palladium and cerium were used as

dopants to investigate their impact on the catalytic performance. It was reported that adding both Ce and Pd improved the catalytic performance. This was attributed to the increase in active surface area due to the high dispersion of the  $\text{Co}_3\text{O}_4$  species on the support, and the reduced size of the  $\text{Co}_3\text{O}_4$  crystallites. It was the higher surface area that enhance the catalytic performance of the modified composites [235].

Yan et al. investigated the nature of the various active species of cobalt oxide supported on  $\text{Al}_2\text{O}_3$  and their involvement in the selective catalytic reduction of  $\text{NO}_x$  [184]. They prepared their samples using wet impregnation (see section 1.6.5.1.3) and deposition-precipitation. They suggested that the only cobalt species that could be dispersed on the surface would be  $\text{Co}^{2+}$  ions, small  $\text{Co}_3\text{O}_4$  clusters, large  $\text{Co}_3\text{O}_4$  clusters and  $\text{CoAl}_2\text{O}_4$ , which is known to be catalytically inactive due to the high interaction between cobalt and support. They proposed that surface-dispersed  $\text{Co}^{2+}$  ions are responsible for  $\text{NO}_x$  reduction. They also suggested that the catalytic performance of the catalyst depends on the Co-loading and on the calcination temperature, which in turn determines the concentration of each active site. It was also reported that using Pd as a promoter in  $\text{Al}_2\text{O}_3$  supported  $\text{Co}_3\text{O}_4$  increased the catalytic performance of the supported cobalt oxide. It does this by creating extra active centres for adsorbing oxygen. The extra active sites decreased the activation energy of the catalytic reaction by  $39 \text{ kJ mol}^{-1}$ , which facilitated the initiation of the reaction. Addition of Pd as a promoter was also reported to increase the dispersion of the  $\text{Co}_3\text{O}_4$  on  $\text{Al}_2\text{O}_3$  [324].

Liquid phase aerobic oxidation of alcohols was catalysed by supported  $\text{Co}_3\text{O}_4$  on various supports such as activated carbon (AC) and a covalent trizaine framework (CTF) using a wet impregnation method (see section 1.6.5.1.3) [236]. It was demonstrated that the nature of the support had significant impact on the catalytic activity of the cobalt modified composites. This was attributed to the size and dispersion of the  $\text{Co}_3\text{O}_4$  nanoparticles depending on the nature of the support. The CTF had an additional effect, in that oxygen stability was higher on the surface of the CTF such that the surface oxygen could not participate in the catalytic reaction.

Cobalt-based catalysts supported on titania ( $\text{TiO}_2$ ) and zirconia ( $\text{ZrO}_2$ ) were prepared using both sol gel and impregnation techniques (see section 1.6.5.1.3). These materials were then used as heterogeneous catalysts in the oxidation of  $\text{NO}$  to  $\text{NO}_2$  in the presence of excess oxygen [332]. It was reported that the nature of the support, the preparation method and the pre-treatment conditions had a high impact on the catalytic performance. The best catalytic performance was obtained from  $\text{Co}_3\text{O}_4$  supported on zirconia by impregnation. This was

attributed to the higher dispersion of the cobalt oxide species on the surface of the zirconia than on titania. It was also reported that the size and orientation of the active sites on different supports could account for differences in the catalytic performance of the catalysts. Kim et al. demonstrated that titania supported cobalt oxide was a promising catalyst for wet oxidation of trichloroethylene to HCl and CO<sub>2</sub> [333].

Mesoporous FSM-16 supported Co<sub>3</sub>O<sub>4</sub> was reportedly prepared using Co(NO<sub>3</sub>)<sub>2</sub>·6H<sub>2</sub>O via wet impregnation (see section 1.6.5.1.2) [334]. The authors investigated the catalytic performance of the Co-composites with various cobalt contents for methane oxidation to formaldehyde. It was shown that low cobalt content facilitated the dispersion of the cobalt oxide species, thus improving the catalytic performance.

Todorova et al. reported the preparation and catalytic activity of cobalt oxide supported on SiO<sub>2</sub> and synthetic kenyaite for benzene oxidation [329]. Here they used Co(NO<sub>3</sub>)<sub>2</sub>·6H<sub>2</sub>O as a metal precursor. It was demonstrated that the preparation method affected the size and dispersion of the active catalyst particles on the supports. The wet impregnation method (see section 1.6.5.1.3) results in formation of larger Co<sub>3</sub>O<sub>4</sub> particles when compared to the ammonia method (see section 1.6.5.4) [256]. This affected the catalytic performance in that the catalyst with higher dispersion and smaller particle size showed the highest catalytic activity.

The effect of particle size, dispersion and composition of supported cobalt oxide catalysts was also investigated by Tang et al. [238]. They demonstrated that the deposition of Co(NO<sub>3</sub>)<sub>2</sub>·6H<sub>2</sub>O on MCM-41 by wet impregnation (see section 1.6.5.1.3) resulted in formation of large Co<sub>3</sub>O<sub>4</sub> particles with poor dispersion. This catalyst did not show high catalytic performance in the aerial epoxidation of styrene due to the low available active surface area. By changing the preparation method to template ion exchange (TIE) while using the same support and metal precursor, a cobalt-based catalyst with better dispersion was reported to be obtained. This method is similar to the ion exchange (see section 1.6.5.2) with a slight modification. In this method the as-synthesized MCM-41 which contained 50 wt% of the original amount of template was added to transition metal ethanolic solution. This facilitated the ion exchange between the cationic template and transition metal cations. This catalyst showed better catalytic performance for the same reaction than the catalyst prepared by wet impregnation, which was attributed to the higher dispersion of the active particles on the support.

It was reported that the type of the support and its surface chemistry can affect the dispersion of the  $\text{Co}_3\text{O}_4$  particles as well as the interaction between the support and cobalt oxide species [247].  $\text{Co}(\text{NO}_3)_2 \cdot 6\text{H}_2\text{O}$  was deposited on MCM-41 via wet impregnation (see section 1.6.5.1.3) and resulted in formation of large  $\text{Co}_3\text{O}_4$  particles. This catalyst was highly active for toluene hydrogenation due to high reducibility of the active sites. However,  $\text{Co}^{2+}$  with strong interaction with the support was reported to be the dominant phase when SBA-15 was used as a support. This was attributed to the presence of highly accessible silanol groups in SBA-15. This catalyst did not show promising results in toluene hydrogenation, since the active sites were hard to reduce. It was also suggested these catalysts could potentially use for oxidation reactions.

Supported cobalt oxide species using various cobalt precursors and  $\text{SiO}_2$  as a support were reported to catalyse the oxidation of phenolic compounds [37]. These catalysts were prepared via wet impregnation (see section 1.6.5.1.3). The nature of the cobalt precursor, more specifically the nature of the anions, affected the catalytic performance, probably because the nature of the precursor influenced the relative concentration of different cobalt species, as well as the interactions between cobalt and  $\text{SiO}_2$ . When  $\text{CoCl}_2 \cdot 6\text{H}_2\text{O}$  (5 wt%) was used as a metal precursor, a better catalytic performance was reported than when  $\text{Co}(\text{NO}_3)_2 \cdot 6\text{H}_2\text{O}$  or  $\text{Co}(\text{CH}_3\text{CHOO})_2 \cdot 4\text{H}_2\text{O}$  (5 wt%) was used as metal precursor. This was attributed to the cobalt leakage when  $\text{CoCl}_2 \cdot 6\text{H}_2\text{O}$  was used as metal precursor and the formation of a heterogeneous-homogeneous system rather than a purely heterogeneous system. No cobalt leakage was reported when the other two cobalt precursors were used. The Co-composites prepared from  $\text{Co}(\text{NO}_3)_2 \cdot 6\text{H}_2\text{O}$  and  $\text{Co}(\text{CH}_3\text{CHOO})_2 \cdot 4\text{H}_2\text{O}$  had the advantage of being reusable up to three times without any significant decrease in their catalytic performance.

The aerobic oxidation of ethylbenzene was reported to be catalysed by SBA-15 supported cobalt oxide species. Here the cobalt-based catalyst was prepared via wet impregnation (see section 1.6.5.1.3) using cobalt acetate  $\text{Co}(\text{CH}_3\text{COO})_2 \cdot 4\text{H}_2\text{O}$  as metal precursor [317]. The blue coloration and UV-vis investigation of the Co-composite confirmed that the dominant phase was  $\text{Co}^{2+}$  in tetrahedral co-ordination. The catalyst was reported to show promising performance in ethylbenzene oxidation.

It was demonstrated that the catalytic performance of Co-composites for hydrodesulfurization of thiophene depended on the nature of the support. Higher dispersion of  $\text{Co}_3\text{O}_4$  was reportedly obtained via deposition of  $\text{Co}(\text{NO}_3)_2 \cdot 6\text{H}_2\text{O}$  by wet impregnation (see section 1.6.5.1.3) on OMSs such as MCM-41 and HMS than on amorphous  $\text{SiO}_2$  [335]. It was

also claimed that using Pd as a dopant hindered the strong interaction between cobalt and the support, hence facilitating the reduction process and improving the catalytic performance of the Co-composites.

Mesoporous silica supported  $\text{Co}_3\text{O}_4$ , prepared at different calcination temperatures, was investigated as a catalyst for NO oxidation. These composites were prepared using wet impregnation method (see section 1.6.5.1.3) and  $\text{Co}(\text{NO}_3)_2 \cdot 6\text{H}_2\text{O}$  as a metal precursor. It was shown that the catalyst prepared at lower calcination temperature had better catalytic activity due to the higher dispersion of the  $\text{Co}_3\text{O}_4$  on the support as well as less aggregated inactive clusters. It was concluded that smaller particle size with higher active surface area resulted in better catalytic performance [326].

Explosive methane combustion can be a problem in industrial combustion processes [336]. Hence, it is crucial for industrial safety to find efficient catalysts to completely oxidise methane at low concentration as well as at low temperature. Palladium-based catalysts are known to be active catalysts for methane combustion. The use of these catalysts is limited, however, due to their high cost and low thermal stability. It is therefore of great interest to find an efficient alternative, such as supported cobalt or manganese oxides.

Supported  $\text{Co}_3\text{O}_4$  was reported to show promising catalytic performance for low concentration methane combustion. The catalysts were prepared using a two-solvent method (see section 1.6.5.9) with  $\text{Co}(\text{NO}_3)_2 \cdot 6\text{H}_2\text{O}$  as the metal precursor [313]. It was demonstrated that the Co-composite with the lowest cobalt content showed the best catalytic performance. This was attributed to high dispersion, and low aggregation of the active sites into large inactive  $\text{Co}_3\text{O}_4$  species. It was also noted that the two-solvent method provides a route to produce size-controlled metal oxide species inside the pores of the mesoporous silica [337].

Su et al. reported liquid phase oxidation of 1-hexene, styrene and benzene using Co-MCM-41. Two catalysts were prepared via direct incorporation (see section 1.6.5.10) of the  $\text{Co}(\text{NO}_3)_2 \cdot 6\text{H}_2\text{O}$  in the mesoporous framework and also wet impregnation (see section 1.6.5.1.3). In both cases  $\text{H}_2\text{O}_2$  was used as an oxidant. The incorporated catalyst showed higher catalytic performance than the impregnated one. This was attributed to the low cobalt content, low dispersion and large particle size of the impregnated catalyst [338].

Cobalt oxide species are also known to be promising catalysts for carbon monoxide (CO) oxidation, which is of great importance in environmental pollution control. A handful of literature articles has been published on the catalytic oxidation of CO using various cobalt-based catalysts. The high catalytic activity of  $\text{Co}_3\text{O}_4$  can be attributed to the relatively low

enthalpy of oxygen vaporization, implying that the Co-O bond strength of  $\text{Co}_3\text{O}_4$  is relatively weak. This facilitates more desorption of lattice oxygen [339]. Therefore,  $\text{Co}_3\text{O}_4$  substitute for precious metals, which have higher sensitivity to sulphur poisoning in exhaust gas emission control.

Mesoporous  $\text{Co}_3\text{O}_4$  was synthesised using a two-solvent method (see section 1.6.5.9), which KIT-6 as the hard template and  $\text{Co}(\text{NO}_3)_2 \cdot 6\text{H}_2\text{O}$  as a metal precursor. The catalytic activity of the mesoporous  $\text{Co}_3\text{O}_4$  was evaluated for the oxidation of CO at low temperature [178]. It was shown that two types of template were obtained by changing the hydrothermal conditions during the preparation of KIT-6. Applying high temperature (130 °C) during the hydrothermal treatment resulted in formation of KIT-6 with a higher concentration of micropores. These micropores were reported to interconnect two sets of mesopores in KIT-6. This mesoporous silica was used to obtain a coupled  $\text{Co}_3\text{O}_4$  replica, which had a high degree of porosity and connectivity. However the KIT-6 prepared at low hydrothermal temperature (40 °C) has less micropore connectivity between the two sets of mesopores. Thus the  $\text{Co}_3\text{O}_4$  replica prepared from this hard template was referred to as uncoupled  $\text{Co}_3\text{O}_4$ . The uncoupled  $\text{Co}_3\text{O}_4$  replica demonstrated higher surface area and more open pores than the coupled one and therefore better catalytic performance in CO oxidation. This better catalytic performance was attributed to the availability of more active surface area.

Cobalt oxides,  $\text{Co}_3\text{O}_4$ , with various surface areas were prepared by different methods to catalyse CO oxidation. It was reported that the catalysts with high surface area accommodated smaller particles, with consequent better catalytic activity [185]. Wang et al. also reported that the nature of the supports, such as  $\text{Al}_2\text{O}_3$ ,  $\text{TiO}_2$  and  $\text{SiO}_2$ , and the calcination temperature applied in the synthesis of the supported cobalt oxide significantly affected the catalytic performance of the Co-composites in CO oxidation [340]. This was attributed to the formation of different cobalt species in interaction with the support. It was demonstrated that the calcination temperature had no effect on the dominant phase,  $\text{Co}_3\text{O}_4$ , when  $\text{SiO}_2$  was used as a support. However, when  $\text{Al}_2\text{O}_3$  and  $\text{TiO}_2$  were used as supports, increasing the calcination temperature changed the dominant phase from  $\text{Co}_3\text{O}_4$  to  $\text{CoAl}_2\text{O}_4$  or  $\text{CoTiO}_3$ , respectively. The latter two species, due to the strong interaction with the support were reported to show low catalytic performance in CO oxidation. The dominance of inactive species, Co-O-Al, was believed to be the main reason for the poor catalytic performance of  $\text{Co}_3\text{O}_4$  supported on  $\text{Al}_2\text{O}_3$  [314]. It was also demonstrated that by increasing the  $\text{Al}_2\text{O}_3$  surface area the proportion of inactive species was increased.

A simple method for fabrication of highly dispersed  $\text{Co}_3\text{O}_4$  on the surface of  $\text{SiO}_2$  was reported by Chen et al. This method modified the support surface by using ethylene glycol before the impregnation process. The Co-composite demonstrated high catalytic performance for CO oxidation, which was attributed to the presence of more  $\text{Co}^{3+}$  on the surface [341].

Xu et al. reported the formation of fine gold nanoparticles less than 5 nm in diameter on SBA-15 supported  $\text{Co}_3\text{O}_4$ . This composite demonstrated high catalytic performance in low-temperature CO oxidation. The high catalytic activity of this composite was attributed to the strong interaction between the supported cobalt oxides and gold nanoparticles [308]. The oxidation of CO was also catalysed by SBA-15 supported  $\text{Co}_3\text{O}_4$  prepared by the two-solvent method (see section 1.6.5.9). It was demonstrated that increasing the cobalt content lowered catalytic activity, due to the increasing inaccessibility of the active sites to the reactants,  $\text{O}_2$  and CO [11].

Cobalt-based composites are also widely known as promising catalysts for FTs. The FTs has attracted enormous attention recently due to strict regulations on sulphur levels in transportation fuels. Various supports including mesoporous silicas, have been employed to improve the low surface area of bulk  $\text{Co}_3\text{O}_4$ .

Prieto et al. investigated the effect of pore diameter and length on the catalytic activity of SBA-15 supported  $\text{Co}_3\text{O}_4$  for FTs [342]. They showed that the pore length had a greater effect on catalytic performance of the Co-composites than pore diameter. This was attributed to the greater restriction of mass transfer of the reactants through long channels than through short ones. It was shown that as the length of the pores decreased, more highly dispersed  $\text{Co}_3\text{O}_4$  was obtained, which was attributed to the shorter residence time of the generated gas during the decomposition of cobalt precursor. This in turn was claimed to improve the catalytic activity of the Co-based catalysts for FTs.

In addition, a complementary study was conducted on the extent of the influence of cobalt-support interactions and of the addition of Pt on the reducibility of cobalt oxide species and also on their catalytic performance in FTs [343]. It was found that cobalt oxide species supported on  $\text{Al}_2\text{O}_3$  had stronger interactions with the support compared to those supported on  $\text{SiO}_2$ . The reducibility of these species and thus their catalytic performance was shown to be increased by (a) increasing the cobalt content, resulting in the formation of larger particles with less interaction with the support, and (b) using Pt as a promoter, which improves the reducibility through  $\text{H}_2$  spill-over. However the mesoporous structure of the support was shown to have much more impact on the final dispersion, size and the catalytic activity of the

supported  $\text{Co}_3\text{O}_4$  particles than the cobalt content [254]. It was shown that SBA-15, with its narrow PSD, resulted in the formation of  $\text{Co}_3\text{O}_4$  with less aggregation and more dispersion than  $\text{Co}_3\text{O}_4$  deposited on commercial  $\text{SiO}_2$  with a broader PSD. The less aggregated more dispersed  $\text{Co}_3\text{O}_4$  was reduced more easily and gave better catalytic performance in FTs.

It is generally accepted that to improve the catalytic performance of the Co-based catalysts, it is of utmost importance to minimize the interaction of the cobalt with the support. Weaker interaction results in easier reduction of the active sites and possibly better dispersion. These properties of the active sites in turn gave higher catalytic activity for FTs by virtue of the higher active surface area [327]. Van de Water et al. reported that using  $\text{CoCO}_3$  in the presence of citric acid as opposed to  $\text{Co}(\text{NO}_3)_2 \cdot 6\text{H}_2\text{O}$  as metal precursor minimized the formation of  $\text{CoAl}_2\text{O}_4$ . These species are hard to reduce and had an adverse impact on catalytic performance in FTs. The decline in the formation of  $\text{CoAl}_2\text{O}_4$  was attributed to the formation of cobalt citrate complexes.

The effect of ruthenium (Ru) addition to SBA-15 supported metallic cobalt on catalytic activity for FTs was investigated [344]. The catalyst was prepared using  $\text{Co}(\text{NO}_3)_2 \cdot 6\text{H}_2\text{O}$  via wet impregnation method (see section 1.6.5.1.3). It was demonstrated that upon adding Ru the catalytic activity of the SBA-15 supported cobalt for FTs increased, probably by adding Ru the reduction of cobalt oxide species was facilitated due to  $\text{H}_2$  spill-over. The resulting high concentration of metallic cobalt on the surface improved the catalytic performance.

SBA-15 with various pore diameters was synthesized and used as supports for nanocasting cobalt oxide species via wet impregnation (see section 1.6.5.1.3) [345].  $\text{Co}(\text{NO}_3)_2 \cdot 6\text{H}_2\text{O}$ ,  $\text{Co}(\text{CH}_3\text{COO})_2 \cdot 4\text{H}_2\text{O}$  and  $\text{Co}(\text{CH}_3\text{COCHCOCH}_3)_2 \cdot 2\text{H}_2\text{O}$  were used as metal precursors to investigate the effect of the cobalt precursor on the crystallinity of the final products. The composite prepared from  $\text{Co}(\text{NO}_3)_2 \cdot 6\text{H}_2\text{O}$  demonstrated the best crystallinity. It was thought that this was because there was less interaction between nitrate ions and the support than between acetate or acetylacetonate ions and the support. Wang et al. investigated the effect of pore regularity on the dispersion, particle size and aggregation behaviour of the cobalt oxide species supported on amorphous  $\text{SiO}_2$  and SBA-15. It was also demonstrated that  $\text{Co}_3\text{O}_4$  was more homogeneously dispersed on SBA-15 relative to amorphous  $\text{SiO}_2$ . Irrespective of cobalt content, no aggregation was observed for Co-SBA-15, which was not the case for Co- $\text{SiO}_2$  [346]. The authors attributed the higher catalytic performance of Co-SBA-15 compared to Co- $\text{SiO}_2$ , to the higher dispersion, lack of aggregation and smaller particle size of Co on SBA-15.

Confining attention to supported catalysts, the general opinion implied by the papers reviewed above is that the catalytic activity of cobalt depends on the size distribution of the metal-containing particles, their dispersion on the catalyst surface, and the cobalt species present, the strength and nature of the interaction between the cobalt species and support are also important.

The value of these quantities in their turn depend on the nature and physical properties (surface area, PSD and geometry) of the support, the counter anion and the cobalt compound used to introduce cobalt on the support. The preparation method used to introduce the cobalt compound, the post preparation treatment of the support (e.g. calcination temperature) and the amount of cobalt loaded per unit volume of the support are also play significant role in the morphology of the catalytically active particles and the catalytic activity.

The promoters added are reported to act by increasing the number of oxygen adsorbing sites, assisting in reduction of the cobalt species, increasing the dispersion of the cobalt species and changing the interaction between the cobalt species added and the support.

Often the authors' aim is directed towards obtaining an active catalyst rather than explaining in more than cursory detail why it is active. This thesis aims to not only to produce an active catalyst, but to look carefully to the factors that determine its activity.

## **1.8 Scope of the present study**

Designing sustainable heterogeneous systems to catalyse a wide range of reactions is of utmost significance. The success depends on the development of evenly dispersed active sites on a high surface area support. If this can be achieved more active surface area can be available for the reactants to interact under mild conditions with resulting high catalytic activity and selectivity towards the desirable products. The stability of the heterogeneous catalysts is also important due to new laws mandating reduction in waste.

The objectives of this work are to engineer Co-based composites and investigate their catalytic performance for liquid phase oxidation reactions. To fulfil our aims, mesoporous silica SBA-15 was used as a support due to its high surface area, tuneable pore size and high thermal and hydrothermal stability.

The effect of different cobalt precursors and various preparation methods on the morphology and catalytic performance of the resulting composites was investigated in detail. The impact of  $\text{Ce}(\text{NO}_3)_3 \cdot 6\text{H}_2\text{O}$  as a dopant on the morphology and dispersion of the cobalt

oxide species, as well as on the catalytic activity of the resulting composites, was also studied.

A wide range of characterisation methods were applied in this thesis to obtain comprehensive understanding of the structural and chemical properties of the Co-based composites. Low-angle XRD, N<sub>2</sub> adsorption-desorption, transmission electron microscopy (TEM), scanning electron microscopy (SEM), scanning transmission electron microscopy (STEM) and elemental mapping profiles were exploited to investigate the morphology of the composites. Additionally, to investigate the composition and chemical properties of the composites, wide-angle XRD, Fourier transform infrared (FTIR), diffuse reflectance ultra violet-visible (DR UV-vis), temperature programmed reduction (TPR), X-ray photoelectron spectroscopy (XPS), <sup>29</sup>Si magnetic angle spinning nuclear magnetic resonance spectroscopy (<sup>29</sup>Si MAS NMR) and inductively coupled plasma mass spectroscopy (ICP-MS) were employed. In order to evaluate the catalytic activity of the composites, various organic substrates were used in the presence of TBHP as an oxidant. The products were identified using gas chromatography (GC) and gas chromatography-mass spectrometry (GC-MS). These investigations shed light on the mechanism of the oxidation reaction which we proposed in our publications.

## **1.9 Thesis overview**

This thesis is presented in a “thesis by publication” format. It is made up of two published journal articles, two submitted articles and four drafted articles. Each chapter contains a brief introduction in which the articles are placed within the context of the thesis as a whole. The outline of the present PhD thesis is as follows:

Chapter 1 (this chapter) provides a literature review on the importance of catalytic reactions, with the main focus on the heterogeneous catalysis. This chapter also provides information about the various supports, typically OMSs and various techniques of depositing active species on these supports. This chapter contains information about supported cobalt/cobalt oxide species, their properties as well as their catalytic performance for a wide range of catalytic applications.

Chapter 2 describes the experimental and characterisation methods used in this thesis. This chapter also contains the basic principles of the characterisation methods with the main focus on the surface area analysis and electron microscopy.

Chapter 3 is concerned with the synthesis of Co-based composites from  $\text{Co}(\text{NO}_3)_2 \cdot 6\text{H}_2\text{O}$  as a cobalt precursor. The impact variation of two variables, Co-loading and preparation methods, on the final morphology and catalytic performance of the resulting composites was thoroughly covered in this chapter. The results were reported in three journal articles: This chapter also contains an appendix with supplementary information which is not included in the articles.

- ❖ Publication 1 - Preparation and characterization of mesoporous silica supported cobalt oxide as a catalyst for oxidation of cyclohexanol
- ❖ Publication 2 - Mesoporous silica SBA-15 supported  $\text{Co}_3\text{O}_4$  nanorods as efficient liquid phase oxidative catalysts
- ❖ Publication 3 - Impact of low cobalt loading on the morphology and dispersion of the crystalline  $\text{Co}_3\text{O}_4$  patches supported on SBA-15

Chapter 4 focuses on the effect of the cobalt precursor on the morphology of the composites, as well as on the dispersion of the cobalt oxide species throughout the support, SBA-15. This chapter also presents the catalytic performance of these composites in liquid phase oxidation of cyclohexanol. The results of this work are summarised in two journal articles. This chapter also comprises an appendix with supplementary information which is not included in the articles however validates the results presented in them.

- ❖ Publication.1- Cobalt precursor impact on the dispersion and morphological development of SBA-15 supported cobalt oxide species
- ❖ Publication 2- SBA-15 supported cobalt oxide species: preparation, morphology and catalytic activity

Chapter 5 contains a brief literature review on the properties and applications of ceria in catalysis. It also focuses on the effect of ceria as a dopant on the dispersion, size and catalytic activity of bulk or supported metal oxide particles. Two series of composites using  $\text{Co}(\text{NO}_3)_2 \cdot 6\text{H}_2\text{O}$  and  $\text{CoCl}_2 \cdot 6\text{H}_2\text{O}$ , prepared via the two-solvent method, were investigated. In both cases  $\text{Ce}(\text{NO}_3)_3 \cdot 6\text{H}_2\text{O}$  was used as a dopant. The findings of these studies are presented in the following publications:

- ❖ Publication 1- Effect of Ce-doping on the dispersion of  $\text{Co}_3\text{O}_4$  nanorods supported on SBA-15
- ❖ Publication 2- Effect of Ce-doping on the structure and redox properties of SBA-15 supported cobalt oxide species in catalytic oxidation reactions

- ❖ Publication 3- The impact of Co:Ce ratio on the dispersion and catalytic activity of cobalt-cerium oxides supported on SBA-15

Chapter 6 This chapter provides a summary of the concluding remarks in this work and discusses some possible avenues for future research.

---

# Chapter 2

## Experimental

---

An experimental section is given in each of the papers that follow but the detailed experimental methods have been collected together in this chapter for the completeness and convenience.

This chapter is divided into three sections. The first section deals with the preparation of the mesoporous silica SBA-15 and SBA-15 supported cobalt oxide species preparations. The main focus of the second section is on the characterization techniques employed during this thesis. The last section is associated with the catalytic evaluation of the Co-composites, Ce-doped Co-composites, the identification of the products as well as the conversion percentage to the products.

## **2.1 Catalysis synthesis**

### **2.1.1 Synthesis of mesoporous silica SBA-15**

SBA-15 was prepared using the method first described by Zhao and co-workers [129]. Typically, tri-block copolymer, EO<sub>20</sub>PO<sub>70</sub>EO<sub>20</sub>, 4g, was dissolved in aqueous hydrochloric acid, 2M, with vigorous stirring. A clear solution indicated the complete dissolution of the surfactant. TEOS, 8.5g, was then added dropwise to this solution at 40 °C with vigorous stirring. Gelation was allowed to proceed for 24 h at 40 °C, after which the mixture was transferred to a sealed Teflon flask for hydrothermal treatment at 100 °C for 24 h. The precipitate was filtered, washed several times with distilled water and dried at RT. Finally, the template was removed by heating in air at 1°C min<sup>-1</sup> from RT to 550 °C, then holding at 550 °C for 6 h and finally cooling to RT.

### **2.1.2 Supported cobalt oxide catalyst preparation**

#### **2.1.2.1 Two-solvent method**

In this method, SBA-15 was first dispersed in dry hexane, a hydrophobic solvent [337]. Co(NO<sub>3</sub>)<sub>2</sub>.6H<sub>2</sub>O and CoCl<sub>2</sub>.6H<sub>2</sub>O were used as cobalt precursors to investigate the impact of metal precursor on the resulting composites. The desired amounts of either Co(NO<sub>3</sub>)<sub>2</sub>.6H<sub>2</sub>O or CoCl<sub>2</sub>.6H<sub>2</sub>O to obtain the nominal 1 wt%, 5 wt%, 10 wt%, 20 wt%, 30 wt% and 40 wt% Co-loading were dissolved in distilled water. The volume of water used corresponded to the pore volume of the SBA-15 in the mixture, determined previously using N<sub>2</sub> adsorption-desorption (see section 2.2.1.1). In the next step the hydrophilic solution was added dropwise to the hydrophobic solution and the mixture stirred for 15 min. The mixture was then sonicated for 15 min and further stirred for 2 h. The solid was recovered by filtration and

dried at RT overnight. A pink powder was obtained regardless of the nature of the cobalt precursor. Finally, the samples were calcined by heating in air at  $2\text{ }^{\circ}\text{C min}^{-1}$  from RT to  $700\text{ }^{\circ}\text{C}$  and holding for 6 h before they were cooled down [337].

After calcination two different Co-composites were obtained. A blue coloration was observed when  $\text{CoCl}_2\cdot 6\text{H}_2\text{O}$  was used as the precursor, with the intensity of the color increasing with color content. A black powder was obtained from  $\text{Co}(\text{NO}_3)_2\cdot 6\text{H}_2\text{O}$ .

For comparison commercial  $\text{Co}_3\text{O}_4$  nanopowder (50 nm particle size) was purchased from Aldrich.

### **2.1.2.2 Impregnation**

Impregnation with an excess amount of the cobalt aqueous solutions was applied (section 1.6.5.1.1) to synthesize Co-composites using  $\text{Co}(\text{NO}_3)_2\cdot 6\text{H}_2\text{O}$  and  $\text{CoCl}_2\cdot 6\text{H}_2\text{O}$  as metal precursors. In all cases, the nominal Co-loading was calculated to be 1 wt% and 5 wt%. Typically, SBA-15 was dispersed in cobalt aqueous solution and the mixture stirred for 6 h to ensure the maximum deposition. Then a pink solid was recovered under reduced pressure for approximately 1 h. The composites were then dried overnight at RT and calcined using the procedure of section 2.1.2.1.

Interestingly, the same coloration behaviour (blue for  $\text{CoCl}_2\cdot 6\text{H}_2\text{O}$ , black for  $\text{Co}(\text{NO}_3)_2\cdot 6\text{H}_2\text{O}$ ) was observed when impregnation was employed to synthesize Co-composites as was observed for the two-solvent method (see section 2.1.2.1).

### **2.1.2.3 Adsorption**

Finally, a series of Co-composites were prepared via adsorption [176]. The desired amounts of cobalt precursors to obtain the nominal 5 wt% Co-loading were dissolved in an excess amount of distilled water relative to the pore volume of the SBA-15. Next SBA-15 was dispersed in the cobalt aqueous solution and the mixture was stirred for 6 h to ensure the maximum interaction between the cobalt precursor and support. The resulting solid was recovered by filtration as a very light pink powder regardless of the nature of the cobalt precursor. The drying and calcination processes were the same as in section 2.1.2.1.

## **2.1.3 Supported Ce-doped Co-composites**

The two-solvent method was also employed to prepare a series of catalysts using  $\text{Co}(\text{NO}_3)_2\cdot 6\text{H}_2\text{O}$  and  $\text{CoCl}_2\cdot 6\text{H}_2\text{O}$  to introduce cobalt to the pores of SBA-15 and

Ce(NO<sub>3</sub>)<sub>3</sub>·6H<sub>2</sub>O as a dopant. In all cases the composites were calculated to have 5 wt% Co and 0.5-2 wt% Ce. Here the cobalt aqueous solution was first added to the hydrophobic solution dropwise and the mixture stirred for 15 min before the addition of cerium aqueous solution. It is noteworthy that the total volume of these solutions corresponded to the relevant pore volume of the SBA-15 in the mixture, which was determined previously by N<sub>2</sub> adsorption-desorption (section 2.2.1.1). The final mixture was then stirred for 15 min, sonicated for 15 min and further stirred for 2 h.

The solid was then recovered by filtration. It was light pink irrespective of the nature of the metal precursor. The solid material was then dried at RT, and then calcined using the same procedure of section 2.1.2.1.

## 2.2 Characterization techniques

These techniques are classified into four main groups:

- (i) adsorption based methods,
- (ii) x-ray based methods,
- (iii) electron microscopy based methods
- (iv) vibrational spectroscopy based methods.

The gas chromatography, gas chromatography-mass spectrometry and elemental analysis will be discussed separately.

### 2.2.1 Adsorption

#### 2.2.1.1 N<sub>2</sub> adsorption-desorption

One of the most common characterization methods in heterogeneous catalysis is the determination of the texture of the porous material, typically the OMS support. This involves:

- (i) specific surface area (m<sup>2</sup> g<sup>-1</sup>), which includes both the geometric surface of the structural units (grains, spheres or sub-particles) and the surface area provided by pore walls (m<sup>2</sup> g<sup>-1</sup>)
- (ii) specific pore volume (cm<sup>3</sup> g<sup>-1</sup>), which included the volume of micropores, mesopores and/or macropores (see section 1.6)
- (iii) pore shape
- (iv) pore size distribution, PSD

The evaluation of all the above mentioned parameters can be obtained by gas physisorption on the porous solid. In this process, the force between adsorbent, solid material,

and adsorbate, gas, is considered to be of Van-der-Waals type [347-351]. The interaction energy between a solid and gas approximates the condensation energy of the gas in the absence of chemisorption. This suggests that the electronic state of the gas atom or molecule does not alter through physisorption [134].

Physisorption is generally quantitatively measured by means of the adsorption-desorption isotherm which gives the quantity of gas adsorbed on the porous surface as a function of gas pressure at constant temperature [349, 352]. The adsorption isotherm is a curve obtained when the gas pressure is increasing, the desorption isotherm is the curve obtained when the pressure is decreasing. If the desorption isotherm is not identical to the adsorption isotherm, this is named “hysteresis” and the continuous curve of the adsorption and desorption branches in the gas pressure range when the branches do not coincide is called a “hysteresis loop”. Adsorption is often expressed as a function of the gas relative pressure ( $p/p_0$ ) over the range  $p/p_0 = 0.001-0.999$ . Here  $p$  is the equilibrium pressure of the adsorbate in contact with the adsorbent and  $p_0$  is the saturated vapour pressure of the gas at the isotherm temperature [353, 354]. The physisorption technique is based on the fact that gas condenses inside small pores at relative pressure less than one. Nitrogen is the most common adsorbate [353], but, for more accurate results argon has been suggested if the pores are smaller than 2 nm, [354, 355]. This is because the argon molecule is spherical.

Generally, adsorption and desorption isotherms for nitrogen are recorded at 77 K, -196 °C, the boiling point of nitrogen [353]. The specific surface area, SSA, is determined from an adsorption isotherm [356]. The desorption isotherm offers additional information, on the mesoporosity of the material [357].

Various types of isotherms were proposed by Brunauer, whose classification was extended and modified by IUPAC [356]. The form of the isotherm and the shape of the hysteresis loop, if any, provide valuable information on the average pore diameter, interaction between gas and porous solid and PSD [134]. Generally six types of isotherms (Figure 2.1) and four types of hysteresis loops (Figure 2.2) [358] have been distinguished in the IUPAC classification. The four most common isotherm types are (I), (II), (IV) and (VI) [354, 359].

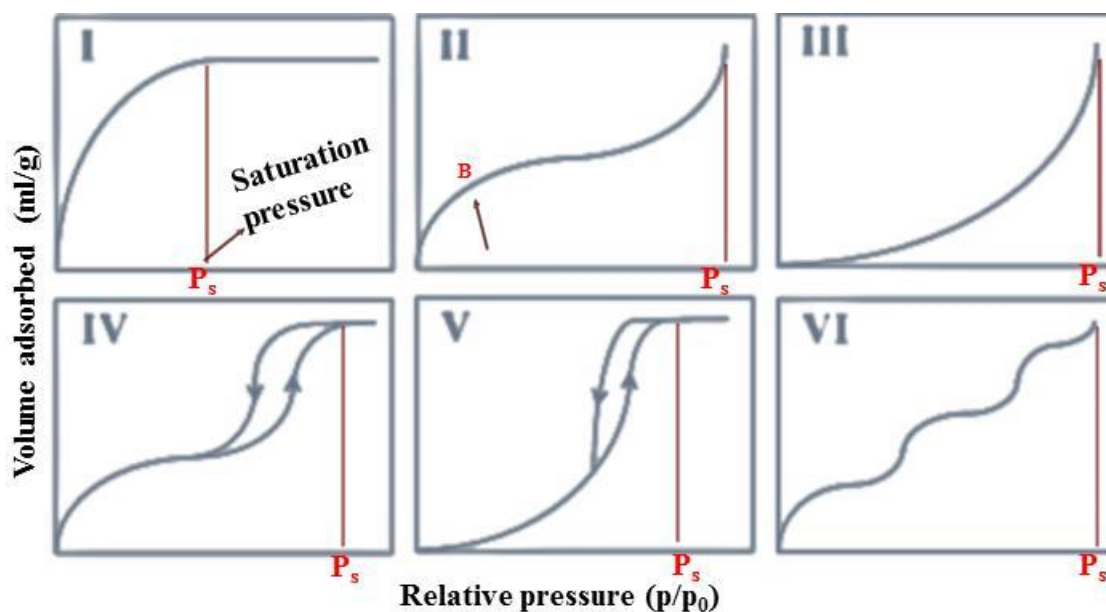


**Figure 2.1.** Schematic diagram of various types of isotherms [356]

The type I isotherm is concave to the relative pressure  $p/p_0$  axis. This type of isotherm is obtained when the adsorption is limited to a few molecular layers. This normally occurs in the micropores, which suggests a high uptake of the liquid  $N_2$  at low relative pressure ( $> 0.1$ ). The high liquid  $N_2$  uptake is due to the narrow pore width and high adsorption potential. This type of isotherm is normally found for microporous materials with pores of average diameter about 2 nm.

Type II isotherms are typically obtained for non-porous or macroporous materials with mono-layer type adsorption up to an inversion point (B) above which pressure multi-layer adsorption occurs.

Type IV is characteristic of mesoporous solids such as MCM-41 [128] and SBA-15 [40]. The isotherms show an inflection which is due to the capillary condensation phenomenon, in which the gas phase rapidly condenses in the pore due to the interaction between the gas and porous surface [352]. The isotherms of some mesoporous materials, for instance, SBA-15 exhibit the presence of both micropores and mesopores [360]. Therefore the initial part of the isotherm is very similar to type I, which is associated with micropore filling. For SBA-15 the capillary condensation occurs at relative pressure  $p/p_0 = 0.4-0.8$  which indicates that the mesopores have pore diameters in the range 5-10 nm. It is noteworthy that the sharpness of the inflection indicates a narrow PSD [361].

Type VI is characteristic of non-porous materials. The isotherm shows groups of adsorption sites with the sites in each group having almost the same adsorption enthalpy.

Type III and V are quite uncommon. Such convex isotherms indicate very weak interaction between gas and the solid surface.

Hysteresis loops convey additional useful information on the texture of the materials as well as their pore structure (Figure 2.2) [134]:

H<sub>1</sub> type hysteresis implies cylindrical pores, which are possibly interlinked. This type of hysteresis loop suggests that the PSD is quite uniform.

H<sub>2</sub> type hysteresis is associated with cylindrical and spherical pores with non-uniform pore shape or distribution.

H<sub>3</sub> type hysteresis is normally observed for lamellar materials with slit-shaped, non-uniform pores.

H<sub>4</sub> type hysteresis corresponds to slit-shaped uniform pores.

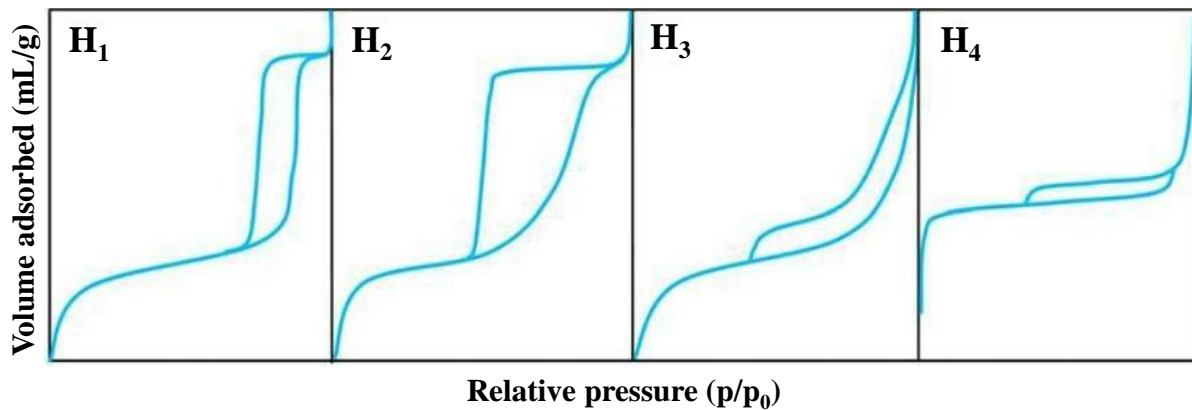


**Figure 2.2.** Type of hysteresis loops [134]

### 2.2.1.1.1 Measuring the specific surface area

There are several methods to determine the specific surface area. The BET method developed by Brunauer, Emmett and Teller [356] is the one most commonly used for catalysis investigations.

The BET equation is;

$$\frac{P}{V_a(P_0-P)} = \frac{1}{V_m C} + \frac{C-1}{V_m C} \cdot \frac{P}{P_0} \quad \text{Eq. 2.1}$$

Where:  $V_a$  is the volume of the adsorbate at pressure  $P$ ,  $V_m$  is the volume of the monolayer adsorbate,  $P_0$  is the saturation pressure,  $P$  is the equilibrium pressure,  $P/P_0$  is the relative pressure and  $C$  is the enthalpy of adsorption.

When BET method is used to measure the surface area, only the data points collected in the range  $0.05 < P/P_0 < 0.3$  are taken, because the mono-layer adsorption normally occurs in this range [347, 356]. This is considered to be the main reason for specifying BET method to determine the surface area of mesoporous materials, since micropore filling is not taken into account in BET theory.

The experimental apparatus used for most of the  $N_2$  adsorption-desorption measurements in this study was a Coulter Omnisorb 360-CX. All the samples were outgassed at 150 °C under vacuum overnight. This temperature was found to be sufficient to remove the usual adsorbates such as water and carbon dioxide, which otherwise would have influenced the measurement. The  $N_2$  adsorption-desorption isotherms were obtained at -196 °C (77 K) on the analysis ports of the same instrument.

However, in some cases, due to the unavailability of the Coulter Omnisorb 360-CX, the samples were analysed using a Micromeritics TriStar II 3020 surface area and porosity analyser with the same settings as for the Coulter. Here the samples were degassed at 150 °C overnight using the Micromeritics VacPrep 061.

### **2.2.1.2 Temperature programmed reduction (TPR)**

One of the most widespread uses of chemical adsorption is in TPR, which monitors the hydrogen consumption and reducibility of a catalyst as a function of temperature [362]. This technique provides information about the degree of the oxidation of metal oxide catalysts [320]. TPR is highly sensitive to the chemical changes occurring either as a result of the interaction between the active sites and support [238] or the presence of a dopant. Therefore, it is considered to be a powerful technique to characterize metal oxides, either in the bulk phase or supported, with or without the presence of a dopant [235, 335, 363].

This technique provides quantitative as well as qualitative information about the catalysts under reducing conditions. Some instruments are equipped with a thermal conductivity detector (TCD), which records the changes in the thermal conductivity of the gas flow as it passes over the sample. The resultant peak displays the concentration of the reducing gas. By integrating the area of this peak vs. time or temperature, the total gas consumption can be easily measured. This exhibits information about the oxidation state of the active sites. Other instruments measure the weight loss of the metal oxides due to the hydrogen consumption as a function of temperature or time. This provides more qualitative information about the oxidation state of the metal oxides.

Generally, the reduction process in TPR is carried out under hydrogen, which is mixed with a carrier gas, typically argon, helium or nitrogen. When a TCD is used, the thermal conductivity of the carrier should ideally differ as much as possible from that of hydrogen. It is always important, whether the TCD is used or not that the carrier gas should remain unreactive to the active particles even at high temperature. As a result, argon (Ar) is widely used as the carrier gas, because helium (He) has a similar thermal conductivity to hydrogen and nitrogen can be reactive during the reduction process.

A 10 % H<sub>2</sub> in argon mixture is commonly used for the reduction process. The gas passes through the solid catalyst in a quartz or alumina reactor. The sample is heated through a predetermined temperature ramp and any changes either in the conductivity of the gas flow or the weight of the sample are recorded as a function of time or temperature. Therefore, it is essential to have a constant gas flow.

The TPR experiments described in this thesis were carried out with a Setaram Thermogravimetric Analyser (TAG 24). The TPR profiles for the catalysts in this thesis were collected using two different target temperatures 900 °C and 1100 °C for Co-composites and Ce-doped Co-composites respectively (Figure 2.3). The catalyst (about 10 mg) was weighed with an accuracy of  $\pm 0.0001$  g into a cup-shaped alumina crucible which was inserted into the furnace at RT. All the samples were heated up to 150 °C (10 °C min<sup>-1</sup>) and kept at this temperature for 20 min under pure Ar. This pre-treatment was carried out to drive off any physically adsorbed impurities or moisture. The sample was then cooled down to RT and heated up to 900 °C or 1100 °C at 5 °C min<sup>-1</sup> under 10 % H<sub>2</sub> in Ar at a constant flow rate of 70 cm<sup>3</sup> min<sup>-1</sup>. During the reduction process any changes in the weight of the catalyst were recorded. Then the sample was kept at the target temperature for 20 min under the reducing condition and 20 min under pure Ar, and finally it was cooled to RT under Ar (Figure 2.3).

In order to determine the small weight loss of the supported cobalt oxide species, it is necessary to account for weight changes in the system (blank correction) and, also, in the SBA-15 support. These effects were evaluated in independent runs and the appropriate corrections applied.

The TPR profiles in this work are reported as the first derivative of the correlated weight loss vs. temperature.

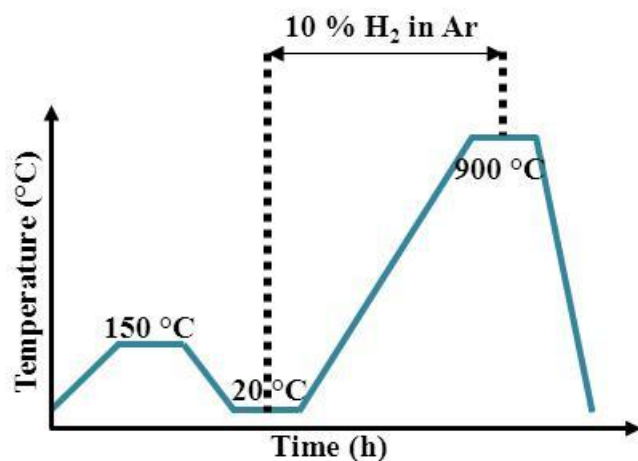


**Figure 2.3.** Diagrammatic profile of TPR program used in this thesis

### 2.2.2 X-ray diffraction (XRD)

X-ray diffraction is a non-destructive, versatile technique to study the chemistry, crystallite size, shape and crystalline phases in a bulk sample [364, 365]. In X-ray diffraction only short wavelength X-rays ranging in wavelength from few angstroms to  $0.1 \text{ \AA}$  (1 keV-120 keV) are used, wavelength which are comparable to atomic sizes [366]. The elastic interaction between a monochromatic parallel X-ray beam and the electron cloud of the atoms in a solid material results in the formation of secondary waves, which can interfere destructively or constructively and produce diffraction patterns.

X-rays were first systematically studied by Wilhelm Rontgen in 1895. In 1914, Max Theodor Von Laue for the first time observed that X-rays were diffracted by crystals [366]. The XRD technique advanced very quickly and the Braggs (Sir Williams Henry Bragg and William Lawrence Bragg) determined the first crystal structures for NaCl, ZnS and diamond. Von Laue and the Braggs received the Noble prize for in 1915.

Generally X-rays are produced by either conventional X-ray tubes or synchrotron radiation. In the former, the X-rays are generated when a metal target (stationary or rotating), typically copper or molybdenum, is bombarded with a focused electron beam. The electron beam is accelerated across a high voltage between the cathode (W) and a water-cooled anode (Cu). As the electrons collide with the target, a weak continuous X-ray spectrum, known as Bremsstrahlung radiation is produced [367]. Electrons with high energy can eject electrons from a core level of the atom. A characteristic X-ray photon of the target material is emitted when the vacant position of the ejected electron is filled by higher level electrons [366]. The most intense X-ray is emitted by Cu and Mo, have wavelengths  $1.54 \text{ \AA}$  and  $0.8 \text{ \AA}$ , respectively and these are the wavelengths used in X-ray diffraction.

A synchrotron is a particle acceleration device, in which the presence of bending magnets results in a circular and hence accelerated motion of charged particles (positrons or electrons). The accelerated motion produces electromagnetic synchrotron radiation, which includes X-rays with typically  $10^8$  the intensity of those from conventional X-ray tubes. The energy and wavelength of these radiations is tuneable so that they can easily interact with light atoms, for instance oxygen and carbon.

The diffraction pattern resulting from the interaction between X-ray and a crystalline solid is characteristic of the chemical composition and crystal structure of the phase present (see section 2.2.3.1). Thus the composition and crystal structure of the solid can be determined by comparing the diffraction pattern with a compendium of known patterns such as JCPDS (Joint Committee for Powder Diffraction Standards), an electronic data base containing approximately 500000 structures.

### 2.2.2.1 Formation of diffraction pattern

An electron in an electromagnetic field oscillates with the same frequency as the field. Thus when an X-ray beam passes through the electronic cloud of a solid material, electrons begin to oscillate with the frequency of the incident beam. These oscillations are in all directions, which results in formation of secondary X-ray waves and both destructive and constructive interference. The former interference results in the “out of phase” waves and the latter causes the “in phase” waves [368]. As a consequence of the destructive interference no energy leaves the solid sample. However, in crystalline materials the atoms are highly ordered and arranged in a regular pattern, so that, in particular, there will be planes of atoms of constant interplanar spacing. This ordered structure of parallel planes results in constructive interference at particular angles and thus the energy leaves the atom as the scattered radiations at these angles [366].

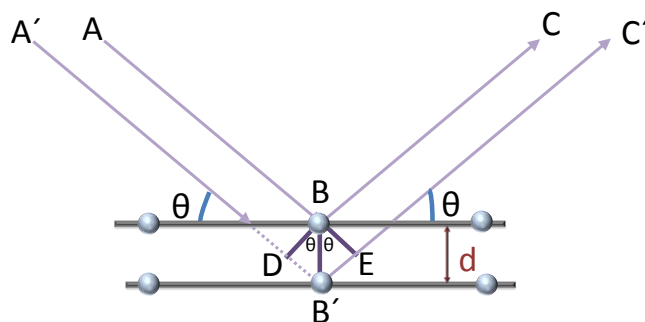


**Figure 2.4.** Schematic diagram of Bragg's Law

Bragg's Law relates the angles at which constructive interference occurs with the structure of the crystal. Suppose a monochromatic X-ray beam of a certain wavelength ( $\lambda$ ) passes through the atoms of a crystal which are located on parallel planes a distance  $d$  apart with angle ( $\theta$ ) relative to the planes (Figure 2.4). Each atom scatters the incident X-ray beam uniformly in all directions [368]. As it is displayed in Figure 2.4, for two rays scattered from atoms B and B' located on adjacent parallel planes the path length ray of ABC is shorter than that of ray A'B'C'. The path difference (B'D+B'E) between these two rays is given by:

$$B'D = B'E = d \sin\theta$$

$$B'D + B'E = 2d \sin\theta$$

If the path difference is an integer multiple ( $n$ ) of the incident beam wavelength ( $\lambda$ ) the interference between the two scattered rays is constructive, so that peaks in X-ray intensity will occur at angles given by Eq. 2.2 which is Bragg's Law:

$$n\lambda = 2d\sin\theta \quad \text{Eq. 2.2}$$

The integer  $n$  is known as the order of reflection [366]. The distribution of interplanar spacings and hence  $\theta$  values will depend on the chemical composition and its crystal structure and so can be used to identify the chemical phases present. The intensity of different X-ray peaks, which will depend on the intensity of electrons in a particular set of planes, is also useful in this regard.

The diffraction peaks can also be used to calculate the average size of the crystals. This is done by employing the Scherrer equation (Eq. 2.3), using typically the peak with highest intensity [369].

$$t = K\lambda / B \cos\theta \quad \text{Eq. 2.3}$$

The variable  $K$  is the Scherrer constant and can range from 0.89-1.39 depending on the geometry of the crystal; for a 2D lattice  $K$  is calculated to be 0.89 whereas for a cubic 3D lattice  $K$  is 0.94 and for a perfect spherical crystal  $K$  equals 1.33.  $B$  is the line broadening at full width at half maximum (FWHM),  $t$  is the average crystal size and  $\lambda$  is the wavelength of the X-ray beam [369].

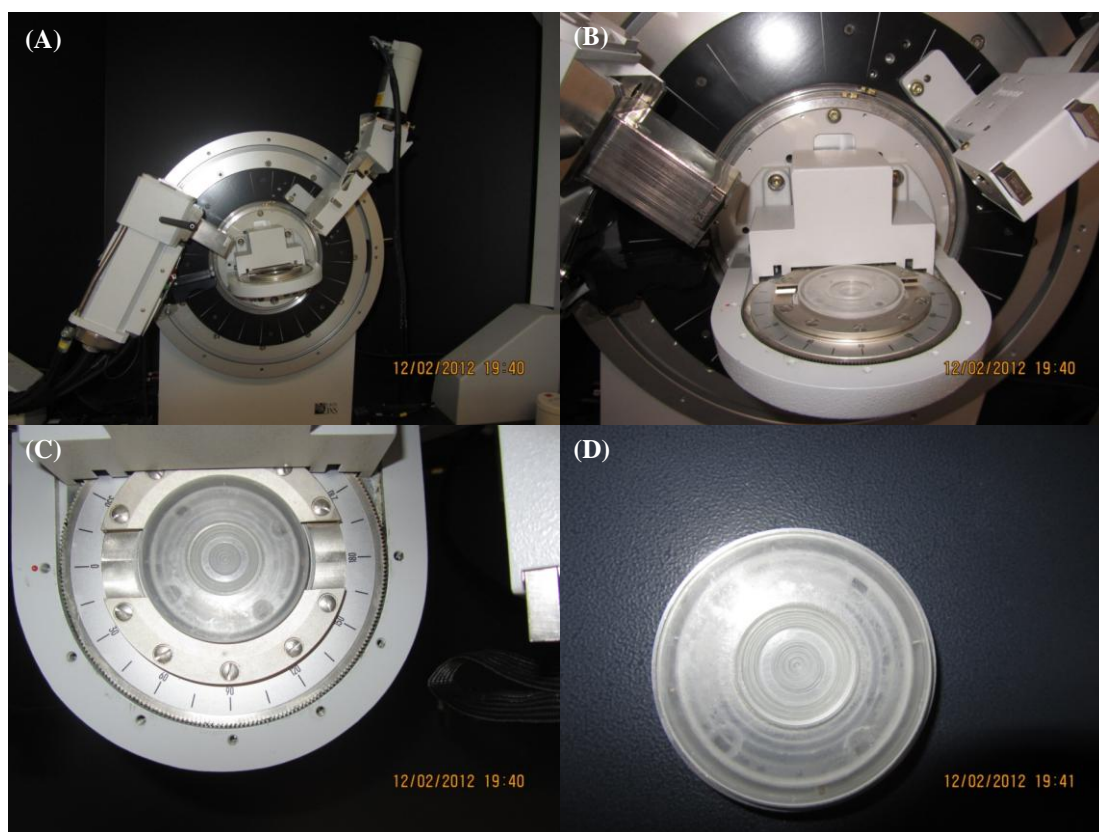


**Figure 2.5.** The Bruker D8 Focus diffractometer (A, B) and the sample holder (C, D)

Diffraction patterns presented in this thesis were obtained using a Bruker D8 Focus powder diffractometer (Figure 2.5). Copper  $K\alpha$  radiation ( $1.54 \text{ \AA}$ ) produced at 40 kV and 30 mA was used with a step size of  $2\theta = 0.02^\circ$  and the step time of 0.1 and 1 minute per step for low and wide-angle XRD, respectively. The XRD patterns were collected from  $2\theta = 0.4\text{-}4^\circ$  (low-angle) and  $2\theta = 15\text{-}80^\circ$  (wide-angle).

### 2.2.3 X-ray photoelectron spectroscopy (XPS)

XPS (also known as ESCA, electron spectroscopy for chemical analysis) [370] is both a qualitative and quantitative surface analysis technique. This technique can be used to determine the elemental composition, oxidation state and electronic environment of the components on the surface a sample [371, 372]. XPS is utilized to investigate the elements with atomic number ( $Z$ ) above three;  $H_2$  and He are generally not detectable by this technique.

The spectroscopic analysis of high energy photoelectrons began in the 1910s, mostly in Rutherford's laboratory in Manchester and in 1914. Rutherford and his group suggested the relationship between the energy of the incident radiation, the binding energy of the elements in the atoms and the kinetic energy of the photoelectron. However, it was Auger in 1925 who

first explained the anomalous peaks at energy levels different from those predicted by Rutherford [373]. The XPS technique did not develop significantly until 1950, when Siegbahn from Uppsala University constructed a high resolution spectrometer and demonstrated that the binding energy of a photoelectron from a particular element depends significantly on the chemical state of the element [370].

In XPS, the sample is bombarded by an X-ray photon beam, usually the  $K\alpha$  radiation from Al or Mg with energy of 1486.6 eV and 1253.6 eV, respectively. As a result of this irradiation three important phenomena occur (Figure 2.6);

(i) Atom specific photoelectron emission (Figure 2.6A)

Electrons from core energy levels of different atoms in the sample are ejected after X-ray bombardment. By analogy with electrons ejected from outer levels by visible light, these are called photoelectrons and collected by a kinetic energy ( $E_k$ ) sensitive detector. The XPS spectra are then plotted as the emitted photoelectron intensity vs.  $E_k$ . Energy conversion then gives the original binding energy of the electron ( $E_B$ ) as a function of  $E_k$  and  $h\nu$ , the energy of the X-ray (Eq. 2.4). Thus the XPS spectra can also be plotted as the emitted photoelectron intensity vs.  $E_B$ . The  $E_B$  values can be used to identify the elements present, because these values are characteristic for each element, and to give some information about the chemical environment of the atoms.

$$h\nu = E_k + E_B \quad \text{Eq. 2.4}$$

Thus as the oxidation state of a certain element increases the  $E_B$  of the electron increases accordingly. This results in a peak shift to higher  $E_B$ . In addition, the intensity of the peaks is indicative of the concentration of an element.

(ii) Auger electron emission (Figure 2.6B)

Subsequent to (i), an electron from a higher energy level fills the “hole” left by the ejected core electron. The excess energy from this electron transition can release another electron known as an Auger electron. This process is known as Auger emission and intensity vs.  $E_k$  plot gives the Auger electron spectrum, AES [374].

(iii) X-ray fluorescence (Figure 2.6C)

Upon X-ray irradiation, an excited inner shell electron is ejected the atom. In the next step, as an electron moves from a higher energy level to fill the vacancy created by the ejected electron, an X-ray is emitted. The emitted X-ray is characteristic of the energy difference between these two shells. X-ray fluorescence is a non-destructive method of characterisation

and can be used for quantitative and qualitative analyses of elements heavier than fluorine (F).

In XPS the emission from p, d or f levels gives rise to two photoemission peaks due to spin-orbit splitting. The EB differences between these doublet lines are of the order of a few tenths of an eV, the exact value depending on the chemical and electronic state of the element. This can further assist the determination of the chemical state of a certain elements in the sample.

The XPS data presented in this thesis was conducted at the Australian Synchrotron with a SPECSlab2 spectrometer using a synchrotron as an X-ray source with selected wavelength of (1486.8 eV) at the constant analyser pass energy 40.0 eV. Binding energies are referenced to the carbon 1s peak (BE = 284.5 eV) arising from adventitious carbon.

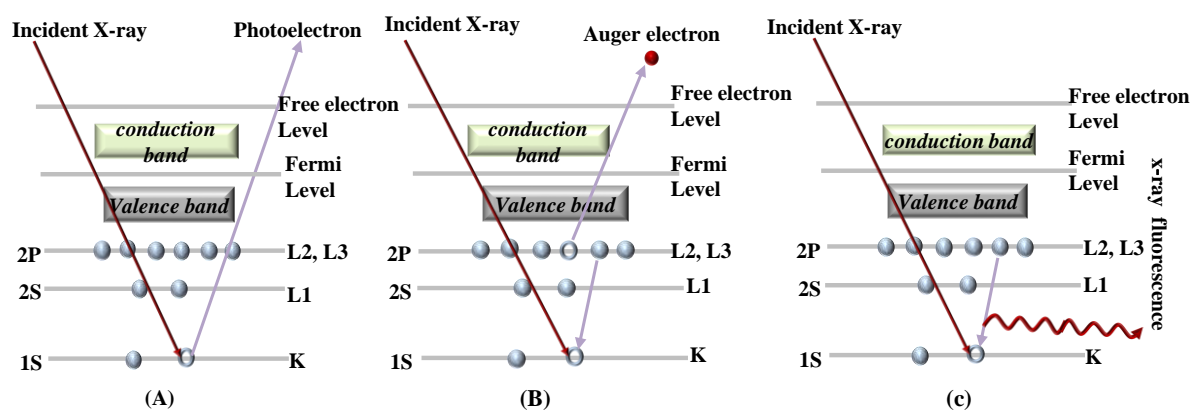


**Figure 2.6.** Excitation and relaxation processes giving rise to (A) XPS, (B) AES and (C) X-ray fluorescence

#### 2.2.4 $^{29}\text{Si}$ magnetic angle spinning nuclear magnetic resonance spectroscopy (MAS NMR)

Pauli first proposed that the magnetic properties of atoms could be attributed to their nuclei in 1924. More than a decade later in 1939, Rabi developed a technique which included the essential ingredients of the nuclear magnetic resonance (NMR) technique, to measure the magnetic properties of atoms. The phenomenon of NMR, however, was first demonstrated in 1946 by Purcell at Harvard and Bloch at Stanford [375].

The chemical usefulness of NMR is based on the fact that the nuclei of atoms have magnetic properties that depend to some extent on the chemical environment of the nucleus. The first requirement for NMR to be observed is non-zero nuclear spin. If the number of protons and neutrons are both even, the nucleus has zero spin. However if the sum of the

number of neutrons and protons is odd, then the nucleus has a half-integer spin ( $I$ ), for instance  $1/2$ ,  $3/2$  or  $5/2$ . If the number of neutrons and protons are both odd, then the nucleus has an integer spin (i.e. 1, 2, 3). All nuclei of non-zero spin have a finite magnetic moment [376].

If atoms with nuclei of non-zero spin are subjected to an external magnetic field of strength  $B_0$ , the nuclear magnetic moment of the nuclei, a vector, can assume  $2I+1$  orientations, which differ from each other in energy (Figure 2.7). The energy difference between two successive levels, neglecting the effect of the electric quadrupole moment of the nucleus is given by Eq. 2.5.

$$\Delta E = (h/2\pi)\gamma B_0 \quad \text{Eq. 2.5}$$

where  $h$  is Planck's constant,  $\gamma$  is the gyromagnetic ratio equal to  $\mu/p$ ,  $\mu$  is the magnitude of the magnetic moment of the nucleus and  $p$  is the kinetic moment of the nucleus.

It is transitions between these levels that give rise to NMR, and it is found that  $\Delta E$  depends on the chemical environment of the nucleus. Thus precise measurement of  $\Delta E$ , or, in practice, comparison of  $\Delta E$  with that for the same element in the suitable reference compound giving the so-called chemical shift, permits conclusions to be drawn about chemical environment of the nucleus.

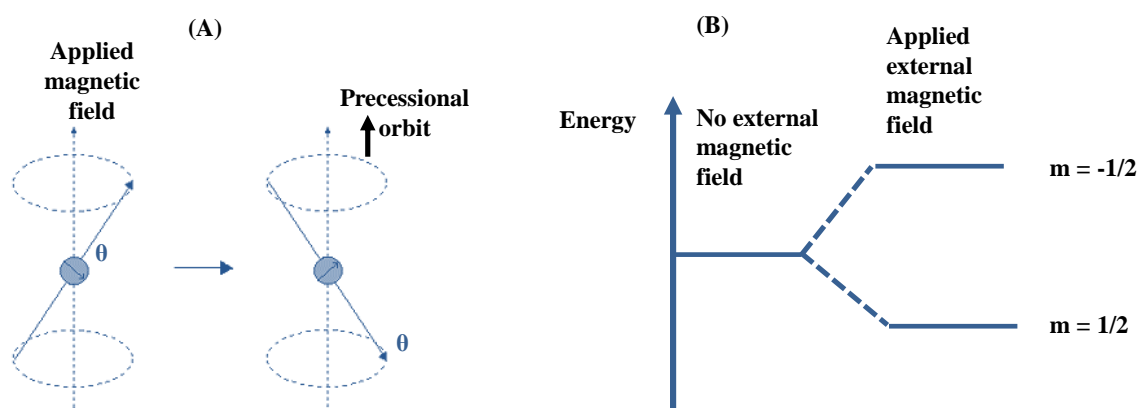


**Figure 2.7.** Schematic diagram of (A) nucleus in an external magnetic field and (B) nuclear spin state in an external magnetic field

NMR spectroscopy is mostly used to analyse liquid samples because without special precautions, the resonance from solid samples are broad and non-informative. The most common NMR analyses are  $^1\text{H}$  NMR and  $^{13}\text{C}$  NMR. However in the magic angle spinning (MAS) mode, NMR can be exploited to characterize solid samples [377, 378]. Solid state  $^{29}\text{Si}$  NMR is a powerful technique to investigate the structure and bonding properties of

mesoporous silica and functionalized mesoporous silica [379]. The first major investigation on solid state  $^{29}\text{Si}$  NMR was conducted by Lippmaa et al. [380]. They reported that the chemical shifts observed in solid state  $^{29}\text{Si}$  NMR can be used to investigate the structure of the aluminosilicate compounds.

In this thesis,  $^{29}\text{Si}$  MAS-NMR was carried out using a Bruker Avance 400 (9.4 Tesla magnet) with a 4 mm multinuclear solid state probe at RT. Solid samples were packed into 4 mm  $\text{ZrO}_2$  rotors with a Kel-F cap and spectra were recorded using cross-polarization (cp) MAS techniques. The spectra were collected and processed using Bruker's Topspin 2.1 program at 79.5 MHz, spin rate 10000 Hz, SW 32468 Hz (408 ppm); acquisition time 47 ms, 3072 data points, a 5 sec delay and a 5 ms contact time. Spectra were referenced to a kaolin external reference.

### 2.2.5 Electron microscopy

Electron microscopy (EM) is a powerful and versatile technique, which provides valuable information about the morphology, phase distribution and phase composition of catalysts. This technique is important in investigate heterogeneous catalysts' morphology, because the particle size, shape and location of the active species have crucial effects on their catalytic activity [381, 382].

In EM, a powdered sample is placed in an ultra-high vacuum chamber and probed with an electron beam. The high vacuum is required because the electrons are very small and can be easily deflected by gas molecules. Upon irradiation with an electron beam of energy  $E$ , two types of interactions occur between the specimen and electron beam (Figure 2.8) [383]:

- upon interaction between the incident electrons and the electronic cloud of the sample elastic scattering occurs. In elastic scattering the direction of the electron beam changes, but the energy of the electron beam does not alter [384].
- the electron beam can interact with an individual electrons in the material and cause inelastic scattering. After this interaction the direction of the beam does not change, but part of the energy of the incident beam transfers to the electron in the material [384].

In elastic scattering, the interaction between the electron beam and electronic cloud of the material results in the deflection of the electron beam by angle  $\theta$ . The electron progresses in the material following a zigzag path. The depth to which the electron penetrates and the shape of the path depend on the atomic number,  $Z$ , of the element. In samples with a relatively low

average  $Z$ , this path is relatively linear and deep. However, it is more zigzag and shallower in samples of higher average  $Z$ .

If the scattering angle  $\theta$  is larger than  $\pi/2$ , the incident electron may exit from the material, it is then called a backscattered electron. The backscattering intensity is in direct proportion to the average  $Z$  of the sample. The information from backscatter electrons is generally used to describe the phase distribution in the sample (Figure 2.8).

In inelastic scattering, an electron with high energy ejects an electron from an atom. The ejected electron is called a secondary electron. This electron has a very low energy and travels a very short path (Figure 2.8). Secondary electrons carry information about the morphology and the texture of the surface of the material.

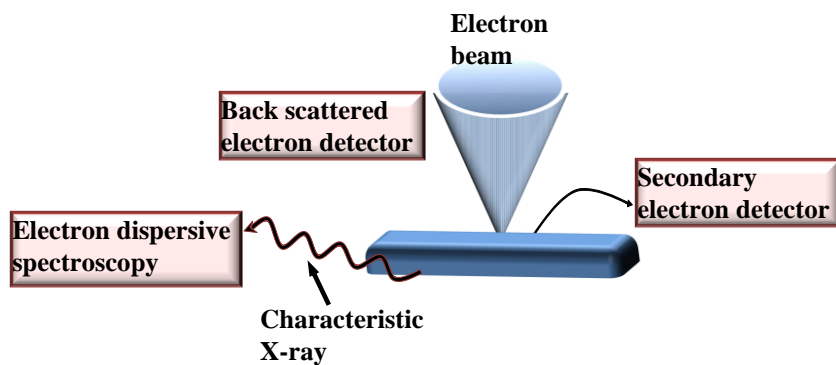


**Figure 2.8.** Incident electron and specimen interaction

An incident electron may have sufficient energy to excite an electron in the core level of the atom. Upon returning from an excited level to the ground level, an X-ray is emitted (Figure 2.8). These emitted X-rays have an energy characteristic of each atom and thus they carry information on the elemental composition of the material.

### 2.2.5.1 Electron gun

Generally in electron microscopes three different electron sources are used: (i) lanthanum hexaboride ( $\text{LaB}_6$ ), (ii) tungsten and (iii) the field emission gun, FEG.

One of the most crucial steps in designing a microscope is choosing the electron source, which in turn determines the vacuum system. This is because different electron emission sources require different vacuum levels. The electron current density of the beam (brightness), the emitted angle (current density per steradian solid angle), the signal to noise ratio of the image and the contrast in the image are the key factors in choosing an electron source.

Electron emission sources can be divided into two groups; (i) thermionic emitters, tungsten and LaB<sub>6</sub> and (ii) field emitters, FEG. The filament in a thermionic electron emission source is heated up via electric current, and the hot filament emits electrons. In a field emission source, the filament is placed in a high potential gradient which include electron emission without the necessity of heating the filament.

A tungsten gun, which is a very stable source of electrons, consists of a hairpin-shaped filament, a Wehnelt cylinder and an anode. A tungsten source provides a very high total beam current due to the large area of the filament.

A LaB<sub>6</sub> gun has a longer lifetime than a tungsten gun and gives up a beam up to ten times brighter than tungsten gun. However it requires a better vacuum. The emission area of a LaB<sub>6</sub> guns are smaller as a result the beam current decreases as the brightness increases.

FEGs are generally used to collect high resolution TEM (HRTEM) images. These sources produce smaller beams with higher currents and brightness than other electron sources.

The required magnification in transmission electron microscopes is the criterion for choosing the electron source choice. If 40-50 kX magnification is required, tungsten guns are recommended, while for magnifications in the range between 50-100 kX, LaB<sub>6</sub> guns are sufficient. For higher magnifications, more than 100 kX, FEGs provide better signals [384].

### **2.2.5.2 Transmission electron microscopy (TEM)**

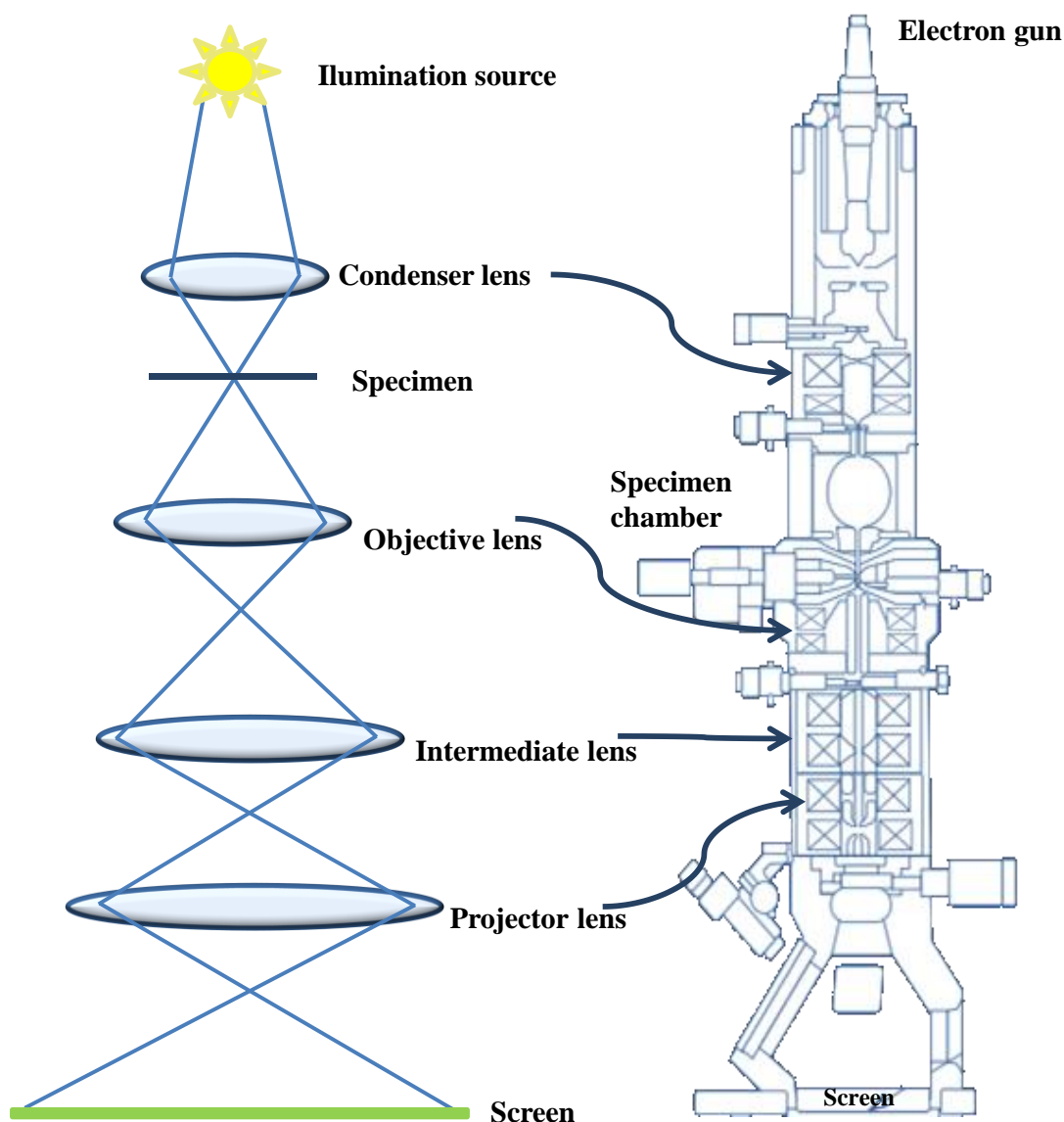
A transmission electron microscope (TEM) operates on the same principle as an optical microscope. While TEM relies on the interaction between the material and the electron beam, the optical microscope relies on the interaction between the material and visible light. The biggest advantage of a TEM over optical microscopes is its greater resolution [385]. An optical microscope's resolution is of the order of 500 nm, whereas a TEM's resolution can be as low as 0.5 Å. This can resolve the individual atomic column [386].

Figure 2.9 illustrates the typical setup of a TEM. In essence an electron beam is produced from an electron source, which is connected to a high voltage source (~ 200 kV). This produces an electron beam with a wavelength of a few picometer ( $10^{-12}$  m) which is directed towards the sample. The magnetic lenses are also used to guide and focus the beam.

Since TEM works in the transmission mode, an ultra-thin electron transparent specimen is required, so that a relatively large proportion of the incident beam can pass through the sample and be detectable. This mode of imaging is known as bright field imaging (BFI), in which the detection of the transmitted electrons occurs directly under the sample. In BFI, the

background (vacuum) is bright due to the absence of any material. The brightness however, is less in the presence of any material due to electron deflection. Consequently, the resulting image displays regions varying in brightness due to (i) specimen thickness and (ii) specimen composition [384].

In this study, a JEOL 2011 transmission electron microscopy equipped with a LaB<sub>6</sub> emitter (point resolution 0.21 nm) and an accelerating voltage (200kV) was used to investigate the morphology and dispersion of the active species on SBA-15.



**Figure 2.9.** Schematic of the transmission electron microscopy (TEM) set up [384, 387]

### 2.2.5.3 Scanning electron microscopy (SEM)

SEM is a 3D mapping technique in which a specific area is rastered with a focused electron beam. This technique is not quantitative and does not operate in transmission mode.

SEM is one the most popular EM technique in material characterisation. The resolving power can lie between a few nm and 1 mm [388].

SEM operates in two modes: (i) backscattered electron mode and (ii) secondary electron detection mode (see section 2.2.6.1). Interaction between the electron beam and electronic cloud of the specimen results in electron scattering. Backscattering increases as the average  $Z$  of the nuclei in the material increases. As a consequence this mode can be used to investigate the chemistry and phase distribution of a material [384, 388].

Upon interaction between the electron beam and electronic cloud of the specimen, a part of the energy of the electron beam may transfer to an individual atomic electron. This results in ejection of the electron from the atom of the specimen, ionization. These ejected electrons are often not detected due to their low kinetic energy, but can observe if they come from the surface or only a few nm below the surface. These electrons therefore convey topographical information [388].

SEM samples are often mounted on conductive carbon tape and coated with high- $Z$  metals such as gold, silver or platinum. The conductive coating prevents local build-up of charge, which will produce electron fields that distort electron paths, giving image drift or artifactual bright spots in the image. The high- $Z$  metal coating restricts the volume interacting with the incident electron beam, so improving the resolution [388].

SEM can be equipped with an energy dispersive X-ray (EDX) attachment, but the EDX resolution in SEM is lower than TEM (see section 2.2.6.4). In the EDX mode the accelerating voltage is generally lower to avoid distortion of the EDX results via charging [388].

For this thesis, SEM micrographs were collected on a JEOL 7001F field emission gun scanning electron microscope. Elemental analyses were carried out with the same instrument equipped with a Bruker X-flash silicon drift type EDX detector (Figure 2.10). Prior to collecting images each specimen was mounted on conductive carbon tape and coated with platinum (2 nm thickness) for 0.5 minutes using a Cressington Sputter Coater. During the coating process the samples were tilted about  $45^\circ$  and rotated at 50~100 rpm.



**Figure 2.10.** Scanning electron microscope, JEOL 7001F, equipped with a Bruker X-flash EDX detector

#### **2.2.5.4 Energy dispersive X-ray (EDX) spectroscopy**

EDX spectroscopy gives an elemental analysis. It can be operated in either a SEM or a TEM mode. The principle of operation is as follows. If the incident beam has enough energy, it may eject a core-level electron energy ( $E_a$ ), from an atom. The electron vacancy at the core level is filled by a higher-level electron energy ( $E_b$ ). As a result of this electron transition, an X-ray of energy ( $E_b - E_a$ ), characteristic of the element, is emitted. This emitted X-ray can be used for compositional investigation of the specimen [388]. The EDX spectra are plots of X-ray intensity vs. X-ray energy. This information can be obtained in a short period of time (minutes or seconds).

EDX can be obtained from the different regions of the specimen to investigate the phase distribution. It is important to condense the electron beam to an appropriate size so that the composition of a specific spot is analysed. The EDX spectra may contain different peaks at various energies, indicative of the presence of different elements. The intensity of each peak measures the concentration of the relevant element. This makes EDX appropriate for both qualitative and quantitative information [384].

#### **2.2.5.5 Scanning transmission electron microscopy (STEM)**

STEM is a special mode of TEM, but the principle of STEM is different to that of TEM. In TEM an extended region is illuminated continuously, whereas in STEM a converging probe beam, typically 1 nm in diameter, rasters across the area of the specimen. This provides good definition over the specific area of the sample under the probe at any time and facilitates the collection of different types of information [384].

This technique has recently become very popular in heterogeneous catalyst characterization, where active particles are dispersed on a support [389, 390]. As for

supported metals or metal oxides, it might be difficult to attribute dark spots in TEM images to either support or active particles. This is because of the thickness of the sample or similarities in scattering of the incident beam either by the support or active particles. However STEM allows access to several different types of electrons, some of which give signals depending on the Z of the sample (see below) so that support and active particles can be distinguished.

The interaction between the incident beam and a specimen generates a variety of signals which can be collected with different detectors (Figure 2.11B). In addition, STEM can collect separately the transmitted electrons scattered at different angles and these generate several post-specimen signals, which form images with different detectors based on the scattering angle ( $\alpha$ ) (Figure 2.11A):

- ❖ If  $\alpha < 10$  (mrad) the signals are collected by a bright field (BF) detector to form the BF-STEM image, which is similar to the TEM images.

- ❖ If  $10 < \alpha < 50$  (mrad) the signals are collected by a dark field (DF) detector. This detector was first introduced at 1980 to generate an annular dark field image (ADF) [391] (see below).

- ❖ If  $\alpha > 50$  (mrad) the signals are collected with an annular DF detector, as was first suggested by Treacy and Howie, with a larger inner diameter to form the high-angle annular dark field image HAADF.[392, 393].

The intensity of the high-angle scattered beam is in direct proportion to the mass density of the specimen. This suggests that heavier elements with higher Z scatter the electron beam more strongly and therefore appear to be brighter. As a result in DF images any material with high Z appears as a bright object as opposed to the vacuum which appears black. These images are therefore referred to as Z-contrast image.

In this study, the STEM micrographs were collected on a JEOL 2100F microscope equipped with a HAADF detector with camera length 10 cm and a 0.5 nm probe (Figure 2.12).

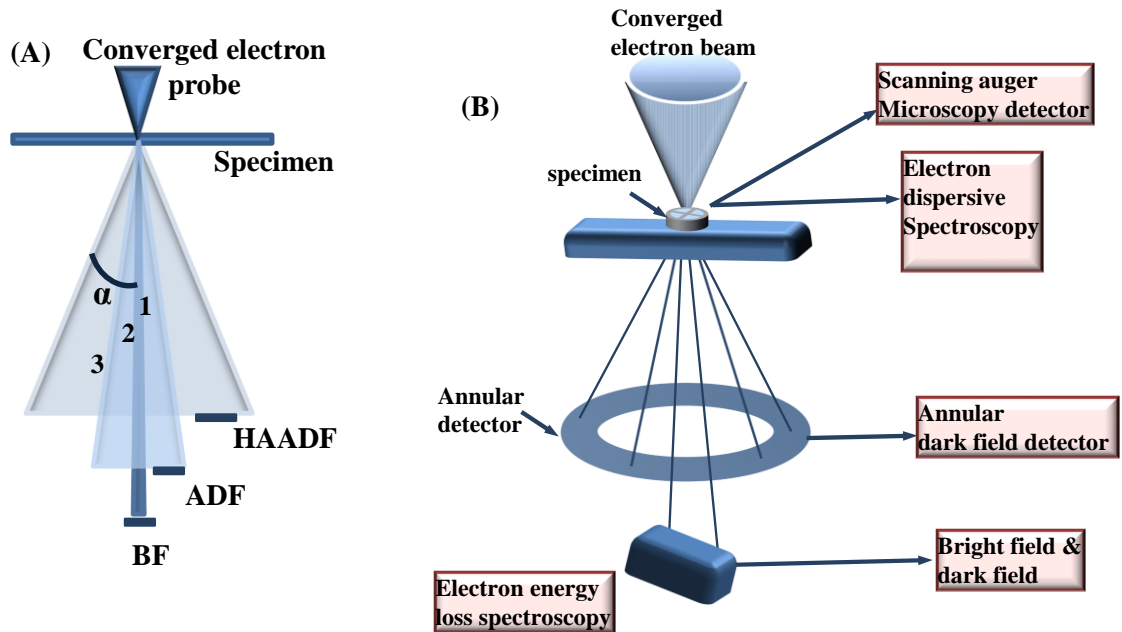


**Figure 2.11.** (A) Schematic diagram presents the position of BF, ADF and HAADF detectors (B) schematic diagram presents the position of various detectors in STEM [375]



**Figure 2.12.** JEOL 2100F microscope (left) and single tilt specimen holder and vacuum pump (right)

### 2.2.5.6 Elemental Mapping

As noted in section 2.2.6.5, one of the advantages of the STEM mode is the possibility of collecting various signals with different detectors simultaneously. As for compositional analysis of the whole specimen, the characteristic X-ray is the most important signal collected by the EDX detector (see section 2.2.6.4). Both the characteristic X-ray photon and the electron energy loss photon contain information related to the specimen composition (Figure 2.13).

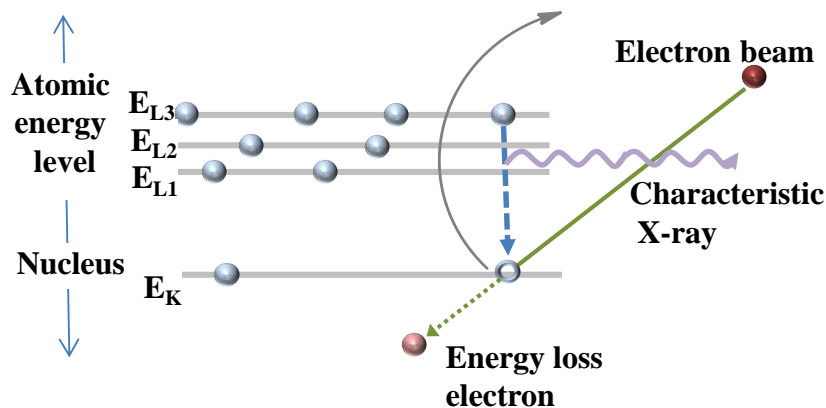


**Figure 2.13.** Schematic diagram of interaction of incident beam with core level electron (inelastic scattering) and generation of characteristic X-ray and energy loss electron [384]

To carry out elemental mapping, using X-ray photons, it is important to be in STEM mode so that the specimen is rastered by the electron beam. A selected region is scanned pixel by pixel with a certain dwell time for each pixel by controlling the position of the convergent probe. As a result highly localised compositional information can be obtained in the form of coloured elemental map as well as in the form of an EDX spectrum [384].

The signal intensity in the map is proportional to the intensity of the X-ray generated from the interaction between the incident beam and specific atoms of the area target by the beam. It should be noted that characteristic X-rays and Bremsstrahlung X-rays are all registered in elemental mapping profile [384]. However, the intensity of the characteristic X-rays due to presence of specific elements is higher than that of the other X-rays, which permit the discrimination between the different kinds of X-rays. The EDX spectra provide complementary information which helps to improve the interpretation of the elemental mapping profiles.

For this thesis the elemental mapping profiles were collected on a JEOL 2100F scanning transmission electron microscope operating at 200 kV accelerating voltage equipped with a JEOL 50 mm<sup>2</sup> Si(Li) EDX detector with ultrathin window. In order to obtain enough counts the probe size was increased to 1.5 nm, with a 10 cm camera length.

## 2.2.6 Fourier-transform infrared spectroscopy (FTIR)

Infrared (IR) radiations, electromagnetic radiation in the wavelength 0.7-1000  $\mu\text{m}$ , were discovered first by Friedrich Wilhelm Herschel in 1800 and named by Becquerel in the 1870s. However, IR did not become commercially available until the 1940s. The number of IR instruments increased noticeably after 1945 due to the technological development of

detectors and chemists' interest in using the instrument. The customary unit for IR frequency is wavenumber ( $\bar{\nu}$ ) in  $\text{cm}^{-1}$  ( $\bar{\nu} = \nu/c = 1/\lambda$ ), where  $\nu$  is frequency in Hz,  $c$  is the velocity of light ( $\text{cm s}^{-1}$ ) and  $\lambda$  is wavelength in cm) [375]. Speed of analysis and sensitivity were increased and noise reduced in the 1970s by the application of Fourier transform (FT) technologies to give FTIR [394].

IR is a powerful technique for basic characterization, because it can provide information both on the functional groups and structure of the sample. Samples in a wide range physical states (liquid, gas, paste, film and powder) can be characterized by FTIR [395].

The vibration of the molecule or crystal can be modelled by replacing the atoms by mass points in the same relative positions as the atoms connected by elastic bonds with nearest neighbours of varying stiffness. Every such system has a set of characteristic frequencies determined by its structure, the masses of the points, the stiffness, length and relative orientation of the elastic bonds; these are the so-called normal modes. In most systems these frequencies are in the infrared ranges and absorption of infrared radiation of one of these frequencies will set the system into vibration and cause absorption of the radiation of this frequency. For some of the frequencies, vibration of large amplitude is confined to a chemically defined functional group and these frequencies are often characteristic of the functional group.

Due to the absorption of the incident beam via sample the intensity of the beam decreases at specific wavenumbers. The resulting spectra can be plotted of absorption or transmission vs. wavenumber.

There are two common methods for preparing solid samples, necessary because a solid sample, unless very thin, will give too high absorption at its characteristic frequencies. Both involve grinding the sample into a fine powder and then diluting the powder with a matrix. This matrix can be either a mineral oil, nujol, or potassium bromide, KBr. The latter is more widely used in catalysis characterisation. The sample is normally diluted 1:300 in dry KBr and transferred to a vacuum die. The sample is pressed at around 10000 psi for 5 min under vacuum, then purged with  $\text{N}_2$  before being analysed.

For this thesis, the FT-IR spectra were collected from a BIO-RAD FTS 40 spectrometer. The materials were diluted 1/300 in dry KBr, (for some Co-composites with low Co-content 3/300 ratio was used to make a pellet) dried at 110 °C for 4-6 h, then pressed into pellets under vacuum immediately prior to analysis.

### 2.2.7 Diffuse reflectance ultraviolet-visible spectroscopy (DR UV-vis)

Ultraviolet-visible spectroscopy (UV-vis) covers the range 200-800 nm (UV=200-400 nm) and provides valuable information about the co-ordination environment and oxidation state of the material. This technique is often referred to as electronic spectroscopy. This is because by absorbing light in this range the valence electrons are promoted from the ground state to the higher energy states. The energy of this electronic promotion depends on the electronic structure of the compound as well as its chemical environment [396]. The UV-vis spectra bands are generally broad, because vibrational and rotational transitions occurred simultaneously with electron transitions.

UV-vis analysis is commonly carried out in the liquid phase where the transmitted light is collected by a detector. This technique can be exploited to investigate charge transfer in complexes, d-d electron transfer in transition metal ions and electron transfer in highly conjugated organic compounds, mainly from  $n \rightarrow \pi^*$  and  $\pi \rightarrow \pi^*$ . These electron transitions are responsible for the colour in compounds [397].

In the case of powder or solid samples, however, it is sometimes difficult to dissolve the sample and, even if this is possible, the chemistry and the co-ordination environment might be affected. In these circumstances DR UV-vis can be profitably used. In this technique the ratio of the light scattered from up to 2-3 nm below the sample surface and an ideal non-absorbing reference is measured as a function of wavelength  $\lambda$ .

The relationship between diffuse reflectance of the sample ( $R_\infty$ ), absorption (K) and scattering (S) coefficient is given by the Schuster-Kebelka-Munk (SKM) remission function (Eq. 2.5) [398]:

$$F(R_\infty) = (1-R_\infty)^2 / 2R_\infty = K/S \quad \text{Eq. 2.5}$$

In this work, the DR UV-vis spectra were collected at RT in air on a Cary 5000 Scan UV-vis -NIR photometer over the range 200-800 nm. The instrument was equipped with an accessory and a special sample holder appropriate for powders and film analyses.

### 2.2.8 Inductively coupled plasma mass spectrometry (ICP-MS)

ICP-MS is a sensitive qualitative and quantitative analytical technique, capable of detecting many elements down to parts per trillion (PPT). This technique was first commercialized in 1983 [375]. The ICP-MS comprises high temperature inductively coupled plasma, as an excitation source and mass spectrometer. Inductively coupled plasma is volume

of Ar, the atom of which are to some extent dissociated into ions and electrons by high frequency radiation in a torch [399].

The Ar plasma is used as an ionizer. The sample of interest is introduced to the ICP-MS via a nebulizer in which it is converted to fine droplets of aerosol. The sample is then transferred to the ionizer by the Ar flow and, due to the high temperature of the plasma, it becomes ionized (Figure 2.14A). The aim is to generate a high proportion of singly charged ions. The generated ions move through an analyser, magnetic or quadrupole (Figure 2.14B), and are sorted based on the mass to charge ratio ( $m/z$ ) [375].

In a magnetic analyser magnetic fields bend the ion path with the extent of bending depending on the  $m/z$  ratio so that ions of different  $m/z$  can be separated. However, in quadrupole analyser oscillating and static electric fields are applied to four parallel rods. At any given magnitude, the oscillating and static electric fields, only ions within a narrow range of  $m/z$  values can pass through the rods. The other ions collide with the rods and do not reach the detector. By varying the magnitudes of the oscillating and static electric fields, ions of different  $m/z$  can reach the detector, so sweeping through the range of magnitudes of electric fields permits a sweep through a range of  $m/z$  ratios.

In this study, ICP-MS analyses were carried out using a GBC OPTIMAS 9500 ICP-MS following sample preparation in the clean lab.

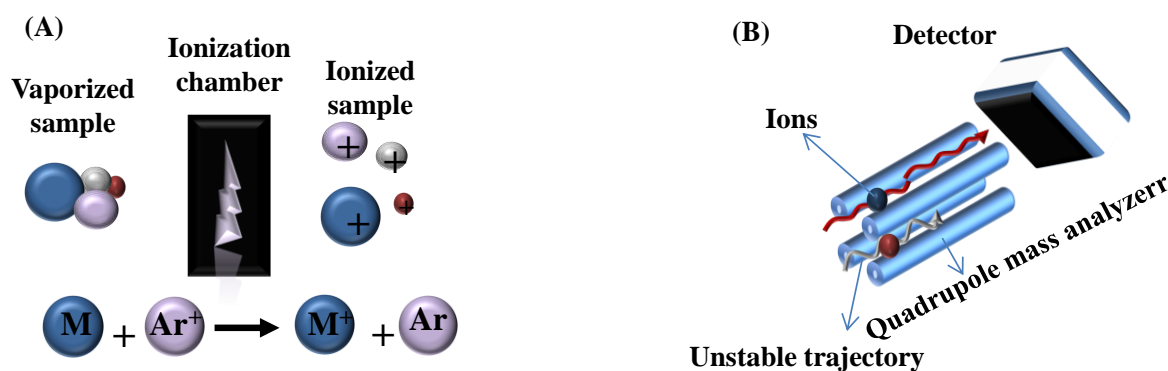


**Figure 2.14.** Schematic diagram of (A) sample ionization in the torch and (B) quadrupole analyser

### 2.2.8.1.1 Sample preparation

There are various methods for sample preparation; (i) acid digestion, (ii) sodium peroxide sinter and (iii) microwave digestion.

For this thesis, all the samples were prepared via acid digestion; a precise amount of sample (10 mg) was weighed using a five digit analytical balance. The sample was transferred to a Teflon cup to which 2 mL of concentrated HF and 1 mL of concentrated HNO<sub>3</sub> were added. The sample was heated a day on the hot plate at 120 °C. The sample was then uncapped and heated overnight on the hot plate at the same temperature, after addition of 1 mL concentrated HNO<sub>3</sub>. Next, 3 mL of concentrated HNO<sub>3</sub> was added to the sample, which was then left to stand overnight in the capped Teflon cups. This solution was used to prepare the first diluted solution. Then the second diluted solution (60 ppb, 100 ml) were made from the first diluted solution. Finally, the second diluted solution was analysed by ICP-MS and after each run HNO<sub>3</sub> (3 wt%) was used as a washing solvent. To calibrate the instrument four reference samples (20, 40, 60, 80 ppb) were prepared and run prior to the samples analyses.

### **2.3 Catalytic performance**

Various approaches were considered for evaluation of the catalytic performance of Co-composites in oxidising organic substrates in the presence of TBHP.

For Co-composites prepared from Co(NO<sub>3</sub>)<sub>2</sub>·6H<sub>2</sub>O as the metal precursor, the catalyst (0.1 g) was added to the organic substrates (20 mmol) and chlorobenzene (200 µl, as an internal standard) in acetonitrile (5mL) in a round bottomed flask. The oxidant, TBHP, (24 mmol) was then added dropwise over approximately 10 minutes. The reactions were carried out under reflux without attempting to exclude air. The progress of the catalytic reaction was monitored by GC and GC-MS through withdrawing samples every 4 h up to 24 h.

For Co-composites prepared from CoCl<sub>2</sub>·6H<sub>2</sub>O, the catalyst (contain  $9 \times 10^{-3}$  g of cobalt) was added to the acetonitrile (5 mL) containing the organic substrate (20 mmol) and chlorobenzene (200 µl as an internal standard). It should be noted that the concentration of cobalt was kept at  $9 \times 10^{-3}$  g for all the reactions. Thus, different masses of catalysts were employed for the different catalysts. The oxidant, TBHP, (24 mmol) was added dropwise over 10 minutes after reaching reflux. The conversion to the products was monitored as for the Co(NO<sub>3</sub>)<sub>2</sub>·6H<sub>2</sub>O samples discussed above.

#### **2.3.1 Gas chromatography (GC)**

Chromatography separates a mixture into its components. After the components of a mixture are separated, they can be identified and determined quantitatively. There are many

kinds of chromatography including gas chromatography (GC), which is widely used in monitoring the products from catalytic reactions.

The GC technique was first used by Archer Martin and Anthony T. James in Austria [375]. They coated the support with non-volatile liquid, the so-called stationary phase, and placed it into a glass tube. This tube was then heated during the analysis after the injection of the mixture. They reported well-defined zones for the organic acids and amines. Since then GC systems have experienced rapid development, because the technique is widely used by petroleum chemists and biochemists. One of the significant milestones in this area was the substitution of a capillary column for the support material. In such systems the liquid was coated onto the walls [400].

In GC, an inert gas (He, Ar or N<sub>2</sub>), a highly pure mobile phase, flows into the injector, through the column and finally to the detector. Once the sample is introduced to the injector via a manual, auto or exterior sampling device, it is heated to 150-200 °C. To vaporize it and the vapour is transported through the column by the carrier gas. The column is in an oven, whose temperature is raised at a predetermined rate, essentially to reduce the analysis time. Components of the sample travel through the column at different rate, which depend on the strength of binding of the components to the column. The components reach the heated detector, where an electric signal is generated from the interaction of the components with the detector.

A chromatogram, a plot of signal strength vs. time is generated. Each component gives a peak in the chromatogram. In an ideal chromatogram, the peaks do not overlap. The retention times, the times at which the peak appears, and the size of the peaks are the most important elements in the chromatogram. The retention times can be used to identify the components because if the column and all the operating conditions are kept the same, a given compound always travels through the column at the same rate and elutes at the same time. The size of the peak gives relative concentration of the component and can be used quantitatively if suitable standards are used.

### **2.3.1.1 Selected stationary phases**

#### **2.3.1.1.1 Polysiloxanes**

They are the most common stationary phases, widely available, and known for their stability and robustness. The basic polysiloxane is 100 % methyl substituted and gives non-polar capillary columns. However, other organic groups can be substituted for methyl groups,

their amount is usually indicated by the percentage. The higher the proportion of methyl groups replaced by phenyl groups, the more polar the column becomes.

#### **2.3.1.1.2 Polyethylene glycols**

These stationary phases are known to be very polar and used mostly for epoxides, alcohol, ketone and aldehyde analysis. Stationary phases with “wax” and “FFAP” in their name belong to this category. These types of stationary phases are not substituted, so that the polymer is 100 % of the stated material. These stationary phases are less stable than polysiloxanes and have lower temperature limits. The appropriate operating temperature for these capillary columns is from 20 °C to 260-280 °C.

### **2.3.2 Gas chromatography-mass spectrometry (GC-MS)**

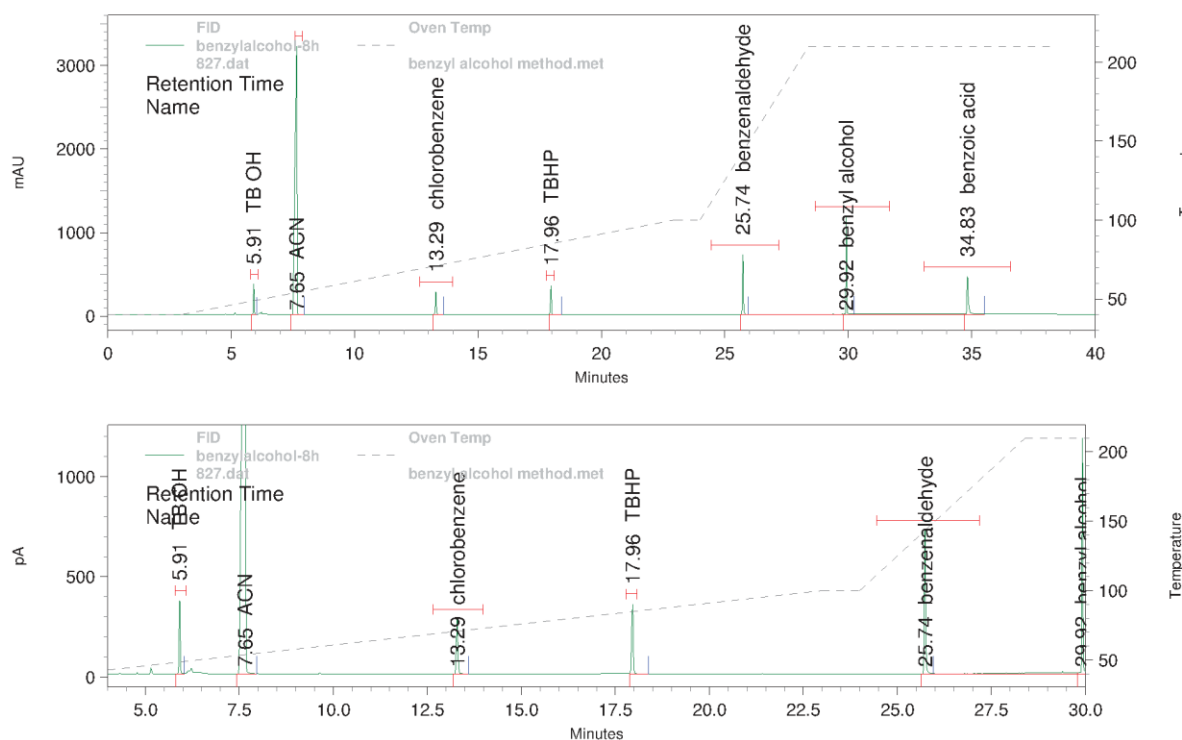
J. J. Thomson first introduced a basic mass spectrometer at the University of Cambridge in 1897, for which he was awarded a Nobel Prize in 1906. The GC-MS comprises two parts: the gas chromatograph and the mass spectrometer. The gas chromatograph as mentioned above separates the components of the sample and passes them to the mass spectrometer (MS) [401].

In the mass spectrometer the molecules of a component are broken down into ionized fragments and then the fragments are separated based on their  $m/z$  ratio (see section 2.2.9). In the next step, the detector converts charge to an electric signal of strength proportional to the ion concentration so that the plot of intensity vs.  $m/z$ , the mass spectrum, is obtained for each component. Once the mass spectrum is obtained, it can be compared to the library of known mass spectra using the MS computer data base.

In this thesis, the GC was carried out on an Agilent 6850 gas chromatograph equipped with an FID detector and a polar capillary column (BP20, 60 m × 0.25 mm, Figure 2.15). Quantitative results were obtained from measured areas of peaks due to the substrate and/or product(s), e.g. benzylalcohol, benzaldehyde or benzoic acid, using the response factor obtained from analysis of a mixture of known concentrations of substrate and/or products with an internal standard (chlorobenzene). Figure 2.16 demonstrates a chromatograph recorded during the oxidation of benzylalcohol to its corresponding products. GC-MS was carried out using an Agilent 5973 MS (source conditions: EI, 70 eV, 200 °C) fed by a 6890 series GC system with a capillary column (HP5, 30 m × 0.25 mm).



**Figure 2.15.** Agilent 6850 gas chromatograph (left) and Capillary column BP20 (right)



COL: BP 20 (60m x 0.25mm x 25um sn# 6880A13)

FID Results

Name	RT	Area	Area %	ESTD conc	Theo plates	K'	Resol	Asym (10%)	Width 1/2HT
TB OH	5.913	771393	<b>2.89</b>	<b>0.00</b>	182868	-0.01	0.00	0.99	0.03
ACN	7.654	18213169	<b>68.13</b>	<b>0.00</b>	30340	0.28	15.07	0.57	0.09
chlorobenzene	13.293	842398	<b>3.15</b>	<b>0.00</b>	427287	1.22	43.86	0.97	0.05
TBHP	17.960	1114927	<b>4.17</b>	<b>0.07</b>	646443	1.99	54.68	0.82	0.05
benzaldehyde	25.737	1758832	<b>6.58</b>	<b>0.00</b>	262134	3.29	101.7	0.92	0.04
benzyl alcohol	29.923	1913685	<b>7.16</b>	<b>0.00</b>	972542	3.99	82.12	0.95	0.02
benzoic acid	34.829	2119076	<b>7.93</b>	<b>0.00</b>	222937	4.80	74.51	1.76	0.05

Figure 2.16. A chromatograph collected from benzylalcohol oxidation

## 2.4 References

- [1] J.J. Berzelius, Vollständiges Sach und Namen Register Ersten Bis Siebenzehnten Jahrgang Jahren-bericht Über Die Fortschritte Physischen Wissenschaften, 1839.
- [2] C.B. Désormes, N. Clément, *Annals Chim.* 329 (1806) 329.
- [3] Y. Moro-oka, A. Ozaki, *J. Catal.* 7 (1967) 23.
- [4] [Http://www.nacatsoc.org](http://www.nacatsoc.org).
- [5] L. Lloyd, *Handbook of Industrial Catalysts*, Springer US, 2011, pp. 23-71.
- [6] Y. Li, Q. Fu, M. Flytzani-Stephanopoulos, *Appl. Catal. B: Environ.* 27 (2000) 179-191.
- [7] A. Corma, D. Kumar, *Stud. Surf. Sci. Catal.*, Elsevier, 1998, pp. 201-222.
- [8] A. Corma, P. Esteve, A. Martínez, *Appl. Catal. A: Gen.* 143 (1996) 87-100.
- [9] R.A. Sheldon, J. Dakka, *Catal. Today.* 19 (1994) 215-245.
- [10] R.A.Sheldon, *Top. Curr. Chem.* 164 (1993) 21.
- [11] I. Lopes, A. Davidson, C. Thomas, *Catal. Commun.* 8 (2007) 2105-2109.
- [12] J. Clark, D. Macquarrie, *Handbook of Green chemistry & Technology*. Blackwell Publishing Company (2002) Oxford.
- [13] J.N. Armor, *Appl. Catal. A: Gen.* 222 (2001) 407-426.
- [14] U. Dingerdissen, A. Martin, D. Herein, H.J. Wernicke, *Handbook of Heterogeneous Catalysis*, Wiley-VCH Verlag GmbH & Co. KGaA, 2008.
- [15] B.H. Davis, *Handbook of Heterogeneous Catalysis*, Wiley-VCH Verlag GmbH & Co. KGaA, 2008.
- [16] R.V. Prasad, N.V. Thakkar, *J. Mol. Catal.* 92 (1994) 9-20.
- [17] B. Heaton, *Mechanism in Homogeneous Catalysis*, Wiley-VCH, 2005.
- [18] B. Sumit, *Wiley-Interscience*, 2000.
- [19] J.A. Dumesic, G.W. Huber, M. Boudart, *Handbook of Heterogeneous Catalysis*, Wiley-VCH Verlag GmbH & Co. KGaA, 2008.
- [20] I. Bertini, M. Mori, R. Romeo, E. Farnetti, R. Di Monte, J. Kaspar, [books@eolssonline.net](mailto:books@eolssonline.net).
- [21] C.N. Satterfield, *Heterogeneous Catalysis in Practice*, McGraw-Hill Book Company, 1980.
- [22] J. Hall, O. Saksager, I. Chorkendorff, *Chem. Phys. Lett.* 216 (1993) 413-417.
- [23] K. Yamaguchi, N. Mizuno, *Angew. Chem. Int. Ed.* 41 (2002) 4538-4542.
- [24] N. Mizuno, K. Yamaguchi, *Catal. Today.* 132 (2008) 18-26.
- [25] K. Yamaguchi, J.W. Kim, J. He, N. Mizuno, *J. Catal.* 268 (2009) 343-349.
- [26] D.V. Bavykin, A.A. Lapkin, P.K. Plucinski, J.M. Friedrich, F.C. Walsh, *J. Catal.* 235 (2005) 10-17.
- [27] M.R. Kantserova, S.N. Orlik, V.P. Kazimirov, *Theor. Exp. Chem.* 40 (2004) 246-253.
- [28] T. Tsoncheva, L. Ivanova, C. Minchev, M. Fröba, *J. Colloid Interface Sci.* 333 (2009) 277-284.
- [29] H. Chen, A. Sayari, A. Adnot, F.ç. Larachi, *Appl. Catal. B: Environ.* 32 (2001) 195-204.

- [30] C. Cannilla, G. Bonura, E. Rombi, F. Arena, F. Frusteri, *Appl. Catal. A: Gen.* 382 (2010) 158-166.
- [31] V.S. Kshirsagar, A.C. Garade, R.B. Mane, K.R. Patil, A. Yamaguchi, M. Shirai, C.V. Rode, *Appl. Catal. A: Gen.* 370 (2009) 16-23.
- [32] H. Su, S. Zeng, H. Dong, Y. Du, Y. Zhang, R. Hu, *Appl. Clay Sci.* 46 (2009) 325-329.
- [33] J. Jiang, K. Ma, Y. Zheng, S. Cai, R. Li, J. Ma, *Appl. Clay Sci.* 45 (2009) 117-122.
- [34] B.-Z. Zhan, M.A. White, T.-K. Sham, J.A. Pincock, R.J. Doucet, K.V.R. Rao, K.N. Robertson, T.S. Cameron, *J. Am. Chem. Soc.* 125 (2003) 2195-2199.
- [35] J. Janas, T. Machej, M. Che, S. Dzwigaj, in: Z.G.J.C. Ruren Xu, Y. Wenfu (Eds.), *Stud. Surf. Sci. Catal.*, Elsevier, 2007, pp. 1466-1470.
- [36] H. Yu, X. Fu, C. Zhou, F. Peng, H. Wang, J. Yang, *Chem. Commun.* (2009) 2408-2410.
- [37] P. Shukla, H. Sun, S. Wang, H.M. Ang, M.O. Tadé, *Sep. Purif. Technol.* 77 (2011) 230-236.
- [38] P.I. Ravikovitch, A.V. Neimark, *Langmuir.* 18 (2002) 9830-9837.
- [39] J.K. Shon, S.S. Kong, Y.S. Kim, J.-H. Lee, W.K. Park, S.C. Park, J.M. Kim, *Micro. Meso. Mater.* 120 (2009) 441-446.
- [40] D. Zhao, J. Feng, Q. Huo, N. Melosh, G. H. Fredrickson, B. F. Chmelka, G.D. Stucky, *Science.* 279 (1998) 548.
- [41] C.T. Kresge, M.E. Leonowicz, W.J. Roth, J.C. Vartuli, J.S. Beck, *Nature.* 359 (1992) 710-712.
- [42] X. Zhong, J. Barbier Jr, D. Duprez, H. Zhang, S. Royer, *Appl. Catal. B: Environ.* 121-122 (2012) 123-134.
- [43] H.H. Kung, *Transition Metal Oxides: Surface Chemistry and Catalysis*, Elsevier Science Publishers B.V., Amsterdam, 1989.
- [44] M. Ziolek, *Catal. Today.* 90 (2004) 145-150.
- [45] L. Lloyd, *Handbook of Industrial Catalysts*, Springer US, 2011, pp. 261-310.
- [46] R.A. Sheldon, J.K. Kochi, *Metal-Catalyzed Oxidations of Organic Compounds*; Academic Press: New York, NY, USA, (1981).
- [47] S.V. Ley, J. Norman, W.P. Griffith, S.P. Marsden, *Tetrapropylammonium Perruthenate, Pr<sub>4</sub>N<sup>+</sup>RuO<sub>4</sub><sup>-</sup>, TPAP: A Catalytic Oxidant for Organic Synthesis*, 1994.
- [48] S.V. Ley, A. Madin, In *Comprehensive Organic Synthesis*, Pergamon: Oxford, UK, 1991.
- [49] Y. Uozumi, Y.M.A. Yamada, *Chem. Rec.* 9 (2009) 51-65.
- [50] R.A. Sheldon, I.W.C.E. Arends, A. Dijksman, *Catal. Today.* 57 (2000) 157.
- [51] T. Mallat, A. Baiker, *Chem. Rev.* 104 (2004) 3037.
- [52] K. Mori, T. Hara, T. Mizugaki, K. Ebitani, K. Kaneda, *J. Am. Chem. Soc.* 126 (2004) 10657-10666.
- [53] T. Nishimura, N. Kakiuchi, M. Inoue, S. Uemura, *Chem. Commun.* (2000) 1245-1246.
- [54] C. Della Pina, E. Falletta, L. Prati, M. Rossi, *Chem. Soc. Rev.* 37 (2008) 2077-2095.
- [55] A. Abad, P. Concepción, A. Corma, H. García, *Angew. Chem. Int. Ed.* 44 (2005) 4066-4069.

- [56] L. Lloyd, *Handbook of Industrial Catalysts*, Springer US, 2011, pp. 119-167.
- [57] T.J.B. Holland, *Am. Mineral.* 65 (1980) 129.
- [58] G.J. Hutchings, *Chem. Commun.* (2008) 1148-1164.
- [59] S. Yamaguchi, M. Inoue, S. Enomoto, *Chem Lett* (1985) 827.
- [60] K.A. Joergensen, *Chem. Rev.* 89 (1989) 431-458.
- [61] B. Notari, *Stud. Surf. Sci. Catal.*, Elsevier, 1988, pp. 413-425.
- [62] U. Romano, A. Esposito, F. Maspero, C. Neri, M.G. Clerici, in: G. Centi, F. Trifiro (Eds.), *Stud. Surf. Sci. Catal.*, Elsevier, 1990, pp. 33-41.
- [63] P.C.C. Smits, B.F.M. Kuster, K. van der Wiele, H.S. van der Baan, *Carbohydr. Res.* 153 (1986) 227-235.
- [64] J.C. van der Waal, M.S. Rigutto, H. van Bekkum, *Appl. Catal. A: Gen.* 167 (1998) 331-342.
- [65] B.M. Choudary, V.L.K. Valli, A.D. Prasad, *J. Chem. Soc. Chem. Commun.* (1990) 721-722.
- [66] B.M. Choudary, A. Durgaprasad, V.L.K. Valli, *Tetrahedron Lett.* 31 (1990) 5785-5788.
- [67] J.C. Cudejans, H. van Bekkum, *J. Mol. Catal.* 12 (1981) 149-157.
- [68] V.I. Sobolev, K.A. Dubkov, E.A. Paukshtis, L.V. Pirutko, M.A. Rodkin, A.S. Kharitonov, G.I. Panov, *Appl. Catal. A: Gen.* 141 (1996) 185-192.
- [69] P.R.H.P. Rao, A.V. Ramaswamy, *J. Chem. Soc. Chem. Commun.* (1992) 1245-1246.
- [70] S. Kanemoto, H. Saimoto, K. Oshima, H. Nozaki, *Tetrahedron Lett.* 25 (1984) 3317-3320.
- [71] V.E. Henrich, P.A. Cox, *The Surface Chemistry of Metal Oxides*, Cambridge Press, Cambridge, 1994.
- [72] J.L.G. Fierro, *Metal Oxides: Chemistry and Applications*, CRC Press, Florida, 2006.
- [73] C. Noguera, *Physics and Chemistry at Oxides Surface* Cambridge University press, Cambridge, 1996.
- [74] A.R. Jose, F.G. Marcos, *Synthesis, properties, Applications of Oxide Nanomaterials*, Willey New York, 2007.
- [75] I.E. Wachs, J.M. Jehng, G. Deo, B.M. Weckhuysen, V.V. Gulians, J.B. Benziger, *Catal. Today.* 32 (1996) 47.
- [76] C.L. Thomas, *Catalytic Processes and Proven Catalysts*, academic press, New York, 1970.
- [77] S.G. Kandalkar, C.D. Lokhande, R.S. Mane, S.-H. Han, *Appl. Surf. Sci.* 253 (2007) 3952-3956.
- [78] A.F. Wells, *Structural Inorganic Chemistry*, 6th ed., Oxford University Press, New York, 1987.
- [79] W.A. Harrison, *Electronic Structure and the Properties of Solids*, Dover Publications, New York, 1989.
- [80] M. Fernández-García, A. Martínez-Arias, J.C. Hanson, J.A. Rodriguez, *Chem. Rev.* 104 (2004) 4063-4104.
- [81] A. Brückner, *Catal. Rev.* 45 (2003) 97-150.
- [82] J. Lee, M. Christopher Orilall, S.C. Warren, M. Kamperman, F.J. DiSalvo, U. Wiesner, *Nat Mater.* 7 (2008) 222-228.

- [83] K.-H. Kim, S.-K. Ihm, *J. Hazard. Mater.* 186 (2011) 16-34.
- [84] F. Li, J. Chen, Q. Zhang, Y. Wang, *Green Chem.* 10 (2008) 553-562.
- [85] A.A. Atia, A.M. Donia, A.E. Shahin, *Sep. Purif. Technol.* 46 (2005) 208-213.
- [86] M.C. Campa, S. De Rossi, G. Ferraris, V. Indovina, *Appl. Catal. B: Environ.* 8 (1996) 315-331.
- [87] M. F. Irfan, J. H. Goo, S.D. Kim, *Appl. Catal. B: Environ.* 78 (2008) 267-274.
- [88] G. Ertl, H. Knozinger, J. Weikamp, *Handbook of Heterogeneous Catalysis*, Wiley-VHC, Weinheim (1997).
- [89] U. Diebold, *Mat. Res. Soc. Symp. Proc.* 654 (2001).
- [90] J.L.G. Fierro, *Metal oxides: Chemistry and Applications* (Taylor & Francis, 2006).
- [91] H. Onishi, Y. Iwasawa, *Phys. Rev. Lett.* 76 (1996) 791-794.
- [92] K. Dyrek, M. Che, *Chem. Rev.* 97 (1997) 305.
- [93] G.A. Somorjai, *Chemistry in Two Dimensions: Surfaces*, Cornell University Press, New York, 1981.
- [94] S.R. Morrison, *The Chemical Physics of Surfaces*, Plenum Press, New York, 1977.
- [95] G. Ertl, J. Kupperts, *Low Energy Electrons and Surface Chemistry*, Weinheim, Germany (1985).
- [96] I.E. Wachs, *Catal. Today.* 27 (1996) 437-455.
- [97] I.E. Wachs, *Top. Catal.* 8 (1999) 57.
- [98] K. Chen, A. Khodakov, J. Yang, A.T. Bell, E. Iglesia, *J. Catal.* 186 (1999) 325-333.
- [99] V. E. Henrich, P.A. Cox, *The Surface Science of Metal Oxides*, Cambridge University Press.
- [100] P. Mars, D.W. van Krevelen, *Chem. Eng. Sci.* 3 (1954) 41-59.
- [101] A.F. Wells, *Structural Inorganic Chemistry*, 4th ed., Clarendon Press, London, 1975.
- [102] K. Hadjiivanov, D. Klissurski, A. Davydov, *J. Chem. Soc. Faraday Trans.* 84 (1988) 37-40.
- [103] K. Ranjit, K. Kenneth, *Surface and Nanomolecular Catalysis*, CRC Press, 2006, pp. 39-62.
- [104] R.L. Burwell Jr, G.L. Haller, K.C. Taylor, J.F. Read, *Advances in Catalysis*, Academic Press, 1969, pp. 1-96.
- [105] M. Nagao, T. Morimoto, *J. Phys. Chem.* 84 (1980) 2054-2058.
- [106] A. Ueno, T. Onishi, K. Tamaru, *J. Chem. Soc. Faraday Trans.* 66 (1970).
- [107] O. Koga, T. Onishi, K. Tamaru, *J. Chem. Soc. Faraday Trans.* 76 (1980).
- [108] C.F. Cullis, D.J. Hucknell, *Catalysis*, The Royal Society of Chemistry, 1982, pp. 273-307.
- [109] M. Haruta, *Cattech.* 6 (2002) 102-115.
- [110] P. Zoltan, *Hydrogen Effects in Catalysis- Fundamental and Practical Applications*, New York: M. Dekker, New York, 1988.
- [111] S.A. Bradley, M.J. Gattuso, R.J. Bertolacini, *Characterisation and Catalyst Development: An Interactive Approach*, American Chemical Society, Washington, DC, 1989.
- [112] M.D. Phillips, A.D. Eastman, *Catal. Lett.* 13 (1992) 157-174.
- [113] J.J. Spivey, J.B. Butt, *Catal. Today.* 11 (1992) 465-500.
- [114] H. Xiong, Y. Zhang, K. Liew, J. Li, *J. Mol. Catal. A: Chem.* 231 (2005) 145-151.

- [115] B.V.d. Sousa, M.G.F. Rodrigues, L.A. Cano, M.V. Cagnoli, J.F. Bengoa, S.G. Marchetti, G. Pecchi, *Catal. Today*. 172 (2011) 152-157.
- [116] E. Iglesia, *Appl. Catal. A: Gen.* 161 (1997) 59-78.
- [117] E.A. Mamedov, V. Cortés Corberán, *Appl. Catal. A: Gen.* 127 (1995) 1-40.
- [118] A.E. Shilov, B. Georgiy, *Activation and Catalytic Reactions of Saturated Hydrocarbons in the Presence of Metal Complexes*, Springer Netherlands, 2002, pp. 371-429.
- [119] M. Ruitenbeek, A.J. van Dillen, F.M.F. de Groot, I.E. Wachs, J.W. Geus, D.C. Koningsberger, *Top. Catalysis*. 10 (2000) 241-254.
- [120] G.I. Golodets, in: G. Centi, F. Trifiro (Eds.), *Stud. Surf. Sci. Catal.*, Elsevier, 1990, pp. 693-700.
- [121] Z. Jacek, *J. Catal.* 80 (1983) 263-273.
- [122] R.K. Grasselli, J.D. Burrington, *Advances in Catalysis*, Academic Press, 1981, pp. 133-163.
- [123] A. Bielanski, J. Haber, *Catal. Rev.* 19 (1979) 1-41.
- [124] F. Farzaneh, J. Taghavi, R. Malakooti, M. Ghandi, *J. Mol. Catal. A: Chem.* 244 (2006) 252-257.
- [125] J.W. Geus, A.J. van Dillen, *Handbook of Heterogeneous Catalysis*, Wiley-VCH Verlag GmbH & Co. KGaA, 2008.
- [126] F. Averseng, M. Vennat, M. Che, *Handbook of Heterogeneous Catalysis*, Wiley-VCH Verlag GmbH & Co. KGaA, 2008.
- [127] Z. Wang, J. Yu, R. Xu, *Chem. Soc. Rev.* 41 (2012) 1729-1741.
- [128] J.S. Beck, J.C. Vartuli, W.J. Roth, M.E. Leonowicz, C.T. Kresge, K.D. Schmitt, C.T.W. Chu, D.H. Olson, E.W. Sheppard, *J. Am. Chem. Soc.* 114 (1992) 10834-10843.
- [129] D. Zhao, Q. Huo, J. Feng, B.F. Chmelka, G.D. Stucky, *J. Am. Chem. Soc.* 120 (1998) 6024-6036.
- [130] K. Kaneko, *J. Membr. Sci.* 96 (1994) 59-89.
- [131] D.E. De Vos, M. Dams, B.F. Sels, P.A. Jacobs, *Chem. Rev.* 102 (2002) 3615-3640.
- [132] A. Corma, *Chem. Rev.* 97 (1997) 2373-2420.
- [133] K. Ishizaki, S. Komarneni, M. Nanko, *Porous Materials- Process Technology and Application*, Kluwer Academic Publisher, Boston (1998, p. 2).
- [134] K.S.W. Sing, D.H. Everet, R.A.W. Haul, L. Moscou, R.A. Pierotti, J. Rouquerol, T. Siemieniowska, *Pure Appl. Chem.* 67 (1985) 603-619.
- [135] R. Zukerman, L. Vradman, L. Titelman, C. Weidenthaler, M.V. Landau, M. Herskowitz, *Micro. Meso. Mater.* 116 (2008) 237-245.
- [136] C. Tang, H. Zhang, C. Sun, J. Li, L. Qi, Y. Quan, F. Gao, L. Dong, *Catal. Commun.* 12 (2011) 1075-1078.
- [137] A.K. Medina-Mendoza, M.A. Cortés-Jácome, J.A. Toledo-Antonio, C. Angeles-Chávez, E. López-Salinas, I. Cuauhtémoc-López, M.C. Barrera, J. Escobar, J. Navarrete, I. Hernández, *Appl. Catal. B: Environ.* 106 (2011) 14-25.
- [138] E. Escalera, M.A. Ballem, J.M. Córdoba, M.-L. Antti, M. Odén, *Powder Technol.* 221 (2012) 359.
- [139] E. Reverchon, R. Adami, *J. Supercrit. Fluids.* 37 (2006) 1-22.
- [140] M Valden, X Lai, D.W. Goodman, *Science*. 281 (1998) 1647.

- [141] R. Xu, W. Pang, J. Yu, Q. Huo, J. Chen, *Chemistry of Zeolites and Related Porous Materials Synthesis and Structure*, Wiley, Singapore, 2007.
- [142] J. W. McBain, *The Sorption of Gases*, G. Routledge & Sons, Ltd., London (1932).
- [143] D. Sherman, *Adsorption and Ion Exchange Separations AICHE Symposium Series*, 1978, p. 98.
- [144] D.L. Bish, D. Ming, W. Natural zeolites: Occurrence, properties, applications Washington, DC. Mineralogical Society of America, 2001.
- [145] D. W. Breck, *Zeolite Molecular Sieves: Structure, Chemistry, and Use*, Wiley, New York, (1973).
- [146] S.J. Chipera, J.A. Apps, *Geochemical Stability of Natural Zeolites Blacksburg, Virginia, USA*, 2001.
- [147] D.S. Coombs, A.J. Ellis, W.S. Fyfe, A.M. Taylor, *The Zeolite Facies*, with comments on the interpretation of hydrothermal syntheses. *Geochimica et Cosmochimica Acta*, 1959.
- [148] V.H. Bekkum, E.M. Flanigen, P.A. Jacobs, J.C. Jansen, *Introduction to Zeolite Science and Practice*, 2nd ed., Elsevier, Amsterdam, 1991.
- [149] D. Georgiev, B. Bogdanov, K. Angelova, I. Markovska, Y. Hristov, *International Science conference. 4th-5th June 2009, Stara Zagora, Bulgaria (2009)*.
- [150] E.M. Flanigen, *Pure Appl.Chem.* 52 (1980) 2191-2211.
- [151] R.I.F. Lobo, *Handbook of Zeolite Science and Technology*, University of Delaware, Newark, Delaware, U.S.A., 2003.
- [152] A.I. Savvatimskiy, *Carbon.* 43 (2005) 1115-1142.
- [153] A.R. Ubbelohde, *Proceedings of the Royal Society of London. Series A. Mathematical and Physical Sciences.* 304 (1968) 25-43.
- [154] F. Céspedes, E. Martínez-Fàbregas, S. Alegret, *TrAC, Trends Anal. Chem.* 15 (1996) 296-304.
- [155] P.R. Wallace, *Phys. Rev.* 71 (1947) 622-634.
- [156] S. Iijima, *Nature.* 354 (1991) 56-58.
- [157] S.J. Tans, M.H. Devoret, H. Dai, A. Thess, R.E. Smalley, L.J. Geerligs, C. Dekker, *Nature.* 386 (1997) 474-477.
- [158] P. M. Ajayan, O. Stephan, C. Colliex, D. Trauth, *Science.* 265 (1994) 1212-1214.
- [159] A.C. Dillon, K.M. Jones, T.A. Bekkedahl, C.H. Kiang, D.S. Bethune, M.J. Heben, *Nature.* 386 (1997) 377-379.
- [160] J.M. Planeix, N. Coustel, B. Coq, V. Brotons, P.S. Kumbhar, R. Dutartre, P. Geneste, P. Bernier, P.M. Ajayan, *J. Am. Chem. Soc.* 116 (1994) 7935-7936.
- [161] Z.-C. Di, J. Ding, X.-J. Peng, Y.-H. Li, Z.-K. Luan, J. Liang, *Chemosphere.* 62 (2006) 861-865.
- [162] J. Li, S. Tang, L. Lu, H.C. Zeng, *J. Am. Chem. Soc.* 129 (2007) 9401-9409.
- [163] G.L. Bezemer, J.H. Bitter, H.P.C.E. Kuipers, H. Oosterbeek, J.E. Holewijn, X. Xu, F. Kapteijn, A.J. van Dillen, K.P. de Jong, *J. Am. Chem. Soc.* 128 (2006) 3956-3964.
- [164] F. Schüth, W. Schmidt, *Adv. Mater.* 14 (2002) 629-638.
- [165] R. Mokaya, *Angew. Chem. Int. Ed.* 38 (1999) 2930-2934.
- [166] Y. Ren, Z. Ma, P.G. Bruce, *Chem. Soc. Rev.* 41 (2012) 4909-4927.
- [167] Z.-R. Tian, W. Tong, J.-Y. Wang, N.-G. Duan, V.V. Krishnan, S.L. Suib, *Science.* 276 (1997) 926-930.

- [168] D.M. Antonelli, *Micro. Meso. Mater.* 30 (1999) 315-319.
- [169] P. Yang, D. Zhao, D.I. Margolese, B.F. Chmelka, G.D. Stucky, *Chem. Mater.* 11 (1999) 2813-2826.
- [170] B. Tian, X. Liu, B. Tu, C. Yu, J. Fan, L. Wang, S. Xie, G.D. Stucky, D. Zhao, *Nat. Mater.* 2 (2003) 159-163.
- [171] F. Jiao, J.-C. Jumas, M. Womes, A.V. Chadwick, A. Harrison, P.G. Bruce, *J. Am. Chem. Soc.* 128 (2006) 12905-12909.
- [172] F. Jiao, A. Harrison, A.H. Hill, P.G. Bruce, *Adv. Mater.* 19 (2007) 4063-4066.
- [173] J. Roggenbuck, M. Tiemann, *J. Am. Chem. Soc.* 127 (2005) 1096-1097.
- [174] H. Kato, K. Asakura, A. Kudo, *J. Am. Chem. Soc.* 125 (2003) 3082-3089.
- [175] W. Zhou, *Solid State Phenom.* 140 (2008) 37-46.
- [176] M. Imperor-Clerc, D. Bazin, M. D. Appay, P. Beaunier, A. Davidson, *Chem. Mater.* 16 (2004) 1813-1821.
- [177] C. Dickinson, W. Zhou, R.P. Hodgkins, Y. Shi, D. Zhao, H. He, *Chem. Mater.* 18 (2006) 3088-3095.
- [178] S. Sun, Q. Gao, H. Wang, J. Zhu, H. Guo, *Appl. Catal. B: Environ.* 97 (2010) 284-291.
- [179] P. Yang, D. Zhao, D.I. Margolese, B.F. Chmelka, G.D. Stucky, *Nature.* 396 (1998) 152-155.
- [180] Y. Xia, H. Dai, H. Jiang, L. Zhang, *Catal. Commun.* 11 (2010) 1171-1175.
- [181] W. Shen, X. Dong, Y. Zhu, H. Chen, J. Shi, *Micro. Meso. Mater.* 85 (2005) 157-162.
- [182] J. Hwang, J. Kim, E. Ramasamy, W. Choi, J. Lee, *Micro. Meso. Mater.* 143 (2011) 149-156.
- [183] M.C. Orilall, F. Matsumoto, Q. Zhou, H. Sai, H.D. Abruña, F.J. DiSalvo, U. Wiesner, *J. Am. Chem. Soc.* 131 (2009) 9389-9395.
- [184] J. Yan, M.C. Kung, W.M.H. Sachtler, H.H. Kung, *J. Catal.* 172 (1997) 178-186.
- [185] C.-B. Wang, C.-W. Tang, S.-J. Gau, S.-H. Chien, *Catal. Lett.* 101 (2005) 59-63.
- [186] B. Coq, V. Gourves, F. Figuéras, *Appl. Catal. A: Gen.* 100 (1993) 69-75.
- [187] J. Kärger, D. Freude, *Chem. Eng. Technol.* 25 (2002) 769-778.
- [188] R. Schmolka, Irving, in: *U.S. Patent (Ed.)*, BASF Wyandotte Corporation, Wyandotte, Mich, 1973.
- [189] R.I. Schmolka, in: *U.S. Patent (Ed.)*, BASF Corporation, Wyandotte, Mich, 1987.
- [190] G. Wanka, H. Hoffmann, W. Ulbricht, *Macromolecules.* 27 (1994) 4145-4159.
- [191] C. Guo, H.Z. Liu, J.Y. Chen, *Colloid Polym. Sci.* 277 (1999) 376-381.
- [192] Q. Huo, D.I. Margolese, U. Ciesla, P. Feng, T.E. Gier, P. Sieger, R. Leon, P.M. Petroff, F. Schuth, G.D. Stucky, *Nature.* 368 (1994) 317-321.
- [193] Q. Huo, D.I. Margolese, U. Ciesla, D.G. Demuth, P. Feng, T.E. Gier, P. Sieger, A. Firouzi, B.F. Chmelka, *Chem. Mater.* 6 (1994) 1176-1191.
- [194] P.T. Tanev, T.J. Pinnavaia, *Science.* 267 (1995) 865.
- [195] P.T. Tanev, T.J. Pinnavaia, *Chem. Mater.* 8 (1996) 2068-2079.
- [196] E. Prouzet, F. Cot, G. Nabias, A. Larbot, P. Kooyman, T.J. Pinnavaia, *Chem. Mater.* 11 (1999) 1498-1503.
- [197] S.A. Bagshaw, T. Kemmitt, N.B. Milestone, *Micro. Meso. Mater.* 22 (1998) 419-433.
- [198] P.T. Tanev, M. Chibwe, T.J. Pinnavaia, *Nature.* 368 (1994) 321-323.

- [199] M. Grün, K.K. Unger, A. Matsumoto, K. Tsutsumi, *Micro. Meso. Mater.* 27 (1999) 207-216.
- [200] C.-F. Cheng, W. Zhou, J. Klinowski, *Chem. Phys. Lett.* 263 (1996) 247-252.
- [201] J.-H. Sun, M.-O. Coppens, *J. Mater. Chem.* 12 (2002).
- [202] V. Alfredsson, M.W. Anderson, *Chem. Mater.* 8 (1996) 1141-1146.
- [203] A. Carlsson, M. Kaneda, Y. Sakamoto, O. Terasaki, R. Ryoo, S.H. Joo, *J. Electron Microsc.* 48 (1999) 795-798.
- [204] K. Schumacher, M. Grun, K.K. Unger, *Micro. Meso. Mater.* 27 (1999) 201.
- [205] F. Farzaneh, J. Taghavi, R. Malakooti, M. Ghandi, *J. Mol. Catal. A: Chem.* 244 (2006) 252-257, Unpublished Information.
- [206] Y. Sakamoto, M. Kaneda, O. Terasaki, D.Y. Zhao, J.M. Kim, G. Stucky, H.J. Shin, R. Ryoo, *Nature.* 408 (2000) 449-453.
- [207] J.L. Guth, M. Mesa, L. Sierra, *Stud. Surf. Sci. Catal.*, Elsevier, 2007, pp. 1850-1855.
- [208] R.C. Hayward, P. Alberius-Henning, B.F. Chmelka, G.D. Stucky, *Micro. Meso. Mater.* 44-45 (2001) 619-624.
- [209] M. Kruk, L. Cao, *Langmuir.* 23 (2007) 7247-7254.
- [210] H.-H. Lee, J. Shibata, J.-W. Ahn, H. Kim, *Mater. Trans.* 49 (2008) 565-571.
- [211] H. Zhang, J. Sun, D. Ma, G. Weinberg, D.S. Su, X. Bao, *J. Phys. Chem. B.* 110 (2006) 25908-25915.
- [212] F. Zhang, Yan, H. Yang, Y. YanMeng, C. Yu, B. Tu, D. Zhao, *J. Phys. Chem. B.* 109 (2005) 8723-8732.
- [213] E.B. Celer, M. Kruk, Y. Zuzek, M. Jaroniec, *J. Mater.Chem.* 16 (2006).
- [214] E.B. Celer, M. Jaroniec, *J. Am. Chem. Soc.* 128 (2006) 14408-14414.
- [215] W.W. Lukens, P. Schmidt-Winkel, D. Zhao, J. Feng, G.D. Stucky, *Langmuir.* 15 (1999) 5403-5409.
- [216] Z. Liu, O. Terasaki, T. Ohsuna, K. Hiraga, H.J. Shin, R. Ryoo, *Chem. Phys. Chem.* 2 (2001) 229-231.
- [217] M. Impéror-Clerc, P. Davidson, A. Davidson, *J. Am. Chem. Soc.* 122 (2000) 11925-11933.
- [218] M. Kruk, M. Jaroniec, C.H. Ko, R. Ryoo, *Chem. Mater.* 12 (2000) 1961-1968.
- [219] A. Sayari, M. Jaroniec, *Nanoporous Materials IV: Proceedings of the 4th International Symposium on Nanoporous Materials.* 156 (2005).
- [220] C. Xiaoyin, D. Guozhong, C. Haiying, L. Quanzhi, *Science in China.* 40 (1997) 278.
- [221] M. Mesa, L. Sierra, J.L. Guth, *Micro. Meso. Mater.* 112 (2008) 338-350.
- [222] S. Ruthstein, V. Frydman, D. Goldfarb, *J. Phys. Chem. B.* 108 (2004) 9016-9022.
- [223] S. Ruthstein, J. Schmidt, E. Kesselman, Y. Talmon, D. Goldfarb, *J. Am. Chem. Soc.* 128 (2006) 3366-3374.
- [224] A. Galarneau, H. Cambon, F. Di Renzo, F. Fajula, *Langmuir.* 17 (2001) 8328-8335.
- [225] G.Q. LU, X.S. Zhao, *Nanoporous Materials - An Overview* (2004).
- [226] F. Bérubé, S. Kaliaguine, *Micro. Meso. Mater.* 115 (2008) 469-479.
- [227] F. Kleitz, W. Schmidt, F. Schüth, *Micro. Meso. Mater.* 44-45 (2001) 95-109.
- [228] F. Kleitz, W. Schmidt, F. Schüth, *Micro. Meso. Mater.* 65 (2003) 1-29.
- [229] Y.K. Bae, O.H. Han, *Micro. Meso. Mater.* 106 (2007) 304-307.

- [230] L.M. Yang, Y.J. Wang, G.S. Luo, Y.Y. Dai, *Micro. Meso. Mater.* 81 (2005) 107-114.
- [231] C.-M. Yang, B. Zibrowius, W. Schmidt, F. Schüth, *Chem. Mater.* 15 (2003) 3739-3741.
- [232] B. Tian, X. Liu, C. Yu, F. Gao, Q. Luo, S. Xie, B. Tu, D. Zhao, *Chem. Commun.* (2002).
- [233] W.-J. Shen, M. Okumura, Y. Matsumura, M. Haruta, *Appl. Catal. A: Gen.* 213 (2001) 225-232.
- [234] M.J. Mendes, O.A.A. Santos, E. Jordão, A.M. Silva, *Appl. Catal. A: Gen.* 217 (2001) 253-262.
- [235] S. Zuo, C. Qi, *Catal. Commun.* 15 (2011) 74-77.
- [236] J. Zhu, K. Kailasam, A. Fischer, A. Thomas, *ACS Catal.* 1 (2011) 342-347.
- [237] R. S. Mulukutla, K. Asakura, T. Kogure, S. Namba, Y. Iwasawa, *Phys. Chem. Chem. Phys.* 1 (1999) 2027-2032.
- [238] Q. Tang, Q. Zhang, H. Wu, Y. Wang, *J. Catal.* 230 (2005) 384-397.
- [239] F. Jiao, H. Frei, *Angew. Chem. Int. Ed.* 48 (2009) 1841-1844.
- [240] H.F. Rase, *Handbook of Commercial Catalysts: Heterogeneous Catalysts*, CRC Press, Florida, 2000.
- [241] A.Y. Khodakov, V.L. Zholobenko, R. Bechara, D. Durand, *Micro. Meso. Mater.* 79 (2005) 29-39.
- [242] M.F.F. Rodrigues, A.J.G. Cobo, *Catal. Today.* 149 (2010) 321-325.
- [243] J. Taghavimoghaddam, G. P. Knowles, A.L. Chaffee, *J. Mol. Catal. A: Chem.* 358 (2012) 79-88.
- [244] E. Marceau, X. Carrier, M. Che, O. Clause, C. Marcilly, *Handbook of Heterogeneous Catalysis*, Wiley-VCH Verlag GmbH & Co. KGaA, 2008.
- [245] Y. Tao, S. Schwartz, C.-Y. Wu, D.W. Mazyck, *Ind. Eng. Chem. Res.* 44 (2005) 7366-7372.
- [246] J. Haber, J.H. Block, B. Delmon, *Pure Appl. Chem.* 67 (1995) 1257-1306.
- [247] Á. Szegedi, M. Popova, V. Mavrodinova, C. Minchev, *Appl. Catal. A: Gen.* 338 (2008) 44-51.
- [248] Q. Yang, H. Choi, Y. Chen, D.D. Dionysiou, *Appl. Catal. B: Environ.* 77 (2008) 300-307.
- [249] L. Jiao, J.R. Regalbuto, *J. Catal.* 260 (2008) 342-350.
- [250] C. Minchev, H. Huwe, T. Tsoncheva, M. Dimitrov, D. Paneva, I. Mitov, M. Fröba, in: I.M.C. E. van Steen, L.H. Callanan (Eds.), *Stud. Surf. Sci. Catal.*, Elsevier, 2004, pp. 841-847.
- [251] L. Chmielarz, P. Kustrowski, R. Dziembaj, P. Cool, E.F. Vansant, *Micro. Meso. Mater.* 127 (2010) 133-141.
- [252] Z. Huang, Z. Zhu, Z. Liu, *Appl. Catal. B: Environ.* 39 (2002) 361-368.
- [253] J. Roggenbuck, T. Waitz, M. Tiemann, *Micro. Meso. Mater.* 113 (2008) 575-582.
- [254] A.Y. Khodakov, R. Bechara, A. Griboval-Constant, *Appl. Catal. A: Gen.* 254 (2003) 273-288.
- [255] Y. Wenbo, A.H. Hill, A. Harrison, Z. Wuzong, *Chem. Commun.* (2007) 2518-2520.
- [256] A. Barbier, A. Hanif, J.-A. Dalmon, G.A. Martin, *Appl. Catal. A: Gen.* 168 (1998) 333-343.

- [257] M. Baltes, O. Collart, P. Van Der Voort, E.F. Vansant, *Langmuir*. 15 (1999) 5841-5845.
- [258] E. Can, J, *Supercrit. Fluids*. 47 (2009) 517-522.
- [259] D.P. Long, J.M. Blackburn, J.J. Watkins, *Adv. Mater*. 12 (2000) 913-915.
- [260] K.S. Morley, P.C. Marr, P.B. Webb, A.R. Berry, F.J. Allison, G. Moldovan, P.D. Brown, S.M. Howdle, *J. Mater. Chem*. 12 (2002).
- [261] X.-R. Ye, Y. Lin, C. Wang, M.H. Engelhard, Y. Wang, C.M. Wai, *J. Mater. Chem*. 14 (2004).
- [262] T.A. Crowley, K.J. Ziegler, D.M. Lyons, D. Ertz, H. Olin, M.A. Morris, J.D. Holmes, *Chem. Mater*. 15 (2003) 3518-3522.
- [263] S.G. Aspromonte, Á. Sastre, A.V. Boix, M.J. Cocero, E. Alonso, *Micro. Meso. Mater*. 148 (2012) 53-61.
- [264] C.-M. Yang, P.-h. Liu, Y.-f. Ho, C.-y. Chiu, K.-j. Chao, *Chem. Mater*. 15 (2002) 275-280.
- [265] J. van der Meer, I. Bardez-Giboire, C. Mercier, B. Revel, A. Davidson, R. Denoyel, J. *Phys. Chem. C*. 114 (2010) 3507-3515.
- [266] S. Zeppieri, J. Rodríguez, A.L. López de Ramos, *J. Chem. Eng. Data*. 46 (2001) 1086-1088.
- [267] J.B. Matthews, *J. Chem. Soc. Faraday Trans*. 35 (1939) 1113-1122.
- [268] M.E. Raimondi, E. Gianotti, L. Marchese, G. Martra, T. Maschmeyer, J.M. Seddon, S. Coluccia, *J. Phys. Chem. B*. 104 (2000) 7102-7109.
- [269] E.P. Reddy, L. Davydov, P.G. Smirniotis, *J. Phys. Chem. B*. 106 (2002) 3394-3401.
- [270] P. Crook, A I. Asphahani, S J. Matthews, Haynes International, Inc., Kokomo, Ind, 1989.
- [271] S. Meseguer, M.A. Tena, C. Gargori, J.A. Badenes, M. Llusar, G. Monrós, *Ceram. Int*. 33 (2007) 843-849.
- [272] S.C. Petitto, E.M. Marsh, G.A. Carson, M.A. Langell, *J. Mol. Catal. A: Chem*. 281 (2008) 49-58.
- [273] H.S. Cheng, Z.Q. Zhang, H.N. Xia, J.C. Jiang, F.J. Yang, *Nucl. Instr. Meth. Phys. Res. B*. 190 (2002) 488-491.
- [274] P. Combes, J.J. Massol, P.C. Alvarez, Saint-Gobain Vitrage International, Courbevoir, France, 1994.
- [275] D. Dingley, *J. Chem. Educ*. 42 (1965) 160.
- [276] C. John. Freche, L. Richard. Ashbrook, J. Stanley. Klima, *J. Metals*. 15 (1963) 928-934.
- [277] J. C. Freche, R. L. Ashbrook, G. D. Sandrock, *J. Eng. Ind*. 87 (1965) 9-20.
- [278] J. Stringer, *J. Mater. Sci. Tech*. 3 (1987) 482-493.
- [279] V. Ratna, D.S. Sarma, *Scripta Metall. Mater*. 29 (1993) 467-472.
- [280] R.L. Norman, *J. Pros. Den*. 14 (1964) 45-51.
- [281] G.W. Goward, *Surf. Coat. Technol*. 108-109 (1998) 73-79.
- [282] G.W. Parshall, *Catal. Rev*. 23 (1981) 107-124.
- [283] H. Yamaura, K. Moriya, N. Miura, N. Yamazoe, *Sensor. Actuat. B: Chem*. 65 (2000) 39-41.

- [284] T.N. Angelidis, E. Tourasanidis, E. Marinou, G.A. Stalidis, *Resour. Conserv. Recy.* 13 (1995) 269-282.
- [285] Y. Tashiro, T. Iwahama, S. Sakaguchi, Y. Ishii, *Adv. Synth. Catal.* 343 (2001) 220-225.
- [286] A.Y. Khodakov, W. Chu, P. Fongarland, *Chem. Rev.* 107 (2007) 1692-1744.
- [287] G.N. Schrauzer, *Accounts Chem. Res.* 1 (1968) 97-103.
- [288] M. Fenech, *Mutation Res.* 475 (2001) 57-67.
- [289] C.-B. Wang, H.-K. Lin, C.-W. Tang, *Catal. Lett.* 94 (2004) 69-74.
- [290] M. Salah A, *J. Magn. Magn. Mater.* 246 (2002) 184-190.
- [291] C.-S. Cheng, M. Serizawa, H. Sakata, T. Hirayama, *Mater. Chem. Phys.* 53 (1998) 225-230.
- [292] P.I. V, *Analytical Chemistry of Cobalt*, Ann Arbor-Humphrey Science Publication, London, 1969.
- [293] Y. Du, K.M. Ok, D. O'Hare, *J. Mater. Chem.* 18 (2008) 4450-4459.
- [294] S.C. Petitto, E.M. Marsh, G.A. Carson, M.A. Langell, *J. Mol. Catal. A: Chem.* 281 (2008) 49-58.
- [295] X.-L. Xu, Z.-H. Chen, Y. Li, W.-K. Chen, J.-Q. Li, *Surf. Sci.* 603 (2009) 653-658.
- [296] Y. Ye, F. Yuan, S. Li, *Mater. Lett.* 60 (2006) 3175-3178.
- [297] L. Bornstein, *Physics of Nontetrahedrally Bonded Binary Compounds*, Springer, New York. 17 (1984).
- [298] K. Ruebenbauer, U.D. Wdowik, *J. Phys. Chem. Solids.* 65 (2004) 1917-1924.
- [299] M.D. Rehtin, B.L. Averbach, *Phys. Rev. Lett.* 26 (1971) 1483-1485.
- [300] A.S. Risbud, L.P. Snedeker, M.M. Elcombe, A.K. Cheetham, R. Seshadri, *Chem. Mater.* 17 (2005) 834-838.
- [301] J. Wang, *Low Energy Electron Diffraction Studies of Transition Metal Oxides Surfaces and Films*, Martin Luther Universitat, Halle Wittenberg (2005).
- [302] M. Figlarz, J. Guenot, F. Fievet-Vincent, *J. Mater. Sci.* 11 (1976) 2267-2270.
- [303] G.A. El-Shobaky, I.F. Hewaidy, T. El-Nabarawy, *Surf. Technol.* 10 (1980) 311-319.
- [304] A. D. Pelton, H. Schmalzried, J. Sticher, *Berichte der Bunsengesellschaft für physikalische Chemie.* 83 (1979) 241-252.
- [305] F. Lichtenberg, K. Kleinsorgen, *J. Power Sources.* 62 (1996) 207-211.
- [306] P. Poizot, S. Laruelle, S. Grugeon, L. Dupont, J.M. Tarascon, *Nature.* 407 (2000) 496-499.
- [307] B. Naoufal, *Appl. Catal., B: Environ.* 67 (2006) 168-176.
- [308] X. Xu, J. Li, Z. Hao, W. Zhao, C. Hu, *Mater. Res. Bull.* 41 (2006) 406-413.
- [309] B. Varghese, C.H. Teo, Y. Zhu, M.V. Reddy, B.V.R. Chowdari, A.T.S. Wee, V.B.C. Tan, C.T. Lim, C.H. Sow, *Adv. Funct. Mater.* 17 (2007) 1932-1939.
- [310] M. Salavati-Niasari, N. Mir, F. Davar, *J. Phys. Chem. Solid.* 70 (2009) 847-852.
- [311] S.H. Lin, S.J. Ho, C.L. Wu, *Ind. Eng. Chem. Res.* 35 (1996) 307-314.
- [312] C.J. Chang, S.-S. Li, C.-M. Ko, *J. Chem. Technol. Biot.* 64 (1995) 245-252.
- [313] G. Laugel, J. Arichi, M. Molière, A. Kiennemann, F. Garin, B. Louis, *Catal. Today.* 138 (2008) 38-42.
- [314] B. Solsona, T.E. Davies, T. Garcia, I. Vázquez, A. Dejoz, S.H. Taylor, *Appl. Catal. B: Environ.* 84 (2008) 176-184.

- [315] T.-L. Lai, Y.-L. Lai, C.-C. Lee, Y.-Y. Shu, C.-B. Wang, *Catal. Today*. 131 (2008) 105-110.
- [316] K. Schmidt-Szalowski, K. Krawczyk, J. Petryk, *Appl. Catal. A: Gen.* 175 (1998) 147-157.
- [317] H. Ma, J. Xu, C. Chen, Q. Zhang, J. Ning, H. Miao, L. Zhou, X. Li, *Catal. Lett.* 113 (2007) 104-108.
- [318] Á. Szegedi, M. Popova, C. Minchev, *J. Mater. Sci.* 44 (2009) 6710-6716.
- [319] T. Mousavand, T. Naka, K. Sato, S. Ohara, M. Umetsu, S. Takami, T. Nakane, A. Matsushita, T. Adschiri, *Phys. Rev. B*. 79 (2009) 144411.
- [320] C. Wang, S. Lim, G. Du, C.Z. Loebicki, N. Li, S. Derrouiche, G.L. Haller, *J. Phys. Chem. C*. 113 (2009) 14863-14871.
- [321] X.-P. Shen, H.-J. Miao, H. Zhao, Z. Xu, *Appl. Phys. A: Mater. Sci. Proc.* 91 (2008) 47-51.
- [322] H.-P. Cong, S.-H. Yu, *Cryst. Growth Des.* 9 (2008) 210-217.
- [323] N. Pasha, N. Lingaiah, N.S. Babu, P.S.S. Reddy, P.S.S. Prasad, *Catal. Commun.* 10 (2008) 132-136.
- [324] J. Lojewska, A. Kolodziej, J. Zak, J. Stoch, *Catal. Today*. 105 (2005) 655-661.
- [325] X.-D. Hou, Y.-Z. Wang, Y.-X. Zhao, *Catal. Lett.* 123 (2008) 321-326.
- [326] Y. Huang, D. Gao, Z. Tong, J. Zhang, H. Luo, *J. Nat. Gas Chem.* 18 (2009) 421-428.
- [327] L.G.A. van de Water, G.L. Bezemer, J.A. Bergwerff, M. Versluijs-Helder, B.M. Weckhuysen, K.P. de Jong, *J. Catal.* 242 (2006) 287-298.
- [328] M. Wolters, L.J.W. van Grotel, T.M. Eggenhuisen, J.R.A. Sietsma, K.P. de Jong, P.E. de Jongh, *Catal. Today*. 163 (2011) 27-32.
- [329] S. Todorova, G. Kadinov, K. Tenchev, Y. Kalvachev, V. Kostov-Kytin, *J. Mater. Sci.* 42 (2007) 3315-3320.
- [330] L. Zhou, J. Xu, H. Miao, F. Wang, X. Li, *Appl. Catal. A: Gen.* 292 (2005) 223-228.
- [331] T. Garcia, S. Agouram, J.F. Sánchez-Royo, R. Murillo, A.M. Mastral, A. Aranda, I. Vázquez, A. Dejoz, B. Solsona, *Appl. Catal. A: Gen.* 386 (2010) 16-27.
- [332] M.M. Yung, E.M. Holmgren, U.S. Ozkan, *J. Catal.* 247 (2007) 356-367.
- [333] W.-H. Yang, M. Kim, *Res. Chem. Intermediat.* 34 (2008) 717-725.
- [334] M.S. Ghattas, *Micro. Meso. Mater.* 97 (2006) 107-113.
- [335] A.M. Venezia, R. Murania, G. Pantaleo, V. La Parola, S. Scirè, G. Deganello, *Appl. Catal. A: Gen.* 353 (2009) 296-304.
- [336] M. Moliere, P. Cozzarin, S. Bouchet, P. Rech, *Proceedings of the ASME Turbo 2005 Conference*, Reno (June 6–9, 2005).
- [337] G. Laugel, J. Arichi, P. Bernhardt, M. Molière, A. Kiennemann, F. Garin, B. Louis, *Comptes Rendus Chimie*. 12 (2009) 731-739.
- [338] V. Parvulescu, B.L. Su, *Catal. Today*. 69 (2001) 315-322.
- [339] B.A. Sazonov, V.V. Popovskii, G.K. Boreskov, *Kinet. Catal.* 9 (1968) 255.
- [340] C.-B. Wang, C.-W. Tang, H.-C. Tsai, S.-H. Chien, *Catal. Lett.* 107 (2006) 223-230.
- [341] J. Chen, Y. Zhang, L. Tan, Y. Zhang, *Ind. Eng. Chem. Res.* 50 (2011) 4212-4215.
- [342] G. Prieto, A. Martínez, R. Murciano, M.A. Arribas, *Appl. Catal. A: Gen.* 367 (2009) 146-156.

- [343] G. Jacobs, Y. Ji, B.H. Davis, D. Cronauer, A.J. Kropf, C.L. Marshall, *Appl. Catal. A: Gen.* 333 (2007) 177-191.
- [344] H. Xiong, Y. Zhang, K. Liew, J. Li, *Fuel Process. Technol.* 90 (2009) 237-246.
- [345] Y. Wang, M. Noguchi, Y. Takahashi, Y. Ohtsuka, *Catal. Today.* 68 (2001) 3-9.
- [346] Y. Wang, B. Hou, J. Chen, Y. Sun, *React. Kinet. Mech. Catal.* 102 (2011) 155-164.
- [347] A.W. Adamson, A.P. Gast, *Physical Chemistry of the Surfaces* 6th ed., J. Wiley & Sons New York, 1997.
- [348] S. Ross, J.P. Olivier, *On Physical Adsorption*, Wiley, New York, 1964.
- [349] R. Roque-Malherbe, *Micro. Meso. Mater.* 41 (2000) 227-240.
- [350] F. Rouquerol, J. Rouquerol, K. Sing, *Adsorption by Powder Porous Solids*, Academic Press, New York, 1999.
- [351] W. Rudzinski, D.H. Everett, *Adsorption of Gases in Heterogeneous Surfaces*, Academic Press, London, 1992.
- [352] R.M.A. Roque-Malherbe, Boca Raton, CRC Press, Florida, 2007.
- [353] G. Leofanti, M. Padovan, G. Tozzola, B. Venturelli, *Catal. Today.* 41 (1998) 207-219.
- [354] S.J. Gregg, K.S.W. Sing, *Adsorption, Surface Area and Porosity*, Academic Press, London, 1982.
- [355] D.M. Young, A.D. Crowell, Butterworths, London, (1962).
- [356] S. Brunauer, P.H. Emmett, E. Teller, *J. Am. Chem. Soc.* 60 (1938) 309-319.
- [357] E.P. Barrett, L.G. Joyner, P.P. Halenda, *J. Am. Chem. Soc.* 73 (1951) 373-380.
- [358] K. Kaneko, *J. Membr. Sci.* 96 (1994) 59-89.
- [359] F. Rodriguez-Reinoso, J. Rouquerol, K.S.W. Sing, K.K. Unger, *Characterization of Porous Solids II*, Elsevier, Amsterdam, 1991.
- [360] J. Taghavimoghaddam, G.P. Knowles, A.L. Chaffee, *J. Mol. Catal. A: Chem.* 358 (2012) 79-88.
- [361] X. Liu, L. Li, Y. Du, Z. Guo, T.T. Ong, Y. Chen, S.C. Ng, Y. Yang, *J. Chromatogr. A.* 1216 (2009) 7767-7773.
- [362] G.C. Bond, S.P. Sarsam, *Appl. Catal.* 38 (1988) 365-377.
- [363] Z. Mu, J.J. Li, M.H. Duan, Z.P. Hao, S.Z. Qiao, *Catal. Commun.* 9 (2008) 1874-1877.
- [364] M.H. Jellinek, I. Fankuchen, in: V.I.K. W.G. Frankenburg, E.K. Rideal (Eds.), *Advances in Catalysis*, Academic Press, 1948, pp. 257-289.
- [365] H.P. Klug, L.E. Alexander, *X-ray Diffraction Procedures for Polycrystalline and Amorphous Materials*, Wiley, New York, 1954.
- [366] E.F. Paulus, A. Gieren, *Handbook of Analytical Techniques*, Wiley-VCH Verlag GmbH, 2008, pp. 373-417.
- [367] D. N. B, *Usp. Fiz. Nauk.* 115 (1975) 361-401.
- [368] V.S. Ramachandran, J.J. Beaudoin, *Handbook of Analytical Techniques in Concrete Science and Technology*, William Andrew Publishing/Noyes Publications, New York, 2001.
- [369] A.L. Patterson, *Phys. Rev.* 56 (1939) 978-982.
- [370] K. Siegbahn, *Atomic, Molecular, and Solid State Structure Studied by Means of Electron Spectroscopy*, Almqvist and Wiksells, Uppsala 1967.
- [371] B. D, *Handbook of X-ray and Ultraviolet Photoelectron Spectroscopy*, Heyden, London, 1978.
- [372] P.K. Ghosh, *Introduction to Photoelectron Spectroscopy*, Wiley, New York, 1983.

- [373] J.C. Rivière, Handbook of Analytical Techniques, Wiley-VCH Verlag GmbH, 2008, pp. 851-949.
- [374] J.F. Watts, J. Wolstenholme, An Introduction to Surface Analysis by XPS and AES, Wiley, Chichester, 2003.
- [375] L. J, Physico-Chemical Analysis of Industrial catalysts, Editions Technip, Paris, 2003.
- [376] R. Meusinger, A. Margaret Chippendale, S.A. Fairhurst, Handbook of Analytical Techniques, Wiley-VCH Verlag GmbH, 2008, pp. 509-559.
- [377] A.T. Bell, Colloid. Surface. A. 158 (1999) 221-234.
- [378] E. G, Handbook of Heterogeneous catalysts, VCH, Weinheim, 1997.
- [379] C.P. Grey, Handbook of Zeolite Science and Technology, Marcel Dekker, New York, 2003.
- [380] E. Lippmaa, M. Maegi, A. Samoson, G. Engelhardt, A.R. Grimmer, J. Am. Chem. Soc. 102 (1980) 4889-4893.
- [381] S. Amelinckx, D. Van Dyck, J. Van Landuyt, Handbook of Microscopy: Application of Materials Science, Solid-State Physics and Chemistry VCH, Weinheim, 1997.
- [382] S. Amelinckx, D. Van Dyck, J. Van Landuyt, Electron Microscopy: Principles and Fundamentals, VCH, Weinheim, 1999.
- [383] J.C. Vedrine, F. Delannay, Characterization of Heterogeneous Catalysts, 1984.
- [384] D.B. Williams, C.B. Carter, Transmission Electron Microscopy A Textbook For Material Science, SpringerLink, 2009.
- [385] M.D. Graef, Introduction to Conventional Transmission Electron Microscopy, Cambridge University Press, Cambridge, 2003.
- [386] C. Kisielowski, B. Freitag, M. Bischoff, H. van Lin, S. Lazar, G. Knippels, P. Tiemeijer, M. van der Stam, S. von Harrach, M. Stekelenburg, M. Haider, S. Uhlemann, H. Müller, P. Hartel, B. Kabius, D. Miller, I. Petrov, E.A. Olson, T. Donchev, E.A. Kenik, A.R. Lupini, J. Bentley, S.J. Pennycook, I.M. Anderson, A.M. Minor, A.K. Schmid, T. Duden, V. Radmilovic, Q.M. Ramasse, M. Watanabe, R. Erni, E.A. Stach, P. Denes, U. Dahmen, Microsc. Microanal. 14 (2008) 469-477.
- [387] <http://fgamedia.org/faculty/rdcormia/NANO53/TEM.htm>.
- [388] J.I. Goldstein, D.E. Newbury, P. Echin, D.C. Joy, C.E. Lyman, E. Lifshin, L. Sawyer, J.R. Michael, Scanning Electron Microscopy and X-Ray Microanalysis, Kluwer Academic/Plenum publishers New York, 2003.
- [389] S. Wang, A.Y. Borisevich, S.N. Rashkeev, M.V. Glazoff, K. Sohlberg, S.J. Pennycook, S.T. Pantelides, Nat. Mater. 3 (2004) 143-146.
- [390] P. D. Nellist, S.J. Pennycook. 274 (1996) 413.
- [391] A.V. Crewe, Rep. Prog. Phys. 43 (1980) 621.
- [392] M.M.J. Treacy, A. Howie, C.J. Wilson, Philos. Mag. A. 38 (1978) 569-585.
- [393] J. Liu, J. Electron Microsc. 54 (2005) 251-278.
- [394] P.R. Griffiths, Handbook of Vibrational Spectroscopy, John Wiley & Sons, Ltd, 2006.
- [395] P.R. Griffiths, J.A. de Haseth, Fourier Transform Infrared Spectroscopy, Wiley, New York, 1986.
- [396] G. Gauglitz, Handbook of Analytical Techniques, Wiley-VCH Verlag GmbH, 2008, pp. 419-463.
- [397] B.M. Weckhuysen, in Spectroscopy of transition metal ions on surfaces, Leuven University Press, 2000.

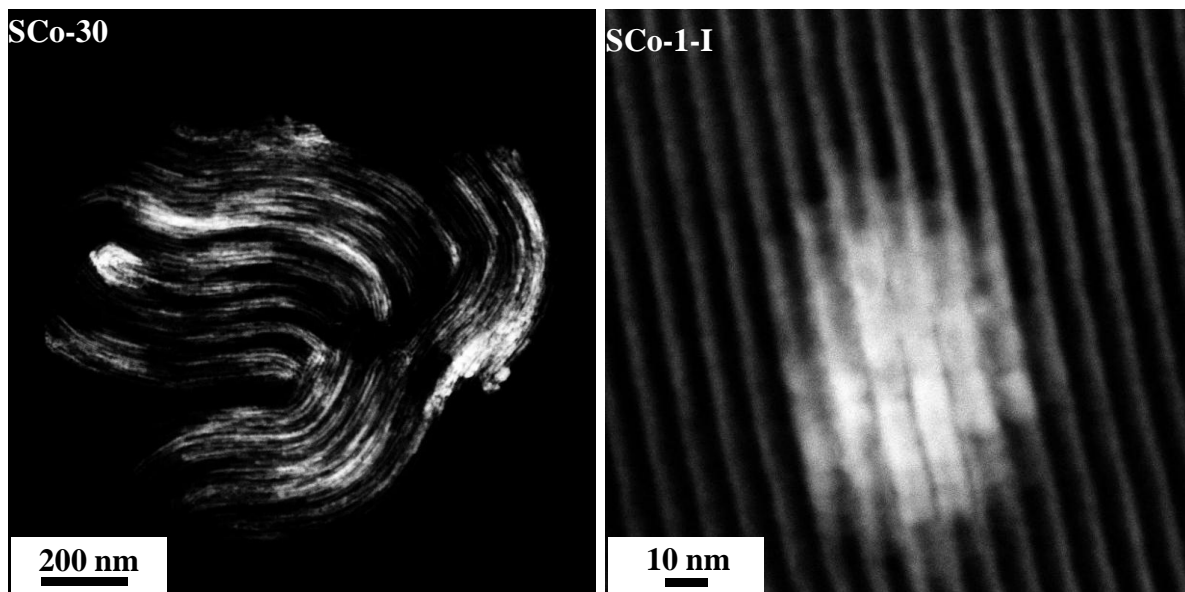
- [398] B.M. Weckhuysen, American Scientific Publishers, 2004, pp. 225-270.
- [399] P.W. Albers, Handbook of Heterogeneous Catalysis, Wiley-VCH Verlag GmbH & Co. KGaA, 2008.
- [400] P.J.F. Sandra, Handbook of Analytical Techniques, Wiley-VCH Verlag GmbH, 2008, pp. 199-259.
- [401] M. Linscheid, Handbook of Analytical Techniques, Wiley-VCH Verlag GmbH, 2008, pp. 579-626.

---

# Chapter 3

SBA-15 supported cobalt  
oxide from  $\text{Co}(\text{NO}_3)_2 \cdot 6\text{H}_2\text{O}$

---



### 3.1 General overview

Chapter three comprises three publications (full papers) and an appendix with supplementary information.

Publication 1, (section 3.2) concerns the preparation and use of SBA-15 supported  $\text{Co}_3\text{O}_4$ . Several composite materials were prepared, via the two-solvent method using  $\text{Co}(\text{NO}_3)_2 \cdot 6\text{H}_2\text{O}$  as cobalt precursor to investigate the impact of Co-content on the morphology and dispersion of the  $\text{Co}_3\text{O}_4$ . For comparison, Co-composites were also prepared using the more conventional methods of adsorption and impregnation.

Regardless of the preparation method, a dark brown coloration was observed for all Co-composites prepared using  $\text{Co}(\text{NO}_3)_2 \cdot 6\text{H}_2\text{O}$ . The colour intensity very clearly increased with Co-loading. It was found that  $\text{Co}_3\text{O}_4$  species were crystallised into nanorods which filled adjacent mesopores and which were also connected via pore-filled micropores (from the original SBA-15) to form 'patches'. The formation of  $\text{Co}_3\text{O}_4$  patches is common to all Co-composites prepared from  $\text{Co}(\text{NO}_3)_2 \cdot 6\text{H}_2\text{O}$ . As for the two-solvent Co-composites,  $\text{Co}_3\text{O}_4$  species were formed predominantly inside the pores, filling the full cross section of the mesopores. The width and length of the patches increased in proportion to the Co-loading. However, impregnation resulted in the formation of  $\text{Co}_3\text{O}_4$  patches both on the external and internal surfaces of SBA-15. When adsorption was used as a preparation method less cobalt from the aqueous solution was incorporated into the composite product. This resulted in the formation of relatively small patches by comparison with the other preparation methods, for the same Co-loading. The patches formed using the adsorption method were also formed to a large extent inside the mesopores. The catalytic activity of the composites was evaluated for the TBHP oxidation of cyclohexanol and it was shown that the Co-composites with the lowest Co-content gave the highest catalytic activity. This was due to reduced pore blockage and better accessibility of active Co-species by the reactants.

Publication 2, (section 3.3) describes further chemical and morphological investigations of SBA-15 supported  $\text{Co}_3\text{O}_4$ . Here the DR UV-vis spectra showed a red-shift which intensified with increasing Co-loading within the series of Co-composites prepared by the two-solvent method. This can be associated with the progressive growth of crystalline patches as the Co-loading increased. The Co-composites were employed in an investigation of the liquid phase oxidation of norbornene, benzyl alcohol and 1-phenylethanol. It was shown that the catalytic activity of the Co-composites varied in reverse proportion to the Co-loading for all of these

substrates. Careful investigation of the extent of conversion of both the reacting substrate and the oxidant led to a proposed mechanism for the oxidation of benzyl alcohol in which TBHP behaved more as an initiator of the reaction, with atmospheric oxygen as co-oxidant.

Publication 3, (section 3.4) concerns low Co-loading composites and compares their dispersion, morphology and catalytic activity. SBA-15 supported  $\text{Co}_3\text{O}_4$  was prepared using the two-solvent method and conventional impregnation with 1 wt% Co-loading. The resulting  $\text{Co}_3\text{O}_4$  patches were smaller and better dispersed throughout the support relative to those reported in publication 3.1. As a result, they exhibited better catalytic performance in the liquid phase oxidation of cyclohexanol, benzyl alcohol, 1-phenylethanol and norbornene, with TBHP. The composite prepared via the two-solvent method demonstrated better catalytic activity compared to its analogues with the same Co-content prepared via the impregnation and adsorption methods. This is attributed to further reduced pore blockage and still better availability of  $\text{Co}_3\text{O}_4$  in this composite.

Appendix 3.5 contains wide-angle XRD patterns of SBA-15 supported  $\text{Co}_3\text{O}_4$  with 30 wt% Co-loading calcined at various temperatures. STEM images and elemental mapping profiles of SBA-15 supported  $\text{Co}_3\text{O}_4$  with 5 wt% and 30 wt% Co-loading are also shown in the appendix. The information in the appendix has not been presented in the publications; however it supports the logic and conclusions reached in the published work.

**Declaration for Thesis Chapter 3.2**

Preparation and characterization of mesoporous silica supported cobalt oxide as a catalyst for oxidation of cyclohexanol

**Declaration by candidate**

In the case of Chapter 3.2 the nature and extent of my contribution to the work was the following:

Nature of contribution	Extent of contribution (%)
Proposed original idea; prepared and analysed samples; identified major issues; developed interpretations; fully drafted papers and conclusions	80%

The following co-authors contributed to the work. Co-authors who are students at Monash University must also indicate the extent of their contribution in percentage terms:

Name	Nature of contribution	Extent of contribution (%) for student co-authors only
Gregory P. Knowles	Aided method development (catalyst characterisation), input to interpretation of results, input to manuscript revision	N/A
Alan L. Chaffee	Supervision, assisted interpretations of results, editorial assistance	N/A

Candidate's Signature

		Date 23-10-12
--	--	------------------

**Declaration by co-authors**

The undersigned hereby certify that:

- (1) the above declaration correctly reflects the nature and extent of the candidate's contribution to this work, and the nature of the contribution of each of the co-authors.
- (2) they meet the criteria for authorship in that they have participated in the conception, execution, or interpretation, of at least that part of the publication in their field of expertise;
- (3) they take public responsibility for their part of the publication, except for the responsible author who accepts overall responsibility for the publication;
- (4) there are no other authors of the publication according to these criteria;
- (5) potential conflicts of interest have been disclosed to (a) granting bodies, (b) the editor or publisher of journals or other publications, and (c) the head of the responsible academic unit; and
- (6) the original data are stored at the following location(s) and will be held for at least five years from the date indicated below:

Location(s) School of Chemistry, Clayton Campus

Gregory P. Knowles		Date 22-10-12
Alan L. Chaffee		22-10-12

## 3.2 Preparation and characterization of mesoporous silica supported cobalt oxide as a catalyst for the oxidation of cyclohexanol

Journal of Molecular Catalysis A: Chemical 358 (2012) 79–88



Contents lists available at SciVerse ScienceDirect

Journal of Molecular Catalysis A: Chemical

journal homepage: [www.elsevier.com/locate/molcata](http://www.elsevier.com/locate/molcata)



## Preparation and characterization of mesoporous silica supported cobalt oxide as a catalyst for the oxidation of cyclohexanol

Jamileh Taghavimoghaddam, Gregory P. Knowles, Alan L. Chaffee\*

School of Chemistry, Monash University, Victoria 3800, Australia

### ARTICLE INFO

#### Article history:

Received 23 November 2011

Received in revised form 27 February 2012

Accepted 29 February 2012

Available online 8 March 2012

#### Keywords:

Supported  $\text{Co}_3\text{O}_4$

Spinel cobalt oxide

Mesoporous silica SBA-15

Oxidative catalyst

Two-solvent method

### ABSTRACT

Cobalt oxide catalysts supported on mesoporous silica SBA-15 were prepared by the “two-solvent” method and compared with analogous catalysts prepared by the more conventional methods of impregnation and adsorption. Cobalt nitrate was used as the precursor. The catalysts were characterized by  $\text{N}_2$  adsorption–desorption, XRD, FTIR, XPS, TPR, ICP-MS, TEM and DR UV–vis. Their activity for the oxidation of cyclohexanol was determined by GC and GC–MS. The effect of metal loading on the morphology and catalytic activity of the catalysts was investigated. The catalyst with the lowest cobalt content exhibited the highest catalytic activity for cyclohexanol oxidation due to the better accessibility of the reactants to the catalytic sites.

© 2012 Elsevier B.V. All rights reserved.

### 1. Introduction

The oxidation of organic substrates is very important industrially [1,2]. For instance oxidation of cyclohexanol to cyclohexanone is a significant step in the syntheses of adipic acid and caprolactam of which about 2.5 and 2 billion kg, respectively, are produced annually. These intermediates are important in the manufacture of nylon 6 and nylon 66 and also as plasticizers and food additives [3].

Commercially cyclohexanol or the mixture of cyclohexanol and cyclohexanone are oxidized to adipic acid using copper and vanadium salts dissolved in excess amount of  $\text{HNO}_3$  [4] as catalysts. In order to produce fewer by-products and develop more environmentally friendly procedures to oxidize cyclohexanol, a variety of metal catalysts have been investigated [5–7]. This has included precious metals [8,9].

Transition metal oxides are known to have promising catalytic behavior for oxidative reactions [10–14]. Compared to precious metal/metal oxides, they are more abundant and less expensive. Bulk metal oxides however, possess a relatively low surface area (SA), which seriously limits their efficiency as catalysts. An appropriate way to circumvent this problem is to disperse the metal oxide particles onto supports with high surface area. If the metal oxide particles can be made as small as possible (i.e., nanoparticles), their catalytic activity should be enhanced by virtue of the increased surface area. If the metal oxide nanoparticles can be confined within

a nanoporous host this may limit the size to which the metal nanoparticle can grow, as they typically sinter during preparation [15]. Supported cobalt oxide nanoparticles have been investigated for a range of catalytic reactions including methane combustion [16,17], propane combustion [18], cyclohexane oxidation [10], ethyl acetate oxidation [19] and CO oxidation [19,20]. Reduced cobalt ( $\text{Co}^0$ ) nanoparticles formed by reduction of  $\text{Co}_3\text{O}_4$  nanoparticles have been used for the Fischer–Tropsch synthesis [21,22].

The preparation of metal oxide nanoparticles is a complex and still poorly understood process. Many factors influence the precise form of a prepared catalyst. These include the chemical nature of the support [23–25], its texture and surface acidity [26], the composition of the metal precursor [23,26], the preparation method [15,21,27,28] and the intended metal loading [29,30]. These factors can influence the final product in terms of dispersion, reduction properties, catalytic activity and product selectivity as well as, the extent of metal–support interactions [31].

Mesoporous silicas such as HMS, MCM-41 and SBA-15 have been considered as suitable hosts for the preparation and stabilization of metal/metal oxide nanoparticles [22,31,32]. The narrow pore size distribution of such supports may prevent sintering and the formation of large catalytically inactive particles [25]. It has been observed that, as the dispersion of the active phase increases, the activity also increases. In general, small nanoparticles are much more reactive due to their high surface area [33–35]. Among the periodic mesoporous silicas SBA-15 [36] has been extensively investigated for the ‘nanocasting’ of catalysts inside the pores of the periodic silica [19,21]. SBA-15 possesses high surface area in the range of  $600\text{--}1000\text{ m}^2\text{ g}^{-1}$  and consists of hexagonal arrays

\* Corresponding author. Tel.: +61 3 9905 4626.

E-mail address: [alan.chaffee@monash.edu](mailto:alan.chaffee@monash.edu) (A.L. Chaffee).

of cylindrical channels with tuneable pore diameters between 5 and 30 nm. Micropores located inside the pore walls interconnect these channels. Moreover, SBA-15 exhibits higher thermal and hydrothermal stability and thicker pore walls in comparison to MCM-41, making it more suitable for catalytic processes where thermal treatments are often encountered [37].

There are several methods reported in the literature for the synthesis of metal-supported catalysts. The conventional procedures are based on ion exchange and impregnation. Ion exchange results in small metal particles at low metal loading [38]. Impregnation can be termed wet or dry, depending whether the volume of the impregnating solution is greater than or equal to the pore volume of the support. Generally speaking impregnation results in large, less catalytically active particles [39]. Large particles can also form as a result of aggregation of adjacent particles during calcination [28]. Adsorption from aqueous solution of metal precursor is another conventional method of depositing metal/metal oxide on supports [40]. However, with this approach the utilization of the metal is poor since only a proportion of the metal cations from the precursor metal solution are deposited on the support. The rest is 'lost' (washed out) upon filtration. To improve this method, typically when mesoporous silicas are used as supports, the pH of the solution can be controlled such that it is higher than the point of zero charge (PZC) of the silica. In this way the silanol groups at the surface are deprotonated and thus have high electrostatic interaction with the metal cations. This circumstance facilitates 'strong electrostatic adsorption' (SEA). This method results in small particle size and high metal dispersion on the support, even at relatively high loadings [41].

Recently a novel method, the so-called "two-solvent" technique has attracted considerable attention [40]. This method is reported to allow the preparation of highly dispersed metal oxide nanoparticles within SBA-15 mesopores, which can then be used as 'nanoreactors'. It has been reported that this method inhibits the growth of metal oxide particles on the external surface of the support [15]. This technique consists of three steps. First a hydrophilic solution of the metal precursor in a volume equal to the pore volume of the mesoporous silica, as determined by  $N_2$  adsorption is prepared. Secondly the mesoporous silica, such as SBA-15 or MCM-41 is dispersed in a hydrophobic solvent, typically hexane. Finally the hydrophilic metal precursor solution is introduced to the hydrophobic solution and consequently the metal is dispersed on hydroxyl sites through hydrophobic–hydrophilic interactions [42]. It is also reported that the type of the hydrophobic solvent (alkanes) plays a key role in the size and dispersion of the metal oxide [43].

The present study deals with the synthesis and characterization of  $Co_3O_4$  nanoparticles selectively grown inside a mesoporous silica SBA-15 support using  $Co(NO_3)_2 \cdot 6H_2O$  as the precursor via the "two-solvent" method. It also compares the nanoparticle properties and catalytic activity with analogous catalysts prepared by the more conventional approaches; adsorption and impregnation. The resultant materials have been characterized by XRD,  $N_2$  adsorption–desorption, FTIR, TPR, XPS, ICP-MS, TEM and diffuse reflectance UV–vis. The catalytic activity of these materials for the oxidation of cyclohexanol has been investigated using tert-butylhydroperoxide (TBHP) as oxidant. The products were identified and characterized by GC and GC–MS.

## 2. Experimental

### 2.1. Synthesis of the SBA-15 support

SBA-15 was prepared using the method first described by Stucky and co-workers [36]. Typically, tri-block copolymer, pluronic P123

(EO20PO70EO20), 4 g, was dispersed in aqueous 2 M hydrochloric acid solution under vigorous stirring to obtain a clear solution. The clear solution indicated the complete dissolution of the surfactant. Tetraethyl orthosilicate (TEOS), 8.5 g, used as the silica source. This was added dropwise to the solution at 40 °C, with vigorous stirring. Gelation was allowed to proceed for 24 h at 40 °C, after which the mixture was transferred to a sealed Teflon flask for hydrothermal treatment at 100 °C for 24 h. The precipitate was filtered, washed several times with distilled water and dried at room temperature. Finally, the tri-block copolymer template was removed by heating in air at 1 °C  $min^{-1}$ , then holding at 550 °C for 6 h.

### 2.2. Supported cobalt oxide catalyst preparations

#### 2.2.1. Two-solvent method

Supported cobalt oxide catalysts (SCo-X, where X represents the nominal cobalt loading percentage) were prepared using the "two-solvent" technique [16]. SBA-15 was first suspended in dry hexane (the hydrophobic solvent). The desired amount of cobalt nitrate (5 wt%, 10 wt% and 30 wt%) was dissolved in distilled water to make the hydrophilic solution. This hydrophilic solution was added dropwise to the hydrophobic solution. The gel was sonicated for 15 min and stirred for 2 h. The solid was recovered by evaporating the solvent under reduced pressure and dried at 100 °C. Finally, the samples were calcined by heating in air at 2 °C  $min^{-1}$ , then holding at 700 °C for 6 h [16].

For comparison commercial  $Co_3O_4$  nanopowder (>50 nm particle size) was purchased from Aldrich.

#### 2.2.2. Impregnation

To prepare samples by impregnation, first the desired amount of cobalt nitrate was dissolved in water and then added to SBA-15 to obtain nominally 5 wt% cobalt loading. This mixture was stirred for 6 h and dried in rotary evaporator for 1 h. The sample was further dried at 100 °C overnight. The sample was then calcined by heating in air at 2 °C  $min^{-1}$ , then holding at 700 °C for 6 h. This material is referred to as SCo-5-I.

#### 2.2.3. Adsorption

To prepare samples using adsorption method, the desired amount of cobalt nitrate was dissolved in water and added to SBA-15 to obtain nominally 5 wt% cobalt loading. The sample was then stirred for 6 h, filtered and then dried at 100 °C overnight. The calcination process is the same as mentioned above. This material is referred to as SCo-5-A.

### 2.3. Characterization techniques

*Low-angle X-ray diffraction patterns* were obtained using a Phillips 1130 powder diffractometer with a monochromatic Cu K $\alpha$  source radiation ( $\lambda = 1.5406 \text{ \AA}$ ) operated at 40 kV and 30 mA over  $2\theta$  range of 0.5–5°. Data was collected with a step size of 0.01° and a step time of 1°  $min^{-1}$ .

*Wide-angle X-ray diffraction patterns* were obtained using a Bruker D8 Focus powder diffractometer with a monochromatic Cu K $\alpha$  source radiation ( $\lambda = 1.5406 \text{ \AA}$ ) operated at 40 kV and 30 mA over the  $2\theta$  range of 15–80°. The data was collected with a step size of 0.02° and a step rate of 1°  $min^{-1}$ .

*$N_2$ -adsorption/desorption isotherms* were obtained at –196 °C on a Coulter Omnisorb 360-CX gas sorption analyzer. Samples were outgassed at 150 °C overnight prior to analysis. Pore volume, BET surface area [44], and the pore size distribution (PSD) (BJH method) [36] were calculated for each data set.

*Fourier transform infrared (FTIR) spectra* were collected from a BIO-RAD FTS 40 spectrometer. The materials were diluted 1/300

**Table 1**  
Elemental analysis results.

Catalyst	Nominal Co content (wt%)	Actual Co content (wt%)
SCo-5-A	5	1.0
SCo-5-I	5	4.5
SCo-5	5	4.5
SCo-10	10	8.2
SCo-30	30	23

in dry KBr, dried (110 °C, 4–6 h), then pressed into pellets (under vacuum) immediately prior to analysis.

Temperature programmed reduction (TPR) experiments were carried out with a Setaram Thermogravimetric Analyser (TAG24). Typically 10 mg of calcined catalyst was flushed with high purity argon at 150 °C for 2 h, to drive off moisture, then cooled to 20 °C. Next, the flow was switched to 10% H<sub>2</sub>/Ar and the temperature raised at 5 °C min<sup>-1</sup> to 900 °C, where it was held for 20 min under 10% H<sub>2</sub>/Ar, and then 20 min under Ar. The gas flow rate over the sample was maintained at 70 cm<sup>3</sup> min<sup>-1</sup>. The weights of the samples both before and after analysis were also separately measured with an analytical balance.

Inductively coupled plasma mass spectrometry (ICP-MS) was carried out using a GBC OPTIMAS 9500 ICP-MS. Prior to measurement all catalysts were digested with nitric acid and hydrofluoric acid at 120 °C for two days to remove silica.

Diffuse reflectance UV–vis spectroscopy (DR UV–vis) was conducted using a Carry 5E UV–visible spectrophotometer, fitted with diffuse reflectance accessory.

Transmission electron microscopy (TEM) was used to obtain detailed information on the morphology and microstructure of supported cobalt oxide. AJEOL 2011 transmission electron microscopy equipped with a LaB<sub>6</sub> emitter (point resolution 0.21 nm) and an accelerating voltage (200 kV) was used for this study.

X-ray photoelectron spectroscopy (XPS) was conducted at the Australian Synchrotron with a SPECSlab2 spectrometer using an Al K $\alpha$  X-ray source (1486.8 eV) at the constant analyzer pass energy 40.0 eV. Binding energies are referenced to the carbon 1 s peak (BE = 284.5 eV) arising from adventitious carbon.

Gas chromatography (GC) was carried out on a Varian 3700 gas chromatograph equipped with an FID detector, a 30 m polar capillary column (SGE 30QC5/BP20 1.0  $\mu$ m, ID 0.53 mm) and an Agilent EZChrom Elite (version 3.2.1) data system.

Gas chromatography–mass spectrometry (GC–MS) was carried out on an Agilent 5973 Network MS equipped with a 6890 series GC system (source conditions: EI, 70 eV, 200 °C).

#### 2.4. Catalytic tests

Liquid-phase oxidation of cyclohexanol to cyclohexanone was performed in a 100 mL flask. In each test, 0.1 g of catalyst was added to 5 mL of acetonitrile and 20 mmol of cyclohexanol. The oxidant, TBHP (24 mmol) was then added dropwise over approximately 10 min. Reactions were carried out under reflux and monitored by gas chromatography, withdrawing samples every 4 h up to 24 h.

### 3. Results and discussion

#### 3.1. Characterization of Co<sub>3</sub>O<sub>4</sub>/SBA-15 catalysts

The cobalt content of synthesized catalysts was measured by ICP-MS after digestion in HF/HNO<sub>3</sub>. The results are summarized in Table 1.

As expected at low cobalt loading, the nominal and actual cobalt contents are very similar for catalysts prepared either by “two-solvent” method or impregnation. However, the catalyst

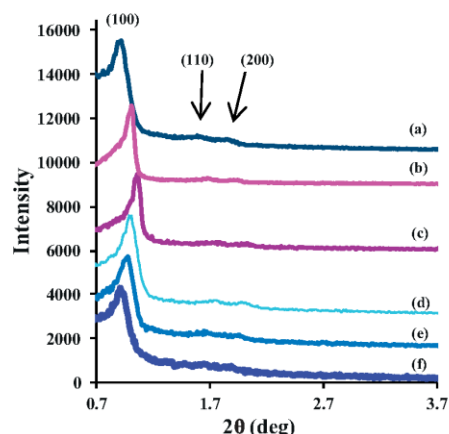


Fig. 1. Low-angle XRD pattern obtained from (a) SBA-15, (b) SCo-5-A, (c) SCo-5-I, (d) SCo-5, (e) SCo-10 and (f) SCo-30.

prepared by adsorption shows lower cobalt content due to weak interactions between the silanol groups of the support and the cobalt precursor. The most highly loaded catalysts, prepared by the two-solvent method, were found to have 23 wt% Co.

#### 3.1.1. X-ray diffraction (XRD)

Fig. 1 shows the low-angle XRD patterns of SBA-15 and supported cobalt oxide catalysts. Three well-resolved diffraction peaks at  $2\theta$  values between 0.5° and 5° were observed both for pure SBA-15 and all catalysts with different cobalt content. The peaks can be indexed as the (100), (110) and (200) peaks [36], which indicates the presence of highly ordered hexagonal mesoporous structure. It is noteworthy that SBA-15 still exhibits a high degree of mesoporous structure even at the highest cobalt loading (SCo-30). All catalysts exhibit a significant reduction of the (100) peak intensity relative to SBA-15. As the cobalt content increased the intensity of the (100) peak decreased. This can be explained by the presence of cobalt oxide nanoparticles in the SBA-15 partially filling the channels. Pore filling in turn, reduces scattering contrast between the pores and the walls of the support [45].

Fig. 2 shows wide-angle XRD patterns obtained from commercial Co<sub>3</sub>O<sub>4</sub> as a reference, the SBA-15 and also all catalysts with different cobalt content. The commercial Co<sub>3</sub>O<sub>4</sub> which shows diffraction peaks at  $2\theta = 18.8^\circ, 31.1^\circ, 36.7^\circ, 38.2^\circ, 44.6^\circ, 55.3^\circ, 59.2^\circ,$

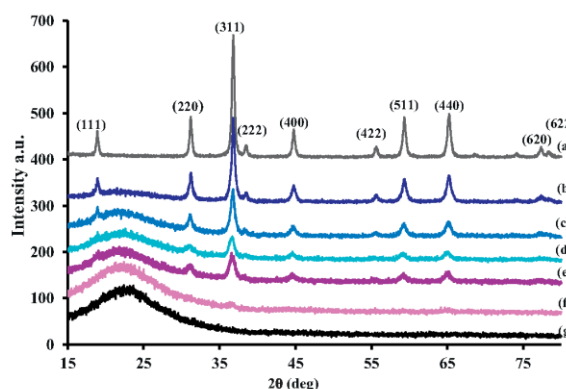


Fig. 2. Wide-angle XRD patterns obtained from (a) commercial Co<sub>3</sub>O<sub>4</sub>, (b) SCo-30, (c) SCo-10, (d) SCo-5, (e) SCo-5-I, (f) SCo-5-A and (g) SBA-15.

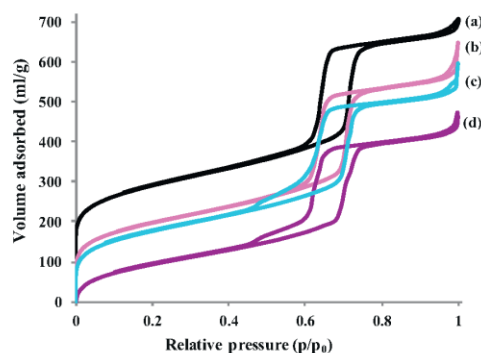


Fig. 3.  $N_2$  adsorption–desorption of (a) SBA-15, (b) SCo-5-A, (c) SCo-5 and (d) SCo-5-I.

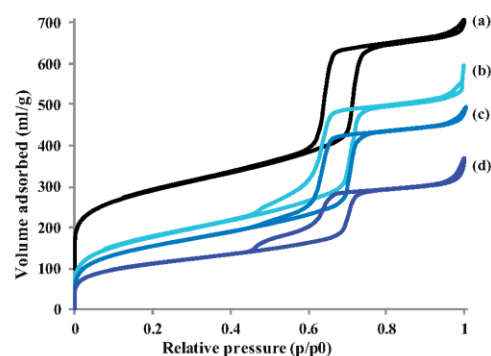


Fig. 4.  $N_2$  adsorption–desorption of (a) SBA-15, (b) SCo-5, (c) SCo-10 and (d) SCo-30.

65.1°, 77° and 77.4°, confirmed the crystallized spinel  $Co_3O_4$  (JCPDF file 01-073-1701) with space group  $Fd\bar{3}m$ : crystallochemical formula  $Co^{2+}Co_2^{3+}O_4$ , where  $Co^{3+}$  occurs in the octahedral position 16d (1/2, 1/2, 1/2) and  $Co^{2+}$  occurs in the tetrahedral position 8a (1/8, 1/8, 1/8) [15,46].

As expected, SBA-15 does not show any sharp diffraction peaks consistent with the amorphous structure of the support. However, a broad peak at  $15^\circ < 2\theta < 30^\circ$  is observed for SBA-15 and all catalysts corresponding to the amorphous silica phase [47]. Unlike the more highly loaded catalysts, it can be seen that SCo-5-A, does not display any diffraction pattern attributed to cobalt oxide. This can be attributed to the low cobalt content and high dispersion of the cobalt oxide species in this case [28]. However, the impregnated catalysts, SCo-5-I, do show diffraction peaks corresponding to  $Co_3O_4$  spinel. As discussed above, impregnation generally results in the formation of large particles, which can be detected by XRD.

All catalysts prepared by the two-solvent method display diffraction peaks corresponding to  $Co_3O_4$  spinel. The intensity of the peaks increases as the cobalt content increases, an indication of the presence of larger cobalt oxide species. When comparing SCo-10 and SCo-30 the latter showed narrower peaks with stronger intensity, which is evidence for the formation of larger  $Co_3O_4$  particles. The size of the cobalt oxide nanoparticles was calculated using the Debye–Scherrer formula from the full width at half maximum (FWHM) of the (3 1 1) diffraction peak [17,48]. The average size of the nanoparticles estimated from the FWHM is 9.6 nm, 12.16 nm and 17.26 nm for SCo-5, SCo-10 and SCo-30, respectively. It can be noted that the particle size is larger than the pore size of the mesoporous silica calculated from  $N_2$  adsorption–desorption (see below). This suggests that the crystals have grown in different adjacent mesopores due to connections through silica walls [48].

### 3.1.2. Textural properties

The  $N_2$  adsorption–desorption isotherms of pure SBA-15 and supported cobalt oxide catalysts are shown in Figs. 3 and 4. The corresponding pore size distributions are illustrated in Figs. 5 and 6, respectively. The isotherm of calcined SBA-15 (Fig. 3a) exhibits a type IV isotherm with H1 hysteresis according to the IUPAC classification [49]. This profile is characteristic of mesoporous materials with two-dimensional cylindrical channels. The isotherm of pure SBA-15 presented a sharp inflection at relative pressure ( $p/p_0$ ) in the range of 0.6–0.8, an indication of a good quality SBA-15 material with two-dimensional cylindrical channels [44]. After loading cobalt, the shapes of the isotherms of the catalysts with different cobalt content were very similar to the original SBA-15. This similarity suggests the uniform mesoporous structure was mostly retained after cobalt loading. The capillary condensation

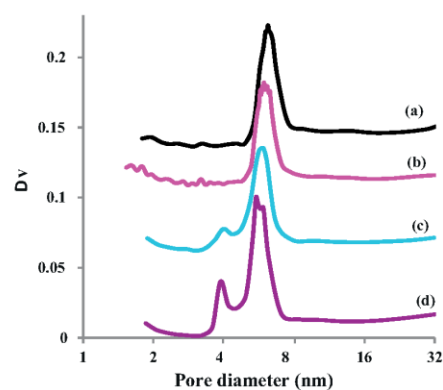


Fig. 5. Pore size distribution of (a) SBA-15, (b) SCo-5-A, (c) SCo-5 and (d) SCo-5-I.

step of SCo-5-A isotherm occurred at slightly lower relative pressure, indicating a decrease of the pore diameter after cobalt loading [15,50]. However, in the case of SCo-5-I and SCo-5, the capillary condensation was obviously shifted to lower relative pressure with a shoulder on the desorption branch. The presence of this shoulder at a relative pressure ( $p/p_0$ ) around 4.5 can be attributed to partial pore blockage, due to the presence of the

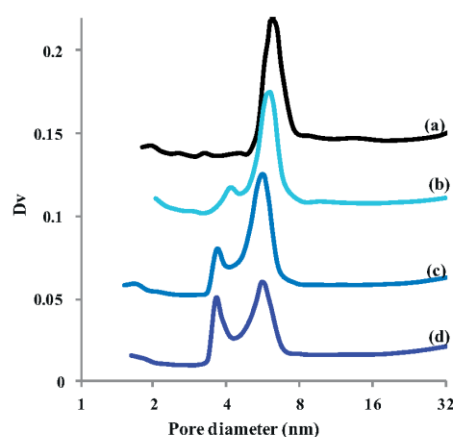


Fig. 6. Pore size distribution of (a) SBA-15, (b) SCo-5, (c) SCo-10 and (d) SCo-30.

**Table 2**  
N<sub>2</sub> adsorption–desorption data obtained from SBA-15 and supported cobalt oxide.

Sample	BET surface area (m <sup>2</sup> g <sup>-1</sup> )	Dp (nm)	Pv (cm <sup>3</sup> g <sup>-1</sup> )
SBA-15	656	6.0	0.86
SCo-5-A	620	5.8	0.81
SCo-5-I	481	5.6	0.70
SCo-5	603	5.7	0.78
SCo-10	510	5.7	0.68
SCo-30	347	5.7	0.46

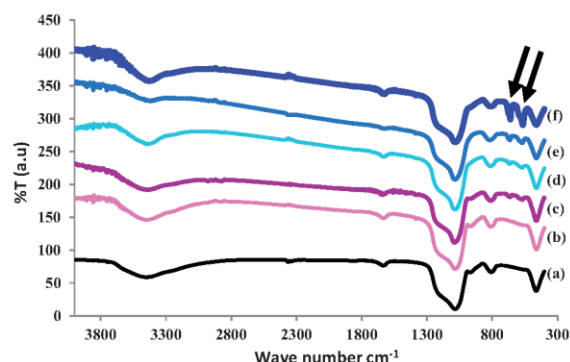
cobalt oxide species in the aperture of the pores. This is known as the cavitation phenomenon [51]. The absence of the shoulder for SCo-5-A (compared to SCo-5 and SCo-5-I) can be attributed to an apparent absence of pore blockage for this catalyst with the lowest cobalt content. The average pore size of the SBA-15 is determined to be 6 nm, while the average pore size of the SCo-5-A, SCo-5 and SCo-5-I is determined to be 5.8, 5.7 and 5.6 nm, respectively. As summarized in Table 2 the decrease in surface area, pore diameter and pore volume and the fact that the capillary condensation shifts to lower relative pressure compared to pure SBA-15, suggests that cobalt oxide has formed inside the SBA-15 channels.

Fig. 5 illustrates the PSD of SBA-15 and all catalysts with 5 wt% cobalt prepared using different methods. The SCo-5-A shows a narrow PSD similar to SBA-15, indicating that the pore structure has not significantly altered. However, SCo-5-I and SCo-5 show a bimodal PSD, with the first peak centered at around 4 nm and the second one at ~6 nm. This suggests that in these cases, there may be partial pore blockage or deposition of cobalt oxide particles against the internal silica walls and/or at the pore apertures.

Fig. 4 shows the N<sub>2</sub> adsorption–desorption isotherms of pure SBA-15, SCo-5, SCo-10 and SCo-30. All catalysts exhibit a type IV isotherm with H1 hysteresis. It is notable that the mesoporosity remained intact even after loading nominally 30 wt% cobalt. However, the capillary condensation steps for all catalysts were shifted to lower relative pressure compared to SBA-15. It is noteworthy that the cavitation phenomenon was observed in the isotherms of all catalysts prepared by the two-solvent method, suggesting there is partial pore blockage due to the presence of cobalt oxide species inside the pore. With increasing cobalt content, less nitrogen was absorbed by the catalysts. The surface area and pore volume of the catalysts decreased in the order of SCo-5 > SCo-10 > SCo-30.

This decrease can be attributed to the formation of the cobalt oxide inside the pores of SBA-15. However, van der Meer et al., who also supported Co<sub>3</sub>O<sub>4</sub> on SBA-15 by the two-solvent method, noted that the loss of pore volume and surface area cannot be attributed to simple pore filling; this is because the volume which is actually occupied by the Co<sub>3</sub>O<sub>4</sub> is very small [52]. In this work, the volume occupied by Co<sub>3</sub>O<sub>4</sub> was determined to be 0.0073–0.0376 cm<sup>3</sup> g<sup>-1</sup> for the SCo-5–SCo-30 cases. This was calculated using the cobalt contents determined by ICP measurements, assuming a Co<sub>3</sub>O<sub>4</sub> density of 6.11 g cm<sup>-3</sup>. It can be seen that pore volume loss between this same sequences of samples (0.08–0.40 cm<sup>3</sup> g<sup>-1</sup>) is far greater. Thus, it is suspected that original pores are partially blocked such that, during BET analysis, N<sub>2</sub> gas cannot access this 'blocked porosity'. This can therefore be ascribed to the existence of Co<sub>3</sub>O<sub>4</sub> nanoparticles, which have formed with diameters smaller than that of the SBA-15 pores such that they partially but incompletely impede access to the channels [52].

Fig. 6 compares the PSD in catalysts with various cobalt content synthesized by two-solvent method. Bimodal PSD is observed for all catalysts. There are three important points that can be highlighted: (i) the volume of adsorbed N<sub>2</sub> decreased with increasing cobalt content, (ii) the portion of pores with diameter around 4 nm increased as the cobalt content increased and (iii) the presence of



**Fig. 7.** FT-IR spectra of (a) SBA-15, (b) SCo-5-A, (c) SCo-5-I, (d) SCo-5, (e) SCo-10 and (f) SCo-30.

bimodal PSD indicates that cobalt oxide species have formed inside the pores.

### 3.1.3. Fourier transform infrared spectroscopy (FT-IR)

Fig. 7 shows the FT-IR spectra of SBA-15 and the various catalysts. The SBA-15 spectrum consists of absorption bands at 1087, 807 and 464 cm<sup>-1</sup>, which arise from the Si–O–Si stretching vibration. The absorption band at around 960 cm<sup>-1</sup> can be assigned to either Si–OH or Si–O–Si stretching vibrations. The broad band at around 3400 cm<sup>-1</sup> is due to the presence of surface –OH groups with strong H-bonding interactions between them. Finally the band at around 1630 cm<sup>-1</sup> can be assigned to the deformation modes of –OH bonds of adsorbed H<sub>2</sub>O [53]. SCo-5-A exhibits a very similar spectrum to SBA-15 due to its low cobalt content, whereas SCo-5-I and SCo-5 exhibits two additional bands at 660 and 570 cm<sup>-1</sup> (black arrows). These latter bands can be ascribed to Co–O vibrations in the cobalt oxide lattice [10,53,54]. The Co–O bands for SCo-5-I are slightly more intense than for SCo-5. As the cobalt content is the same for both catalysts, we attribute this to the presence of larger particles on the external surface of the pores for SCo-5-I. SCo-10 and SCo-30 also exhibit the same absorbance bands, with progressively increasing intensity [54].

### 3.1.4. X-ray photoelectron spectroscopy (XPS)

Fig. 8 shows XPS spectra from SCo-10. The spectrum exhibits an intense doublet, due to the two spin–orbit components Co 2p<sub>3/2</sub> (780.5 eV) and Co 2p<sub>1/2</sub> (795.5 eV). It is known that spin–orbit splitting ( $\Delta E$ ) between the 2p level peaks can be used to distinguish the

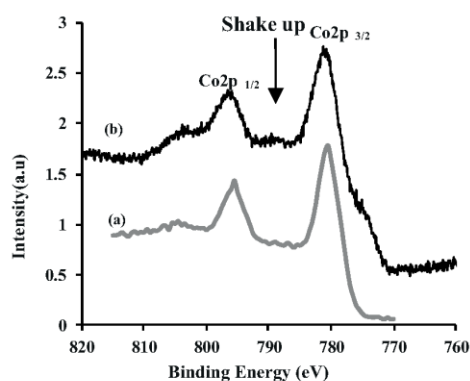


**Fig. 8.** XPS Co 2p spectra obtained from (a) Commercial Co<sub>3</sub>O<sub>4</sub> (b) SCo-10.

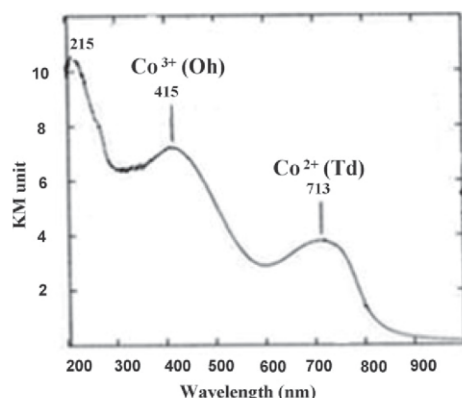


Fig. 9. DR UV-vis spectrum of SCo-5.

oxidation state of the catalyst. It is reported that spin-orbit splitting for  $\text{Co}_3\text{O}_4$  is 15 eV, while it is 16 eV for  $\text{CoO}$  [55]. Here, the spin-orbit splitting of 14.8 eV is consistent with  $\text{Co}_3\text{O}_4$ . Similar results were obtained for SCo-5-I, SCo-5 and SCo-30. There is always a shallow feature, known as the shake-up satellite [56], which is about 9 eV higher than the  $2p_{3/2}$  peak. Since the shake-up satellite is associated with  $\text{Co}^{2+}$ , it is stronger for  $\text{CoO}$  as compared to  $\text{Co}_3\text{O}_4$ , with  $\text{Co}^{3+}/\text{Co}^{2+}$  ratio of 2:1 [21,54,57–62]. Hence, the intensity of the satellite peak is consistent with  $\text{Co}_3\text{O}_4$  as the phase assignment, in agreement with the XRD results.

### 3.1.5. Diffuse reflectance UV-vis spectroscopy (DR UV-vis)

SCo-5 was investigated by UV-vis spectroscopy in order to investigate the environment of cobalt ions. Fig. 9 exhibits three distinct absorption bands for SCo-5. The broad band at around 215 nm can be assigned to the charge transfer from  $\text{O}^{2-}$  to  $\text{Co}^{3+}$  [63]. The absorption band at around 415 nm can be attributed to octahedrally coordinated  $\text{Co}^{3+}$  in the well-ordered spinel  $\text{Co}_3\text{O}_4$  species [14,64]. The broad band at around 715 nm is ascribed to the electronic ligand-field  ${}^4A_2(F) \rightarrow {}^4T_1(P)$  transition of  $\text{Co}^{2+}$  in tetrahedral coordination [14,65,66]. Hence, the DR UV-vis result is consistent with  $\text{Co}_3\text{O}_4$  as the phase assignment (determined for the SCo-5 case only).

### 3.1.6. Temperature programmed reduction (TPR)

It is known that bulk  $\text{Co}_3\text{O}_4$  is completely reduced at around  $400^\circ\text{C}$  [19]. The TPR profile of  $\text{Co}_3\text{O}_4$  supported on mesoporous silica typically shows three peaks. The first peak at lower temperature is due to the reduction of  $\text{Co}^{3+}$  to  $\text{Co}^{2+}$  and the second peak at higher temperature is ascribed to the reduction of  $\text{Co}^{2+}$  to  $\text{Co}^0$  [22,24,67]. The presence of a third peak above  $600^\circ\text{C}$  is typically attributed to the reduction of cobalt species with strong-metal-support-interactions (SMSI) [67,68].

Fig. 10 shows the TPR profile of commercial  $\text{Co}_3\text{O}_4$  nanopowder (reference material), which comprises of a main reduction peak, centered at  $305^\circ\text{C}$  but with a shoulder at lower temperature ( $220^\circ\text{C}$ ). This can be attributed to the two-step reduction of  $\text{Co}^{3+}$  to  $\text{Co}^{2+}$  and then  $\text{Co}^{2+}$  to  $\text{Co}^0$ , as described above.

Fig. 11 shows the TPR profile of the catalysts prepared in this study. The TPR profiles of SCo-5 and SCo-5-I are similar with the first ( $T_1$ ) and the second ( $T_2$ ) reduction peaks apparently merged into one peak due to the low cobalt content. The main reduction peak ( $T_1$ ) centered at  $280^\circ\text{C}$  for both catalysts. However the reduction starts at lower temperature for SCo-5-I ( $140^\circ\text{C}$ ) compared to SCo-5 ( $155^\circ\text{C}$ ). This is attributed to the difference in synthesis method, since it is generally accepted that impregnation (incipient wetness)

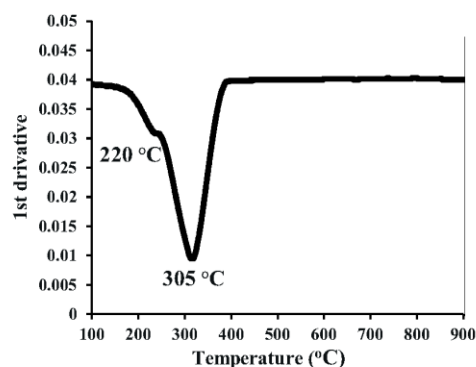


Fig. 10. TPR profile of commercial  $\text{Co}_3\text{O}_4$  nanopowder.

results in the formation of large aggregated particles that are more easily reduced at lower temperature [67,69]. Also for SCo-5, the presence of the rod-like particles inside the pores (see Section 3.1.7) might partially hinder hydrogen diffusion throughout the metal oxide phase so that the reduction process starts at higher temperature. The second peak, which is attributed to the reduction of  $\text{Co}^{2+}$  to  $\text{Co}^0$  seems relatively more resolvable for SCo-5-I compared to SCo-5. The TPR profile of SCo-5-A (not shown in here) is quite similar to that of SCo-5 however due to the low cobalt content the reduction peaks were of low intensity.

Fig. 11 c and d shows the TPR profiles for SCo-10 and SCo-30. The first reduction steps ( $T_1$ ) are at approx  $280^\circ\text{C}$  and  $260^\circ\text{C}$  respectively. The second step ( $T_2$ ) for SCo-10 and SCo-30 are at around  $390^\circ\text{C}$  and  $450^\circ\text{C}$ , respectively. The third step ( $T_3$ ), occurs above  $520^\circ\text{C}$  [67,70].

With increasing cobalt content, there is more agglomeration into larger particles, for which more facile reduction is usually expected [71]. The reduction in the  $T_1$  peak temperature for SCo-30 is consistent with the expectation [19,69]. However, the  $T_2$  reduction step occurs at higher temperature for SCo-30 compared to SCo-10. This is attributed to more extensive filling of the SBA-15 pores by the cobalt oxide in SCo-30 relative to SCo-10 (see Section 3.1.7), which would make it more difficult for the water produced by reduction to escape from the pores. This is expected to increase the residence time of the water in the pores and result in an overall inhibition of the reduction process [31].

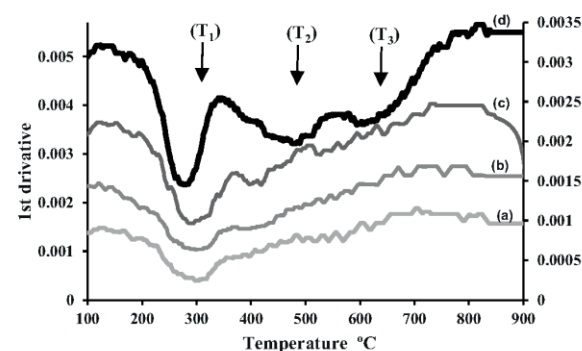


Fig. 11. TPR profile of the (a) SCo-5, (b) SCo-5-I, (c) SCo-10 and (d) SCo-30. SCo-5-Imp, (c) SCo-10 and (d) SCo-30.

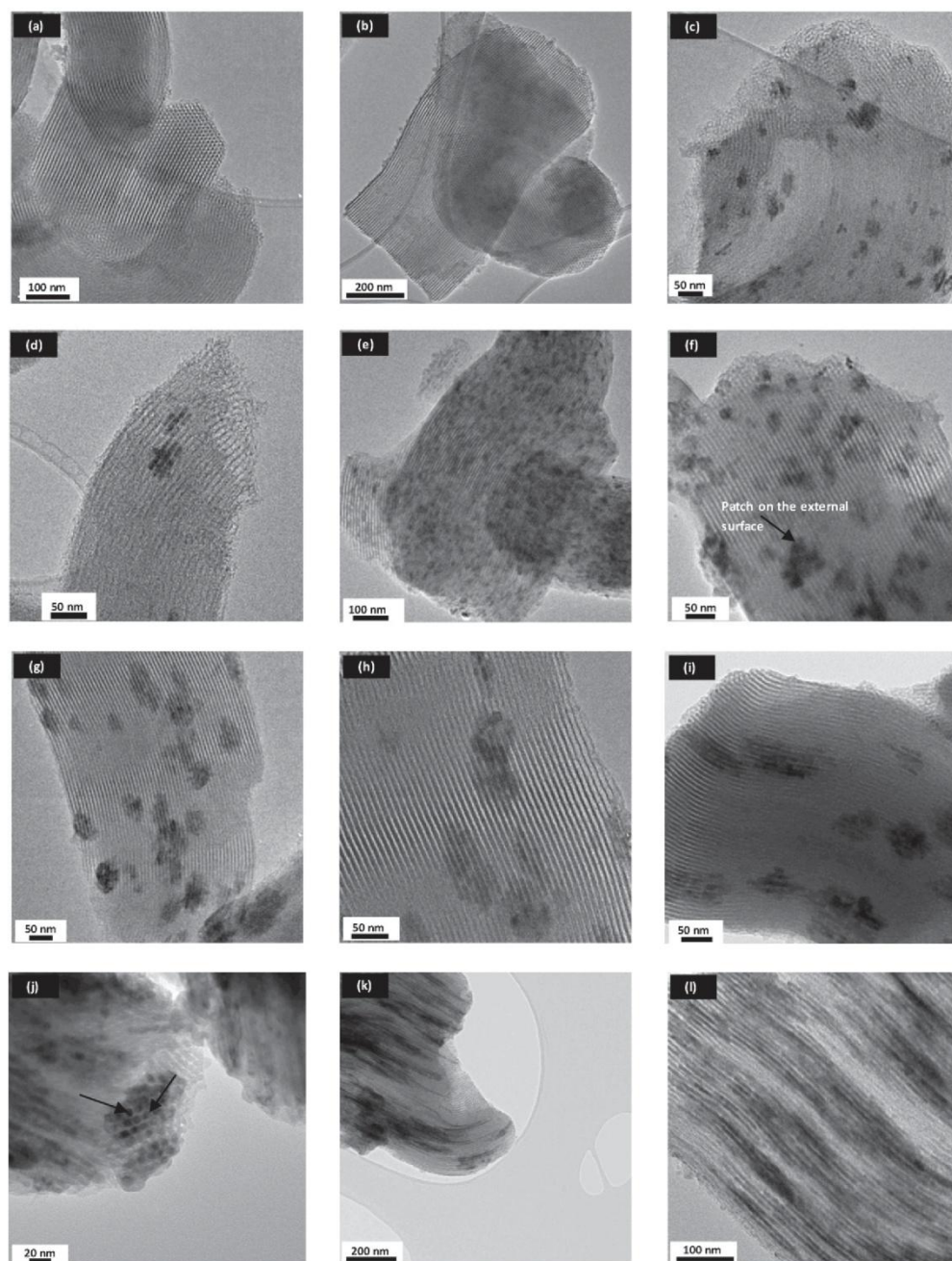


Fig. 12. TEM images obtained from (a, b) SBA-15, (c, d) SCo-5-A, (e, f) SCo-5-I, (g, h) SCo-5, (i, j) SCo-10 and (k, l) SCo-30.

### 3.1.7. Transmission electron microscopy (TEM)

Fig. 12 provides TEM images of the various supported cobalt oxide catalysts. Good contrast is apparent in all cases and clearly demonstrates the preservation of the channels in the mesoporous silica host after cobalt loading. This is in agreement with the results obtained from low angle XRD. Due to differences in electronic density, the areas of darker contrast can be assigned to cobalt oxide whilst the areas of lighter contrast are due to the silica support.

In all cases, 'patches' of cobalt oxide can be seen to be dispersed throughout the support; however the patches have different morphologies, depending on both the method of synthesis and the cobalt content. Interestingly, in all cases the patches are of larger diameter than the SBA-15 channels. This can be attributed to the fact that in SBA-15 mesopores are interconnected through micropores, which facilitate extended crystallite growth; a phenomena that has been observed previously for cobalt oxide [72,73].

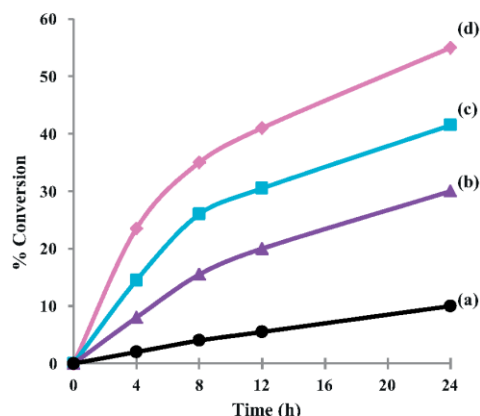


Fig. 13. Cyclohexanol oxidation (a) SBA-15, (b) SCo-5-I, (c) SCo-5 and (d) SCo-5-A.

Empty mesopores are visible as well as cobalt oxide patches grown in adjacent mesopores. Considering the density of  $\text{Co}_3\text{O}_4$ , 22 mmol  $\text{Co}_3\text{O}_4$  would be required to completely fill the porous volume ( $0.86 \text{ cm}^3$ ) in 1 g of this SBA-15. When the channels are parallel to the electron beam, the highly ordered honeycomb-like structure [50,74] remains clearly visible with cobalt oxide particles apparently filling the channels (Fig. 12j), as shown by black arrows; whereas, when the channels are perpendicular to the electron beam, the highly ordered channels are clearly evident (Fig. 12b).

As can be seen, the size of the 'patches' varies between the catalysts. The average width and length of the patches for SCo-5 are 35 nm and 70 nm. Since the cobalt content is lower in SCo-5-A the patches are smaller (25 nm and 45 nm). It can be clearly observed in Fig. 12g and h that rod-like particles are formed within the channels (not on the external surface). This is not surprising since the whole point of the two-solvent method is to encapsulate the catalyst within the mesoporosity of the support [43]. In the case of SCo-5-A a similar behavior is observed, presumably because the cobalt ions have preferentially located themselves on the internal surfaces, where the concentration of silanol groups is a relatively high. This is consistent with the suggestion that, during catalyst preparation, the solution capillary pressure within the mesopores is much higher than that in the cavities between them (macropores) so that the salt deposits on the internal surface rather than the external surface of the mesoporous substrate [75]. The patches appear to be the smallest in the case of SCo-5-I. Also, in this case, there are cobalt oxide patches contained both within the pores and on the external surface of the support, where they obscure the channels underneath (Fig. 12f), as is typically the case for impregnated catalysts [76]. For SCo-10 (Fig. 12i and j) and SCo-30 (Fig. 12k and l) it can be seen that the 'patches' are significantly larger. The average width and length of the patches for SCo-10 are 40–50 nm and 80–100 nm, respectively. Whereas by increasing the cobalt content to 30 wt% the average width and length of the patches increases to 60–80 nm and  $\geq 400$  nm respectively. They generally exhibit a rod-like morphology, which fill the individual channels along their length; yet, at the same time, the 'nanorods' are clustered into 'patches' along adjacent channels. The formation of larger 'patches' is in general agreement with the results from wide-angle XRD and TPR, which suggested the occurrence of larger cobalt oxide particles size in these cases [20,48]. The growth of nanorods within the channels (pore blockage) adversely affects the catalytic activity of the catalysts prepared by the two-solvent method (discussed in Section 3.1.8).

### 3.1.8. Catalytic activity

The supported cobalt oxide catalysts were evaluated for the oxidation of cyclohexanol to cyclohexanone (Figs. 13 and 14) in the presence of TBHP as oxidant.

It can be seen that the SCo-5-A sample exhibited the highest activity of the catalysts examined. This is interesting because this catalyst also had the lowest cobalt loading (Table 1). At the same time this catalyst exhibits the highest internal pore volume (Table 2), just slightly less than that of the SBA-15 support. Thus, it appears that the catalytically active species are very accessible to the substrate and oxidizing reagents.

The SCo-5 sample exhibited the second highest catalytic activity. This sample has slightly further reduced pore volume and also substantially more cobalt (4.5 wt%), compared to SCo-5-A, such that the cobalt oxide in this sample must be less homogeneously dispersed. The increased cobalt oxide patch size for SCo-5 relative to SCo-5-A (Section 3.1.7) is consistent with this interpretation.

The SCo-5-I sample exhibits further reduced catalytic activity, even though the cobalt content is identical to that of SCo-5. The cobalt oxide patches in the TEM images of this sample appear relatively small and more homogeneously dispersed. However, the patches can be observed both inside the channels and on the external surface (Section 3.1.7). Aggregation of cobalt oxide particles, mostly on the external surface results in pore blockage, such that the pore volume of this catalyst is significantly lower compared to those of SCo-5 and SCo-5-A. Indications are that much of the cobalt is not accessible to the reagents. There is also evidence from XRD that the cobalt oxide particles (more specifically those aggregated on the external surface) on average are larger in SCo-5-I relative to SCo-5-A and SCo-5. This is because crystalline  $\text{Co}_3\text{O}_4$  is evident for SCo-5-I, whereas for SCo-5 the intensity of the peaks are lower, indicating particles with smaller size. However, SCo-5-A shows no peaks due to a crystalline cobalt oxide phase, since the cobalt content is very low for this catalyst. Furthermore, more intense Co–O absorbance bands in the FTIR spectrum of SCo-5-I relative to SCo-5 and SCo-5-A, is also evidence for the existence of more cobalt oxide on the external surface of this particular catalyst.

To check the effect of cobalt oxide on catalytic activity, the same reaction was carried out with SBA-15 and also in absence of any solid substrate. In both cases the conversion was negligible after 24 h. These results highlight the catalytic role played by  $\text{Co}^{2+}/\text{Co}^{3+}$  in this reaction and the importance of the redox cycle they facilitate [77].

Within the series of catalysts prepared by the two-solvent method it can be seen that the order of activity decreases as the cobalt content increases, i.e., SCo-5 > SCo-10 > SCo-30. In spite of

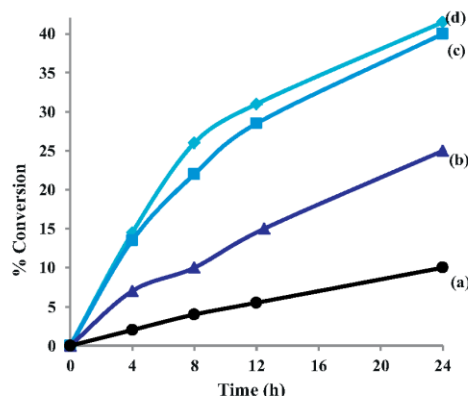


Fig. 14. Cyclohexanol oxidation (a) SBA-15, (b) SCo-30, (c) SCo-10 and (d) SCo-5.

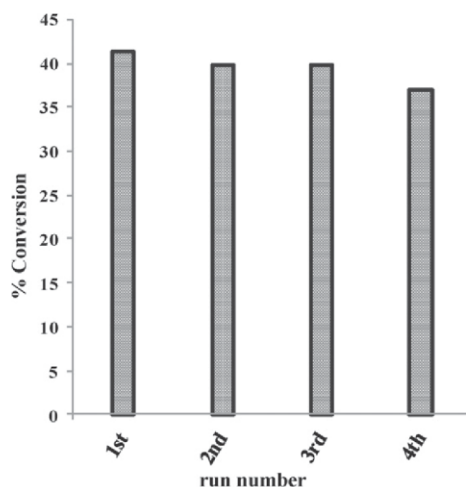


Fig. 15. Reusability of SCo-5 for cyclohexanol oxidation.

the difference in metal content, the activity difference between the SCo-5 and SCo-10 is only slight, whereas SCo-30 is significantly less active. The reducing catalytic activity correlates with the progressive reduction in accessible pore volume (from 0.78 to 0.68 and 0.46 cm<sup>3</sup> g<sup>-1</sup>). In the higher cobalt loading cases, the pore volume is reduced because it is now occupied by large cobalt oxide patches which mostly appear in the form of rods that totally fill the mesopores channels (see Section 3.1.7). Hence, most of the cobalt oxide cannot be accessed by the reagents. The catalytically active cobalt oxide can only be that portion, which is near the pore apertures of the SBA-15. It is interesting to note that the TPR plot (Fig. 11d) for the poorly active SCo-30 catalyst shows that a very high proportion of the cobalt oxide does not reduce below 500 °C. Usually this is interpreted as being due to SMSIs. However, here it is suggested to be due to the circumstance that much of the cobalt oxide species are located deep within the blocked mesopores and/or micropores where it is likely to be very difficult to reduce because of the poor accessibility and consequent limitations of hydrogen diffusion (in) and water diffusion (out).

A similar phenomenon has previously been reported for supported (SBA-15 and silica) cobalt oxide catalysts used for methane combustion in the gas phase; and the poor activity of highly loaded catalysts was likewise attributed to poor cobalt oxide accessibility [16,20].

It can be seen that SCo-5-I (Fig. 13b) exhibited nearly identical catalytic reactivity as SCo-30 (Fig. 14b). This implies there is a nearly identical abundance of accessible catalytically active sites. As previously discussed, channels within the SCo-5-I catalyst seem to be blocked by aggregations of cobalt oxide near the apertures of the pores. However for SCo-30 much of the cobalt oxide is inaccessible because of the rod-like morphology of the cobalt oxide, which completely fills the pores.

Since it was the catalyst with the lowest Co content of only 1% (SCo-5-A) that exhibited the highest activity, it would be interesting to know the activity of catalysts prepared by the two-solvent and impregnation methods that have only this lower level of Co. It is planned to investigate this aspect in future work.

The recyclability of the SCo-5 catalyst was also evaluated. Fig. 15 summarizes the results obtained after the catalyst was used, recovered by filtration, washed several times with acetonitrile, and subsequently dried at 100 °C then reused. The catalyst was used up to four times without significant change in its catalytic activity.

#### 4. Conclusion

Supported cobalt oxides with various cobalt contents were successfully synthesized using the “two-solvent” method. These composites were compared with analogs, synthesized by the more conventional methods of impregnation and adsorption. The mesoporosity of the support maintained intact even after loading nominally 30 wt% cobalt, regardless of preparation method. The presence of cobalt oxide (Co<sub>3</sub>O<sub>4</sub>) in the form of spinel was demonstrated by XRD and XPS. TEM investigations showed that the various methods of preparation resulted in catalysts with different morphologies and dispersion of the cobalt oxide. It also showed that both the adsorption and the two-solvent method resulted in heterogeneous dispersion of cobalt oxide patches within the pores of SBA-15. These patches are made of rod-like particles, which are interconnected through micropores. Impregnation resulted in the formation of patches both inside the channels and on the external surface of the support. The patches, from impregnation were smaller than the patches observed for SCo-5 and SCo-5-A; however they were more homogeneously dispersed on the support. Furthermore, the size of the patches increased as the cobalt content increased. TPR indicated that the location of the particles affected their reducibility such that the particles located deep within the blocked mesopores and/or micropores are hard to reduce.

The two-solvent method was effective for preparing catalysts, where the cobalt oxide was accommodated inside the pores. However, with increasing cobalt content most of this cobalt oxide was ineffective for catalysis, because of its inaccessibility to the reagents. It was found that the SCo-5 catalyst could be simply treated and reused up to three times without significant change in its catalytic activity.

The catalyst prepared by impregnation (SCo-5-I) was also relatively ineffective for catalysis, at least largely because of pore blockage at the aperture of the channels.

The catalyst prepared by the adsorption method (SCo-5-A) exhibited the highest catalytic activity for cyclohexanol oxidation in the presence of TBHP. This material has the highest pore volume and surface area, indicating a lack of pore blockage and also has Co patches of the smallest size, suggesting that a higher percentage of the Co present is accessible and available to facilitate catalysis.

#### Acknowledgments

The authors thank Tim Williams, and Ms Ellen Lavoie (Monash Centre for Electron Microscopy) for assistance in developing microscopy procedures, Bruce Cowie and Anton Tadich (Australian Synchrotron) for help in processing XPS spectra, Mr Rod Mackie (School of Physics, Monash University) for acquisition of XRD data, Massimo Raveggi (School of Geosciences, Monash University) for elemental analysis (ICP-MS), Mr Victor DeGuzman (School of Chemistry, Monash University) for help with the establishment of GC methods and Andrew Scully and Anton Launikonis (CSIRO, Clayton) for provision of DRIFT-UV spectra. Financial support from the Australia Research Council Discovery program and scholarship support from the Monash Research Graduate School and the Faculty of Science, Monash University (to JT) is gratefully acknowledged.

#### References

- [1] R.A. Sheldon, J. Dakka, *Catal. Today* 19 (1994) 215–245.
- [2] A.K. Suresh, M.M. Sharma, T. Sridhar, *Ind. Eng. Chem. Res.* 39 (2000) 3958–3997.
- [3] S. Martínez-Méndez, Y. Henríquez, O. Domínguez, L. D’Ornelas, H. Krentzien, *J. Mol. Catal. A: Chem.* 252 (2006) 226–234.
- [4] A. Castellan, J.C.J. Bart, S. Cavallaro, *Catal. Today* 9 (1991) 285–299.
- [5] G.B. Shulpin, M.G. Matthes, V.B. Romakh, M.I.F. Barbosa, J.L.T. Aoyagi, D. Mandelli, *Tetrahedron* 64 (2008) 2143–2152.
- [6] M. Jhansi, L. Kishore, K.A. Anand, A. Kumar, *Catal. Commun.* 10 (2008) 285–290.
- [7] S.K. Jana, Y. Kubota, T. Tatsumi, *J. Catal.* 255 (2008) 40–47.

- [8] I. Manninger, Z. Paál, P. Tétényi, *J. Catal.* **48** (1977) 442–444.
- [9] T. Szilágyi, A. Sárkány, J. Mink, P. Tétényi, *J. Catal.* **66** (1980) 191–199.
- [10] L. Zhou, J. Xu, H. Miao, F. Wang, X. Li, *Appl. Catal. A: Gen.* **292** (2005) 223–228.
- [11] Q. Tang, Q. Zhang, H. Wu, Y. Wang, *J. Catal.* **230** (2005) 384–397.
- [12] T. Garcia, S. Agouram, J.F. Sánchez-Royo, R. Murillo, A.M. Mastral, A. Aranda, I. Vázquez, A. Dejoz, B. Solsona, *Appl. Catal. A: Gen.* **386** (2010) 16–27.
- [13] Y. Xia, H. Dai, H. Jiang, L. Zhang, *Catal. Commun.* **11** (2010) 1171–1175.
- [14] Á. Szegedi, M. Popova, C. Minchev, *J. Mater. Sci.* **44** (2009) 6710–6716.
- [15] G. Laugel, J. Arichi, M. Molière, A. Kiennemann, F. Garin, B. Louis, *Catal. Today* **138** (2008) 38–42.
- [16] G. Laugel, J. Arichi, P. Bernhardt, M. Molière, A. Kiennemann, F. Garin, B. Louis, *CR. Chim.* **12** (2009) 731–739.
- [17] G. Laugel, J. Arichi, H. Guerber, M. Molière, A. Kiennemann, F. Garin, B. Louis, *Catal. Lett.* **125** (2008) 14–21.
- [18] I. Yuranov, L. Kiwi-Minsker, A. Renken, *Appl. Catal. B: Environ.* **43** (2003) 217–227.
- [19] T. Tsoncheva, L. Ivanova, J. Rosenholm, M. Linden, *Appl. Catal. B: Environ.* **89** (2009) 365–374.
- [20] I. Lopes, A. Davidson, C. Thomas, *Catal. Commun.* **8** (2007) 2105–2109.
- [21] H. Xiong, Y. Zhang, K. Liew, J. Li, *Fuel Process. Technol.* **90** (2009) 237–246.
- [22] A. Martínez, C. López, F. Márquez, I. Diaz, *J. Catal.* **220** (2003) 486–499.
- [23] T. Vrålstad, G. Øye, M. Rønning, W.R. Glomm, M. Stöcker, J. Sjöblom, *Micropor. Mesopor. Mater.* **80** (2005) 291–300.
- [24] S. Bessell, *Appl. Catal. A: Gen.* **96** (1993) 253–268.
- [25] A.Y. Khodakov, R. Bechara, A. Griboval-Constant, *Appl. Catal. A: Gen.* **254** (2003) 273–288.
- [26] E. v. Steen, G.S. Sewell, R.A. Makhothe, C. Micklethwaite, H. Manstein, M. de Lange, C.T. O'Connor, *J. Catal.* **162** (1996) 220–229.
- [27] L. Jiao, J.R. Regalbuto, *J. Catal.* **260** (2008) 342–350.
- [28] C. Wang, S. Lim, G. Du, C.Z. Loebicki, N. Li, S. Derrouiche, G.L. Haller, *J. Phys. Chem. C* **113** (2009) 14863–14871.
- [29] R.C. Reuel, C.H. Bartholomew, *J. Catal.* **85** (1984) 63–77.
- [30] J. Panpranot, J.G. Goodwin, A. Sayari, *Catal. Today* **77** (2002) 269–284.
- [31] D. Yin, W. Li, W. Yang, H. Xiang, Y. Sun, B. Zhong, S. Peng, *Micropor. Mesopor. Mater.* **47** (2001) 15–24.
- [32] Y. Ohtsuka, Y. Takahashi, M. Noguchi, T. Arai, S. Takasaki, N. Tsubouchi, Y. Wang, *Catal. Today* **89** (2004) 419–429.
- [33] D. Yuming, et al., *Nanotechnology* **18** (2007) 435602.
- [34] T.E. Davies, T. García, B. Solsona, S.H. Taylor, *Chem. Commun.* (2006) 3417.
- [35] B. Solsona, I. Vázquez, T. Garcia, T. Davies, S. Taylor, *Catal. Lett.* **116** (2007) 116–121.
- [36] D. Zhao, Q. Huo, J. Feng, B.F. Chmelka, G.D. Stucky, *J. Am. Chem. Soc.* **120** (1998) 6024–6036.
- [37] J. Jarupatrakorn, T.D. Tilley, *J. Am. Chem. Soc.* **124** (2002) 8380–8388.
- [38] B. Nohair, C. Espécel, G. Lafaye, P. Marécot, L.C. Hoang, J. Barbier, *J. Mol. Catal. A: Chem.* **229** (2005) 117–126.
- [39] K. Bourikas, J. Vakkos, C. Fountzoula, C. Kordulis, A. Lycourghiotis, *Catal. Today* **128** (2007) 138–144.
- [40] M. Imperor-Clerc, D. Bazin, M.D. Appay, P. Beauvier, A. Davidson, *Chem. Mater.* **16** (2004) 1813–1821.
- [41] L. Jiao, J.R. Regalbuto, *J. Catal.* **260** (2008) 329–341.
- [42] M. Gu, B. Yue, R. Bao, H. He, *Mater. Res. Bull.* **44** (2009) 1422–1427.
- [43] J. van der Meer, I. Bardez-Giboire, C. Mercier, B. Revel, A. Davidson, R. Denoyel, *J. Phys. Chem. C* **114** (2010) 3507–3515.
- [44] D. Zhao, J. Feng, Q. Huo, N. Melosh, G.H. Fredrickson, B.F. Chmelka, G.D. Stucky, *Science* **279** (1998) 548.
- [45] J. Wang, Q. Liu, *Micropor. Mesopor. Mater.* **83** (2005) 225–232.
- [46] Y. Ding, Y. Wang, B. Li, Y. Lei, *Biosens. Bioelectron.* **25** (2010) 2009–2015.
- [47] O. González, H. Pérez, P. Navarro, L.C. Almeida, J.G. Pacheco, M. Montes, *Catal. Today* **148** (2009) 140–147.
- [48] I. Lopes, N. El Hassan, H. Guerber, G. Wallez, A. Davidson, *Chem. Mater.* **18** (2006) 5826–5828.
- [49] K.S.W. Sing, D.H. Everett, R.A.W. Haul, L. Mosenu, R.A. Pierotti, *Pure Appl. Chem.* **57** (1985) 603.
- [50] C. Yang, Z. Wang, X. Zhou, X. Tian, Z. Pi, Y. Wang, *J. Porous Mater.* **18** (2011) 31–35.
- [51] P. Van Der Voort, P.J. Ravikovitch, K.P. De Jong, A.V. Neimark, A.H. Janssen, M. Benjelloun, E. Van Bavel, P. Cool, B.M. Weckhuysen, E.F. Vansant, *Chem. Commun.* (2002) 1010–1011.
- [52] J. van der Meer, I. Bardez, F. Bart, P.-A. Albouy, G. Wallez, A. Davidson, *Micropor. Mesopor. Mater.* **118** (2009) 183–188.
- [53] T. Tsoncheva, L. Ivanova, C. Minchev, M. Fröba, *J. Colloid Interface Sci.* **333** (2009) 277–284.
- [54] L. Ji, J. Lin, H.C. Zeng, *J. Phys. Chem. B* **104** (2000) 1783–1790.
- [55] Y. Okamoto, H. Nakano, T. Imanaka, S. Teranishi, *Bull. Chem. Soc. Jpn.* **84** (1975) 1163–1168.
- [56] J. van Elp, J.L. Wieland, H. Eskes, P. Kuiper, G.A. Sawatzky, F.M.F. de Groot, T.S. Turner, *Phys. Rev. B* **44** (1991) 6090.
- [57] W.S. Epling, G.B. Hofflund, J.F. Weaver, S. Tsubota, M. Haruta, *J. Phys. Chem.* **100** (1996) 9929–9934.
- [58] W.T.L. Lim, Z. Zhong, A. Borgna, *Chem. Phys. Lett.* **471** (2009) 122–127.
- [59] W.-H. Yang, M. Kim, *Res. Chem. Intermed.* **34** (2008) 717–725.
- [60] H. Xiong, Y. Zhang, K. Liew, J. Li, *J. Mol. Catal. A: Chem.* **231** (2005) 145–151.
- [61] P. Jiang, T. Cheng, Y. Liu, X. Cui, Y. Bi, K. Zhen, *React. Kinet. Catal. Lett.* **82** (2004) 49–56.
- [62] A.M. Venezia, R. Murania, G. Pantaleo, V. La Parola, S. Scirè, G. Deganello, *Appl. Catal. A: Gen.* **353** (2009) 296–304.
- [63] J. Wang, S. Uma, K.J. Klabunde, *Micropor. Mesopor. Mater.* **75** (2004) 143–147.
- [64] A.P. Katsoulidis, D.E. Petrakis, G.S. Armatas, P.N. Trikalitis, P.J. Pomonis, *Micropor. Mesopor. Mater.* **92** (2006) 71–80.
- [65] J. Yan, M.C. Kung, W.M.H. Sachtler, H.H. Kung, *J. Catal.* **172** (1997) 178–186.
- [66] B. Solsona, T.E. Davies, T. Garcia, I. Vázquez, S.H. Taylor, *Appl. Catal. B: Environ.* **84** (2008) 176–184.
- [67] H. Li, S. Wang, F. Ling, J. Li, *J. Mol. Catal. A: Chem.* **244** (2006) 33–40.
- [68] E.L. Rodrigues, J.M.C. Bueno, *Appl. Catal. A: Gen.* **232** (2002) 147–158.
- [69] C. Minchev, H. Huwe, T. Tsoncheva, M. Dimitrov, D. Paneva, I. Mitov, M. Fröba, in: I.M.C.E. van Steen, L.H. Callanan (Eds.), *Stud. Surf. Sci. Catal.*, 2004, pp. 841–847.
- [70] G. Jacobs, Y. Ji, B.H. Davis, D. Cronauer, A.J. Kropf, C.L. Marshall, *Appl. Catal. A: Gen.* **333** (2007) 177–191.
- [71] J. Li, X. Xu, Z. Hao, W. Zhao, *J. Porous Mater.* **15** (2008) 163–169.
- [72] B. Tian, X. Liu, H. Yang, S. Xie, C. Yu, B. Tu, D. Zhao, *Adv. Mater.* **15** (2003) 1370–1374.
- [73] F. Jiao, H. Frei, *Angew. Chem. Int. Ed.* **48** (2009) 1841–1844.
- [74] M.-Y. Cheng, C.-J. Pan, B.-J. Hwang, *J. Mater. Chem.* **19** (2009) 5193–5200.
- [75] J.R.A. Sietsma, J.D. Meeldijk, M. Versluijs-Helder, A. Broersma, A.J. v. Dillen, P.E. de Jongh, K.P. de Jong, *Chem. Mater.* **20** (2008) 2921–2931.
- [76] Y. Wang, B. Hou, J. Chen, Y. Sun, *React. Kinet. Mech. Catal.* **102** (2011) 155–164.
- [77] A.M. Garrido Pedrosa, M.J.B. Souza, D.M.A. Melo, A.S. Araujo, L.B. Zimmer, J.D.G. Fernandes, A.E. Martinelli, *Solid State. Sci.* **5** (2003) 725–728.

Monash University

**Declaration for Thesis Chapter 3.3**

**Mesoporous silica SBA-15 supported  $\text{Co}_3\text{O}_4$  nanorods as efficient liquid phase oxidative catalyst**

**Declaration by candidate**

In the case of Chapter 3 the nature and extent of my contribution to the work was the following:

Nature of contribution	Extent of contribution (%)
Proposed original idea; prepared and analysed samples; identified major issues; developed interpretations; fully drafted papers and conclusions	80%

The following co-authors contributed to the work. Co-authors who are students at Monash University must also indicate the extent of their contribution in percentage terms:

Name	Nature of contribution	Extent of contribution (%) for student co-authors only
Gregory P. Knowles	Aided method development (catalyst characterisation), input to interpretation of results,	N/A
Alan L. Chaffee	Supervision, assisted interpretations of results, editorial assistance	N/A

Candidate's  
Signature

	Date 23.10.12
--	------------------

Declaration by co-authors



The undersigned hereby certify that:

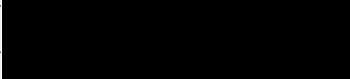
- (1) the above declaration correctly reflects the nature and extent of the candidate's contribution to this work, and the nature of the contribution of each of the co-authors.
- (2) they meet the criteria for authorship in that they have participated in the conception, execution, or interpretation, of at least that part of the publication in their field of expertise;
- (3) they take public responsibility for their part of the publication, except for the responsible author who accepts overall responsibility for the publication;
- (4) there are no other authors of the publication according to these criteria;
- (5) potential conflicts of interest have been disclosed to (a) granting bodies, (b) the editor or publisher of journals or other publications, and (c) the head of the responsible academic unit; and
- (6) the original data are stored at the following location(s) and will be held for at least five years from the date indicated below:

Location(s)

School of Chemistry, Clayton Campus

Gregory P. Knowles

Alan L. Chaffee

	Date 22.10.12
	Date 22.10.12

### 3.3 Mesoporous silica SBA-15 supported $\text{Co}_3\text{O}_4$ nanorods as efficient liquid phase oxidative catalyst

Top Catal (2012) 55:571–579  
DOI 10.1007/s11244-012-9834-y

ORIGINAL PAPER

## Mesoporous Silica SBA-15 Supported $\text{Co}_3\text{O}_4$ Nanorods as Efficient Liquid Phase Oxidative Catalysts

Jamileh Taghavimoghaddam · Gregory P. Knowles · Alan L. Chaffee

Published online: 27 June 2012  
© Springer Science+Business Media, LLC 2012

**Abstract** Mesoporous silica SBA-15 supported cobalt oxide composites prepared via the “double-solvent”, impregnation and adsorption techniques were characterized by diffuse reflectance UV–Vis (DR UV–Vis), scanning electron microscopy (SEM) and transmission electron microscopy (TEM). The potential of these cobalt modified composites to oxidize norbornene, benzyl alcohol and 1-phenylethanol was determined by gas chromatography (GC) and gas chromatography-mass spectrometry (GC-MS). SEM images indicated that, irrespective of cobalt content (Co-content), the integrity of the mesoporous channels remained intact for all methods. DR UV–Vis exhibited a red-shift which increased with Co-content for catalysts prepared by the double-solvent technique and is attributed to more extensive crystal growth. The morphology of the cobalt oxide species had a direct impact on the pore volume (Pv) and surface area (SA) of the composites and this, in turn affected the catalytic activity. For catalysts prepared by the double-solvent technique, the activity was in reverse proportion to the Co-content. This is attributed to reduced Pv which limits the active SA available.

**Keywords** Supported cobalt oxide · Oxidation reaction · Nanorod particles · Mesoporous silica SBA-15 · Double-solvent · Spinel  $\text{Co}_3\text{O}_4$

#### 1 Introduction

The selective oxidation of alcohols and olefins is an atom-efficient molecular transformation yielding epoxides,

aldehydes, ketones and carboxylic acids that are valuable intermediates for the fine chemical, pharmaceutical and agricultural sector industries. These reactions are considered challenging from a ‘green chemistry’ perspective [1], since many commonly used processes require stoichiometric amounts of toxic heavy metal oxidants which, in turn, result in significant amounts of waste products.

The use of heterogeneous catalysts to mediate the reactions is of great importance since the catalysts can, in principal, be separated and reused [2]. Typically, active metals and/or oxides are dispersed on supports with high surface area (SA), such as alumina [3], ceria [4], titania [5] and carbon aerogel [6] to circumvent their low SA. Recently mesoporous silicas such as SBA-15 and MCM-41 have been identified as promising catalyst supports due to their tuneable and uniform pore structure together with high SAs [7–9].

Various methods have been reported for dispersing metal/oxides on mesoporous silica and other high SA supports. Impregnation and ion-exchange are the most conventional methods; impregnation generally results in formation of large, aggregated particles on the external surface of the mesoporous silica [9]. Ion-exchange generally results in the formation of very fine particles inside the pores with relatively low metal loading [10]. Other methods of catalyst dispersion have recently been reported with the aim of controlling the size of the particles inside the pores. Strong electrostatic adsorption [11], results in highly-dispersed, fine particles even at relatively high metal loading. Molecular designed dispersion provides high dispersion of metal oxide nanoparticles on the mesoporous silica SBA-15 [12]. Supercritical fluid decomposition is reported as a promising method to nanocast metal oxides homogeneously on mesoporous silica [13]. The double-solvent technique is another new method, which

J. Taghavimoghaddam · G. P. Knowles · A. L. Chaffee (✉)  
School of Chemistry, Monash University, Clayton, VIC 3800,  
Australia  
e-mail: alan.chaffee@monash.edu

seems to disperse metal oxide nanoparticles exclusively inside the pores of mesoporous silica [14]. This latter method consists of three steps: (i) the desired amount of metal precursor is dissolved in water of volume equal to the pore volume (Pv) of the support determined by N<sub>2</sub> physisorption, (ii) mesoporous silica (SBA-15) is dispersed in an alkane (n-hexane) to form a hydrophobic solution, (iii) the metal aqueous solution is added to the hydrophobic solution dropwise and the mixture stirred for 2 h, then calcined in air after filtration. It is reported that the type of the hydrophobic solvent (alkanes) used in this method affects the dispersion of the metal oxides on the support [15]. This can be attributed to a difference in the interfacial tension between water and various alkanes that can be used, as well as to different adsorption enthalpies for various alkanes on silica.

Supported cobalt oxide catalysts have previously been used for oxidation of water, CO and NO [16–18], propane [19], ethyl acetate [20], ethylbenzene and toluene [21, 22]. The gas phase oxidation of isopropylbenzene [23], styrene epoxidation [24, 25] and methane combustion [26, 27] have also been reported.

It has recently been reported that cobalt oxide supported on SBA-15 can be applied to liquid phase oxidation of cyclohexanol [28]. Mesoporous silica SBA-15 supported cobalt oxide (Co<sub>3</sub>O<sub>4</sub>) composites with various Co-content (nominally 5, 10 and 30 wt%) were prepared via the double-solvent technique. Analogous catalysts with 5 wt% (nominal) loading were also prepared by impregnation (I) and adsorption (A). Here, the same Co-modified composites are evaluated for a wider range of substrates. The nature of the catalysts was also further investigated by DR UV–Vis, SEM, HRTEM and STEM.

## 2 Experimental

### 2.1 Catalyst Preparation

SBA-15 was prepared using a general approach first described by Stucky and co-workers [29]. Co-modified composites (SCO-X, where X represents the nominal Co-loading percentage) were prepared using the double-solvent technique [26] with some modification. For comparison Co-modified composites were prepared by A and I. Co(NO<sub>3</sub>)<sub>2</sub>·6H<sub>2</sub>O was used as the Co precursor in all cases. The detailed preparation methods have been reported elsewhere [28].

### 2.2 Characterization Techniques

N<sub>2</sub> physisorption isotherms were obtained at –196 °C on a Coulter Omnisorb 360-CX gas sorption analyser. Samples

were outgassed at 150 °C overnight prior to analysis. Pore volume, BET surface area [30], and the pore size distribution (BJH method) [29] were calculated for each data set.

Inductively coupled plasma mass spectrometry (ICP-MS) was carried out using a GBC OPTIMAS 9500 ICP-MS. Prior to measurement catalysts were digested with HNO<sub>3</sub> and HF at 120 °C for 2 days to remove silica.

Scanning electron microscopy (SEM) was carried out using a JEOL 7001F field emission gun SEM. Transmission electron microscopy (TEM) and high resolution transmission electron microscopy (HRTEM) was carried out using a JEOL 2011 transmission electron microscopy equipped with a LaB<sub>6</sub> emitter (point resolution 0.21 nm) and an accelerating voltage of 200 kV.

Diffuse reflectance UV–Vis (DR UV–Vis) spectra were obtained at room temperature in air on a Cary 500 Scan UV–Vis–NIR photometer over the range from 200 to 800 nm.

Gas chromatography (GC) was carried out on an Agilent 6850 gas chromatograph equipped with an FID detector and a polar capillary column (BP20, 60 m × 0.25 mm). Gas chromatography-mass spectrometry (GCMS) was carried out using an Agilent 5973 MS equipped (source conditions: EI, 70 eV, 200 °C) using a 6890 series GC system with a capillary column (HP5, 30 m × 0.25 mm).

### 2.3 Catalytic Tests

Liquid phase oxidation of organic substrates was performed in a 100 mL flask. In each test 0.1 g of catalyst was added to 5 mL of acetonitrile (ACN) and 20 mmol of substrate. The oxidant, tert-butylhydroperoxide (TBHP) (24 mmol) was then added dropwise over approximately 10 min. Reactions were carried out under reflux and monitored by GC, withdrawing samples every 4 h up to 12 h, then again after 24 h. There was no attempt to exclude atmospheric oxygen from the reaction.

## 3 Results and Discussion

### 3.1 Morphological and Chemical Characterization

The general morphological features of these catalysts have been previously reported [28]. Low-angle X-ray diffraction (XRD) confirmed the ordered hexagonal lattice of SBA-15 (P6 mm). The d-spacing between the (100) planes and the cell parameter ( $a_0 = 2d_{100} / \sqrt{3}$ ) were calculated to be 10.13 and 11.57 nm, respectively. It was also shown that the porosity and hexagonal structure of the support remained intact after Co-loading and also after calcination for the various Co-loadings and preparative methods. Wide-angle XRD and XPS established the presence of

spinel  $\text{Co}_3\text{O}_4$  (JCPDF file 01-073-1701) as the dominant crystalline Co phase.

### 3.1.1 $\text{N}_2$ Physisorption and ICP-MS

Table 1 details the textural parameters determined by  $\text{N}_2$  physisorption, including BET surface area, pore diameter and  $V_p$ , together with the Co-content determined from ICP-MS. Previously it was shown that, upon loading Co on mesoporous silica SBA-15, some changes were distinguishable in the isotherms. As the Co-content increased: (I) the volume of adsorbed  $\text{N}_2$  decreased, (II) the capillary condensation shifted to lower relative pressure and (III) a shoulder developed on the desorption branch [28].

In addition, the SA, the total  $V_p$  and the micropore volume are observed to decrease with increasing Co-loading, indicating that cobalt oxide species exist within the pores of SBA-15. However, the average pore diameter did not change significantly suggesting that partial pore blockage is occurring. Furthermore, the presence of the shoulder on the desorption branch of both double-solvent and impregnated composites [28] is consistent with this cavitation phenomenon [31, 32].

### 3.1.2 Scanning Electron Microscopy (SEM)

Figure 1 shows SEM images of SBA-15 and selected composites. SBA-15 exhibits a rope-like macrostructure, consisting of rod-like subparticles with approximate length of 1  $\mu\text{m}$  and 250 nm in diameter. These subparticles exhibit various forms (U-shaped, curved and straight), which aggregate from end to end and/or side to side to form a macrostructure [33]. On the smooth surface of the SBA-15 subparticles parallel stripes can be observed, which are attributed to the highly ordered channels. In addition, silica plates/aggregates are formed randomly on the surface of the subparticles (shown by dotted circles). It is thought

that, during SBA-15 preparation, these silica aggregates formed during the hydrolysis and condensation steps, then partially crystallized during the calcination step. Irrespective of Co-content, the macroscopic structure of the SBA-15 as well as the subparticle morphology remained intact after Co-loading onto the SBA-15 (Fig. 1c, d).

### 3.1.3 Transmission Electron Microscopy (TEM)

Figure 2 shows TEM images of SBA-15 and selected Co-modified composites. The images confirm that, in all cases, the integrity of the channels remained intact after cobalt was loaded inside the SBA-15 pores [34]. As discussed previously [28],  $\text{Co}_3\text{O}_4$  filled sections of individual mesopores, forming nanorods, which aggregate along adjacent pores as ‘patches’ [16]. The formation of patches can be attributed to the nanorods being linked to each other via  $\text{Co}_3\text{O}_4$  bridges forming in originally micropores linking the mesopore channels [35].

For the double-solvent technique there is a systematic increase in the width and length of these patches with increasing Co-content. It is also the case that, for lower loadings, a number of the SBA-15 subparticles contain no  $\text{Co}_3\text{O}_4$  species [36]. However as the Co-content increased to 30 wt%, very few ‘empty’ subparticles can be found (Fig. 2e). Figure 2e also shows that the length of these nanorods can exceed 400 nm. The HRTEM of SCo-30 shows the lattice fringes of cubic  $\text{Co}_3\text{O}_4$  (JCPDF file 01-073-1701) with 0.24 nm spacing, which can be assigned to (311) plane (Fig. 2e inset), consistent with the XRD data previously reported [28].

In the case of SCo-5A, the patches are small relative to the other composites and clearly located within the pores. For SCo-5I,  $\text{Co}_3\text{O}_4$  patches occur inside the pores, but also as clusters on the external surface [37] of the support where, in some cases, they appear to block the pore apertures [38].

**Table 1**  $\text{N}_2$  physisorption data obtained from SBA-15 and Co-modified composites

Sample	BET SA ( $\text{m}^2 \text{g}^{-1}$ ) <sup>a</sup>	$D_p$ (nm) <sup>b</sup>	$V_t$ ( $\text{cm}^3 \text{g}^{-1}$ ) <sup>c</sup>	$V_m$ ( $\text{cm}^3 \text{g}^{-1}$ ) <sup>d</sup>	Co (wt%) <sup>e</sup>
SBA-15	656	6.0	0.86	0.26	–
SCo-5A	620	5.8	0.81	0.24	1
SCo-5I	481	5.6	0.70	0.18	4.5
SCo-5	603	5.7	0.78	0.24	4.5
SCo-10	510	5.7	0.68	0.20	8
SCo-30	347	5.7	0.46	0.13	23

<sup>a</sup> Surface area

<sup>b</sup> Pore diameter

<sup>c</sup> Total pore volume ( $p/p_0 = 0.9$ )

<sup>d</sup> Micropore volume ( $p/p_0 < 0.1$ )

<sup>e</sup> Actual Co-content

**Fig. 1** SEM images of **a**, **b** SBA-15, **c** SCo-5 and **d** SCo-30

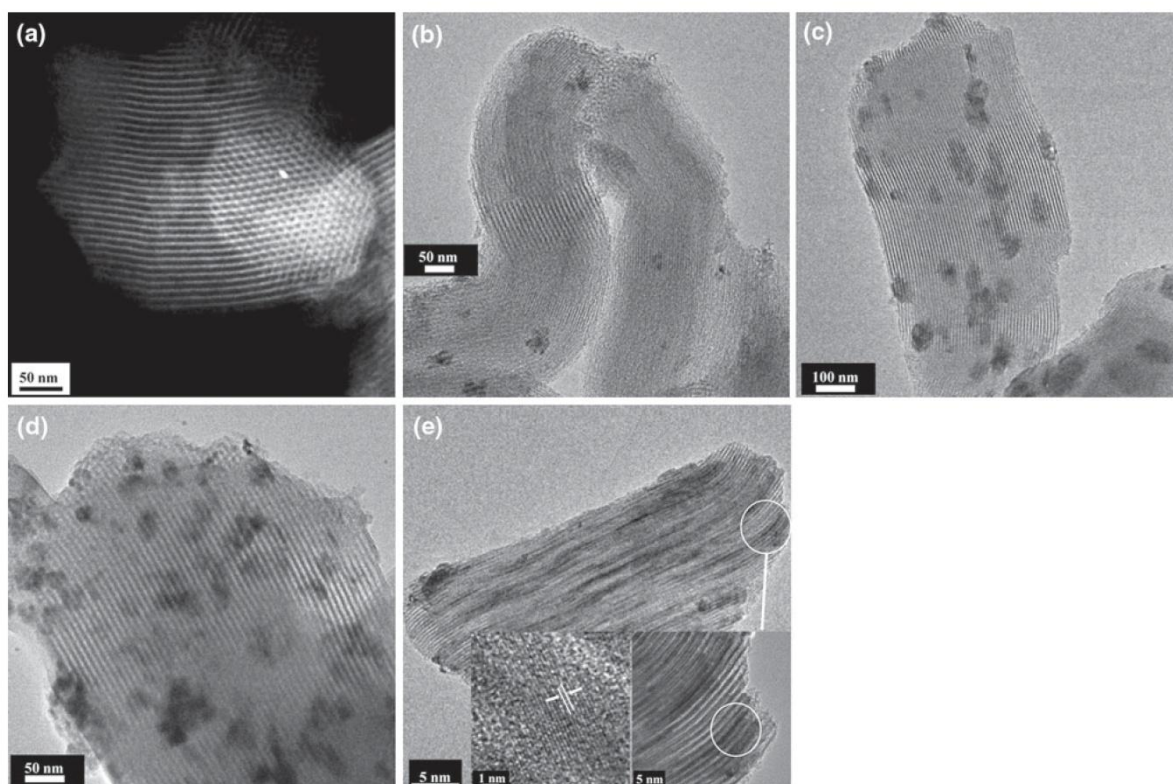
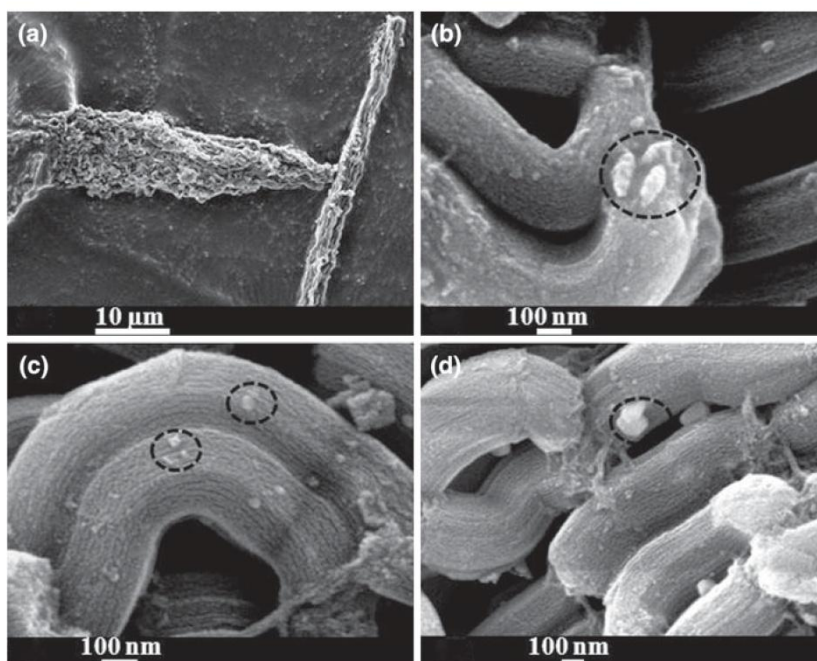


**Fig. 2** STEM image of **a** SBA-15 and TEM images **b** SCo-5A, **c** SCo-5, **d** SCo-5I and **e** SCo-30

When the morphology of supported catalysts is compared, their ‘dispersion’ is usually considered. The dispersion of a catalyst is that fraction of the active component, in this case  $\text{Co}_3\text{O}_4$ , that is located at the particle surface and available for reaction. Thus smaller catalyst particles have higher dispersion. In the present case, the active component occurs as patches that (in most cases) fill the pores of the support. The bulk of the  $\text{Co}_3\text{O}_4$  is bounded by the silica walls rather than occurring as discrete particles located on its surface. As such, the conventional notion of dispersion seems inappropriate for these materials. However, it is noted that the size of the  $\text{Co}_3\text{O}_4$  patches clearly increases through the series in the order  $\text{SCo-5A} < \text{SCo-5} < \text{SCo5-I} < \text{SCo-30}$  following a sequence that is analogous to reducing dispersion [28]. It is reasonable to anticipate that such differences in the extent of pore-filling and ‘dispersion-like’ character of the patches between the catalysts will influence their relative activity (see Sect. 3.1.5).

### 3.1.4 Diffuse Reflectance Ultra Violet–Visible (DR UV–Vis) Spectroscopy

Figure 3 exhibits DR UV–Vis spectra of all the Co-modified composites. Two broad absorption bands are observed, which are known to be characteristic for  $\text{Co}_3\text{O}_4$  [8]. The first band at around 550–590 nm can be attributed to octahedrally coordinated  $\text{Co}^{3+}$  and the second peak at around 715 nm is ascribed to the electronic ligand-field  ${}^4\text{A}_2(\text{F}) \rightarrow {}^4\text{T}_1(\text{P})$  transition of  $\text{Co}^{2+}$  in tetrahedral coordination [39]. As can be seen, with increasing Co-content the center of the first absorption band shows a progressive red-shift from 456 to 480 to 490 nm for SCo-5, SCo-10 and SCo-30 respectively. These adsorption peaks are also red-

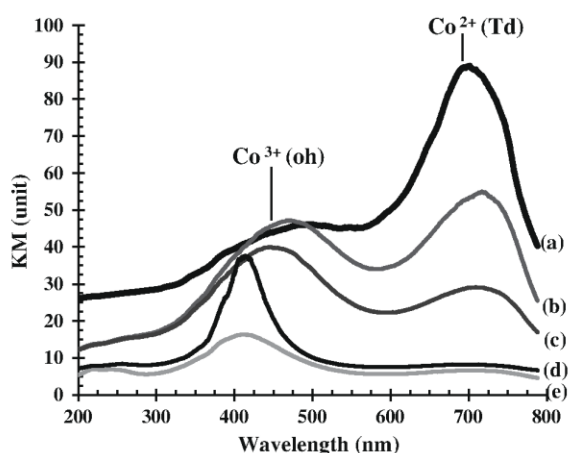


**Fig. 3** DR UV–Vis spectra of *a* SCo-30, *b* SCo-10, *c* SCo-5, *d* SCo-5I and *e* SCo-5A

shifted by 40–80 nm compared with the position reported by Esposito et al. [39] for  $\text{Co}_3\text{O}_4$  supported on amorphous silica. This significant red-shift can be mainly attributed to the increasing size of the nanocrystals [40] in proportion with the Co-content.

Furthermore, Bourikas et al. [41] found that the intensity of the second absorption band, centered at around 700 nm, was proportional to the crystallite size of  $\text{Co}_3\text{O}_4$  supported on alumina. This is in good agreement with the results obtained here. Since the second absorption band is attributed to  $\text{Co}^{2+}$  in tetrahedral coordination, it is suggested that there is also the possibility that the concentration of  $\text{Co}^{2+}$  species increases through the double-solvent series of composites. This would be due to more extensive interaction of the Co with the silica support, for example as cobalt silicate.

The red-shift in SCo-5A and SCo-5I (425 nm) is less than that in SCo-5, indicating that the particle size in these two composites is smaller than that of SCo-5. Furthermore, the intensity of the second absorption band in both composites is much lower than those prepared by double-solvent technique, which is evidence of less  $\text{Co}^{2+}$  interaction with the support.

### 3.1.5 Catalytic Properties

The catalytic activity of Co-modified composites was evaluated for the oxidation of 1-phenylethanol, cyclohexanol, benzyl alcohol and norbornene in the presence of TBHP as an oxidant (Fig. 4). Figure 5 plots the conversions versus time of the Co-modified composites for the oxidation of cyclohexanol to cyclohexanone and norbornene to norbornene oxide. As can be seen, SCo-5A showed the highest catalytic activity. It is noteworthy that this catalyst has the lowest Co-content; however it also records the highest SA, micropore and total Pvs (Table 1), which suggests there is less pore blockage and, in turn, a greater availability of active sites for catalytic reactions to occur.

Interestingly, the catalytic activity of the composites prepared by the double-solvent technique was observed to decrease in reverse proportion to the Co-content for both reactions. This can be attributed to the systematic increase in the degree of pore blockage upon increasing the Co-content. Thus it is the poor availability of the active sites due to the efficient isolation of the cobalt oxide within the

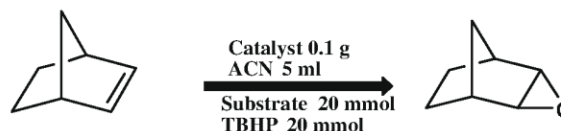


**Fig. 4** Reaction scheme for norbornene oxidation

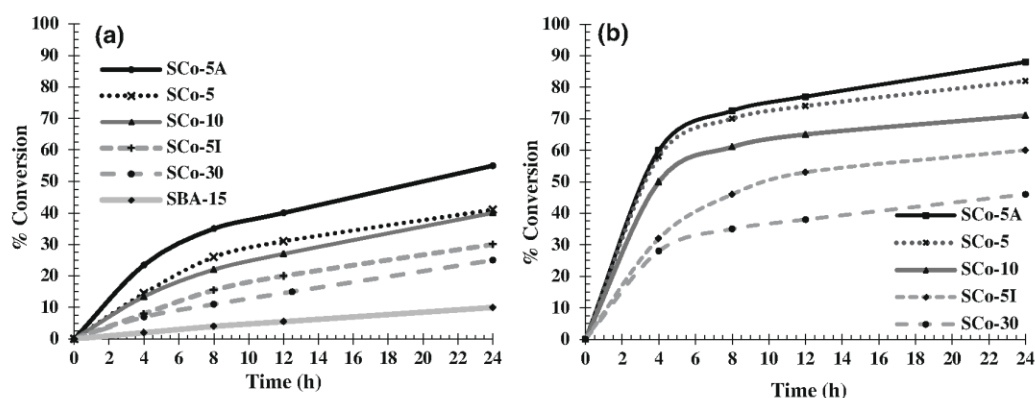


**Fig. 5** Conversion percentage of **a** cyclohexanol and **b** norbornene

micro/mesopores of the SBA-15 which results in the low activity of the more highly loaded catalysts. A similar phenomenon was previously reported for SBA-15 and SiO<sub>2</sub> supported cobalt oxide catalysts used for methane combustion in the gas phase where the poor activity of the highly loaded catalysts was likewise attributed to poor accessibility of the cobalt oxide species [17, 26].

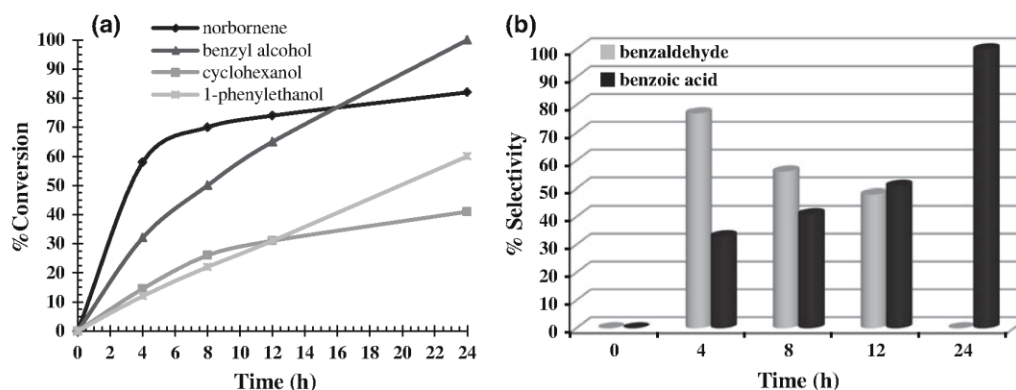
For the composite prepared by impregnation, SCo-5I, the catalytic activity is slightly higher than SCo-30 for both reactions. This composite showed the second lowest SA and micropore volume. This can be assigned to the presence of external clusters which aggregate on the aperture of the pores, blocking them such that the reactants could not penetrate and interact with the cobalt oxide within the pores.

As already discussed the concept of dispersion seems somewhat inappropriate for catalysts of this type which tend to fill the pores of the mesoporous support. Nevertheless it is the case that the catalyst activity decreases through the series in the order SCo-5A > SCo-5 > SCo-5I > SCo-30. This is the inverse of the order of increasing patch size (see Sect. 3.1.3). So it is the case that the catalysts with smaller patch size (higher dispersion-like character) exhibit higher activity. But, as the catalysts also differ in terms of their absolute Co-loading (Table 1), it is the pore blockage mechanism that seems to be more significant in limiting the number of active sites available for reaction. The dispersion of Co<sub>3</sub>O<sub>4</sub> catalysts can be determined by carbon monoxide chemisorption; however this method was not available for the current study [42].

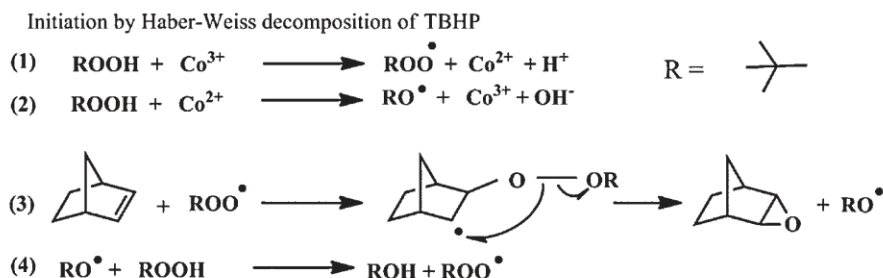
To confirm the catalytic effect of the cobalt oxide species blank experiments were carried out using cyclohexanol as substrate. Neat SBA-15 was used alone (without any Co). Reaction was also carried out in the absence of any solid substrate to check the oxidation activity of TBHP in solution. In both cases the conversion was negligible after 24 h, thus confirming the catalytic role played by the cobalt [43].

Figure 6a illustrates the conversion versus time for a variety of different substrates catalyzed by SCo-5. Norbornene is oxidized relatively fast compared to the other substrates as might be expected due to the high reactivity of the exposed double bond in the strained ring of this substrate. A proposed mechanism of norbornene oxidation is shown in Scheme 1. As the reaction proceeds, tert-butoxy radicals form due to norbornene oxidation. These, in turn, can react with TBHP to form tert-butylperoxy radicals and tert-butanol as a by-product. As a result TBHP concentration is reduced and this, in turn, seems to have reduced the rate of the reaction over time. Benzyl alcohol shows the second highest activity early in the experiment. This can be attributed to the reactivity of the benzylic hydrogen, the relative stability of the intermediate benzylic radical and the lack of steric hindrance in proximity to the active functional group (relative to the other substrates in the series). In this case the maximum conversion (100 %) was obtained after 24 h. It is important to note that benzyl alcohol was oxidized to both benzaldehyde and benzoic acid. The selectivity to benzaldehyde is high early in the experiment, but then reduces (Fig. 6b), indicating that oxidation of benzaldehyde to benzoic acid occurs sequentially. However, the GC results indicate the presence of the TBHP after the completion of the reaction. Moreover, there was insufficient TBHP present in the reaction mixture to facilitate ‘double’ oxidation of the substrate through to benzoic acid. This indicates that TBHP cannot be the only oxidant and that oxygen from ambient air must contribute to the oxidation.

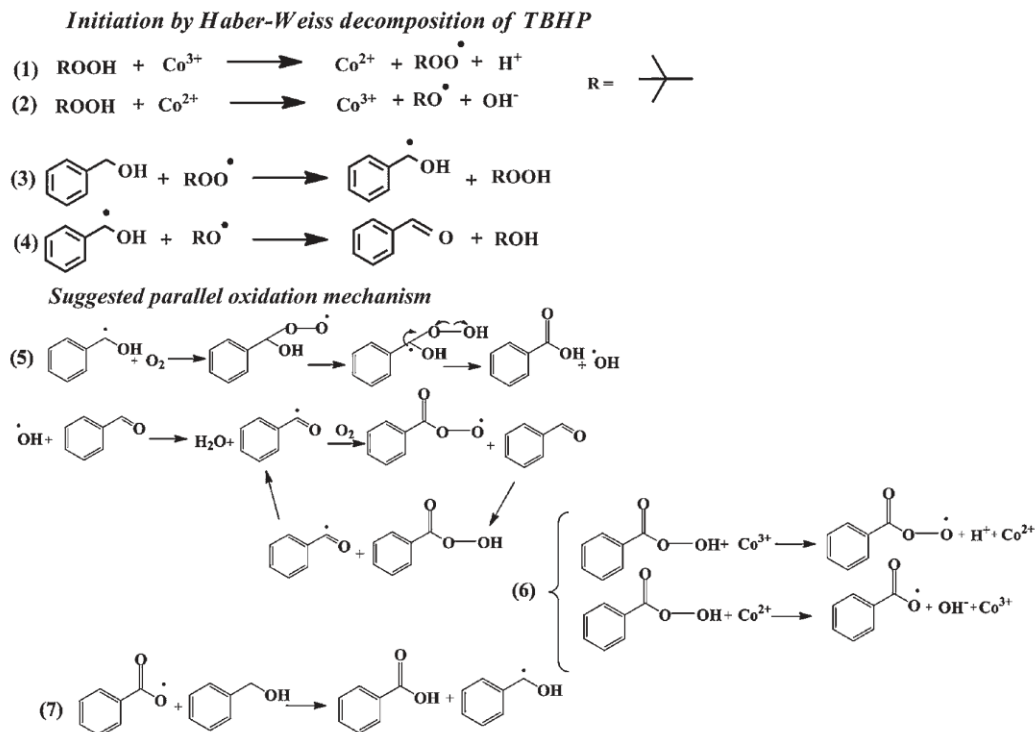
Scheme 2 provides a proposed mechanism for benzyl alcohol oxidation where, after initiation of the reaction by TBHP (Eq. 3), the oxidation is propagated by reaction between the hydroxybenzyl radical and O<sub>2</sub> (Eq. 5). 1-Phenyl ethanol shows a lower conversion rate than benzyl alcohol and this can be attributed to greater steric hindrance at the reaction site due to the presence of the



**Fig. 6** a Catalytic activity of SCo-5 in oxidation of various organic substrates and b percentage selectivity of the benzyl alcohol products



**Scheme 1** Proposed mechanism for norbornene oxidation [44]



**Scheme 2** Proposed mechanism for benzyl alcohol oxidation

methyl group on the benzylic carbon atom. GC analysis showed that the rate of TBHP conversion was considerably less than that of 1-phenylethanol, indicating that ambient O<sub>2</sub> must also have been involved in this oxidation.

The relatively low rate of cyclohexanol oxidation can be associated with its inability to form a radical stable intermediate upon H abstraction. GC analysis in this case indicates that the TBHP consumption is nearly stoichiometrically equivalent to cyclohexanol conversion, suggesting that the involvement of ambient oxygen is limited under the condition employed here. It is interesting to note that the reaction rate declines with time in a manner similar to norbornene.

To evaluate the recyclability of the catalysts, the SCo-5 was recovered after the first run by filtration and washed several times with acetonitrile, dried at 100 °C, then reused. It was observed that the catalyst could be used up to four times (cyclohexanol oxidation) without significant change in its catalytic activity [28].

#### 4 Conclusion

The integrity of the Co-modified composites remained intact even after loading 30 wt% cobalt. The presence of spinel Co<sub>3</sub>O<sub>4</sub> was determined previously by both XRD and XPS and was further demonstrated in this study by HRTEM. The morphology and dispersion of the Co<sub>3</sub>O<sub>4</sub> nanorods on the support varied based on Co-content and preparation method. These nanorods were extensively formed inside the pores of SBA-15 and fully occupied cross-sectional areas of the pores for the series prepared by the double-solvent technique and by adsorption. The length of the nanorods clearly increased in proportion to the Co-content. As for the composite prepared via impregnation, Co<sub>3</sub>O<sub>4</sub> patches were found inside the pores and Co<sub>3</sub>O<sub>4</sub> clusters on the external surface of the support.

The double-solvent technique was effective for preparing catalysts that have cobalt located inside the pores. There was essentially no migration of the cobalt to the external surface of the support as occurs with impregnation (see below). However, as the Co-content increased the activity of the double-solvent catalysts decreased; this is attributed to pore blockage which limits the active SA available. The composite prepared via adsorption showed the highest catalytic activity. Although this material had the lowest Co-content, there is no evidence of pore blockage and it appears that most of this cobalt is available to facilitate catalysis. The composite synthesized via impregnation showed lower catalytic activity than composites prepared by other methods with the same nominal Co-loading. It also had the lowest SA and Pv of this group. This is due to the formation of clusters on the external

surface which causes pore blockage and hinders the interaction of the catalyst with the reactants [45, 46].

For the SCo-5 catalyst, the initial rate of substrate oxidation was determined by the inherent reactivity (i.e., double bond > unhindered benzylic alcohol > sterically hindered benzylic alcohol ~ aliphatic alcohol). The stoichiometry observed for the reactions of the benzylic alcohols indicated that ambient oxygen must contribute to the conversion of these substrates in addition to TBHP. The SCo-5 catalyst could also be recovered and reused up to four times without significant changes in activity.

**Acknowledgments** The authors acknowledge use of facilities with the Monash Centre for Electron Microscopy. This research used equipment funded by the Australian Research Council (RIEFP 99 and ARC COE for Design in Light Metals, Massimo Raveggi (School of Geosciences, Monash University) for ICP-MS, Victor DeGuzman (School of Chemistry, Monash University) for help with the establishment of GC methods. Financial support from the Australia Research Council Discovery program and scholarship support from the Monash Research Graduate School and the Faculty of Science, Monash University (to JT) is gratefully acknowledged.

#### References

1. Abad A, Concepción P, Corma A, García H (2005) *Angew Chem Int Ed* 44:4066–4069
2. González-Arellano C, Corma A, Iglesias M, Sánchez F (2004) *Adv Synth Catal* 346:1316–1328
3. Kim S-K, Ihm S-K (2005) *Top Catal* 33:171–179
4. Kim K-H, Ihm S-K (2011) *J Hazard Mater* 186:16–34
5. Tsoncheva T, Ivanova L, Minchev C, Fröba M (2009) *J Colloid Interface Sci* 333:277–284
6. Hardjono Y, Sun H, Tian H, Buckley CE, Wang S (2011) *Chem Eng J* 174:376–382
7. El Haskouri J, Cabrera S, Gómez-García CJ, Guillem C, Latorre J, Beltrán A, Beltrán D, Marcos MD, Amorós P (2004) *Chem Mater* 16:2805–2813
8. Takada S, Fujii M, Kohiki S, Babasaki T, Deguchi H, Mitome M, Oku M (2001) *Nano Lett* 1:379–382
9. Xu X, Li J, Hao Z, Zhao W, Hu C (2006) *Mater Res Bull* 41:406–413
10. Jarupatrakorn J, Tilley TD (2002) *J Am Chem Soc* 124:8380–8388
11. Lambert S, Job N, D'Souza L, Pereira MFR, Pirard R, Heinrichs B, Figueiredo JL, Pirard J-P, Regalbutto JR (2009) *J Catal* 261:23–33
12. Chmielarz L, Kuśtrowski P, Drozdek M, Rutkowska M, Dziembaj R, Michalik M, Cool P, Vansant E (2011) *J Porous Mater* 18:483–491
13. Aspromonte SG, Sastre Á, Boix AV, Cocero MJ, Alonso E (2012) *Microporous Mesoporous Mater* 148:53–61
14. Imperor-Clerc M, Bazin D, Appay MD, Beaunier P, Davidson A (2004) *Chem Mater* 16:1813–1821
15. van der Meer J, Bardez-Giboire I, Mercier C, Revel B, Davidson A, Denoyel R (2010) *J Phys Chem C* 114:3507–3515
16. Jiao F, Frei H (2009) *Angew Chem Int Ed* 48:1841–1844
17. Lopes I, Davidson A, Thomas C (2007) *Catal Commun* 8:2105–2109
18. Irfan MF, Goo JH, Kim SD (2008) *Appl Catal B* 78:267–274
19. Solsona B, Davies TE, García T, Vázquez I, Dejoz A, Taylor SH (2008) *Appl Catal B* 84:176–184

20. Tsoncheva T, Ivanova L, Rosenholm J, Linden M (2009) *Appl Catal B* 89:365–374
21. Ma H, Xu J, Chen C, Zhang Q, Ning J, Miao H, Zhou L, Li X (2007) *Catal Lett* 113:104–108
22. Szegedi Á, Popova M, Minchev C (2009) *J Mater Sci* 44: 6710–6716
23. Vetrivel S, Pandurangan A (2005) *J Mol Catal A* 227:269–278
24. Zhan HJ, Xia QH, Lu XH, Zhang Q, Yuan HX, Su KX, Ma XT (2007) *Catal Commun* 8:1472–1478
25. Tang Q, Zhang Q, Wu H, Wang Y (2005) *J Catal* 230:384–397
26. Laugel G, Arichi J, Bernhardt P, Molière M, Kiennemann A, Garin F, Louis B (2009) *C R Chim* 12:731–739
27. Laugel G, Arichi J, Guerba H, Molière M, Kiennemann A, Garin F, Louis B (2008) *Catal Lett* 125:14–21
28. Taghavimoghaddam J, Knowles GP, Chaffee AL (2011) *J Mol Catal A*. doi: [10.1016/j.molcata.2012.02.014](https://doi.org/10.1016/j.molcata.2012.02.014)
29. Zhao D, Huo Q, Feng J, Chmelka BF, Stucky GD (1998) *J Am Chem Soc* 120:6024–6036
30. Zhao D, Feng J, Huo Q, Melosh N, Fredrickson GH, Chmelka BF, Stucky GD (1998) *Science* 279:548
31. Janssen AH, Yang CM, Wang Y, Schüth F, Koster AJ, de Jong KP (2003) *J Phys Chem B* 107:10552–10556
32. Van Der Voort P, Ravikovitch PI, De Jong KP, Neimark AV, Janssen AH, Benjelloun M, Van Bavel E, Cool P, Weckhuysen BM, Vansant EF (2002) *Chem Commun* 1010–1011
33. Zhao D, Sun J, Li Q, Stucky GD (2000) *Chem Mater* 12:275–279
34. Cheng M-Y, Pan C-J, Hwang B-J (2009) *J Mater Chem* 19:5193–5200
35. Tian B, Liu X, Yang H, Xie S, Yu C, Tu B, Zhao D (2003) *Adv Mater* 15:1370–1374
36. Lopes I, El Hassan N, Guerba H, Wallez G, Davidson A (2006) *Chem Mater* 18:5826–5828
37. Lanzafame P, Perathoner S, Centi G, Frusteri F (2007) *J Porous Mater* 14:305–313
38. Martínez A, López C, Márquez F, Díaz I (2003) *J Catal* 220: 486–499
39. Esposito S, Turco M, Ramis G, Bagnasco G, Pernice P, Pagliuca C, Bevilacqua M, Aronne A (2007) *J Solid State Chem* 180: 3341–3350
40. Xu R, Zeng HC (2004) *Langmuir* 20:9780–9790
41. Bourikas K, Vakros J, Fountzoula C, Kordulis C, Lycourghiotis A (2007) *Catal Today* 128:138–144
42. Pope D, Walker DS, W-Halley L, Moss RL (1973) *J Catal* 31: 335–345
43. Garrido Pedrosa AM, Souza MJB, Melo DMA, Araujo AS, Zinner LB, Fernandes JDG, Martinelli AE (2003) *Solid State Sci* 5:725–728
44. Koola JD, Kochi JK (1987) *J Org Chem* 52:4545–4553
45. Wolters M, van Grotel LJW, Eggenhuisen TM, Sietsma JRA, de Jong KP, de Jongh PE (2011) *Catal Today* 163:27–32
46. Wang Y, Hou B, Chen J, Sun Y (2011) *React Kinet Mech Catal* 102:155–164

**Monash University**

**Declaration for Thesis Chapter 3.4**

Impact of low cobalt loading on the morphology and dispersion of crystalline Co<sub>3</sub>O<sub>4</sub> patches supported on SBA-15

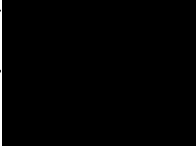
**Declaration by candidate**

In the case of Chapter 3 the nature and extent of my contribution to the work was the following:

Nature of contribution	Extent of contribution (%)
Proposed original idea; prepared and analysed samples; identified major issues; developed interpretations; fully drafted papers and conclusions	80%

The following co-authors contributed to the work. Co-authors who are students at Monash University must also indicate the extent of their contribution in percentage terms:

Name	Nature of contribution	Extent of contribution (%) for student co-authors only
Gregory P. Knowles	Aided method development (catalyst characterisation), input to interpretation of results, input to manuscript revision	N/A
Alan L. Chaffee	Supervision, assisted interpretations of results, editorial assistance	N/A

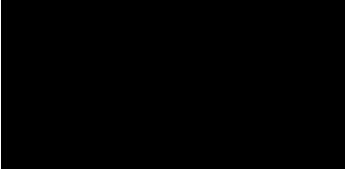
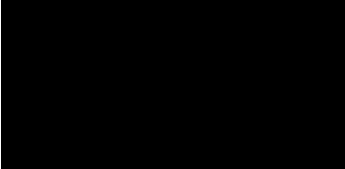
Candidate's Signature  Date 23-10-12

**Declaration by co-authors**

The undersigned hereby certify that:

- (1) the above declaration correctly reflects the nature and extent of the candidate's contribution to this work, and the nature of the contribution of each of the co-authors.
- (2) they meet the criteria for authorship in that they have participated in the conception, execution, or interpretation, of at least that part of the publication in their field of expertise;
- (3) they take public responsibility for their part of the publication, except for the responsible author who accepts overall responsibility for the publication;
- (4) there are no other authors of the publication according to these criteria;
- (5) potential conflicts of interest have been disclosed to (a) granting bodies, (b) the editor or publisher of journals or other publications, and (c) the head of the responsible academic unit; and
- (6) the original data are stored at the following location(s) and will be held for at least five years from the date indicated below:

Location(s) School of Chemistry, Clayton Campus

Gregory P. Knowles  Date 22-10-12  
 Alan L. Chaffee  Date 22-10-12

### **3.4 Impact of low cobalt loading on the morphology and dispersion of the crystalline Co<sub>3</sub>O<sub>4</sub> patches supported on SBA-15**

*Jamileh Taghavimoghaddam, Gregory P. Knowles, Alan L. Chaffee\**

School of Chemistry, Monash University, Victoria 3800 Australia

**KEYWORDS** Spinel Co<sub>3</sub>O<sub>4</sub>, Supported Co<sub>3</sub>O<sub>4</sub>, Two-solvent method, High dispersion, Pore blockage.

Abstract Cobalt/SBA-15 composites with low Co-content (1 wt%) were prepared via the “two-solvent” method and impregnation. The impact of the low Co-content and preparation method on the morphology and dispersion of the resultant Co<sub>3</sub>O<sub>4</sub> particles was investigated using a variety of characterisation techniques (XRD, N<sub>2</sub> adsorption-desorption, ICP-MS, DR UV-vis, FTIR, TEM and STEM). The Co<sub>3</sub>O<sub>4</sub> patches that formed were smaller and better dispersed throughout the support than for previously reported higher Co-content composites. As a result, they exhibited better catalytic performance in the liquid phase oxidation of cyclohexanol, benzylalcohol, 1-phenylethanol and norbornene, with tert-butylhydroperoxide (TBHP). The composite prepared by the two-solvent method demonstrated better catalytic activity compared to its analogues with the same Co-content prepared by the impregnation and adsorption methods. This is attributed to less pore blockage by and better availability of Co<sub>3</sub>O<sub>4</sub> in this composite.

#### **3.4.1 Introduction**

Supported cobalt/cobalt oxides have drawn attention in a variety of catalytic applications [1]. Specific examples include methane combustion [2], oxidation of wide range of chemicals [3-8] and the Fischer Tropsch synthesis [9]. The better catalytic performance of supported cobalt/cobalt oxides relative to bulk forms is attributed to the high surface area over which

the active species are better dispersed [10, 11]. Since the discovery of mesoporous silicas MCM-41 [12] and later SBA-15 [13], these materials have been extensively investigated as supports for heterogeneous catalysis [14, 15]. This is attributed to their high surface area (SBA-15, 600-1000 m<sup>2</sup> g<sup>-1</sup> and MCM-41, 800-1400 m<sup>2</sup> g<sup>-1</sup>), tuneable pore size and high thermal and hydrothermal stability [16]. The ultimate goal in heterogeneous catalysis is usually to prepare catalysts with small particle size and high dispersion. This therefore facilitates effective interaction between the reactants and catalytically active species [17, 18]. The preparation method and amount of metal loading, among other factors, affect the particle's size and their dispersion throughout the support [4, 19, 20]. It has been recently reported that the two-solvent method results in formation of the metal oxide species which are predominantly inside the pores of SBA-15 [21]. The confinement of the metal oxide species inside the pores prevents sintering and as a result eliminates the formation of large metal oxide particles which are relatively inactive for catalysis.

In previous studies we investigated the effect of various preparation methods and Co-loading on the morphology and catalytic performance of the composites [8, 22]. It was observed that regardless of the Co-content and preparation method the cobalt oxide, Co<sub>3</sub>O<sub>4</sub>, formed into patches which were relatively evenly dispersed throughout the SBA-15. These patches were comprised of nanorods with width and length proportional to the Co-content. These nanorods fully occupied the cross section of the SBA-15 mesopores. Adjacent nanorods were also interconnected to each other via nanosized cobalt oxide bridges which appear to fill what originally was SBA-15 intrawall micropores [8].

When the two-solvent method was used to deposit the Co<sub>3</sub>O<sub>4</sub> on SBA-15, the resulting Co-content was approximately as expected (5 wt%, 10 wt% and 30 wt%). No particles were formed on the external surface of the SBA-15. By contrast, the conventional impregnation method resulted in the formation of the Co<sub>3</sub>O<sub>4</sub> particles both on the external and internal

surface of the SBA-15 with the predetermined Co-content (5 wt%) [8]. However using adsorption as a method of preparation, due to the weak interaction between the support and metal precursor, the actual Co-content (1 wt%) was much less than the amount available in the aqueous synthesis solution (5 wt%) [8]. The resultant composite, referred to as SCo-1-A, also contained all the cobalt oxide species within the mesopores of the SBA-15 support.

The catalytic activity of these composites was evaluated for the liquid phase oxidation of a selection of alcohols and olefins. The activity of the series of composites prepared by the two-solvent method was found to be in reverse proportion to the Co-content; that is the 5% composite displayed the highest catalytic activity [8]. The poorer activity for higher Co-content composites was attributed to pore blockage and, hence, poorer accessibility of the active sites to the reactants in solution. The impregnated catalyst (Co 5 wt%) showed only slightly higher catalytic activity than the poorest of the two-solvent composites (30 wt%). This was attributed to the presence of aggregated inactive species on the external surface [8]. However, it was the composite prepared by adsorption that showed the highest catalytic activity. This composite also had the lowest Co-content (1 wt%), highest surface area and better dispersion of all those investigated.

Therefore it was of interest to investigate the morphology, dispersion and catalytic performance of lower loading Co-composites prepared via (a) the two-solvent method and (b) impregnation and to compare these with the composites reported previously, especially SCo-1-A. For this purpose the same metal precursor,  $\text{Co}(\text{NO}_3)_2 \cdot 6\text{H}_2\text{O}$ , was used to deposit 1 wt% cobalt on the SBA-15. The composites were characterized using  $\text{N}_2$  adsorption-desorption, XRD, DR UV-vis, ICP-MS, FTIR and TEM and STEM. The catalytic performance of the Co-composites was investigated for liquid phase oxidation of cyclohexanol, 1-phenylethanol, benzylalcohol and norbornene in the presence of TBHP and the conversion of the products was monitored using GC and GC-MS.

## 3.4.2 Experimental

### 3.4.2.1 Preparation of SBA-15 and Co-composites

The detailed procedures used to prepare SBA-15 and Co-composite materials via the two-solvent and impregnation methods have been reported elsewhere [8]. In this work the composite prepared via the two-solvent method is referred to as SCo-1. The composite prepared by impregnation is referred to as SCo-1-I.

### 3.4.2.2 Characterization techniques

*Low-angle and wide-angle powder X-ray diffraction patterns* were obtained with a Bruker D8 Focus powder diffractometer with a monochromatic  $\text{CuK}_\alpha$  source radiation ( $\lambda = 1.5406 \text{ \AA}$ ) operated at 40 kV and 30 mA over  $2\theta$  range of  $0.4\text{-}4^\circ$  and  $15\text{-}80^\circ$  respectively. Data in the  $2\theta$  range of  $0.4\text{-}4^\circ$  was collected with a step size of  $0.02^\circ$  and a step time of  $0.1^\circ \text{ min}^{-1}$ . Data in the  $2\theta$  range of  $15\text{-}80^\circ$  were collected with step size of  $0.02^\circ$  and step time of  $1^\circ \text{ min}^{-1}$ .

*$\text{N}_2$ -adsorption-desorption isotherms* were obtained at 77 K on a Micromeritics TriStar II 3020 surface area and porosity analyser. Samples were outgassed at  $150^\circ \text{C}$  overnight prior to analysis via Micromeritics VacPrep 061. The BET surface area [13] was calculated from relative pressure ( $p/p_0$ ) data points in the range 0.046-0.304. The pore size distribution, PSD using the BJH method [23] was calculated from the desorption branch.

*Fourier transform infrared (FTIR) spectra* were collected from a BIO-RAD FTS 40 spectrometer. The materials were diluted 3/300 in dry KBr. The mixtures were further dried at  $110^\circ \text{C}$  (4-6 hours), then pressed into pellets (under vacuum) immediately prior to analysis.

*Inductively coupled plasma mass spectrometry (ICP-MS)* was carried out using a GBC OPTIMAS 9500 ICP-MS. Prior to the measurement all the catalysts were digested with  $\text{HNO}_3$  and HF to remove silica [24].

*Diffuse reflectance UV-vis spectroscopy (DR UV-Vis)* was carried out using a Cary 5000 UV visible spectrophotometer, fitted with the diffuse reflectance accessory.

*Transmission electron microscopy (TEM)* was carried out on a JEOL 2011 transmission electron microscope equipped with a LaB<sub>6</sub> emitter (point resolution 0.21 nm) and an accelerating voltage (200kV). Fast Fourier Transform (FFT) analyses of TEM images are carried out by the image analysis software, Gatan Digital Micrograph.

*Scanning transmission electron microscopy (STEM)* was carried out on a JEOL 2100F transmission electron microscope equipped with a high angular annular dark field (HAADF) detector (camera length 10 cm and 0.5 nm probe).

*Gas chromatography (GC)* was carried out on a Varian 3700 gas chromatograph equipped with an FID detector, a 30 m polar capillary column (SGE 30QC5/BP20 1.0 $\mu$ , ID 0.53 mm) and an Agilent EZChrom Elite (version 3.2.1) data system. *Gas chromatography-mass spectrometry (GCMS)* was carried out on an Agilent 5973 Network MS equipped with a 6890 series GC system (source conditions: EI, 70 eV, 200 °C).

### **3.4.3 Catalytic tests**

Liquid phase oxidation of cyclohexanol, 1-phenylethanol, benzylalcohol and norbornene was performed in a round bottom flask. In each test, 0.1 g of the catalyst (0.001 g cobalt) was added to the acetonitrile (5 mL) containing the organic substrate (20 mmol) and chlorobenzene (200  $\mu$ L as an internal standard). The solvent mixture was brought to reflux temperature (83 °C), after which the oxidant, TBHP (24 mmol), was added dropwise over approximately 10 minutes. All the reactions were carried out without attempting to exclude air and monitored by GC, withdrawing samples every 4 h up to 24 h.

### **3.4.4 Results and discussion**

Fig.1 A shows the low-angle XRD patterns of both SBA-15 and the Co-composites prepared by the two-solvent method (SCo-1) and impregnation (SCo-1-I). Three well-resolved diffraction peaks, indexed to the (100), (200) and (110) planes in the range of  $2\theta = 0.5-4^\circ$ , were observed for all the composites [25]. These are indicative of high quality SBA-15 [13].

Since the XRD patterns for the composites resembled that of pure SBA-15, it is concluded that the structural integrity of the SBA-15 remained intact upon Co-loading via both methods. The d-spacing between the (100) planes is 9.01 nm, the cell parameter and wall thickness were calculated to be 10.41 nm, 4.3 nm, respectively. The intensity of the first diffraction peak decreased after loading cobalt, which suggests that the degree of periodicity of the Co-composites was decreased. As shown by TEM images (see below), after Co-loading pores were filled unevenly, some pores were filled and some left empty, consistent with this lower periodicity[26]. However, the cell parameter value of the Co-composites did not alter after Co-loading, suggesting that no further shrinkage in the support structure occurred during the calcination of the composites.

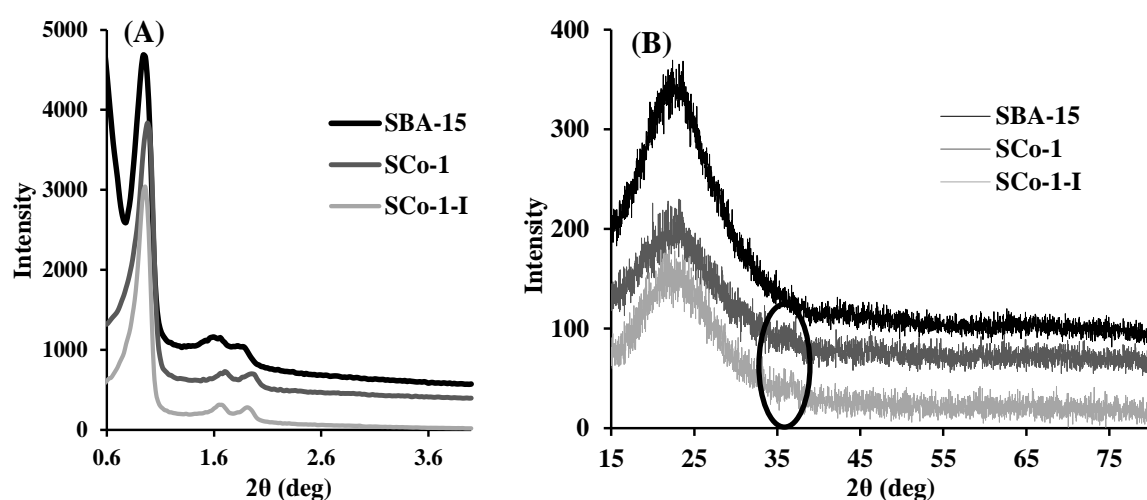


**Figure 1.** XRD patterns of SBA-15 and Co-composites (A) low-angle and (B) wide-angle

The wide-angle XRD patterns were collected over the range  $2\theta=15-80^\circ$  for SBA-15 and the composite materials (Fig.1 B). A broad peak is observed at  $15<2\theta<25^\circ$  for all the samples, which is attributed to the amorphous silica of the SBA-15 walls. No further diffraction peaks are observed for SBA-15 [27]. The XRD patterns for SCo-1 and SCo-1-I exhibited only very weak diffraction peaks at around  $2\theta=35.5^\circ$ . This peak is characteristic of spinel  $\text{Co}_3\text{O}_4$ , (JCPDF file 01-073-1701) with space group  $Fd3m$  [28]. Thus presence of this weak peak suggests the formation of some crystalline  $\text{Co}_3\text{O}_4$ . However the absence of any other

diffraction peaks as well as the very low intensity of this characteristic peak can be attributed to very small  $\text{Co}_3\text{O}_4$  crystal size [29] and/or high dispersion of the crystals on the support [30]. The same behaviour (very weak diffraction pattern) was observed previously for SCo-1-A [8].

Fig.2 A displays the  $\text{N}_2$  adsorption-desorption isotherms of the SBA-15 and Co-composites. These are type IV isotherms with H1 hysteresis loops according to the IUPAC classification [31]. This profile is associated with 2-D hexagonal channels in mesoporous silica SBA-15 [13]. The presence of hysteresis and the sharpness of the inflection over the relative pressure range 0.45-0.8 is characteristic of the mesoporous silica with a narrow PSD. The textural properties of the SBA-15 and all the Co-composites are summarized in Table 1.

Upon Co-loading, regardless of the preparation method, less  $\text{N}_2$  was adsorbed on the surface

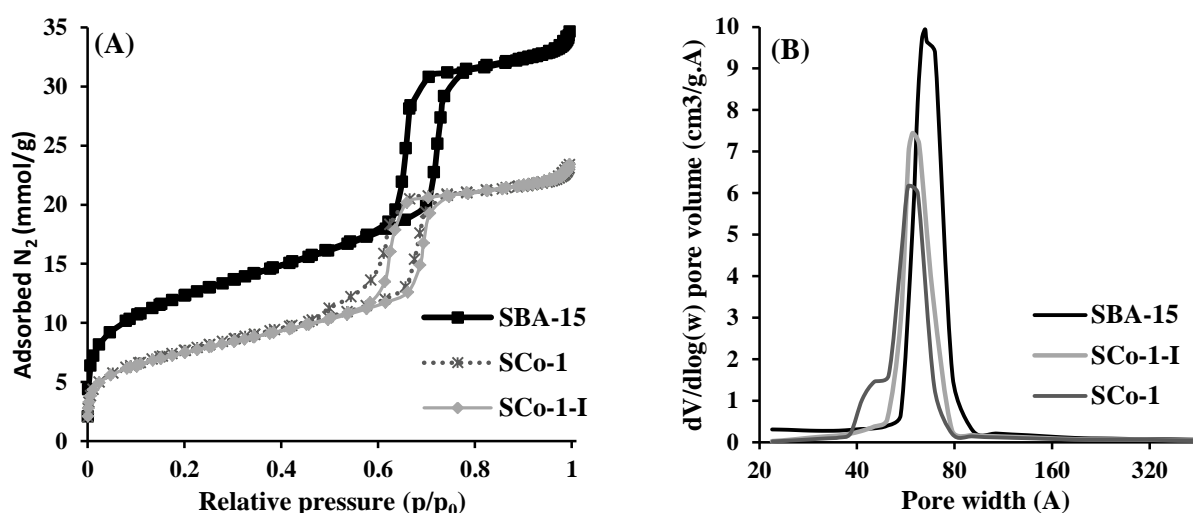


**Figure 2.**  $\text{N}_2$  adsorption-desorption (A) and PSD (B) of SBA-15 and the Co-composites

of the composites. Furthermore, the capillary condensation was shifted to the lower relative pressure with the hysteresis loops being slightly broader. The broadness of the hysteresis loops compared to the pure SBA-15 suggests that the PSD in the Co-composites is somewhat broader than that of the pure SBA-15 [32]. The decrease in surface area and pore volume in the Co-composites compared to the pure SBA-15 suggests the formation of the particles inside the pores. It is also noteworthy that upon Co-loading the volume of adsorbed  $\text{N}_2$  in the

micropore region ( $p/p_0 < 0.05$ ) decreased noticeably. This suggests that a fraction of micropores were blocked upon formation of  $\text{Co}_3\text{O}_4$  inside the mesopores.

Pore volume of the Co-composites decreased by  $0.3 \text{ cm}^3$  relative to the pure SBA-15. This decrease cannot be simply attributed to the pore filling. This is because the calculated volume occupied by  $\text{Co}_3\text{O}_4$  (based on the assumption that all the deposited cobalt is in the form of  $\text{Co}_3\text{O}_4$ ) would be about  $0.002 \text{ cm}^3$ , considering that the density of  $\text{Co}_3\text{O}_4$  is  $6.11 \text{ g cm}^{-3}$ . Thus the actual decrease in the pore volume is approximately 140 times more than that which could be expected if  $\text{Co}_3\text{O}_4$  was perfectly crystallized within the pores. This suggests that there is probably a significant pore blockage, such that the formation of the  $\text{Co}_3\text{O}_4$  at one or both ends of the pores hinders  $\text{N}_2$  from entering the pores (Fig.3). In this case the volume exists between two  $\text{Co}_3\text{O}_4$  rods is inaccessible and considered as an occupied volume.

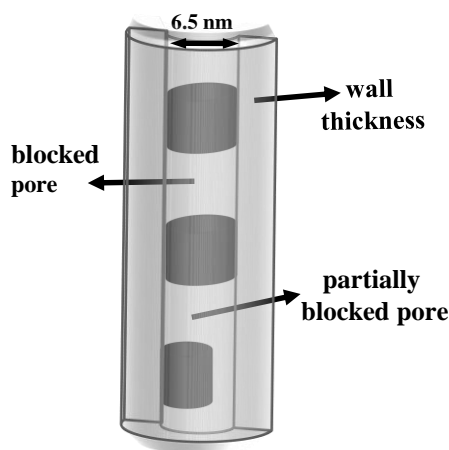
Furthermore, a shoulder is observed on the desorption branch of SCo-1 at a relative pressure  $p/p_0 = 0.45$ . A similar behavior was observed previously for zirconia supported on SBA-15 and attributed to partial pore blockage (cavitation) phenomenon [33]. It is suggested that the cobalt oxide nanorods grew against the silica walls such that the pore volume between the two cobalt oxide particles were accessible via a narrow pore neck (Fig.3). Therefore, nitrogen desorption from empty pores occurred at the relative pressure  $p/p_0 = 0.6$ . However partially blocked pores showed delayed  $\text{N}_2$  desorption until the vapor pressure was reduced such that the condensed  $\text{N}_2$  transformed into gas ( $p/p_0 = 0.45$ ) at which point desorption took place [34]. The cavitation phenomenon was not observed either for SCo-1-I or SCo-1-A. This can be attributed to the absence of the pores with partial blockage [8].

**Table 1.** Textural properties of SBA-15 and the Co-composites

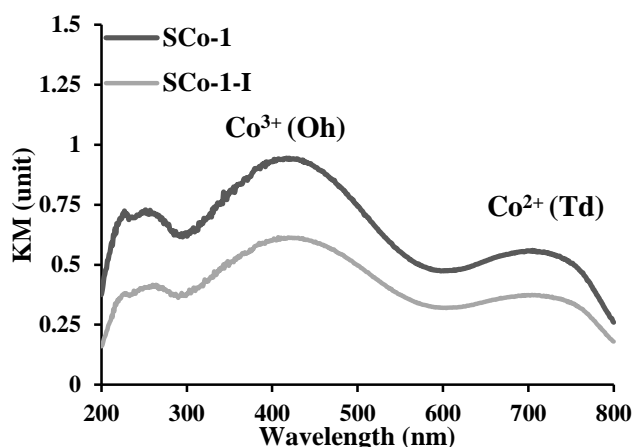
Sample	BET( $\text{m}^2 \text{ g}^{-1}$ ) <sup>a</sup>	Dp (nm) <sup>b</sup>	Vt( $\text{cm}^3 \text{ g}^{-1}$ ) <sup>c</sup>	Co wt% <sup>d</sup>
SBA-15	947	6.5	1.15	-
SCo-1	601	5.8	0.84	1.00
SCo-1-I	586	6.1	0.83	1.00

a: surface area, b: pore diameter, c: total pore volume and d: the actual Co-content

The PSD of all the samples is shown in Fig.2 B with SBA-15 displaying a narrow PSD centred at 6.5 nm. As for Co-composites both the SCo-1-I and SCo-1 showed slightly broader PSD compared to the pure SBA-15. However in the case of SCo-1 a small fraction of pores have a pore diameter of about 4 nm which is in agreement with the occurrence of some partially blocked pores. It can be seen that for both Co-composites, irrespective of preparation method, the centre of the peak slightly shifted to a lower pore width. This indicates the decrease in the average pore diameter after the formation of  $\text{Co}_3\text{O}_4$  inside the pores of the support. The Co-content for both composites was calculated using ICP-MS and the results are summarized in Table 1. The PSD of SCo-1-A resembled that of SCo-1-I [8].



**Figure 3.** Diagram of blocked and partially blocked pores



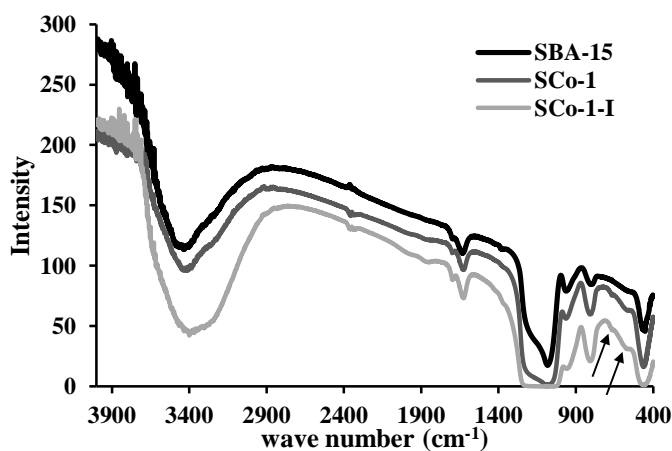
**Figure 4.** DR UV-vis spectra of Co-composites

Fig.4 presents DR UV-vis spectra of SCo-1 and SCo-1-I. In both cases, three distinct peaks centred at around 240 nm, 440 nm and 720 nm are observed. The first peak is associated with  $\text{O}^{2-}$  to  $\text{Co}^{3+}$  charge transfer, while the 2<sup>nd</sup> and 3<sup>rd</sup> peaks are attributed to the d-d electron transitions of  $\text{Co}^{3+}$  ( $d^6$ ) and  $\text{Co}^{2+}$  ( $d^7$ ) in octahedral and tetrahedral co-ordination states, respectively [35-37]. The second peaks (440 nm) in this work demonstrate a blue shift relative to the composites with higher Co-contents prepared by the two-solvent method [22]. This blue shift is attributed to the presence of relatively smaller  $\text{Co}_3\text{O}_4$  particles in SCo-1 and SCo-1-I compared to the higher Co-content composites [22, 38]. The DR UV-vis spectra of

S-Co-1, S-Co-1-I and S-Co-1-A [22] are all at a very similar wavelengths since the  $\text{Co}_3\text{O}_4$  particles in all these composites are of very similar size.

The intensity of the second peak (720 nm) relative to the first peak (440 nm) for these low Co-content composites is lower relative to those reported previously with higher Co-content [22]. This suggests that the proportion of tetrahedral  $\text{Co}^{2+}$  in these composites is reduced relative to the higher Co-content catalyst composites reported previously. These tetrahedral  $\text{Co}^{2+}$  species are usually thought to strongly interact with the silica of the support, and therefore be relatively ineffective for catalytic activity [39].

Fig.5 shows the FT-IR spectra of SBA-15, S-Co-1 and S-Co-1-I. In all spectra, the adsorption bands at around 3500 and 1670  $\text{cm}^{-1}$  can be attributed to the H-bonded OH groups on the surface and also -OH bonds of the adsorbed  $\text{H}_2\text{O}$  (stretching and deformation respectively). The adsorption bands at 1100, 841 and 482  $\text{cm}^{-1}$  are due to the stretching vibrations of siloxane groups  $-(\text{SiO})_n-$  [40]. However, the stretching vibration of either Si-OH or Si-O-Si is observed at 960  $\text{cm}^{-1}$ . The two additional adsorption bands with low intensity at around 590  $\text{cm}^{-1}$  ( $\bar{\nu}_1$ ) and 680  $\text{cm}^{-1}$  ( $\bar{\nu}_2$ ) are observed for both Co-composites. These bands are attributed to  $\text{Co}^{2+}$ -O vibrations in tetrahedral and  $\text{Co}^{3+}$ -O vibrations in octahedral of spinel  $\text{Co}_3\text{O}_4$ , respectively [41].



**Figure 5.** FT-IR spectra of SBA-15 and Co-composites

Fig.6 displays STEM and TEM images of both S-Co-1 and S-Co-1-I. It is clear that the integrity of the SBA-15 structure is preserved after Co-loading via either preparation method.

The honeycomb structure, (Fig.6 D, dotted line) as well as highly-ordered cylindrical channels can be observed with the electron beam parallel and perpendicular to the pores of the SBA-15, respectively [42, 43]. The pore diameter and the wall thickness of the channels were calculated from the TEM images and are approximately 6.8 nm and 3.5 nm, respectively. This is in agreement with the results obtained from the low-angle XRD and N<sub>2</sub> adsorption-desorption.

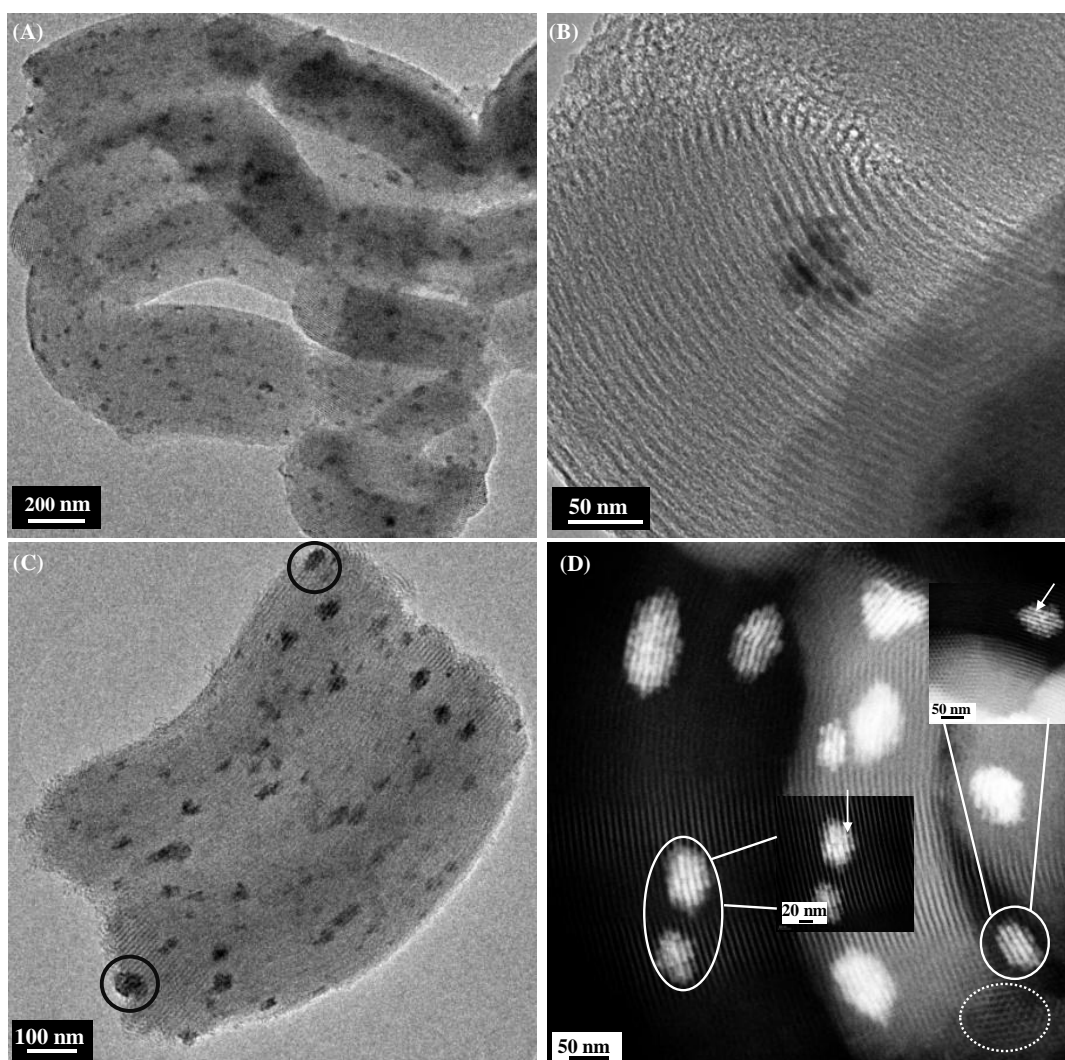


**Figure 6.** TEM and STEM images of (A, B) SCo-1 and (C, D) SCo-1-I

Upon Co-loading, the Co<sub>3</sub>O<sub>4</sub> nanorods can be seen to be accommodated in adjacent pores to form patches which are homogeneously dispersed throughout the SBA-15. The formation of these patches were reported previously by our group [8, 22] and Jiao et al [44]. Small bridges can be observed (white arrows) within the patches, which appeared to connect the nanorods in the adjacent pores randomly. The presence of the micropores is known to be associated

with extended growth of the  $\text{Co}_3\text{O}_4$  crystallites (patches) within SBA-15 at sufficiently high calcination temperature [22, 44].

The average patch size of SCo-1 is just slightly smaller than for SCo-1-I. The average width and length of the patches in SCo-1 range between 25-35 nm and 30-45 nm and those for SCo-1-I are 30-35 nm and 40-50 nm, respectively. These results are well-correlated with the  $\text{N}_2$

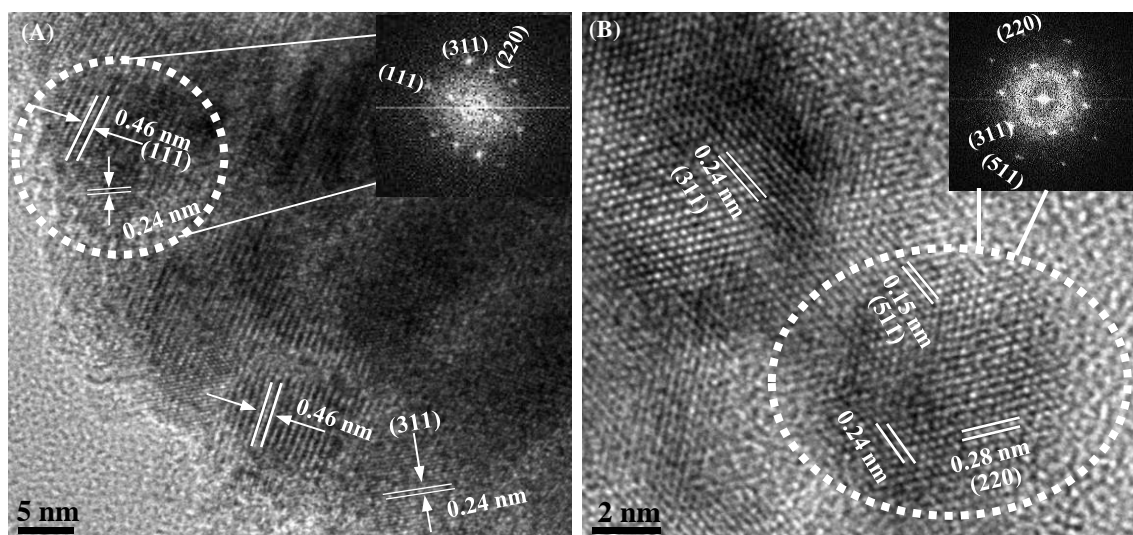


**Figure 7.** HRTEM images of (A) SCo-1-I and (B) SCo-1

adsorption-desorption results, which indicates slightly less pore volume and surface area for SCo-1-I compared to SCo-1. The formation of  $\text{Co}_3\text{O}_4$  patches on the aperture of the pores in SCo-1-I (Fig.6 C, black circles) is evident. The  $\text{Co}_3\text{O}_4$  patches of SCo-1 and SCo-1-I have similar size and dispersion to SCo-1-A, reported previously [8]. The lattice fringes of cubic  $\text{Co}_3\text{O}_4$  (JCPDF file 01-073-1701) nanorods can be observed in HRTEM images. The lattice spacing in the  $\text{Co}_3\text{O}_4$  was measured using FFT analysis (Fig.7 A and B inset) to be 0.15, 0.24, 0.28 and 0.4 nm assigned to lattice planes (511), (311), (220) and (111) planes, respectively. These observations are consistent with the XRD results.

The catalytic performance of SCo-1 and SCo-1-I was evaluated for the oxidation of organic substrates (norbornene, benzylalcohol, 1-phenylethanol and cyclohexanol) in the presence of

TBHP as an oxidant and/or initiator. The products were identified qualitatively and quantitatively using GC-MS and GC, respectively withdrawing samples every 4 h until 24 h. As shown in Fig.8 A and B the catalytic performance of SCo-1 is slightly higher than SCo-1-I for norbornene and benzylalcohol oxidation during the first 8 h. This is attributed to more  $\text{Co}_3\text{O}_4$  being available to the reactant in the former case. The presence of the pores which are only partially blocked could increase the catalytic activity of SCo-1 relative to SCo-1-I.

Among the organic substrates in this work norbornene is the most reactive. This is attributed to the presence of the exposed double bond in the strained ring of norbornene. Benzylalcohol is the next most reactive substrate due to the lack of steric hindrance at its reactive centre relative to 1-phenylethanol and the relative stability of the benzylic radical intermediate [22]. It is interesting that benzylalcohol is oxidized first to benzaldehyde and then on to benzoic acid. For a stoichiometric reaction this requires 40 mmol of TBHP whereas only 24 mmol was provided. Moreover after the completion of the catalytic oxidation reaction the GC results indicated the presence of a considerable amount of residual TBHP. This suggests that TBHP was not the only oxidant in this reaction and that oxygen in air must have contributed as co-oxidant.

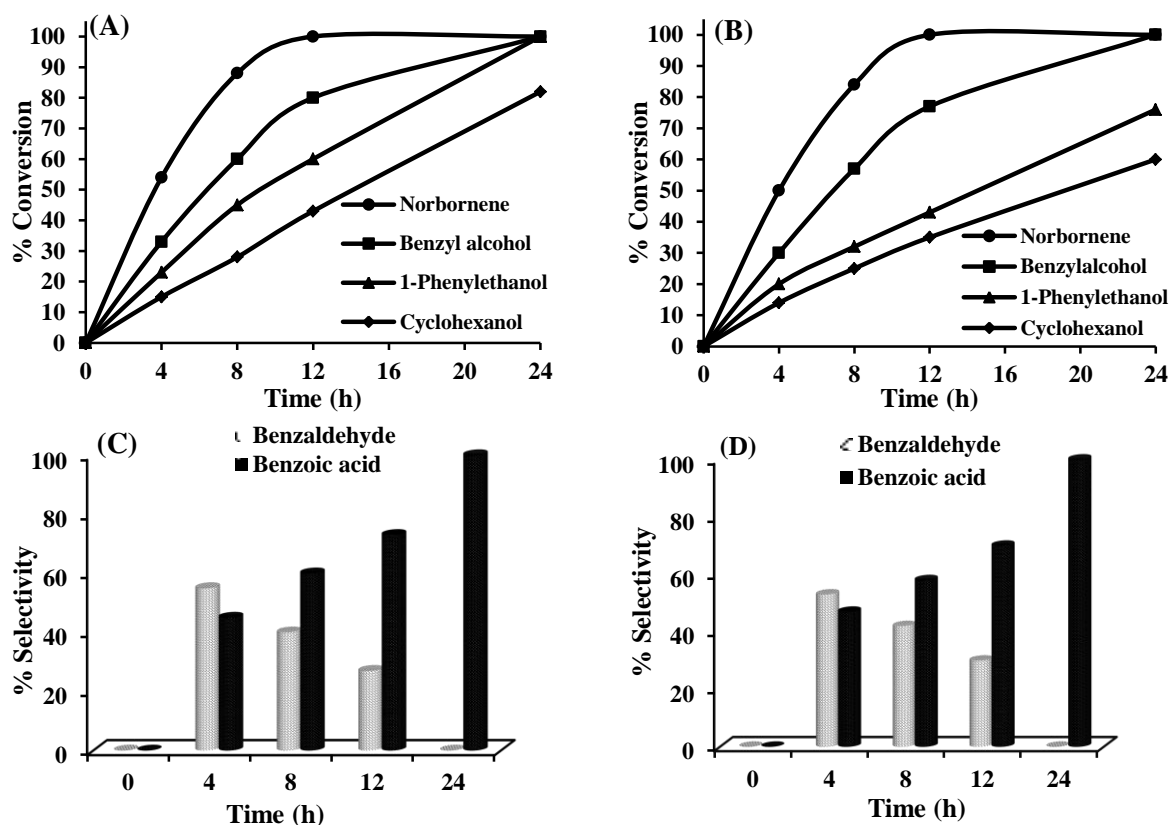


**Figure 8.** Catalytic evaluation for liquid phase oxidation of organic substrates (A) SCo-1 and (B) SCo-1-I. Percentage selectivity of the benzylalcohol products over (C) SCo-1 and (D) SCo-1-I

The mechanism by which aerial oxygen is thought to participate in the catalytic reactions is elaborated elsewhere [22]. To confirm this mechanism, the oxidation of benzylalcohol was carried out under the same condition, but using an inert atmosphere ( $N_2$ ) with SCo-1 as the catalyst. The results, shown in Fig.9, indicate the total conversion after 24 h of catalytic reaction under inert atmosphere is slightly higher than 20 %, which is five times less than that obtained in air. The conversion in this inert atmosphere reaction was found to be stoichiometric (equivalent to TBHP consumption), thus demonstrating the importance of oxygen for obtaining high conversions. In the light of these results it can be suggested that TBHP behaves more as an initiator under the standard reaction conditions [45].

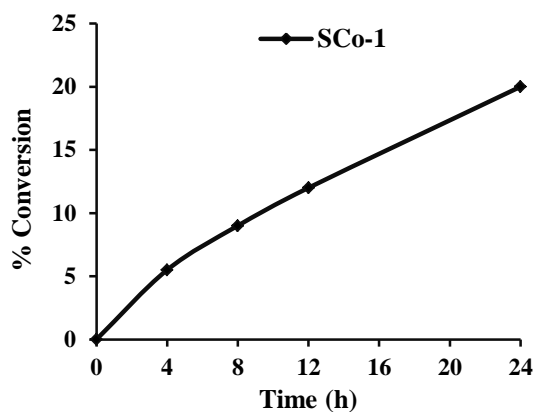


**Figure 9.** Benzylalcohol oxidation under inert atmosphere

Fig.8 C and D show how the selectivity to the products benzaldehyde and benzoic acid progresses in the catalytic oxidation of benzylalcohol. After 4 h of reaction, benzaldehyde slightly dominated benzoic acid in the product mixture which suggests the presence of a parallel mechanism [22]. As the oxidation progressed, benzaldehyde diminished and benzoic acid became the dominant product. Through this parallel reaction mechanism, atmospheric oxygen promoted the oxidation of either benzylic radical or benzaldehyde to the benzoic acid [22]. Finally, after 24 h the complete conversion to benzoic acid was obtained.

For 1-phenylethanol, SCo-1 showed higher catalytic performance than SCo-1-I. In the first 4 h of the reaction, the catalytic performance of both catalysts was nearly the same. However as the reaction continued SCo-1 displayed higher catalytic performance relative to SCo-1-I. This can be attributed to the less pore blockage and better availability of  $\text{Co}_3\text{O}_4$  in the case of SCo-1. Similar observations were obtained for cyclohexanol oxidation over SCo-1 and SCo-1-I.

When comparing the catalytic performance of these two composites with SCo-1-A for cyclohexanol oxidation, the composite prepared via the two-solvent method, SCo-1, showed the highest catalytic performance [8]. This catalyst also contained some partially blocked pores. This suggests that the pore structure of SCo-1 enabled better interaction between  $\text{Co}_3\text{O}_4$  and the reactants relative to both SCo-1-I and SCo-1-A.

The longevity of the catalyst SCo-1 was evaluated by recovering the catalyst from the reaction media via filtration. The catalyst was then washed several times with acetonitrile and

dried at 100 °C and added to a fresh reaction mixture. For SCo-1 the catalytic active for cyclohexanol oxidation retained its activity through four of these cycles.

### 3.4.5 Conclusion

Low Co-content composites were prepared using the two-solvent method and impregnation. XRD patterns displayed a very low intensity characteristic diffraction peak associated with spinel  $\text{Co}_3\text{O}_4$ . This suggests a high dispersion of the  $\text{Co}_3\text{O}_4$  particles throughout the support. DR UV-vis and FTIR further confirmed the presence of tetrahedral  $\text{Co}^{2+}$  and octahedral  $\text{Co}^{3+}$  in the spinel structure.  $\text{N}_2$  adsorption-desorption analysis suggests the formation of  $\text{Co}_3\text{O}_4$  particles inside the pores of the SBA-15 while the TEM images of both composites also confirmed this.

These Co-composites were used to catalyse oxidation of selected organic substrates in the presence of TBHP as an oxidant and/or initiator with atmospheric oxygen as the co-oxidant. SCo-1 showed higher catalytic performance than SCo-1-I and this can be attributed to better dispersion, smaller patches and more available  $\text{Co}_3\text{O}_4$  on the support. The catalytic performance of SCo-1 is relatively higher than SCo-1-A which was reported previously. This is attributed to the occurrence of the partial pore blockage in the latter composite. As a result the  $\text{Co}_3\text{O}_4$  is more available to the reactants within SCo-1 than within SCo-1-A. SCo-1 can also be reused at least three times without significant change in its catalytic performance.

### Corresponding Author

\* [REDACTED] Tel.: [REDACTED]

### ACKNOWLEDGMENT

The authors thank Massimo Raveggi (School of Geosciences, Monash University) for elemental analysis (ICP-MS). Financial support from the Australia Research Council Discovery program and scholarship support from the Monash Research Graduate School and the Faculty of Science, Monash University (to JT) is gratefully acknowledged. The authors

acknowledge use of facilities within the Monash Centre for Electron Microscopy including the use of equipment supported by the Australian Research Council's Centres of Excellence funding scheme (COE for Design in Light Metals).

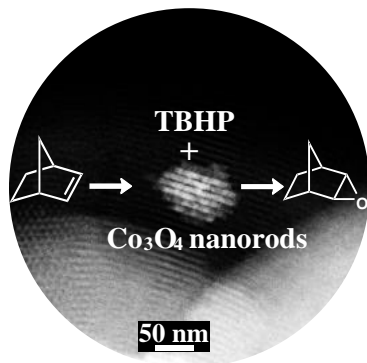
### 3.4.6 REFERENCES

- [1] J. Wöllenstein, M. Burgmair, G. Plescher, T. Sulima, J. Hildenbrand, H. Böttner, I. Eisele, *Sens. Actu. B: Chem.* 93 (2003) 442-448.
- [2] G. Laugel, J. Arichi, M. Molière, A. Kiennemann, F. Garin, B. Louis, *Catal. Today*. 138 (2008) 38-42.
- [3] B. Solsona, T.E. Davies, T. Garcia, I. Vázquez, A. Dejoz, S.H. Taylor, *Appl. Catal. B: Environ.* 84 (2008) 176-184.
- [4] I. Lopes, A. Davidson, C. Thomas, *Catal. Commun.* 8 (2007) 2105-2109.
- [5] H. Ma, J. Xu, C. Chen, Q. Zhang, J. Ning, H. Miao, L. Zhou, X. Li, *Catal. Lett.* 113 (2007) 104-108.
- [6] Á. Szegedi, M. Popova, C. Minchev, *J. Mater. Sci.* 44 (2009) 6710-6716.
- [7] Q. Tang, Q. Zhang, H. Wu, Y. Wang, *J. Catal.* 230 (2005) 384-397.
- [8] J. Taghavimoghaddam, G.P. Knowles, A.L. Chaffee, *J. Mol. Catal. A: Chem.* 358 (2012) 79-88.
- [9] G. Prieto, A. Martínez, R. Murciano, M.A. Arribas, *Appl. Catal. A: Gen.* 367 (2009) 146-156.
- [10] L.F. Liotta, M. Ousmane, G. Di Carlo, G. Pantaleo, G. Deganello, G. Marci, L. Retaillieu, A. Giroir-Fendler, *Appl. Catal. A: Gen.* 347 (2008) 81-88.
- [11] J. Zhu, K. Kailasam, A. Fischer, A. Thomas, *ACS Catal.* 1 (2011) 342-347.
- [12] J.S. Beck, J.C. Vartuli, W.J. Roth, M.E. Leonowicz, C.T. Kresge, K.D. Schmitt, C.T.W. Chu, D.H. Olson, E.W. Sheppard, *J. Am. Chem. Soc.* 114 (1992) 10834-10843.
- [13] D. Zhao, J. Feng, Q. Huo, N. Melosh, G. H. Fredrickson, B. F. Chmelka, G.D. Stucky, *Science*. 279 (1998) 548.
- [14] F. Farzaneh, J. Taghavi, R. Malakooti, M. Ghandi, *J. Mol. Catal. A: Chem.* 244 (2006) 252-257.
- [15] T. Tsoncheva, M. Järn, D. Paneva, M. Dimitrov, I. Mitov, *Micro. Meso. Mater.* 137 (2011) 56-64.
- [16] F. Zhang, Yan, H. Yang, Y. YanMeng, C. Yu, B. Tu, D. Zhao, *J. Phys. Chem. B.* 109 (2005) 8723-8732.
- [17] Z. Li, C. Kübel, V.I. Pârvulescu, R. Richards, *ACS Nano*. 2 (2008) 1205-1212.
- [18] M. Wolters, L.J.W. van Grotel, T.M. Eggenhuisen, J.R.A. Sietsma, K.P. de Jong, P.E. de Jongh, *Catal. Today*. 163 (2011) 27-32.
- [19] S. Lambert, N. Job, L. D'Souza, M.F.R. Pereira, R. Pirard, B. Heinrichs, J.L. Figueiredo, J.-P. Pirard, J.R. Regalbutto, *J. Catal.* 261 (2009) 23-33.
- [20] K. Bourikas, J. Vakros, C. Fountzoula, C. Kordulis, A. Lycourghiotis, *Catal. Today*. 128 (2007) 138-144.
- [21] M. Imperor-Clerc, D. Bazin, M. D. Appay, P. Beaunier, A. Davidson, *Chem. Mater.* 16 (2004) 1813-1821.

- [22] J. Taghavimoghaddam, G.P. Knowles, A.L. Chaffee, *Top. Catalysis*. 55 (2012) 571-579.
- [23] D. Zhao, Q. Huo, J. Feng, B.F. Chmelka, G.D. Stucky, *J. Am. Chem. Soc.* 120 (1998) 6024-6036.
- [24] C. Dickinson, W. Zhou, R.P. Hodgkins, Y. Shi, D. Zhao, H. He, *Chem. Mater.* 18 (2006) 3088-3095.
- [25] X. Zhang, C. Yuan, M. Li, B. Gao, X. Wang, X. Zheng, *J. Non-Cryst. Solids*. 355 (2009) 2209-2215.
- [26] P.F. Fulvio, S. Pikus, M. Jaroniec, *ACS Appl. Mater. Interfaces*. 2 (2009) 134-142.
- [27] R. Zukerman, L. Vradman, L. Titelman, C. Weidenthaler, M.V. Landau, M. Herskowitz, *Micro. Meso. Mater.* 116 (2008) 237-245.
- [28] C.-B. Wang, C.-W. Tang, H.-C. Tsai, S.-H. Chien, *Catal. Lett.* 107 (2006) 223-230.
- [29] J.S. Yang, W.Y. Jung, G.D. Lee, S.S. Park, E.D. Jeong, H.G. Kim, S.-S. Hong, *J. Ind. Eng. Chem.* 14 (2008) 779-784.
- [30] C. Wang, S. Lim, G. Du, C.Z. Loebicki, N. Li, S. Derrouiche, G.L. Haller, *J. Phys. Chem. C*. 113 (2009) 14863-14871.
- [31] K. Kaneko, *J. Membr. Sci.* 96 (1994) 59-89.
- [32] X. Liu, L. Li, Y. Du, Z. Guo, T.T. Ong, Y. Chen, S.C. Ng, Y. Yang, *J. Chromatogr. A*. 1216 (2009) 7767-7773.
- [33] A.H. Janssen, C.M. Yang, Y. Wang, F. Schüth, A.J. Koster, K.P. de Jong, *J. Phys. Chem. B*. 107 (2003) 10552-10556.
- [34] P. Van Der Voort, P.I. Ravikovitch, K.P. De Jong, M. Benjelloun, E. Van Bavel, A.H. Janssen, A.V. Neimark, B.M. Weckhuysen, E.F. Vansant, *J. Phys. Chem. B*. 106 (2002) 5873-5877.
- [35] L.F. Liotta, G. Pantaleo, A. Macaluso, G. Di Carlo, G. Deganello, *Appl. Catal. A: Gen.* 245 (2003) 167-177.
- [36] G.A.H. Mekhemer, H.M.M. Abd-Allah, S.A.A. Mansour, *Colloid. Surface. A*. 160 (1999) 251-259.
- [37] S. Tuti, F. Pepe, *Catal. Lett.* 122 (2008) 196-203.
- [38] R. Xu, H.C. Zeng, *Langmuir*. 20 (2004) 9780-9790.
- [39] J. Li, X. Xu, Z. Hao, W. Zhao, *J. Porous Mater.* 15 (2008) 163-169.
- [40] T. Kang, Y. Park, K. Choi, J.S. Lee, J. Yi, *J. Mater. Chem.* 14 (2004) 1043-1049.
- [41] T. Tsoncheva, L. Ivanova, C. Minchev, M. Fröba, *J. Colloid Interface Sci.* 333 (2009) 277-284.
- [42] M. K. Naskar, M. Eswaramoorthy, *J. Chem. Sci.* 120 (2008) 181-186.
- [43] J. Sun, H. Zhang, D. Ma, Y. Chen, X. Bao, A. Klein-Hoffmann, N. Pfander, D.S. Su, *Chem. Commun.* (2005) 5343-5345.
- [44] F. Jiao, H. Frei, *Angew. Chem. Int. Ed.* 48 (2009) 1841-1844.
- [45] I.J. Shannon, T. Maschmeyer, G. Sankar, J.M. Thomas, R.D. Oldroyd, M. Sheehy, D. Madill, A.M. Waller, R.P. Townsend, *Catal. Lett.* 44 (1997) 23.

Title and graphic for table of content:

# Impact of low cobalt loading on the morphology and dispersion of the crystalline $\text{Co}_3\text{O}_4$ patches supported on SBA-15



### 3.5 Appendix

#### 3.5.1 Wide-angle XRD

Figure 1 shows the wide-angle XRD patterns of SBA-15 supported  $\text{Co}_3\text{O}_4$  (30 wt%) calcined at different temperatures. The characteristic peaks of  $\text{Co}_3\text{O}_4$  can be observed even when the calcination temperature was as low as 200 °C. This is attributed to the decomposition of  $(\text{NO}_3)^-$  ions which apparently occurred before 200 °C [1]. The intensity and the broadness of the peaks did not change noticeably, which suggests that the particles size remained roughly the same for the composites calcined at different temperatures. It is suggested that since  $\text{Co}_3\text{O}_4$  nanorods were formed inside the adjacent pores, with in the confinement of silica walls, increasing the calcination temperature did not affect their crystal size due to the aggregation.

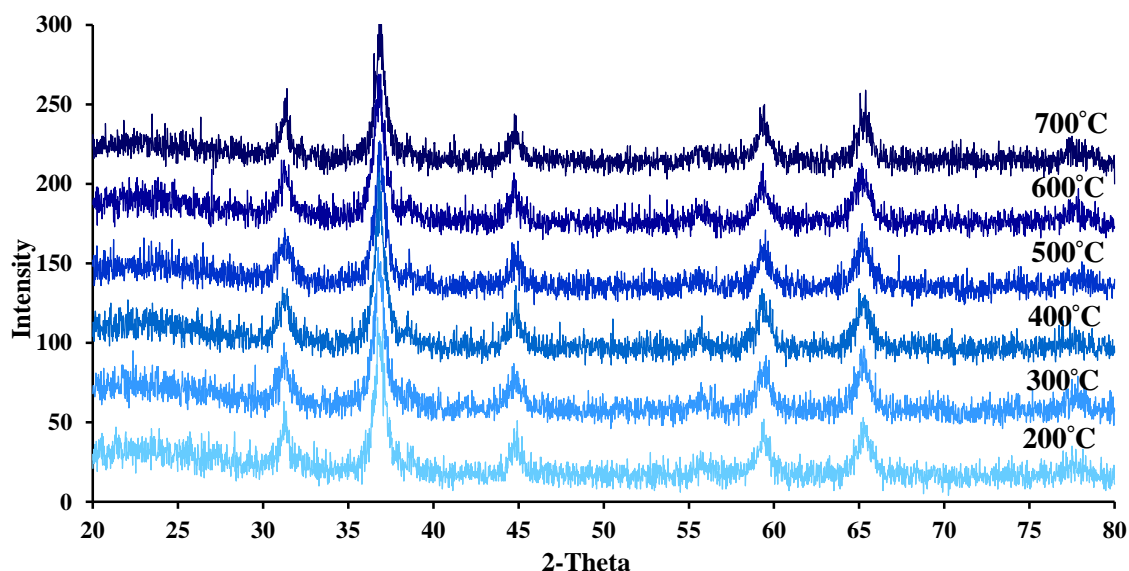


**Figure 1.** Wide-angle XRD patterns of SCo-30 calcined at different temperature

#### 3.5.2 Scanning transmission electron microscopy and elemental mapping

Figure 2 shows the STEM and elemental mapping profiles of SCo-5 and SCo-30. The growth of  $\text{Co}_3\text{O}_4$  nanorods in the adjacent pores of SBA-15 can be clearly observed in both cases. These rods are connected to each other through bridges, which were originally micropores, and have formed patches. The patches are evenly dispersed throughout the support. The length and width of the patches are proportional to the Co-loading. It is clear that the composite with 30 wt% Co-loading has more extensive patches than Co-composite with 5 wt% Co.

The elemental mapping profiles for these Co-composites confirmed that the patches consist of cobalt with a patch size that increases with the Co-loading.

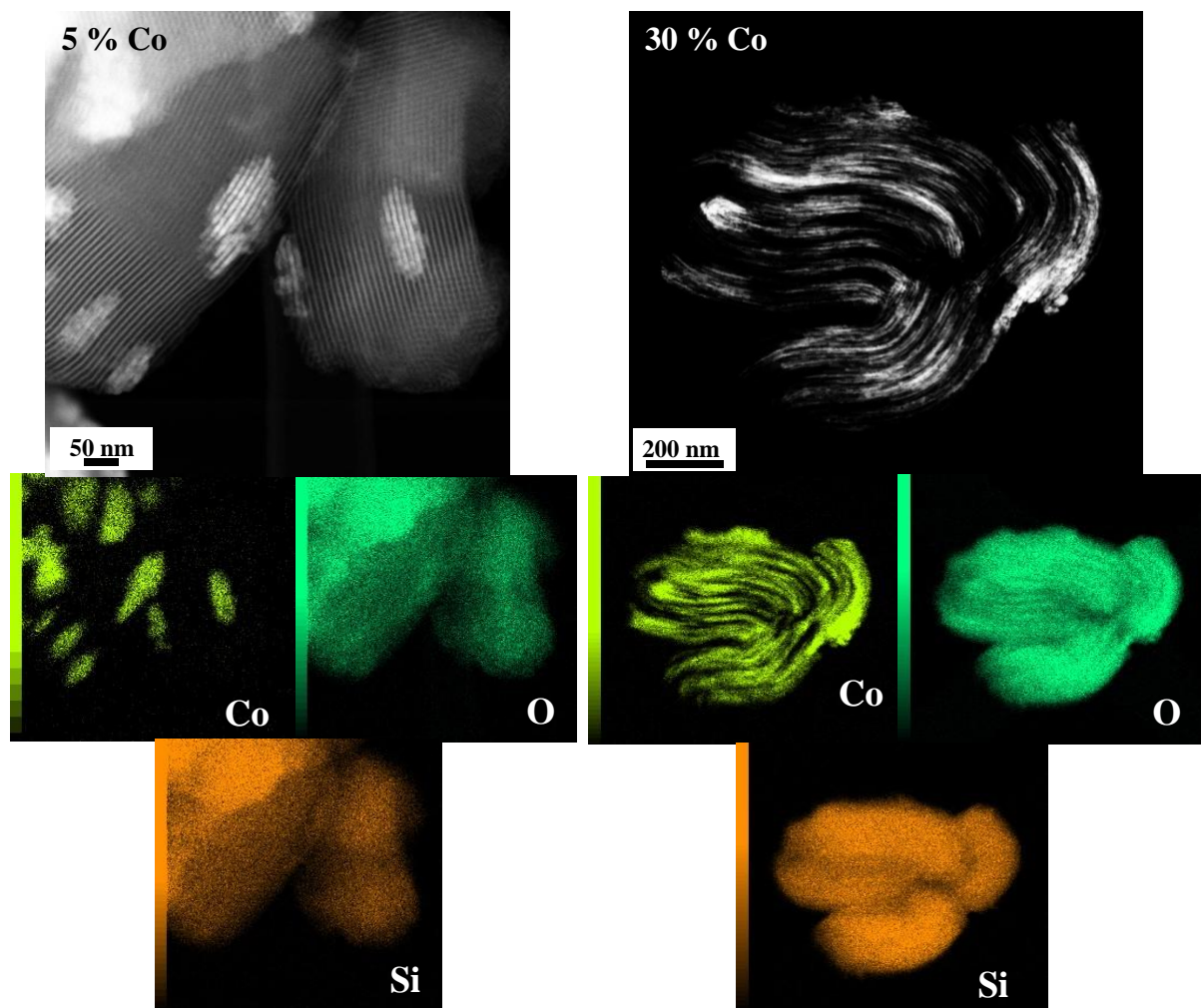


**Figure 2.** STEM images and elemental mapping of SCo-5 and SCo-30

### 3.5.3 Reference

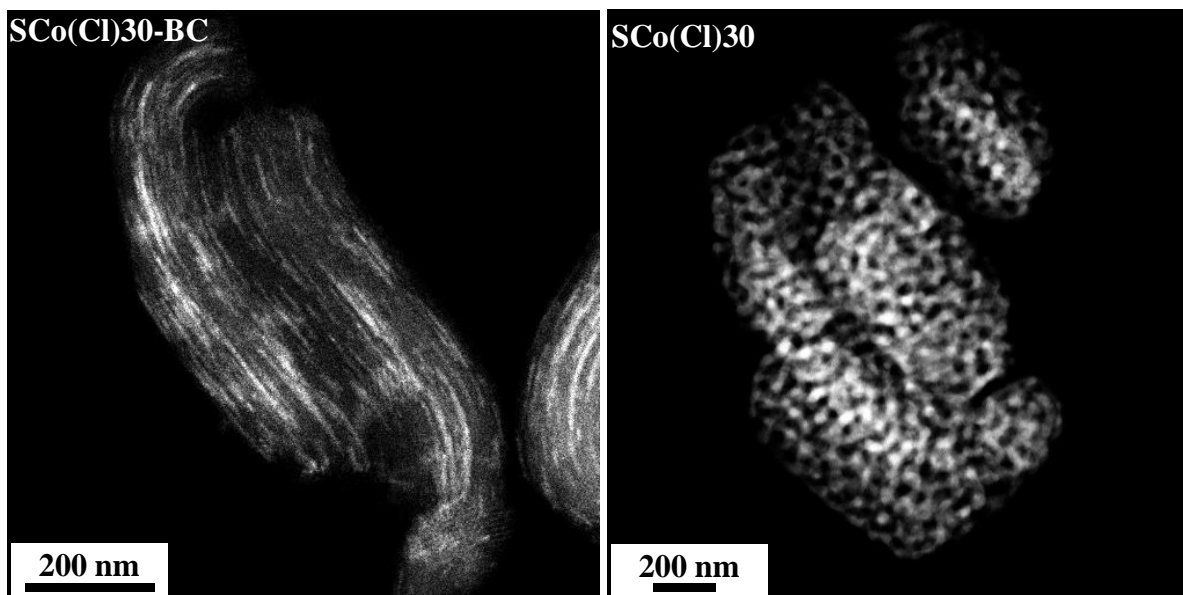
- [1] J.-S. Girardon, A.S. Lermontov, L. Gengembre, P.A. Chernavskii, A. Griboval-Constant, A.Y. Khodakov, *J. Catal.* 230 (2005) 339-352.

---

# Chapter 4

## SBA-15 supported cobalt oxide from $\text{CoCl}_2 \cdot 6\text{H}_2\text{O}$

---



## 4.1 General overview

Chapter four comprises of two publications; a communication paper and a full paper. This chapter also contains an appendix with supplementary information which was not included in the publications however validates the results which were discussed in the journal articles in this chapter.

Publication 1, (section 4.2) concerns the preparation of highly dispersed cobalt oxide species supported on SBA-15, using  $\text{CoCl}_2 \cdot 6\text{H}_2\text{O}$  as cobalt precursor, via the two-solvent-method. Co-composites with various Co-loadings (5 wt%, 10 wt%, 20 wt%, 30 wt% and 40 wt%) were prepared. Regardless of the preparation method the Co-composites displayed a blue coloration with intensity proportional to the Co-loading. At higher loadings ( $\geq 30$  wt % Co) unexpected morphological changes were observed upon calcination. These changes resulted in collapse of the highly ordered (SBA-15) channels of the support, however the cobalt remained highly dispersed throughout the support. DR UV-vis and XPS analyses suggest that the cobalt exists as  $\text{Co}^{2+}$  in a tetrahedral co-ordination, consistent with the aforementioned blue coloration.

Publication 2, (section 4.3) concerns the preparation of a series of Co-composites in which SBA-15 type silica was loaded with  $\text{CoCl}_2 \cdot 6\text{H}_2\text{O}$  via the two-solvent method, impregnation or adsorption. These Co-composites were prepared to investigate the effects of the cobalt precursor, preparation method and Co-loading on the final composites morphology and catalytic activity. The use of  $\text{CoCl}_2 \cdot 6\text{H}_2\text{O}$  as the precursor always resulted in blue composites with highly dispersed cobalt throughout the support after calcination. Thus, there appears to be strong interaction between  $\text{Co}^{2+}$  and the oxygen of the silica walls, but this cobalt is amorphous (non-crystalline). All the Co-composites in this study demonstrated high activity in the liquid phase oxidation of cyclohexanol with TBHP. Some cobalt leakage was observed in this system such that it might appropriately be described as a mixed heterogeneous-homogeneous system. The Co-composites prepared from  $\text{CoCl}_2 \cdot 6\text{H}_2\text{O}$  exhibited higher catalytic activity than those prepared from  $\text{Co}(\text{NO}_3)_2 \cdot 6\text{H}_2\text{O}$  (chapter 3). This can be attributed to the higher dispersion of active species in the former composites and/or the leakage of cobalt into the solution.

Appendix 4.4 contains  $^{29}\text{Si}$  MAS-NMR obtained from SBA-15 and Co-composites with 5 wt%, 10 wt% and 30 wt% Co-loading respectively. The information in the appendix has not

been presented in the publications; however it supports the logic and conclusions reached in the published work.

**Declaration for Thesis Chapter 4.2**

Cobalt precursor impact on the dispersion and morphological development of SBA-15 supported cobalt oxide species

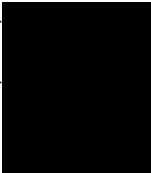
**Declaration by candidate**

In the case of Chapter 4 the nature and extent of my contribution to the work was the following:

Nature of contribution	Extent of contribution (%)
Come up with the original idea, prepared and analysed samples, identified major issues, performed the majority of interpretations and fully drafted papers and conclusions (80%)	80%

The following co-authors contributed to the work. Co-authors who are students at Monash University must also indicate the extent of their contribution in percentage terms:

Name	Nature of contribution	Extent of contribution (%) for student co-authors only
Tim Williams	STEM and elemental mapping method development, initial revision of the manuscript	N/A
Alan L. Chaffee	Supervision and refinement of manuscript	N/A

Candidate's Signature		Date 23.10.2012
-----------------------	--	--------------------

**Declaration by co-authors**

The undersigned hereby certify that:

- (1) the above declaration correctly reflects the nature and extent of the candidate's contribution to this work, and the nature of the contribution of each of the co-authors.
- (2) they meet the criteria for authorship in that they have participated in the conception, execution, or interpretation, of at least that part of the publication in their field of expertise;
- (3) they take public responsibility for their part of the publication, except for the responsible author who accepts overall responsibility for the publication;
- (4) there are no other authors of the publication according to these criteria;
- (5) potential conflicts of interest have been disclosed to (a) granting bodies, (b) the editor or publisher of journals or other publications, and (c) the head of the responsible academic unit; and
- (6) the original data are stored at the following location(s) and will be held for at least five years from the date indicated below:

Location(s)	School of Chemistry, Clayton Campus
-------------	-------------------------------------

Tim Williams		Date 22.10.2012
Alan L. Chaffee		Date 22.10.2012

## 4.2 Cobalt precursor impact on the dispersion and morphological development of SBA-15 supported cobalt oxide species

Jamileh Taghavimoghaddam<sup>a</sup>, Tim Williams<sup>b</sup>, Alan L. Chaffee<sup>a†</sup>

<sup>a</sup>School of Chemistry, Monash University, Victoria 3800 Australia

<sup>b</sup>Monash Centre for Electron Microscopy, Monash University, VIC 3800, Australia

**ABSTRACT:** Highly dispersed cobalt oxide species supported on SBA-15 were obtained when  $\text{CoCl}_2 \cdot 6\text{H}_2\text{O}$  was loaded using the two-solvent method. At higher loadings ( $\geq 30$  wt % Co) unexpected morphological changes were observed upon calcination. These changes resulted in distortion of the pore periodicity, nevertheless the Co remained highly dispersed throughout the resulting composite due to the strong interaction with the silica support. The composite materials had a blue coloration with intensity proportional to the cobalt loading. This feature, together with evidence from DR UV-Vis and XPS analyses, suggests that the cobalt exists as  $\text{Co}^{2+}$  in a tetrahedral co-ordination.

**KEYWORDS:** Mesoporous silica SBA-15, Morphology, Cobalt oxide, Dispersion, Structural transformation

### 4.2.1 Introduction

Interesting composite materials can be prepared by introducing metal precursors into the pores of ordered mesoporous silicas such as HMS [1], MCM-41 [2] and SBA-15 [3]. The subsequent calcination or reduction of the as-synthesized materials forms the corresponding metal or metal oxide. In such systems the silica substrate provides high surface area on which metal or metal oxide particles can be dispersed to provide highly

---

<sup>†</sup> Corresponding author. Tel.: [REDACTED]  
E-mail address: [REDACTED] (A.L. Chaffee).

accessible active sites. This property offers a wide range of applications in the nanotechnology field, such as removal of volatile organic compounds [4] and catalysis [5]. Among mesoporous silicas SBA-15 has attracted considerable attention due to its relatively high surface area ( $600\text{-}1000\text{ m}^2\text{ g}^{-1}$ ), larger pore diameter and thicker pore walls (5-30 nm) [6].

Cobalt oxides bulk or supported have wide range of applications which make them an interesting field of research in both industry and academia. They have been used to catalyse Fischer-Tropsch synthesis [7], NO<sub>x</sub> reduction [8] and various oxidation reactions [4, 9, 10]. They have also been exploited in sensors [11], magnetic nanomaterials [12] and electrodes in supercapacitors [13].

We have recently reported a thorough investigation on the impact of loading cobalt oxide onto SBA-15 via various techniques [14, 15]. In these cases  $\text{Co}(\text{NO}_3)_2 \cdot 6\text{H}_2\text{O}$  was used as the metal precursor. When the cobalt was deposited into the SBA-15 channels via the ‘two-solvent’ method [16], the formation of  $\text{Co}_3\text{O}_4$  patches that were comprised of nanorods interconnected through the SBA-15 micropores was observed [15, 17]. These nanorods filled the individual mesopores of the SBA-15, while its morphology was preserved. As the loading of Co was increased the mesopores became increasingly filled with Co. This was clearly evidenced by decrease in the surface area and pore volume of the composites relative to the pure SBA-15 [15].

In extending our investigations to employ other cobalt precursors,  $\text{CoCl}_2 \cdot 6\text{H}_2\text{O}$  was “nanocast” into the pores of SBA-15, using the “two-solvent” method [16]. The structural and chemical properties of the composites were probed by scanning electron microscopy (SEM), high angle annular dark field (HAADF) STEM, elemental mapping, diffuse reflectance ultraviolet-visible spectroscopy (DR UV-Vis) and X-ray photoelectron spectroscopy (XPS). This communication reports unexpected changes in the composite structure at cobalt loadings  $\geq 30\text{ wt}\%$  only if  $\text{CoCl}_2 \cdot 6\text{H}_2\text{O}$  was used as the metal precursor.

## **4.2.2 Experimental**

### **4.2.2.1 Material preparation**

Synthesis of SBA-15 was carried out using the method first described by Zhou and co-workers [3]. All the cobalt composites were prepared using the two-solvent method

[16] with a slight modification. In this method SBA-15 was first dispersed in n-hexane (hydrophobic solution) and stirred for 15 min. Then the desired amount of the metal precursor,  $\text{Co}(\text{NO}_3)_2 \cdot 6\text{H}_2\text{O}$  or  $\text{CoCl}_2 \cdot 6\text{H}_2\text{O}$ , was dissolved in water of a volume corresponds to the pore volume of the SBA-15 determined by  $\text{N}_2$  adsorption-desorption. This aqueous solution was then added drop-wise to the hydrophobic solution and the mixture stirred for 15 min. Next, the mixture was sonicated for 15 min and stirred for further 2 h. The solid was recovered by filtration and air dried overnight. Finally the composite was calcined by heating in air at  $2\text{ }^\circ\text{C min}^{-1}$ , then holding at  $700\text{ }^\circ\text{C min}^{-1}$  for 6 h.

#### 4.2.3 Characterization methods

*N<sub>2</sub>-physorption isotherms* were obtained at  $-196\text{ }^\circ\text{C}$  on a Coulter Omnisorb 360-CX gas sorption analyser. Samples were outgassed at  $150\text{ }^\circ\text{C}$  overnight prior to analysis. Pore volume, BET surface area and the pore size distribution (PSD) (BJH method) were calculated for each data set.

*Scanning electron microscopy (SEM)* was carried out using a JEOL 7001F field emission gun scanning electron microscope.

*Scanning Transmission Electron Microscopy (STEM)* was carried out using a JEOL 2100F microscope equipped with a high angular annular dark field (HAADF) detector (camera length 10 cm and 0.5 nm probe) to collect elemental mapping profiles.

*Diffuse reflectance UV-Vis (DR UV-Vis)* spectra were measured at room temperature in air on a Cary 500 Scan UV-Vis-NIR photometer over the range from 200 to 800 nm.

*X-ray photoelectron spectroscopy (XPS)* was conducted at the Australian Synchrotron with a SPECSlab2 spectrometer using an Al  $K\alpha$  X-ray source (1486.8 eV) at the constant analyzer pass energy 40.0 eV. Binding energies are referenced to the carbon 1s peak (BE = 284.5 eV) arising from adventitious carbon.

#### 4.2.4 Results and discussion

Fig.1 demonstrates the SEM images of both the SBA-15 and all the cobalt composites prepared either from  $\text{Co}(\text{NO}_3)_2 \cdot 6\text{H}_2\text{O}$  or  $\text{CoCl}_2 \cdot 6\text{H}_2\text{O}$ . It can be seen that the individual particles of the composite materials are typically  $1\text{ }\mu\text{m}$  long and 300 nm wide, very similar to the SBA-15 support material itself (Fig. 1a). They often have a

straight, curved or even U-shaped appearance (Fig. 1b-d). These overall particle dimensions are common to all composites regardless of Co loading or precursor.

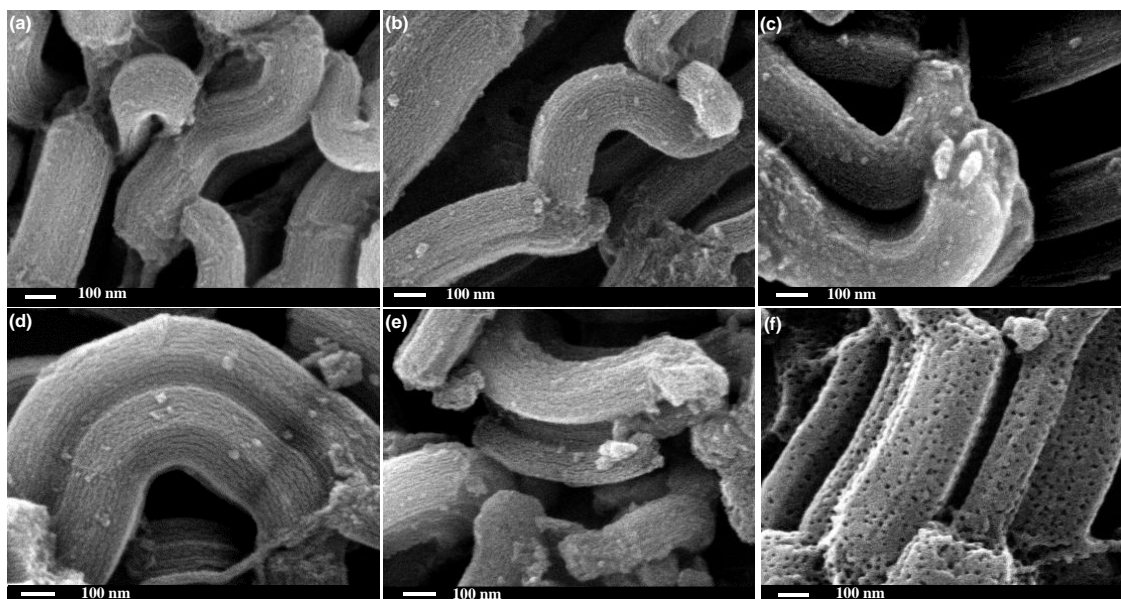


**Figure 1.** SEM images of (a) SBA-15, (b) SCo-5(Cl), (c) SCo-5(N), (d) SCo-30(N), (e) SCo-30(Cl) before calcination and (f) SCo-30(Cl). Labels: S – refers to support; 5, 10 and 30 refer to Co loading; (N) refers to nitrate precursor, (Cl) refers to chloride precursor.

When  $\text{Co}(\text{NO}_3)_2 \cdot 6\text{H}_2\text{O}$  was used as the metal precursor, the morphology of the support was preserved even at Co loading as high as 30 wt% (Fig. 1 c and d). This preservation in the support structure is common to the composites prepared from  $\text{CoCl}_2 \cdot 6\text{H}_2\text{O}$  at Co loadings less than 30 wt%. However, to our surprise, at higher Co loadings  $\geq 30$  wt% a significant structural transformation occurred during calcination. As can be seen in Fig. 1e, the overall size and shape of the individual particles was maintained, however the morphology within the individual particles changed significantly. This new morphology appears as a continuous surface with randomly distributed cavities approximately 20 nm in diameter. The surface area of this new morphology was  $47 \text{ m}^2 \cdot \text{g}^{-1}$ , considerably less than the values of  $655 \text{ m}^2 \cdot \text{g}^{-1}$  determined for the precursor SBA-15.

Fig.2 demonstrates the STEM images and elemental mapping profiles of the composites prepared from either  $\text{Co}(\text{NO}_3)_2 \cdot 6\text{H}_2\text{O}$  and  $\text{CoCl}_2 \cdot 6\text{H}_2\text{O}$ . At Co loadings of 1–20 wt% ( $\text{CoCl}_2 \cdot 6\text{H}_2\text{O}$ ) the cobalt oxide species did not aggregate into patches but

were evenly dispersed throughout the SBA-15 matrix (Fig. 2a). In these cases, the SBA-15 micro/mesopore structure remained intact after calcination and the channels can be seen on the surface of the SBA-15 particles (Fig. 1b). The surface area and porosity of these composites was approximately inversely proportional to the Co loading. The cobalt dispersion remains similarly high, even in the morphologically transformed composites which formed at high Co loading (Fig. 2b). Thus, the Co distribution differs very significantly from cases where  $\text{Co}(\text{NO}_3)_2 \cdot 6\text{H}_2\text{O}$  was used as precursor (Fig. 2c).

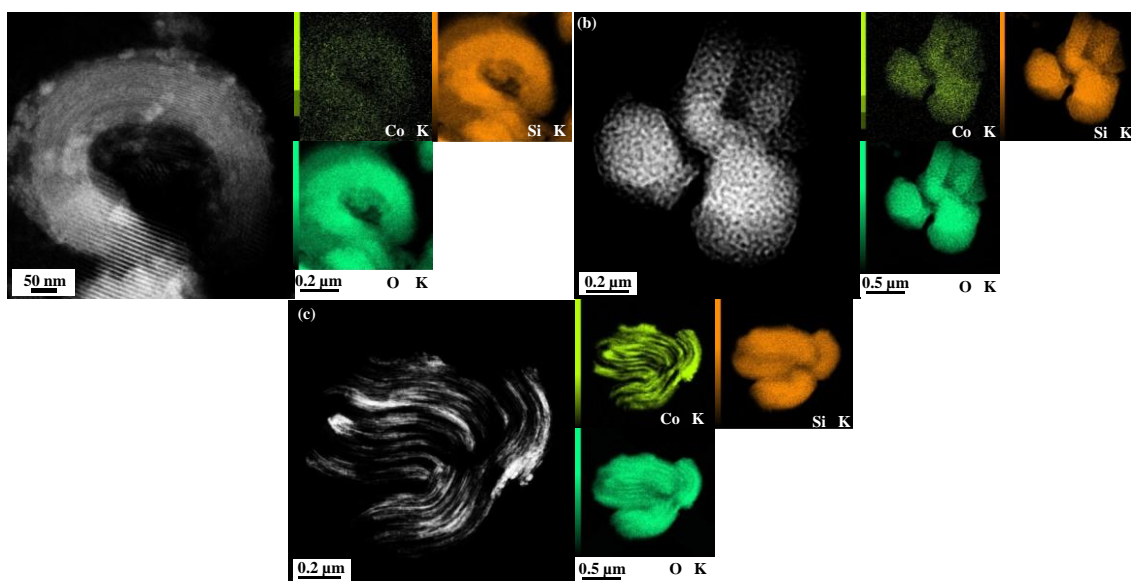


**Figure 2.** HAADF-STEM images and elemental mapping (a) SCo-5(Cl), (b) SCo-30(Cl) and (c) SCo-30(N)

Upon loading with either precursor, the colour of all composites was pink before calcination, suggesting that the cobalt was present as  $\text{Co}^{2+}$  with octahedral co-ordination of residual  $\text{H}_2\text{O}$  molecules. A blue coloration, with intensity proportional to the Co loading, developed for all the composites prepared from  $\text{CoCl}_2 \cdot 6\text{H}_2\text{O}$  after calcination at  $700\text{ }^\circ\text{C}$ . This observation suggests that, for these composites, the cobalt is present as  $\text{Co}^{2+}$  with tetrahedral co-ordination. Presumably the coordinating ligands after calcination are the silica oxygen atoms [18]. This differs from the black colour of the composites prepared from  $\text{Co}(\text{NO}_3)_2 \cdot 6\text{H}_2\text{O}$ .

When  $\text{Co}(\text{NO}_3)_2 \cdot 6\text{H}_2\text{O}$  was used as precursor, X-ray diffraction (XRD) indicated the presence of crystalline  $\text{Co}_3\text{O}_4$ , which formed as nanorods and patches within the SBA-15 substrate's mesopores [14, 15]. For the composites prepared from  $\text{CoCl}_2 \cdot 6\text{H}_2\text{O}$ , however, the Co did not crystallize upon calcination and remained in an amorphous

state. In the case where  $\text{Co}(\text{NO}_3)_2 \cdot 6\text{H}_2\text{O}$  was used as precursor, it was observed that crystallisation of  $\text{Co}_3\text{O}_4$  commenced during calcination at a temperature of about 200 °C. This is presumably associated with the fact that the nitrate counter ion starts decomposing at lower temperatures than this [19]. By contrast, it is known that  $\text{CoCl}_2 \cdot 6\text{H}_2\text{O}$  dehydrates and then decomposes above 500 °C [20], hence the crystallisation of  $\text{Co}_3\text{O}_4$  is clearly hindered due to the nature of the counter ion.

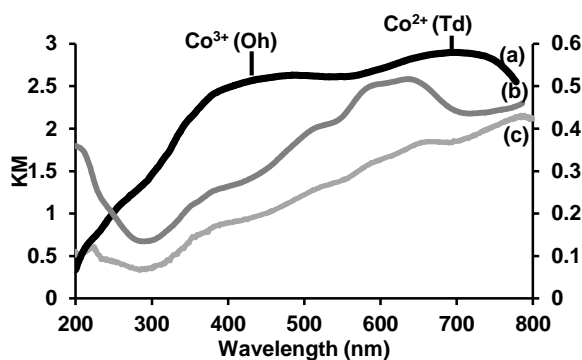


**Figure 3.** DR UV-Vis spectra of SCo-30(N), SCo-30(Cl) and SCo-5(Cl)

The nature of the cobalt species was investigated more comprehensively by DR UV-Vis and the results are shown in Fig. 3. For composites prepared from  $\text{Co}(\text{NO}_3)_2 \cdot 6\text{H}_2\text{O}$  the two broad absorption bands at 428 nm and 727 nm associated with the presence of spinel  $\text{Co}_3\text{O}_4$  was previously reported [14]. However, the DR UV-Vis spectra for both SCo-5(Cl) and SCo-30(Cl) are quite different. Here an intense broad absorption band in the 520-725 nm region was observed which is attributed to the triplet d-d electron transitions;  ${}^4\text{A}_2(\text{F}) \rightarrow {}^4\text{T}_1(\text{P})$ ,  ${}^4\text{A}_2(\text{F}) \rightarrow {}^4\text{T}_1(\text{F})$  and  ${}^4\text{A}_2(\text{F}) \rightarrow {}^4\text{T}_2(\text{F})$  characteristic of  $\text{Co}^{2+}$  in tetrahedral co-ordination [21]. There is also a weak absorption band at around 380 nm which can be assigned to  $\text{O}^{2-} \rightarrow \text{Co}^{2+}$  charge transfer [22]. It is interesting to note that based on DR UV-Vis results, the co-ordination sphere of the Co seems to be unaffected by the phase transformation. This is because the spectra of both the SCo-5(Cl) and SCo-30(Cl) samples are similar, except for the intensity of the absorption bands. These results correlate well with the colour of the composites.

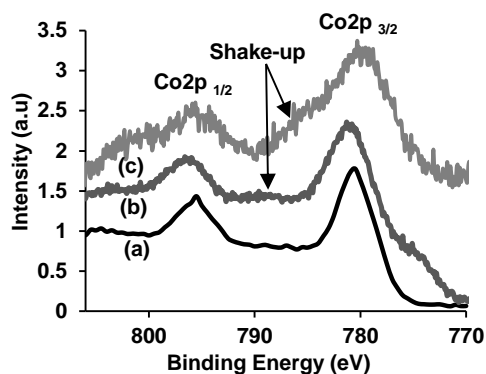


**Figure 4.** XPS spectra of (a) commercial  $\text{Co}_3\text{O}_4$ , (b) SCo-30(N) and (c) SCo-30(Cl)

X-ray photoelectron spectroscopy (XPS) was used for further investigation of the chemical environment and surface composition of both composites (Fig. 4). In all cases, a spin orbit doublet at around  $780.5 \pm 0.3$  and  $795.5 \pm 0.8$  eV is observed which indicates the presence of  $\text{Co}^{3+}$  and  $\text{Co}^{2+}$  [4]. The asymmetry of the  $\text{Co}2p_{3/2}$  component depends on the dominant oxidation state of the surface Co species with  $\text{Co}^{3+}$  at lower and  $\text{Co}^{2+}$  at higher binding energy (BE). The shape of the  $\text{Co}2p_{3/2}$  for SCo-30(Cl) relative to SCo-30(N) and commercial  $\text{Co}_3\text{O}_4$ , suggests that  $\text{Co}^{2+}$  is the dominant phase in the former composite [23].

The spin orbit splitting ( $\Delta E$ ) can also be used to distinguish the oxidation state of the Co-composites. This is known to be 16 eV and 15 eV for  $\text{Co}^{2+}$  and  $\text{Co}^{3+}$  respectively [24]. The  $\Delta E$  in this work was measured to be 16 eV and 15 eV for SCo-30(Cl) and SCo-10(N) respectively. Furthermore, a shallow feature appearing at 9 eV higher than  $\text{Co}2p_{3/2}$  refers to the “shake-up satellite” which is associated with  $\text{Co}^{2+}$  species [25]. It is obvious from the spectra that the shake-up satellite is stronger (shoulder) for SCo-30(Cl) compared to other samples.

#### 4.2.5 Conclusion

Although  $\text{CoCl}_2 \cdot 6\text{H}_2\text{O}$  has previously been used as a catalyst precursor [26], to the best of our knowledge, there are no prior reports of its use in combination with the two-solvent method for incorporating the active metal within a mesoporous substrate. It was observed that this approach provides composite materials with more highly dispersed Co. The blue colouration together with the DR UV-Vis and XPS data indicates that cobalt is present mainly as  $\text{Co}^{2+}$  tetrahedral coordinated to the oxygen of the silica support. At cobalt loadings at or above 30 wt%, the interaction between the Co and the

support may be the reason for the morphological transformation that occurs upon calcination.

The high Co dispersion that is apparent in the composites made with  $\text{CoCl}_2 \cdot 6\text{H}_2\text{O}$  as precursor may make these materials more attractive as catalysts than those prepared from  $\text{Co}(\text{NO}_3)_2 \cdot 6\text{H}_2\text{O}$ . Their application as oxidation catalysts is under investigation in this laboratory.

### **Acknowledgment**

Financial support from the Australia Research Council Discovery program and scholarship support from the Monash Research Graduate School and the Faculty of Science, Monash University (to JT) is gratefully acknowledged. The authors acknowledge use of the facilities and the assistance of Dr. Xi-Ya Fang at Monash Centre for Electron Microscopy. This research was supported under the Australian Research Council's Centres of Excellence funding scheme (COE for Design in Light Metals).

### **4.2.6 References**

- [1] D. Sellam, M. Bonne, S. Arrii-Clacens, G. Lafaye, N. Bion, S. Tezkratt, S. Royer, P. Marécot, D. Duprez, *Catal. Today*. 157 (2010) 131-136.
- [2] J.S. Beck, J.C. Vartuli, W.J. Roth, M.E. Leonowicz, C.T. Kresge, K.D. Schmitt, C.T.W. Chu, D.H. Olson, E.W. Sheppard, *J. Am. Chem. Soc.* 114 (1992) 10834-10843.
- [3] D. Zhao, J. Feng, Q. Huo, N. Melosh, G. H. Fredrickson, B. F. Chmelka, G.D. Stucky, *Science*. 279 (1998) 548.
- [4] T. Garcia, S. Agouram, J.F. Sánchez-Royo, R. Murillo, A.M. Mastral, A. Aranda, I. Vázquez, A. Dejoz, B. Solsona, *Appl. Catal. A: Gen.* 386 (2010) 16-27.
- [5] S. Vetrivel, A. Pandurangan, *J. Mol. Catal. A: Chem.* 227 (2005) 269-278.
- [6] X. Liu, L. Li, Y. Du, Z. Guo, T.T. Ong, Y. Chen, S.C. Ng, Y. Yang, *J. Chromatogr. A*. 1216 (2009) 7767-7773.
- [7] G. Prieto, A. Martínez, R. Murciano, M.A. Arribas, *Appl. Catal. A: Gen.* 367 (2009) 146-156.
- [8] J.M. Planeix, N. Coustel, B. Coq, V. Brotons, P.S. Kumbhar, R. Dutartre, P. Geneste, P. Bernier, P.M. Ajayan, *J. Am. Chem. Soc.* 116 (1994) 7935-7936.
- [9] J. Li, X. Xu, Z. Hao, W. Zhao, *J. Porous Mater.* 15 (2008) 163-169.
- [10] Q. Tang, Q. Zhang, H. Wu, Y. Wang, *J. Catal.* 230 (2005) 384-397.
- [11] P. M. Ajayan, O. Stephan, C. Colliex, D. Trauth, *Science*. 265 (1994) 1212-1214.
- [12] Z.-C. Di, J. Ding, X.-J. Peng, Y.-H. Li, Z.-K. Luan, J. Liang, *Chemosphere*. 62 (2006) 861-865.

- [13] A.C. Dillon, K.M. Jones, T.A. Bekkedahl, C.H. Kiang, D.S. Bethune, M.J. Heben, *Nature*. 386 (1997) 377-379.
- [14] J. Taghavimoghaddam, G.P. Knowles, A.L. Chaffee, *Top. Catalysis*. 55 (2012) 571-579.
- [15] J. Taghavimoghaddam, G. P. Knowles, A.L. Chaffee, *J. Mol. Catal. A: Chem.* 358 (2012) 79-88.
- [16] M. Imperor-Clerc, D. Bazin, M. D. Appay, P. Beaunier, A. Davidson, *Chem. Mater.* 16 (2004) 1813-1821.
- [17] F. Jiao, H. Frei, *Angew. Chem. Int. Ed.* 48 (2009) 1841-1844.
- [18] C.C. Harrison, X. Li, I. Hopkinson, S.E. Stratford, A.G. Orpen, *J. Chem. Soc. Faraday Trans.* 89 (1993) 4115-4122.
- [19] J.-S. Girardon, A.S. Lermontov, L. Gengembre, P.A. Chernavskii, A. Griboval-Constant, A.Y. Khodakov, *J. Catal.* 230 (2005) 339-352.
- [20] A. Abiona, J. Ajao, S. Chigome, J. Kana, G. Osinkolu, M. Maaza, *J. Sol-Gel Sci. Technol.* 55 (2010) 235-241.
- [21] Y. Okamoto, K. Nagata, T. Adachi, T. Imanaka, K. Inamura, T. Takyu, *J. Phys. Chem.* 95 (1991) 310-319.
- [22] S. Dzwigaj, M. Che, *J. Phys. Chem. B.* 110 (2006) 12490-12493.
- [23] Y. Xia, H. Dai, H. Jiang, L. Zhang, *Catal. Commun.* 11 (2010) 1171-1175.
- [24] Y. Okamoto, H. Nakano, T. Imanaka, S. Teranishi, *Bull. Chem. Soc. JPN.* 84 (1975) 1163-1168.
- [25] W.S. Epling, G.B. Hoflund, J.F. Weaver, S. Tsubota, M. Haruta, *J. Phys. Chem.* 100 (1996) 9929-9934.
- [26] C. Wang, S. Lim, G. Du, C.Z. Loebicki, N. Li, S. Derrouiche, G.L. Haller, *J. Phys. Chem. C.* 113 (2009) 14863-14871.

Monash University

**Declaration for Thesis Chapter 4.3**

SBA-15 supported cobalt oxide species: preparation, morphology and catalytic activity

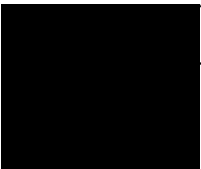
**Declaration by candidate**

In the case of Chapter 4 the nature and extent of my contribution to the work was the following:

Nature of contribution	Extent of contribution (%)
Come up with the original idea, prepared and analysed samples, identified major issues, performed the majority of interpretations and fully drafted papers and conclusions (80%)	80%

The following co-authors contributed to the work. Co-authors who are students at Monash University must also indicate the extent of their contribution in percentage terms:

Name	Nature of contribution	Extent of contribution (%) for student co-authors only
Gregory. P. Knowles	Method development, assist interpretation results and initial revision of the journal paper	N/A
Alan. L. Chaffee	Supervisory, assist interpretation results and editorial assistance	N/A

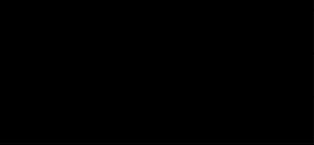
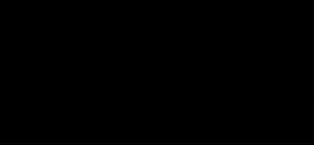
Candidate's Signature		Date	23.10.12
-----------------------	--	------	----------

**Declaration by co-authors**

The undersigned hereby certify

- (1) the above declaration correctly reflects the nature and extent of the candidate's contribution to this work, and the nature of the contribution of each of the co-authors.
- (2) they meet the criteria for authorship in that they have participated in the conception, execution, or interpretation, of at least that part of the publication in their field of expertise;
- (3) they take public responsibility for their part of the publication, except for the responsible author who accepts overall responsibility for the publication;
- (4) there are no other authors of the publication according to these criteria;
- (5) potential conflicts of interest have been disclosed to (a) granting bodies, (b) the editor or publisher of journals or other publications, and (c) the head of the responsible academic unit; and
- (6) the original data are stored at the following location(s) and will be held for at least five years from the date indicated below:

Location(s)	School of Chemistry, Clayton Campus
-------------	-------------------------------------

Gregory. P. Knowles		Date	22.10.12
Alan. L. Chaffee		Date	22.10.12

### 4.3 SBA-15 supported cobalt oxide species: preparation, morphology and catalytic activity

Jamileh Taghavimoghaddam, Gregory P. Knowles and Alan. L. Chaffee

School of Chemistry, Monash University, Victoria 3800 Australia

#### Abstract

SBA-15 type silica was loaded with  $\text{CoCl}_2 \cdot 6\text{H}_2\text{O}$  via either the two-solvent method, impregnation or adsorption and then calcined to prepare a range of supported cobalt oxides with varying Co-loadings. The various materials were prepared to investigate the effects of the preparation methods and the Co-loading on the final composite morphology and catalytic activity. A variety of methods: XRD,  $\text{N}_2$  adsorption, TPR, XPS, DR UV-vis, FT-IR, ICP-MS, SEM, HRTEM and TEM were used to characterize the Co-composites. Each of the products had a blue color with intensity proportional to the Co-loading. DR UV-vis and XPS binding energies are consistent with the presence of  $\text{Co}^{2+}$  in tetrahedral co-ordination. cobalt was found to be highly dispersed throughout the SBA-15 support, where it is associated with the channel walls, suggesting there is good interaction between  $\text{Co}^{2+}$  and the oxygen of the silica walls. An unexpected morphological transformation was observed in composites prepared with Co-loadings of 30 wt% or more such that the original SBA-15 channels were no longer present. Nevertheless, all the composite materials exhibited high activity in catalyzing the liquid phase oxidation of cyclohexanol using tert-butylhydroperoxide (TBHP) as an oxidant. Some leakage of the catalytically active species into the solution was observed, implying that the catalyst is behaving as a mixed heterogeneous-homogeneous system. Thus, the high catalytic activity for these Co-composites can be attributed to either high dispersion of the active sites throughout the support or the presence of active species in solution.

**Keywords:** Mesoporous silica SBA-15; Tert-butylhydroperoxide; Cobalt oxide; Oxidative catalyst; Two-solvent method; Cobalt (II) tetrahedral

### 4.3.1 Introduction

Catalytic oxidations and epoxidations of readily available organic substrates can provide a wide range of functionalized molecules including alcohols, ketones, epoxides and carboxylic acids [1, 2]. For example the oxidation of cyclohexanol to cyclohexanone is a significant commercial transformation. In 1995, 1.1 trillion pounds of cyclohexanone was produced in America, most of which was used for the manufacture of Nylon 6 and Nylon 66 [3]. Due to the industrial importance of cyclohexanone production a great deal of effort has been expended to develop promising catalytic systems [4].

Heterogeneous catalysts have a number of advantages over homogeneous analogues. Since they can be more easily separated and recovered, while also producing less waste, they are favorable from both industrial and environmental points of view. Transition metal-based heterogeneous catalysts have been extensively investigated. Various transition metal-based heterogeneous catalysts have been used for cyclohexanol oxidation with promising results [5-8]

The catalytic potential of the transition metal-based catalysts is limited when they are used in bulk because of their low surface area [9, 10]. Therefore transition metal/metal oxides are usually dispersed on high surface area supports. This approach allows a greater proportion of the metal/metal oxide to be accessible to the reaction substrate, i.e., it provides higher 'active surface area' and, consequently, improves catalytic performance. For this reason, ordered mesoporous silica materials, such as MCM-48 [11], HMS [12] MCM-41 [13] and SBA-15 [14] have attracted enormous attention. Among these, MCM-41 and SBA-15 have been extensively investigated [15]. SBA-15 is often preferred over MCM-41 due to its larger pore diameter, thicker pore walls and consequent higher thermal and hydrothermal stability [14, 16].

Cobalt oxides, in both bulk and supported forms, have been widely investigated due to their interesting structure and surface redox reactivity [17, 18]. Cobalt can occur in two oxidation states,  $\text{Co}^{2+}$  and  $\text{Co}^{3+}$ , which are thermodynamically competitive under common ambient conditions. The two main cobalt oxide species,  $\text{CoO}$  and  $\text{Co}_3\text{O}_4$ , are both stable in the natural environment [19]. Pure  $\text{CoO}$  is difficult to obtain and small amounts of  $\text{Co}_3\text{O}_4$  and metallic cobalt always occur as impurities [20]. These oxides are

involved in many advanced physical applications such as sensors [21], supercapacitors [22] as well as catalytic applications such as, CO oxidation and methane combustion [23, 24]. Metallic cobalt particles formed by the reduction of the cobalt oxides have also been used for Fischer-Tropsch synthesis, (FTs) [25, 26].

It is well known that the nature and dispersion of the metal oxide species are the most important factors in determining the catalytic activity and selectivity of the supported catalysts [27-29]. The nature of the metal precursor [30], the preparation method [31] and metal loading [32, 33], among other factors, are also known to affect the morphology and dispersion of the metal oxide species on the support.

We recently investigated the effect of Co-loading and preparation method on the morphology and dispersion of the resulting SBA-15 supported cobalt oxide [33, 34]. To prepare the Co-composites,  $\text{Co}(\text{NO}_3)_2 \cdot 6\text{H}_2\text{O}$  was deposited on SBA-15 via the two-solvent method [35], impregnation and adsorption. Irrespective of preparation method, spinel  $\text{Co}_3\text{O}_4$  patches were formed on the SBA-15 with their size proportional to the Co-loading. The two-solvent method of catalyst preparation resulted in the formation of  $\text{Co}_3\text{O}_4$  patches located inside the pores of the SBA-15, whereas the conventional impregnation method resulted in formation of  $\text{Co}_3\text{O}_4$  patches on both the internal and external surfaces. In the series of composites prepared via the two-solvent method, the catalytic performance in liquid phase oxidation of cyclohexanol was found to be in reverse proportion to the Co-loading [33].

In the present study  $\text{CoCl}_2 \cdot 6\text{H}_2\text{O}$  was used as the cobalt precursor. The morphology, dispersion and structure of the cobalt oxide species supported on SBA-15 were characterized by X-ray diffraction (XRD),  $\text{N}_2$  adsorption-desorption, temperature programmed reduction (TPR), X-ray photoelectron spectroscopy (XPS), diffuse reflectance ultraviolet-visible spectroscopy (DR UV-vis), fourier transform infrared (FTIR), inductively coupled plasma-mass spectrometry (ICP-MS), scanning electron microscopy (SEM) and transmission electron microscopy (TEM) and high resolution transmission electron microscopy (HRTEM). The catalytic performance of the Co-composites for cyclohexanol oxidation in the presence of TBHP was also investigated and the conversion and product selectivity were determined by gas chromatography (GC) and gas chromatography-mass spectrometry (GC-MS).

## 4.3.2 Experimental

### 4.3.2.1 Preparation of SBA-15 and Co-composites

Mesoporous silica SBA-15 was prepared using the method first described by Zhao and co-workers [14]. SBA-15 supported cobalt oxide species were prepared using the “two-solvent” method with a slight modification. The detailed procedure is provided elsewhere [33]. However in this work after cobalt was loaded on SBA-15 via the two-solvent method, solid samples were recovered by filtration and air dried at room temperature overnight. The Co-composites are referred to as SCo(Cl)X, where S represents SBA-15, Co(Cl): CoCl<sub>2</sub>.6H<sub>2</sub>O as cobalt precursor and X the nominal Co-loading in wt%. Co-composites were also prepared via adsorption (SCo(Cl)5-A) and conventional impregnation (SCo(Cl)5-I) [33]. In order to study the effect of the calcination process on the morphological transformation of SCo(Cl)30, this composite was also isolated before the calcination (BC) process and investigated. This composite is referred to as SCo(Cl)30-BC. It is noteworthy that in this work the starting SBA-15 had been calcined at 550 °C, whereas all the Co-composite products were calcined at 700 °C.

### 4.3.2.2 Characterization techniques

*Low-angle XRD* patterns were obtained with a Bruker D8 Focus powder diffractometer with a monochromatic CuK<sub>α</sub> source radiation ( $\lambda=1.5406 \text{ \AA}$ ) operated at 40 kV and 30 mA over  $2\theta$  range of 0.5-4°. Data was collected with a step size of 0.02° and a step time of 0.1° min<sup>-1</sup>.

*N<sub>2</sub> adsorption-desorption isotherms* were obtained at -196 °C on a Coulter Omnisorb 360-CX gas sorption analyzer. Samples were outgassed at 150 °C overnight prior to analysis. Pore volume, BET surface area [17] and the pore size distribution, PSD, (BJH method) [14] were calculated for each data set.

TPR experiments were carried out with a Setaram Thermogravimetric Analyser (TAG24). Typically 10 mg of the calcined composite was flushed with high purity argon (Ar) at 150 °C for 2 h, to drive off moisture, and then cooled to 20 °C. Next, the flow was switched to 10 % H<sub>2</sub>/Ar and the temperature raised at 5 °C min<sup>-1</sup> to 900 °C, where it was held for 20 min under 10 % H<sub>2</sub>/Ar, and then 20 min under pure Ar. The

gas flow rate over the sample was maintained at  $70 \text{ cm}^3 \text{ min}^{-1}$ . The weight of the samples both before and after analysis was also separately measured with an analytical balance.

*FTIR* spectra were collected via a BIO-RAD FTS 40 spectrometer. Samples were diluted 1/300 in dry KBr, then pressed into pellets (under vacuum) prior to analysis.

ICP-MS was carried out using a GBC OPTIMAS 9500 ICP-MS. Prior to measurement all composites were digested with  $\text{HNO}_3$  and HF [36].

DR UV-vis was carried out using a Cary 5000 UV-Vis-NIR spectrophotometer, fitted with the diffuse reflectance accessory.

TEM and HRTEM were carried out using a JEOL 2011 transmission electron microscope (accelerating voltage 200 kV) equipped with a  $\text{LaB}_6$  emitter (point resolution 0.21 nm)

SEM was carried out using a JEOL 7001F field emission gun scanning electron microscope.

XPS was conducted at the Australian Synchrotron with a SPECSlab2 spectrometer using the synchrotron as an X-ray source with selected wavelength of 1486.8 eV and a constant analyzer pass energy 40.0 eV. Binding energies are referenced to the carbon 1s peak (BE = 284.5 eV) arising from adventitious carbon.

GC was carried out on an Agilent 6850 gas chromatograph equipped with an FID detector and a polar capillary column (BP20, 60 m  $\times$  0.25 mm). GC-MS was carried out using an Agilent 5973 MS (source conditions: EI, 70 eV, 200 °C) coupled a 6890 series GC system with a capillary column (HP5, 30 m  $\times$  0.25 mm).

#### **4.3.2.3 Catalytic tests**

The liquid phase oxidation of cyclohexanol was performed in a round bottomed flask. In each test, the catalyst (contain  $9 \times 10^{-3}$  g of cobalt) was added to acetonitrile (5 ml) containing cyclohexanol (20 mmol) and chlorobenzene (internal standard, 200  $\mu\text{l}$ ). It should be noted that the cobalt concentration was kept at  $9 \times 10^{-3}$  g for all the reactions and thus different masses of composites were employed. After reaching the reflux temperature (83 °C) the oxidant, TBHP, (24 mmol) was added to the mixture dropwise.

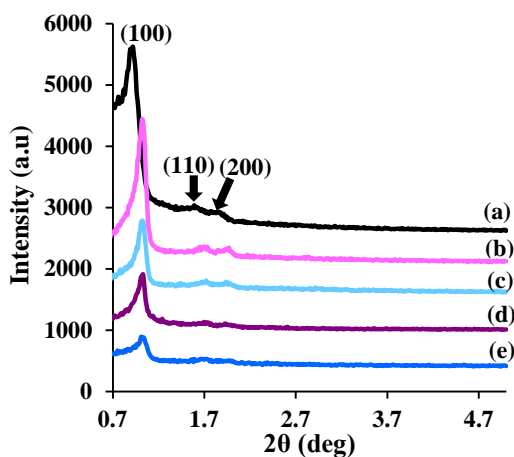
No attempt was made to exclude air from the reaction. The reactions were monitored using GC and GC-MS by withdrawing samples every 4 h up to 24 h.

### 4.3.3 Results and discussion

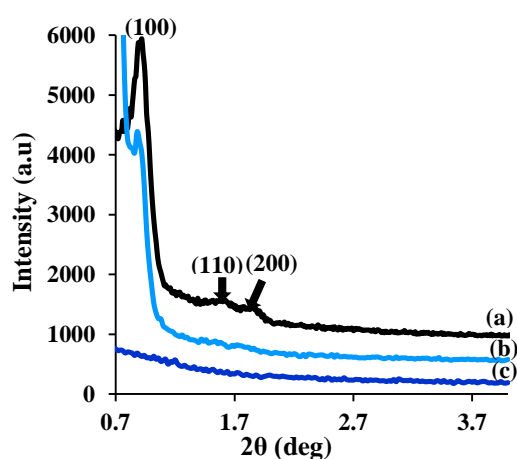
#### 4.3.3.1 Composites characterization

##### 4.3.3.1.1 X-ray Diffraction (XRD)

Fig. 1 shows the low-angle XRD patterns of mesoporous silica SBA-15 and some of the Co-composites prepared via different methods and at various Co-loadings. SBA-15 itself displayed three well-resolved peaks, which are indexed to (100), (110) and (200) diffractions in the hexagonal space group  $p6mm$ . This indicates the presence of highly ordered hexagonal mesoporous structure [17]. The XRD patterns of samples with low amounts of Co-loading (SCo(Cl)5, SCo(Cl)10, SCo(Cl)5-A and SCo(Cl)5-I) are similar to that of SBA-15. This signifies that the integrity of the porous structure of SBA-15 was preserved after loading cobalt via different methods. The intensity of the (100) diffraction peak decreased after Co-loading which can be attributed to a reduction in the extent of periodicity of the SBA-15. In addition, the (100) peak shifted slightly towards higher  $2\theta$  upon Co-loading. This suggests that the mesoporous network of the Co-composites shrank upon calcination at 700 °C [36].



**Fig. 1.** Low-angle XRD pattern of (a) SBA-15, (b) SCo(Cl)5-A, (c) SCo(Cl)5, (d) SCo(Cl)5-I and (e) SCo(Cl)10



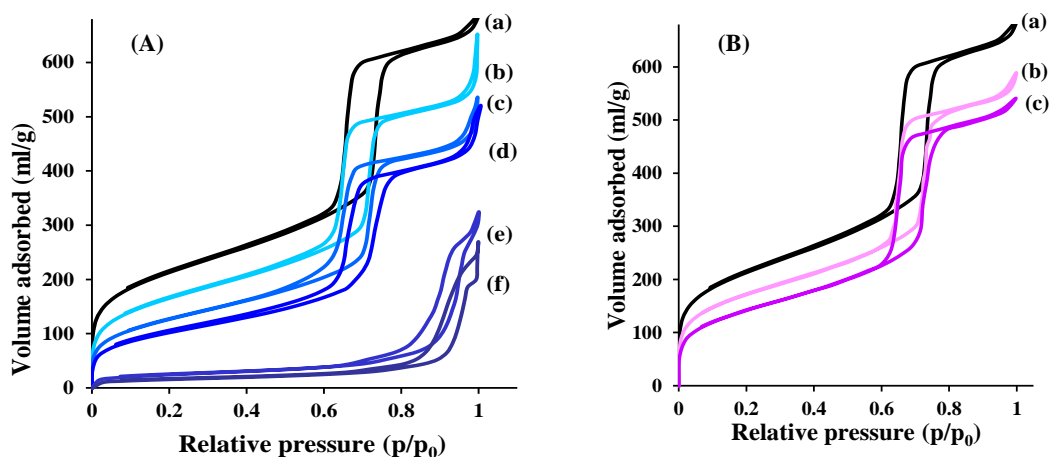
**Fig. 2.** Low-angle XRD pattern of (a) SBA-15, (b) SCo(Cl)30-BC and (c) SCo(Cl)30

Fig.2 gives the XRD pattern of SBA-15, SCo(Cl)30 and SCo(Cl)30-BC. It can be seen that at 30 wt% Co-loading, prior to calcination, SCo(Cl)30-BC, the mesoporosity of the support was preserved. However, the XRD pattern of SCo(Cl)30, after calcination, did not show any characteristic diffraction peaks related to the mesoporous silica. This suggests that the periodicity of the composite was lost during the calcination step. A similar structural change was reported for Cs<sub>2</sub>O-MCM-41 with 22 wt% Cs-loading [37]. However, no such effect was observed at 30 wt% loading when Co(NO<sub>3</sub>)<sub>2</sub>.6H<sub>2</sub>O was used as the precursor [33].

#### 4.3.3.1.2 N<sub>2</sub> adsorption-desorption

Fig. 3A and B show the N<sub>2</sub> adsorption-desorption isotherms of the SBA-15 and all the Co-composites. The textural parameters of these composites, including BET surface area, average pore diameter, total pore volume and micropore volume, are also summarized in Table 1. Generally, the adsorption branch of SBA-15 type mesoporous silica consists of three important regions: (1) the region  $p/p_0 < 0.20$  is associated with the presence of intrawall micropores which connect mesoporous channels; (2) the region  $0.20 < p/p_0 < 0.45$  is associated with multilayer N<sub>2</sub> adsorption in the ordered mesopores; (3) the region  $p/p_0 = 0.55-0.85$  where capillary condensation of N<sub>2</sub> occurs in the mesopores. Each isotherm also includes a desorption branch which provides complementary information about the PSD [38]. All the samples except SCo(Cl)30 and SCo(Cl)40 showed type IV isotherms with H1-type hysteresis loops, typical for mesoporous materials with 2D hexagonal channels. Fig. 3A shows the isotherms of SBA-15 itself and the Co-composites synthesized via the two-solvent method. SBA-15, SCo(Cl)5, SCo(Cl)10 and SCo(Cl)20 presented isotherms of similar shape, indicative of the preservation of the mesoporous structure for relatively low Co-loadings. Thus these results are consistent with those obtained by low-angle XRD.

However two changes occurred in the isotherms of the low Co-loading composites as Co-loading increased. Firstly, the capillary condensation region shifted to lower partial pressure. At the same time the volume of adsorbed N<sub>2</sub> decreased in both the microporous and mesoporous regions. These changes, along with decrease in the calculated surface areas of the Co-composites, are attributed to the existence of cobalt oxide species inside the pores (Table 1) [39, 40].



**Fig. 3.** N<sub>2</sub> adsorption-desorption isotherm A: (a) SBA-15 (b) SCo(Cl)5, (c) SCo(Cl)10, (d) SCo(Cl)20, (e) SCo(Cl)30 and (f) SCo(Cl)40 and B: (a) SBA-15, (b) SCo(Cl)5-A and (c) SCo(Cl)5-I

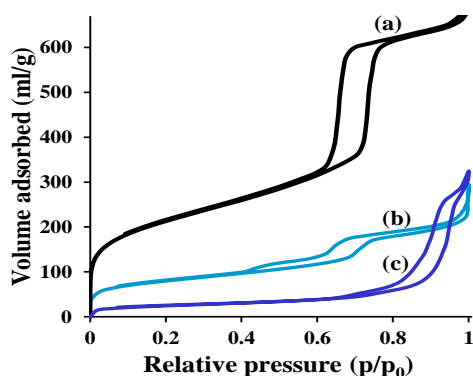
In the case of SCo(Cl)30 and SCo(Cl)40 the capillary condensation region shifted to a higher relative pressure  $p/p_0 = 0.8-0.95$ , which is generally associated with mesopores of pore diameter larger than 20 nm [41]. The amount of N<sub>2</sub> adsorbed across the  $p/p_0$  range increased sharply from 42 to 305 ml g<sup>-1</sup> and 34 to 247 ml g<sup>-1</sup> for SCo(Cl)30 and SCo(Cl)40, respectively. This is due to the capillary condensation in larger pores relative to SBA-15, and accounts for about 80 % of the total N<sub>2</sub> adsorption. Thus it appears that SCo(Cl)30 underwent a significant morphological transformation during calcination. The volume of N<sub>2</sub> adsorbed by SCo(Cl)30 in the micropore region was a factor of 15 less than that adsorbed by SBA-15. However the volume of adsorbed N<sub>2</sub> in the micropore region only decreased by factor of 5 for SCo(Cl)30 relative to SCo(Cl)30BC, This suggests that the microporosity of the support is significantly changed upon loading 30 wt% cobalt.

Fig. 3B displays N<sub>2</sub> adsorption-desorption isotherms of SBA-15 and Co-composites prepared via adsorption and impregnation. The isotherms of these composites were of identical shape to that of SBA-15, indicative of structural preservation of SBA-15 during composites preparation. However, the micropore and mesopore volumes decreased after Co-loading. The decrease in the volume of adsorbed N<sub>2</sub> was more pronounced for the composite prepared by impregnation and can be attributed to higher actual Co-loading in that composite (see section 4.3.3.1.5).

**Table 1** N<sub>2</sub> adsorption-desorption data for SBA-15 and Co-composites

Sample	BET (m <sup>2</sup> g <sup>-1</sup> )	Dp (nm)	V <sub>micro</sub> (cm <sup>3</sup> g <sup>-1</sup> )	V <sub>t</sub> (cm <sup>3</sup> g <sup>-1</sup> )
SBA15	655	6.2	0.31	0.98
SCo(Cl)5	439	6.0	0.24	0.80
SCo(Cl)10	390	6.0	0.18	0.67
SCo(Cl)20	341	6.0	0.15	0.63
SCo(Cl)30	47	7/25	0.02	0.45
SCo(Cl)40	47	7/25	0.02	0.41
SCo(Cl)5-I	403	6.2	0.20	0.67
SCo(Cl)5-A	555	6.0	0.25	0.82
SCo(Cl)30-BC	285	5.8	0.11	0.3

When comparing lower Co-loading composites with SCo(Cl)30-BC, it can be seen that the volume of adsorbed N<sub>2</sub> in both micropores and mesopores was much lower in the latter (Fig. 4). This is attributed to the presence of cobalt precursor inside the pores, which appears to block a large fraction of both the micropores and mesopores. The isotherm of SCo(Cl)30-BC exhibited capillary condensation in the range of  $p/p_0 = 0.45$ -0.8, in a manner similar to SCo(Cl)10 and SCo(Cl)20. In addition a shoulder was observed on the desorption branch of the SCo(Cl)30-BC isotherm which can be attributed to partial pore blockage due to the presence of the cobalt precursor [33].

**Fig. 4.** N<sub>2</sub> adsorption-desorption isotherm of (a) SBA-15, (b) SCo(Cl)30-BC and (c) SCo(Cl)30

The PSD of the Co-composites are shown in Fig. 5A and B. The pore diameter was calculated from the desorption branch of the isotherms using the BJH method [14]. SBA-15, SCo(Cl)5, SCo(Cl)10, SCo(Cl)5-A and SCo(Cl)5-I showed narrow PSDs, indicating the preservation of the mesoporous network after loading cobalt. In the case of SCo(Cl)30-BC, a bimodal PSD was observed with the first and second peaks centered at 3.5 nm and 5.8 nm (Fig. 5A inset). This is attributed to the partial pore blockage which suggests cobalt precursor was depositing against the walls of SBA-15.

The PSD for SCo(Cl)30 and SCo(Cl)40 (Fig. 5B) was significantly different from those for SBA-15 and the Co-composites with lower Co-loading. The two major differences are the existence of a much broader and bimodal PSD with the first peak centered at 7 nm and the second at approximately 25 nm. This signifies the morphological transformation of the mesoporous channels such that the pores are no longer uniform.

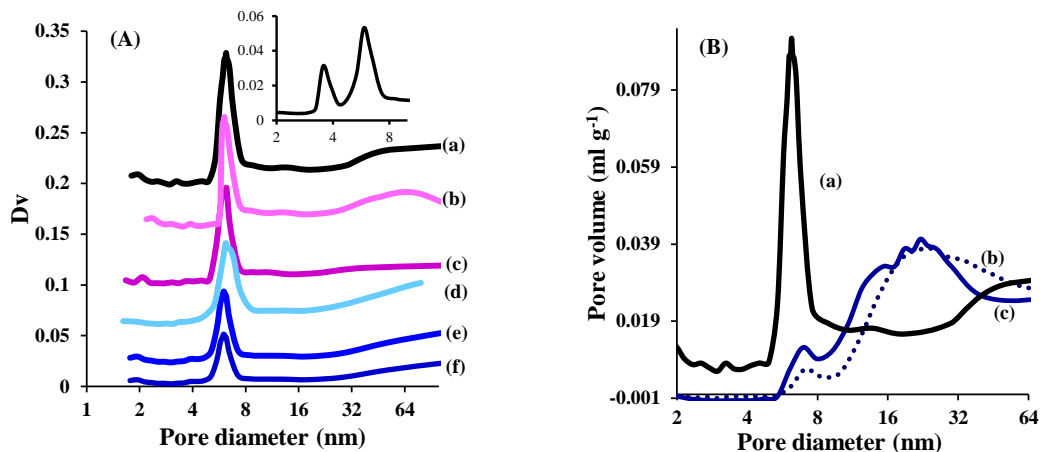


**Fig. 5.** (A) PSD of (a) SBA-15 (b) SCo(Cl)5-A, (c) SCo(Cl)5-I, (d) SCo(Cl)5, (e) SCo(Cl)10, (f) SCo(Cl)20, inset (SCo(Cl)30-BC) and (B) PSD of (a) SBA-15, (b) SCo(Cl)30 and (c) SCo(Cl)40

#### 4.3.3.1.3 Scanning electron microscopy

Fig. 6 shows SEM images of SBA-15 and some Co-composites. The SBA-15 images show that it consists of rod-like structural units or particles that are aggregated from end to end and in parallel to form a rope-like macrostructure [42]. The particles have straight, wavy and even curved shapes (Fig. 6c, d and e). The width and length of the particles are on average about  $220 (\pm 20)$  nm and  $900 (\pm 50)$  nm, respectively. Many parallel stripes can be observed on the surface of these particles and can be attributed to the uniform array of hexagonal channels, which are characteristic of the SBA-15 structure.

After loading cobalt below 30 wt% no significant changes were observed in the morphology of the Co-composites. This is in agreement with the results obtained from XRD and  $N_2$  adsorption-desorption. However, increasing the Co-loading to 30 wt% and beyond caused significant changes to the morphology of the particles. As can be seen in Fig. 6e and f, the surface of the particles no longer showed the parallel stripes but,

instead, cavities with diameters in the range 20-30 nm. However, the overall macroscopic morphology of the composite particles appeared similar to that of the particles in SBA-15 type composites with lower Co-loading.

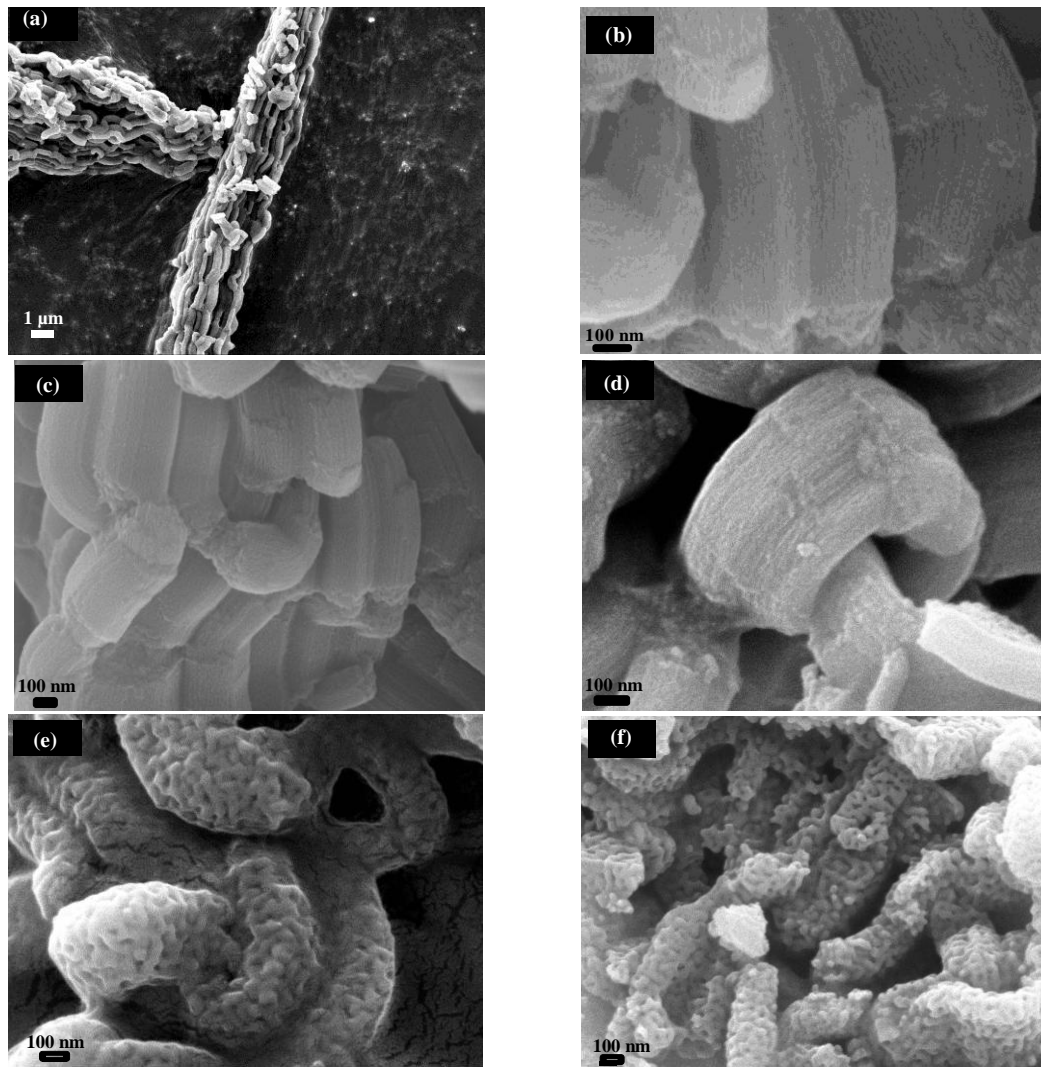


**Fig. 6.** SEM images of (a, b) SBA-15, (c) SCo(Cl)5, (d) SCo(Cl)10, (e) SCo(Cl)30 and (f) SCo(Cl)40

#### 4.3.3.1.4 Transmission electron microscopy

Fig. 7 shows the overall morphology of SBA-15 and some Co-composites at higher magnification. The parallel channels could be observed when the electron beam was perpendicular to the channels. However when the electron beam was parallel to the channels, the highly ordered honeycomb-like structure was observed (white circles) [33]. Fig. 7a illustrates a curved particle with the internal channels clearly visible. Due to electronic contrast the channels are white and the silica walls are grey [33].

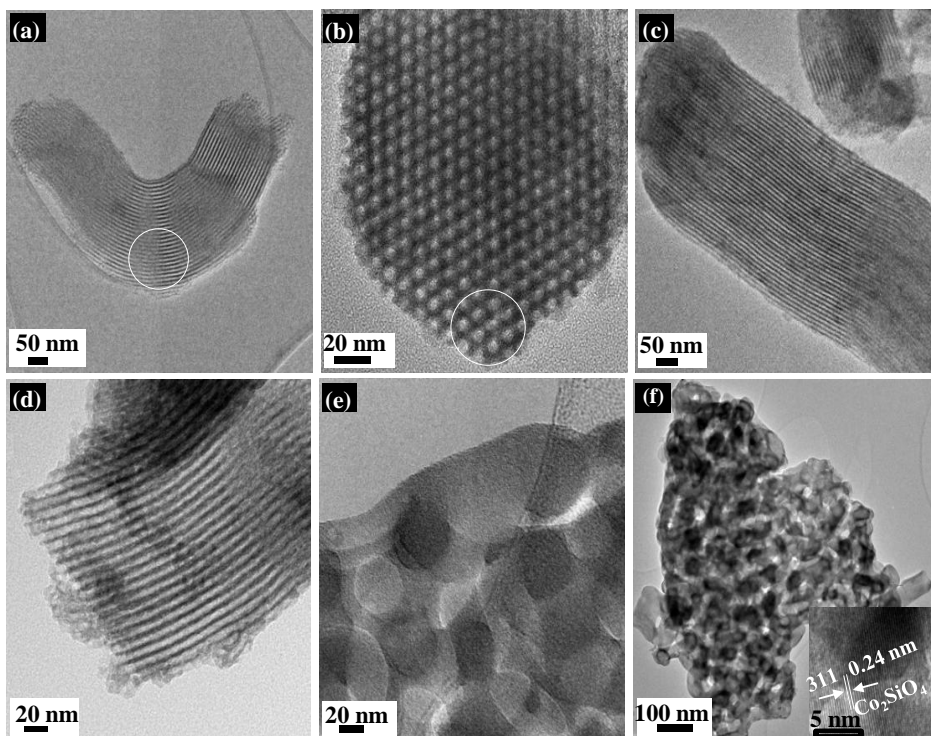


**Fig. 7.** TEM images obtained from (a) SBA-15, (b) SCo(Cl)5, (c) SCo(Cl)10, (d) SCo(Cl)20 and (e, f) SCo(Cl)30

The Co-composites, SCo(Cl)5, SCo(Cl)10, SCo(Cl)20, exhibited the same morphological features as SBA-15. It is noteworthy that there was little contrast between the support and cobalt oxide species inside the pores. This was contrary to what was observed in composites with  $\text{Co}(\text{NO}_3)_2 \cdot 6\text{H}_2\text{O}$  as the metal precursor, where patches of  $\text{Co}_3\text{O}_4$  were observed throughout the SBA-15 [33]. Here, however, only some dark spots of dimension 2-3 nm, relatively well dispersed along the walls of the SBA-15 channels, were observed. In this case it appears that the cobalt oxide species are more effectively interacting with the silica walls, rather than aggregating as cobalt oxide clusters within the mesopores as observed with  $\text{Co}(\text{NO}_3)_2 \cdot 6\text{H}_2\text{O}$  as precursor.

Increasing the Co-loading to 30 wt% and beyond (SCo(Cl)30 and SCo(Cl)40) made the original mesoporosity of the SBA-15 unobservable. In these composites some darker areas which can be referred to as cobalt rich domains were observed. Fig. 8f inset shows a HRTEM image of SCo(Cl)30 with lattice fringes which correspond to cubic  $\text{Co}_2\text{SiO}_4$  (JCPDF file 00-029-0506, 0.24 nm lattice spacing of the (311) plane).

#### 4.3.3.1.5 Elemental analysis (ICP-MS)

The Co-content of the composites was measured after silica was digested in HF/HNO<sub>3</sub> and the results are summarized in Table 2. There was little difference between the actual and nominal Co-loading of the composites with lower loadings, prepared using either the two-solvent method or impregnation (SCo(Cl)5, SCo(Cl)10 and SCo(Cl)5-I). The composite that was made via adsorption, SCo(Cl)5-A, had the lowest Co-content. This is because the weak interaction between the cobalt precursor and support in the adsorption method results in low metal deposition. SCo(Cl)30, as expected, had the highest Co-content.

**Table 2 Elemental analysis results**

Catalyst	Nominal Co content (wt %)	Actual Co content (wt %)
SCo(Cl)5	5	4.8
SCo(Cl)10	10	9.2
SCo(Cl)30	30	22.0
SCo(Cl)5-I	5	5.0
SCo(Cl)5-A	5	1.0

#### 4.3.3.1.6 Diffuse reflectance UV-vis spectroscopy

Fig. 8A shows the DR UV-vis spectra of SCo(Cl)30 and SCo(Cl)30-BC. The UV-vis spectrum of SCo(Cl)30-BC exhibited a broad absorption band centered at 510 nm which is attributed to Co<sup>2+</sup> in octahedral co-ordination [43]. A triplet absorption band at around 610-700 nm was also observed for this composite and is attributed to the <sup>4</sup>A<sub>2</sub>(F) → <sup>4</sup>T<sub>1</sub>(P) d-d electron transition in [Co(H<sub>2</sub>O)<sub>4</sub>]<sup>2+</sup> [44].

The UV-vis spectrum for SCo(Cl)30 was quite different to that of SCo(Cl)30-BC. The spectrum of SCo(Cl)30 demonstrates a triplet at 539 nm, 613 nm and 664 nm. These bands are attributed to d-d electron transitions, <sup>4</sup>A<sub>2</sub>(F) → <sup>4</sup>T<sub>2</sub>(F), <sup>4</sup>A<sub>2</sub>(F) → <sup>4</sup>T<sub>1</sub>(F) and <sup>4</sup>A<sub>2</sub>(F) → <sup>4</sup>T<sub>1</sub>(P), characteristic of Co<sup>2+</sup> in tetrahedral co-ordination [2, 44-46].

The blue color of the sample, SCo(Cl)30 after calcination also signifies the presence of Co<sup>2+</sup> in tetrahedral co-ordination [2, 47, 48]. However the pink color of SCo(Cl)30BC before calcination suggests the presence of Co<sup>2+</sup> in octahedral co-ordination. This implies that during calcination the co-ordination chemistry underwent change. As a result cobalt could possibly coordinate to the oxygen of the silica wall. Harrison et al. reported a similar phenomenon when CoCl<sub>2</sub>.6H<sub>2</sub>O was loaded onto silica

gel glasses via impregnation. He reported color changes of the composites after filtration, drying and calcination processes and investigated the co-ordination chemistry of cobalt ions by means of DR UV-vis [43].

In this work, there were three ligands with the potential to co-ordinate to cobalt before calcination;  $\text{Cl}^-$ , superficially adsorbed  $\text{H}_2\text{O}$  and oxygen atoms from silica. Upon calcination the first two ligands were presumably volatilized as a result of decomposition and thus the oxygen atoms from the surface silica remained the only available ligands to co-ordinate to cobalt (Fig. 8B).

A broad band with low intensity can also be observed at around 400 nm, which can be attributed to the presence of  $\text{Co}^{3+}$  in octahedral co-ordination. Thus it can be suggested that a fraction of cobalt precursor was oxidized to spinel  $\text{Co}_3\text{O}_4$  and coexisted with the dominant  $\text{Co}^{2+}$  in tetrahedral co-ordination [33].

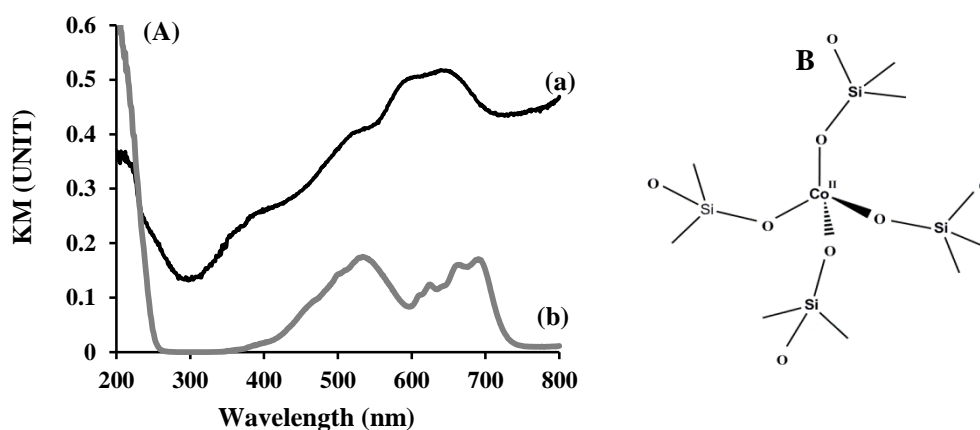
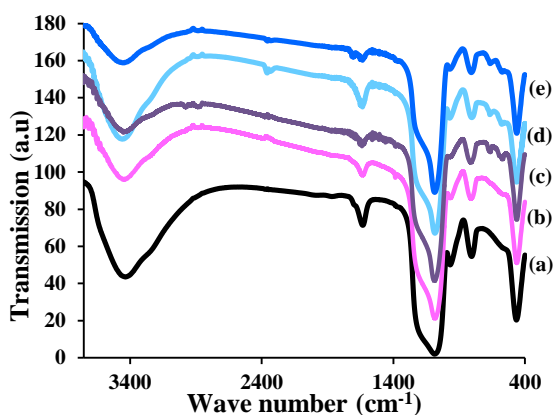


**Fig. 8.** (A) DR UV-vis spectrum of (a) SCo(Cl)30, (b) SCo(Cl)30-BC and (B) Schematic structure of  $\text{Co}^{2+}$  species

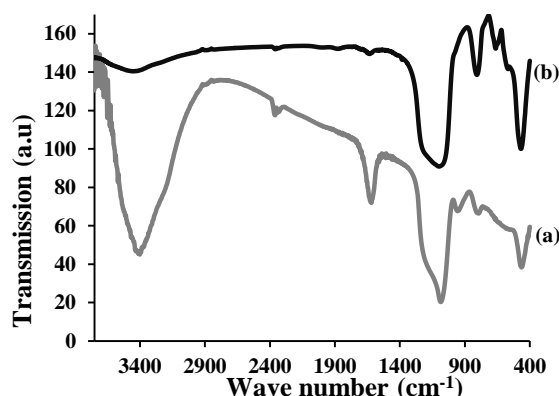
#### 4.3.3.1.7 Fourier transform infrared spectroscopy

Fig. 9 shows the FTIR spectra of SBA-15 and all the Co-composites. The SBA-15 spectrum consisted of a broad adsorption band at around  $3400\text{ cm}^{-1}$ , which is attributed to the presence of geminal silanol groups with strong hydrogen bonds between them. In addition, there was a low intensity band at  $1630\text{ cm}^{-1}$  arising from the deformation modes of O–H bonds from adsorbed water [49]. The adsorption band at  $960\text{ cm}^{-1}$  can be attributed to the Si-OH and Si-O-Si stretching vibration. The bands at around  $1100\text{ cm}^{-1}$ ,  $820\text{ cm}^{-1}$  and  $470\text{ cm}^{-1}$  are due to Si-O-Si bending and asymmetric stretching vibrations [50]. The lowest frequency bands at  $470\text{ cm}^{-1}$  and  $820\text{ cm}^{-1}$  are attributed to the rocking

mode of oxygen atom motion and bending vibrations of the oxygen atoms between silicon atoms (Si-O-Si).



**Fig. 9.** FTIR spectra of (a) SBA-15, (b) SCo(Cl)5-A, (c) SCo(Cl)5-I, (d) SCo(Cl)5 and (e) SCo(Cl)10



**Fig. 10.** FTIR spectra of (a) SCo(Cl)30-BC and (b) SCo(Cl)30

All Co-composites except for SCo(Cl)30-BC spectra showed two additional adsorption bands at around  $580\text{ cm}^{-1}$  ( $\bar{\nu}_1$ ) and  $690\text{ cm}^{-1}$  ( $\bar{\nu}_2$ ), attributed to Co-O vibration in the spinel  $\text{Co}_3\text{O}_4$  lattice [39]. Since the intensity of these two peaks did not increase upon increasing Co-loading, it is suggested that only small concentration of incorporated cobalt is in the form of  $\text{Co}_3\text{O}_4$  which is in agreement with the results obtained from DR UV-vis. This is different to our previous work using  $\text{Co}(\text{NO}_3)_2 \cdot 6\text{H}_2\text{O}$  where the intensity of Co-O peaks increased as the Co-loading increased, but this was accompanied by a concomitant increase in cobalt oxide patch size [33].

When comparing SCo(Cl)30-BC with SCo(Cl)30 (Fig. 10) and Co-composites of lower Co-loading, two major changes are distinguishable. First the absence of bands at around  $580\text{ cm}^{-1}$  and  $690\text{ cm}^{-1}$  for SCo(Cl)30-BC is indicative of the absence of cobalt oxide species before calcination. Second, the significant decrease in the intensity of  $3400\text{ cm}^{-1}$ ,  $1630\text{ cm}^{-1}$  and  $960\text{ cm}^{-1}$  bands for SCo(Cl)30 relative to Co-composites with

lower Co-loading suggests that during calcination most of the hydroxyl groups were replaced by cobalt ions. The interaction between Si-OH and  $\text{Co}^{2+}$  is known to lead to the formation of a Si-O-Co amorphous phase [51]. Cui et al. reported an adsorption band at  $1029\text{ cm}^{-1}$  and attributed it to Si-O-Co bond [52]. In the present study this adsorption band has probably overlapped with the Si-O-Si band centered at  $1100\text{ cm}^{-1}$  such that it is not distinctly observable.

#### 4.3.3.1.8 X-Ray photoelectron spectroscopy (XPS)

Fig. 11 shows the XPS spectrum, from SCo(Cl)30, which consisted of two doublets. The main doublet was comprised of peaks at binding energy  $780.7\text{ eV}$  ( $2p_{3/2}$ ) and  $796.7\text{ eV}$  ( $2p_{1/2}$ ). A second and broader spin-orbit doublet was observed at higher binding energy, around  $785$  and  $801\text{ eV}$ . The binding energy values and the shape of the main doublet indicate that the cobalt species were in an oxidized state [53]. The presence of the second spin-orbit doublet at a higher binding energy than the main doublet is evidence of the presence of  $\text{Co}^{2+}$  as the dominant phase.

The presence of these two doublets is attributed to the different charge-transfer type screening on the Co 2p electrons created by photoemission. The main doublet arises from a well-screened final state and the second doublet corresponds to a weakly-screened final state. The second doublet is known as the shake-up satellite, which is less strong for  $\text{Co}^{3+}$  due to the enhanced screening of Co 2p electrons by 3d electrons. However the intensity of the shake-up satellite in this work is more than what reported previously for the Co-composites prepared from  $\text{Co}(\text{NO}_3)_2 \cdot 6\text{H}_2\text{O}$  [33].

In addition it is generally known that the spin orbit splitting ( $\Delta E$ ) can be used to distinguish the oxidation state of the catalyst. This  $\Delta E$  is reported to be  $16\text{ eV}$  and  $15\text{ eV}$  for  $\text{Co}^{2+}$  and  $\text{Co}^{3+}$  species respectively [54]. The  $\Delta E$  between 2p level peaks in this work was  $16\text{ eV}$ , which further suggests that the dominant species in this sample was  $\text{Co}^{2+}$ . The  $\Delta E$  determined in our previous study using  $\text{Co}(\text{NO}_3)_2 \cdot 6\text{H}_2\text{O}$  as precursor was found to be  $15\text{ eV}$ , indicating the formation of spinel  $\text{Co}_3\text{O}_4$  in that case [33].

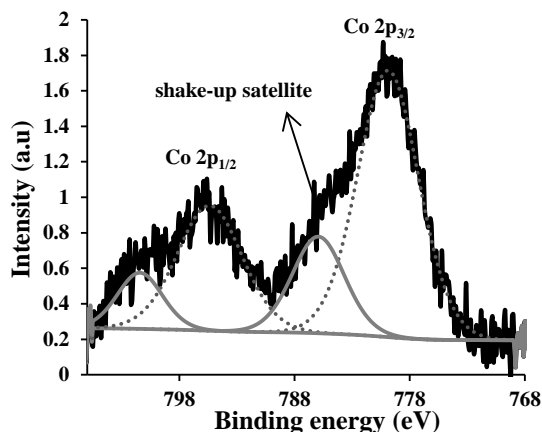


**Fig. 11.** Deconvoluted XPS spectrum of SCo(Cl)30

#### 4.3.3.1.9 Temperature programmed reduction

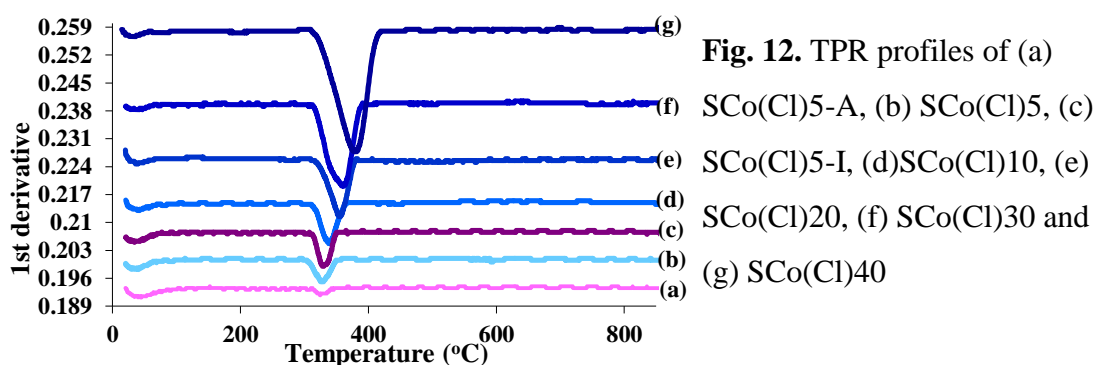
The reduction behavior for supported metal oxides is typically more complicated than that of a bulk metal oxide. This is often attributed to variation in particle size on the support, the porous structure of the support, the preparation method [55] and the interaction between the metal oxide and the support [56, 57]. It has been reported that bulk cobalt oxide,  $\text{Co}_3\text{O}_4$ , reduction is complete at 400 °C [33].

Fig. 12 shows TPR profiles of all the Co-composites. In all cases one reduction peak was observed, suggesting the presence of predominantly one type of cobalt ions. The reduction peaks for SCo(Cl)5, SCo(Cl)10, SCo(Cl)20, SCo(Cl)30, SCo(Cl)40, SCo(Cl)5-A and SCo(Cl)5-I were centered at 319 °C, 341 °C, 351 °C, 356 °C, 368 °C, 317 °C and 324 °C, respectively. The intensity of the reduction peaks as well as the position of the peak maximum increased in proportion to the Co-loading [32]. The change in the position of the peak maximum can probably be attributed to reduced hydrogen diffusion rates in the composites with progressively higher Co-loading. The  $\text{N}_2$  adsorption-desorption analyses demonstrated that with increased Co-loading the micropore volume decreased more than that of the mesopores, indicative of progressively increased pore blockage, especially in the micropores. Hydrogen diffusion might also be hindered due to the formation of water during the reduction process. As the Co-loading increases, more water would be formed in the pores, thus restricting hydrogen diffusion [58].

When comparing SCo(Cl)5 and SCo(Cl)5-I, the former's reduction started at lower temperature (280 °C) with the reduction peak centered at 319 °C. However the reduction in SCo(Cl)5-I started at 295 °C with the peak centered at slightly higher

temperature (324 °C). Since the Co-content was quite similar in both composites, the changes in the reduction behavior can be attributed to the nature of the cobalt oxide species, most specifically their size. Since impregnation results in formation of larger particles which probably resulted in more pore blockage [33, 59], (see section 4.3.3.1.2). This in turn may limit the diffusion rate of the hydrogen and increase the reduction temperature.

The TPR profiles of the Co-composites prepared in this study are very different to those previously reported using  $\text{Co}(\text{NO}_3)_2 \cdot 6\text{H}_2\text{O}$  as precursor [33]. In the previous study the dominant phase was the spinel  $\text{Co}_3\text{O}_4$  with two reduction peaks evident, corresponding to  $\text{Co}^{3+}$  to  $\text{Co}^{2+}$  and  $\text{Co}^{2+}$  to metallic Co. A further reduction peak was also observed, at high temperature, which was attributed to the fraction of cobalt oxide species having strong interactions with the support [33]. This comparing of behaviors clearly suggests that the nature of the cobalt precursor affects the nature of the supported active species.



**Fig. 12.** TPR profiles of (a) SCo(Cl)5-A, (b) SCo(Cl)5, (c) SCo(Cl)5-I, (d) SCo(Cl)10, (e) SCo(Cl)20, (f) SCo(Cl)30 and (g) SCo(Cl)40

#### 4.3.4 Catalytic evaluation

The effectiveness of the Co-composites in liquid phase oxidation of cyclohexanol in the presence of TBHP as an oxidant was investigated and the results are summarized in Fig. 14A.

Fig. 14A demonstrates that the composite with the lowest Co-loading, SCo(Cl)5-A, showed the highest catalytic activity. This catalyst also showed the highest surface area and micro/mesopore volume (Table 1). This suggests that, due to less pore blockage in SCo(Cl)5-A, more catalytically active species were accessible for the reactants in this composite. When comparing the catalytic activity of SCo(Cl)5 and SCo(Cl)5-I, the former showed higher catalytic activity. In addition, SCo(Cl)5 showed higher surface area and micro/mesopore volume than SCo(Cl)5-I. These data therefore suggest there

was more pore blockage in SCo(Cl)5-I and thus less accessibility of active species for the reactants. In addition, since the size and dispersion of the supported active species had a noticeable impact on the catalytic activity, it is suggested that the low catalytic activity of the SCo(Cl)5-I can also be partially attributed to the presence of relatively larger particles both on the external and internal surface.

The catalytic activity of the composites prepared by the two-solvent method decreased as the Co-loading increased from 5 wt% to 10 wt%. This corresponds to the decrease in the surface area and micro/mesopore volume of SCo(Cl)10. However further increasing the Co-loading to 30 wt%, SCo(Cl)30, did not change the catalytic activity from that for SCo(Cl)10. It can be suggested that for SCo(Cl)30 the transformation of the structure of the support eliminated the pores and therefore no longer hindered the mass transfer of the reactants. As a result the catalytic performance was quite similar to that of SCo(Cl)10.

A free radical mechanism is thought to be responsible for the oxidation reaction for the Co-composites (Fig. 13). Through this mechanism  $\text{Co}^{2+}$  serves to initiate the Haber-Weiss decomposition of TBHP into tert-butoxy and tert-butylperoxy radicals as well as  $\text{H}^+$  and  $\text{OH}^-$  [60]. In the next step, the tert-butylperoxy radicals propagate the reaction by producing cyclohexanol radical, the active intermediate. Through this process TBHP is reformed and can reenter the reaction cycle. The catalytic mechanism continues through abstraction of a second hydrogen radical by tert-butoxy radical. This then results in the formation of cyclohexanone as the desired product and tert-butanol as the byproduct.

The presence of tert-butanol was confirmed by GC and GC-MS and its concentration observed to increase as the reaction proceeded. Simultaneously the concentration of TBHP decreased which demonstrates the consumption of the oxidant through the catalytic reaction.

### Initiation by Haber-Weiss decomposition of TBHP

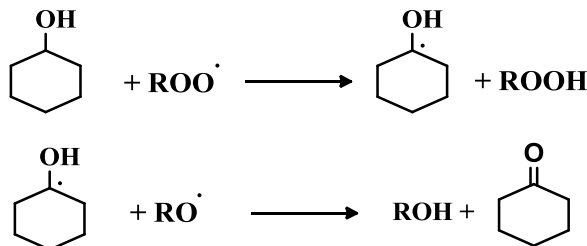
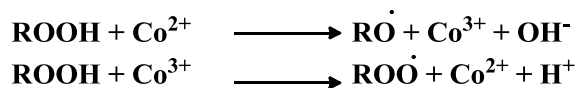


**Fig. 13.** Suggested radical chain mechanism for oxidation reaction [61]

In order to confirm the catalytic activity of the cobalt oxide species, the same oxidation reaction was conducted without the catalyst, but still in the presence of TBHP. A maximum conversion of 7 % was obtained (Fig. 14B). When SBA-15 was used as a catalyst under the same reaction conditions the maximum conversion of 10 % was obtained [33]. Upon reducing the amount of catalyst by half  $\text{SCo}(\text{Cl})_5$ , the maximum conversion also decreased by a factor of two. These data indicate that cobalt oxide is essential for the efficient progress of the oxidation reaction. This is thought to be because the initiation of Haber-Weiss mechanism and TBHP decomposition are strongly dependent on the concentration of the cobalt ions [61]. To investigate the effect of the oxidant on the catalytic reaction, cyclohexanol was oxidized using  $\text{SCo}(\text{Cl})_5$  as the catalyst in the absence of TBHP. A maximum conversion of 2 % was obtained. This result demonstrates that the presence of the oxidant is essential to propagate the catalytic reaction.

To investigate the stability of the catalyst, the same reaction conditions were used to catalyze cyclohexanol using  $\text{SCo}(\text{Cl})_5$  as the catalyst. The solid catalyst was filtered out of the mixture after 4 h (while the reaction mixture was still hot) and the reaction was continued in its absence. It was found that the solution was still active even in the absence of the solid catalyst. This suggests that a fraction of the active species must have leached into the solution during the first 4 hours. ICP-MS analysis showed a trace of Co (approximately 10% of the original concentration of cobalt in  $\text{SCo}(\text{Cl})_5$ ) had leaked in to the solution.

It is interesting to note that the Co-composites in the current work demonstrated higher catalytic activity than the composites prepared using  $\text{Co}(\text{NO}_3)_2 \cdot 6\text{H}_2\text{O}$  as the

cobalt precursor [33]. This can be attributed to the higher dispersion of the cobalt oxide species throughout the support or presence of the active species in the solution such that the catalytic system is heterogeneous-homogeneous rather than simply heterogeneous. A similar leak test was carried out for the catalyst prepared from  $\text{Co}(\text{NO}_3)_2 \cdot 6\text{H}_2\text{O}$  confirmed that this catalytic system was strictly heterogeneous. Further study is required to determine if the leakage of the active species can be controlled.

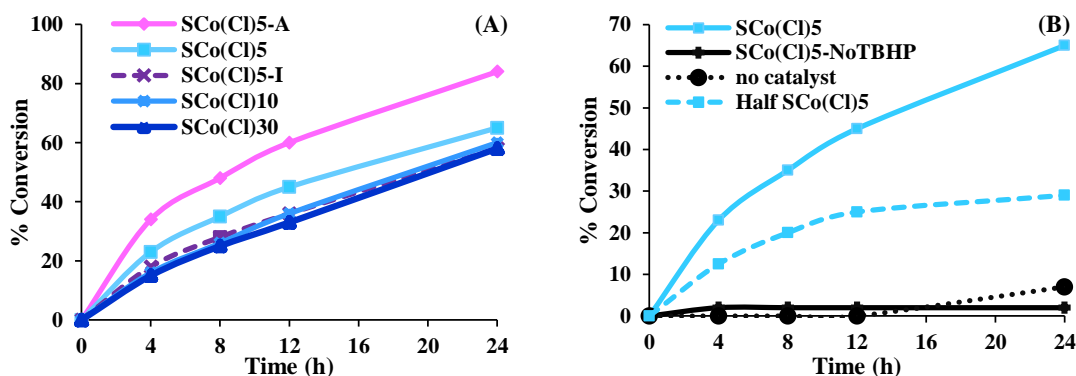


**Fig. 14.** Cyclohexanol oxidation (A) using various Co-composites and (B) under various condition

#### 4.3.5 Conclusion

The two-solvent method and  $\text{CoCl}_2 \cdot 6\text{H}_2\text{O}$  were used to prepare a series of SBA-15 supported cobalt oxide composites with various Co-loadings. Analogous Co-composites were also prepared by the more conventional methods of impregnation and adsorption. A blue coloration was observed for all the Co-composites, regardless of the preparation method, with the intensity in direct proportion to the Co-loading.

The mesoporous structure of the support, SBA-15, was preserved below 30 wt% (nominal) Co-loading. SEM images showed parallel stripes on the surface of the SBA-15 particles for the composites with Co-loadings lower than 30 wt%, which signified the retention of the hexagonal channels of the support. Upon increasing the Co-loading to 30 wt% (nominal) and beyond, a morphological transformation was observed in the Co-composites. This transformation occurred during calcination and was confirmed by  $\text{N}_2$  adsorption-desorption, XRD, SEM and TEM. SEM images demonstrates the new morphology of the SCo(Cl)30 as a continuous surface with random cavities of approximately 20-30 nm in diameter. The stripes on the surface of the Co-composites with lower Co-loadings were no longer observable in SCo(Cl)30.

DR UV-vis results suggest that the dominant species in the composites after calcination was  $\text{Co}^{2+}$  in tetrahedral co-ordination. The XPS results support this interpretation.

The composite with the lowest Co-loading, prepared by adsorption, exhibited the highest catalytic activity. This can be attributed to its higher surface area, higher total pore volume and more accessible active sites. Regarding composites prepared by the two-solvent method, the catalytic activity was in order of  $\text{SCo}(\text{Cl})_5 > \text{SCo}(\text{Cl})_{10} \geq \text{SCo}(\text{Cl})_{30}$ . The maximum conversion of cyclohexanol to cyclohexanone in the absence of either catalyst ( $\text{SCo}(\text{Cl})_5$ ) or TBHP was negligible. It was also observed that a fraction of the active species was leached into the solution, so that some of the activity for these series of composites in the liquid phase oxidation of cyclohexanol may be attributable to this phenomenon.

#### 4.3.6 References

- [1] A.K. Suresh, M.M. Sharma, T. Sridhar, *Ind. Eng. Chem. Res.* 39 (2000) 3958-3997.
- [2] Á. Szegedi, M. Popova, C. Minchev, *J. Mater. Sci.* 44 (2009) 6710-6716.
- [3] K. Weissmehl, H.J. Arpe, *Industrial Organic Chemistry*, 3rd Completely Revised Edition, VCH, New York, 1997.
- [4] R. Shiozaki, H. Goto, Y. Kera, *Bull. Chem. Soc. JPN.* 66 (1993).
- [5] A. Corma, P. Esteve, A. Martínez, *Appl. Catal. A: Gen.* 143 (1996) 87-100.
- [6] S.K. Jana, Y. Kubota, T. Tatsumi, *J. Catal.* 255 (2008) 40-47.
- [7] R. Kumar Rana, B. Viswanathan, *Catal. Lett.* 52 (1998) 25-29.
- [8] M.L. Parentis, N.A. Bonini, E.E. Gonzo, *Reac. Kinet. Catal. Lett.* 76 (2002) 243-248.
- [9] N.A. Hodge, C.J. Kiely, R. Whyman, M.R.H. Siddiqui, G.J. Hutchings, Q.A. Pankhurst, F.E. Wagner, R.R. Rajaram, S.E. Golunski, *Catal. Today.* 72 (2002) 133-144.
- [10] U.R. Pillai, S. Deevi, *Appl. Catal. B: Environ.* 64 (2006) 146-151.
- [11] H. Li, S. Wang, F. Ling, J. Li, *J. Mol. Catal. A: Chem.* 244 (2006) 33-40.
- [12] D. Sellam, M. Bonne, S. Arrii-Clacens, G. Lafaye, N. Bion, S. Tezkratt, S. Royer, P. Marécot, D. Duprez, *Catal. Today.* 157 (2010) 131-136.
- [13] J.S. Beck, J.C. Vartuli, W.J. Roth, M.E. Leonowicz, C.T. Kresge, K.D. Schmitt, C.T.W. Chu, D.H. Olson, E.W. Sheppard, *J. Am. Chem. Soc.* 114 (1992) 10834-10843.
- [14] D. Zhao, Q. Huo, J. Feng, B.F. Chmelka, G.D. Stucky, *J. Am. Chem. Soc.* 120 (1998) 6024-6036.
- [15] Y. Wan, Zhao, *Chem. Rev.* 107 (2007) 2821-2860.

- [16] C.T. Kresge, M.E. Leonowicz, W.J. Roth, J.C. Vartuli, J.S. Beck, *Nature*. 359 (1992) 710-712.
- [17] D. Zhao, J. Feng, Q. Huo, N. Melosh, G. H. Fredrickson, B. F. Chmelka, G.D. Stucky, *Science*. 279 (1998) 548.
- [18] X.-L. Xu, Z.-H. Chen, Y. Li, W.-K. Chen, J.-Q. Li, *Surf. Sci.* 603 (2009) 653-658.
- [19] S.C. Petitto, E.M. Marsh, G.A. Carson, M.A. Langell, *J. Mol. Catal. A: Chem.* 281 (2008) 49-58.
- [20] Y. Ye, F. Yuan, S. Li, *Mater. Lett.* 60 (2006) 3175-3178.
- [21] C.-Y. Liu, C.-F. Chen, J.-P. Leu, *Sensor. Actuat. B: Chem.* 137 (2009) 700-703.
- [22] S.G. Kandalkar, C.D. Lokhande, R.S. Mane, S.-H. Han, *Appl. Surf. Sci.* 253 (2007) 3952-3956.
- [23] G. Laugel, J. Arichi, M. Molière, A. Kiennemann, F. Garin, B. Louis, *Catal. Today*. 138 (2008) 38-42.
- [24] I. Lopes, A. Davidson, C. Thomas, *Catal. Commun.* 8 (2007) 2105-2109.
- [25] A.Y. Khodakov, R. Bechara, A. Griboval-Constant, *Appl. Catal. A: Gen.* 254 (2003) 273-288.
- [26] O. González, H. Pérez, P. Navarro, L.C. Almeida, J.G. Pacheco, M. Montes, *Catal. Today*. 148 (2009) 140-147.
- [27] P. Lanzafame, S. Perathoner, G. Centi, F. Frusteri, *J. Porous Mater.* 14 (2007) 305-313.
- [28] M. Wolters, L.J.W. van Grotel, T.M. Eggenhuisen, J.R.A. Sietsma, K.P. de Jong, P.E. de Jongh, *Catal. Today*. 163 (2011) 27-32.
- [29] S. Sun, Q. Gao, H. Wang, J. Zhu, H. Guo, *Appl. Catal. B: Environ.* 97 (2010) 284-291.
- [30] J. Panpranot, S. Kaewgun and, P. Praserthdam, *Reac. Kinet. Catal. Lett.* 85 (2005) 299-304.
- [31] Q. Tang, Q. Zhang, H. Wu, Y. Wang, *J. Catal.* 230 (2005) 384-397.
- [32] C. Wang, S. Lim, G. Du, C.Z. Loebicki, N. Li, S. Derrouiche, G.L. Haller, *J. Phys. Chem. C.* 113 (2009) 14863-14871.
- [33] J. Taghavimoghaddam, G.P. Knowles, A.L. Chaffee, *J. Mol. Catal. A: Chem.* 358 (2012) 79-88.
- [34] J. Taghavimoghaddam, G.P. Knowles, A.L. Chaffee, *Top. Catalysis.* 55 (2012) 571-579.
- [35] M. Imperor-Clerc, D. Bazin, M. D. Appay, P. Beaunier, A. Davidson, *Chem. Mater.* 16 (2004) 1813-1821.
- [36] P.F. Fulvio, S. Pikus, M. Jaroniec, *ACS Appl. Mater. Interfaces.* 2 (2009) 134-142.
- [37] L. Martins, W. Hölderich, P. Hammer, D. Cardoso, *J. Catal.* 271 (2010) 220-227.
- [38] P.F. Fulvio, S. Pikus, M. Jaroniec, *J. Mater. Chem.* 15 (2005) 5049-5053.
- [39] T. Tsoncheva, L. Ivanova, C. Minchev, M. Fröba, *J. Colloid Interface Sci.* 333 (2009) 277-284.

- [40] P.I. Ravikovitch, A.V. Neimark, *Langmuir*. 18 (2002) 9830-9837.
- [41] A. Martin, G. Morales, F. Martinez, R. van Grieken, L. Cao, M. Kruk, *J. Mater. Chem.* 20 (2010) 8026-8035.
- [42] O.A. Anunziata, A.R. Beltramone, M.L. Martínez, L.L. Belon, *J. Colloid Interface Sci.* 315 (2007) 184-190.
- [43] C.C. Harrison, X. Li, I. Hopkinson, S.E. Stratford, A.G. Orpen, *J. Chem. Soc. Faraday Trans.* 89 (1993) 4115-4122.
- [44] S. Esposito, M. Turco, G. Ramis, G. Bagnasco, P. Pernice, C. Pagliuca, M. Bevilacqua, A. Aronne, *J. Solid State Chem.* 180 (2007) 3341-3350.
- [45] Z. Lou, R. Wang, H. Sun, Y. Chen, Y. Yang, *Micro. Meso. Mater.* 110 (2008) 347-354.
- [46] A.A. Verberckmoes, B.M. Weckhuysen, R.A. Schoonheydt, *Micro. Meso. Mater.* 22 (1998) 165-178.
- [47] H. Ma, J. Xu, C. Chen, Q. Zhang, J. Ning, H. Miao, L. Zhou, X. Li, *Catal. Lett.* 113 (2007) 104-108.
- [48] L.G.A. van de Water, G.L. Bezemer, J.A. Bergwerff, M. Versluijs-Helder, B.M. Weckhuysen, K.P. de Jong, *J. Catal.* 242 (2006) 287-298.
- [49] P. Innocenzi, *J. Non-Cryst. Solids.* 316 (2003) 309-319.
- [50] X. Wang, P. Wang, Z. Dong, Z. Ma, J. Jiang, R. Li, J. Ma, *Nanoscale Res Lett.* 5 (2010) 1468-1473.
- [51] M. Stoia, M. Stefanescu, T. Dippong, O. Stefanescu, P. Barvinschi, *J. Sol-Gel Sci. Technol.* 54 (2010) 49-56.
- [52] H. Cui, M. Zayat, D. Levy, *J. Sol-Gel Sci. Technol.* 40 (2006) 83-87.
- [53] L. Fu, Z. Liu, Y. Liu, B. Han, P. Hu, L. Cao, D. Zhu, *Adv. Mater.* 17 (2005) 217-221.
- [54] Y. Okamoto, H. Nakano, T. Imanaka, S. Teranishi, *Bull. Chem. Soc. JPN.* 84 (1975) 1163-1168.
- [55] L. Jiao, J.R. Regalbuto, *J. Catal.* 260 (2008) 342-350.
- [56] Y. Okamoto, K. Nagata, T. Adachi, T. Imanaka, K. Inamura, T. Takyu, *J. Phys. Chem.* 95 (1991) 310-319.
- [57] Á. Szegedi, M. Popova, V. Mavrodinova, C. Minchev, *Appl. Catal. A: Gen.* 338 (2008) 44-51.
- [58] D. Yin, W. Li, W. Yang, H. Xiang, Y. Sun, B. Zhong, S. Peng, *Micro. Meso. Mater.* 47 (2001) 15-24.
- [59] K. Bourikas, J. Vakros, C. Fountzoula, C. Kordulis, A. Lycourghiotis, *Catal. Today.* 128 (2007) 138-144.
- [60] Gadi Rothenberg, Liron Feldberg, H. Wiener, Y. Sasson, *J. Chem. Soc., Perkin Trans.* 2 (1998) 2429.
- [61] M. Nowotny, L.N. Pedersen, U. Hanefeld, T. Maschmeyer, *Chem. Eur. J.* 8 (2002) 3724-3731.

## 4.4 Appendix

### 4.4.1 $^{29}\text{Si}$ Magnetic angle spinning nuclear magnetic resonance spectroscopy

Figure 1 demonstrates  $^{29}\text{Si}$  MAS NMR of SBA-15 as well as SBA-15 supported cobalt oxide species with 5 wt%, 10 wt% and 30 wt% Co-loading. Mesoporous silica SBA-15 demonstrates three peaks at -92 ppm corresponds to the surface silicon atoms with two silanol and two siloxane bonds  $(\text{OSi})_2*\text{Si}(\text{OH})_2$ ;  $\text{Q}_2$ . These silanol groups are known as geminal silanol groups [1]. The second peak is at -101 ppm and attributed to surface silicon atoms with one silanol group and three siloxane groups  $(\text{SiO})_3*\text{Si}(\text{OH})$ ; ( $\text{Q}_3$ ). These silanol groups are known as single silanol groups either isolated or hydrogen-bonded. The third peak at -110 ppm is assigned to the silica backbone, which is silicon atoms with four siloxane bonds,  $(\text{SiO})_4*\text{Si}$ ; ( $\text{Q}_4$ ) [2].

The high intensity of  $\text{Q}_3$  and  $\text{Q}_2$  associates with the high concentration of silanol groups in SBA-15 [3]. As the Co-loading increased two significant changes were observed in the spectra: (i) a progressive decrease in the intensity of  $\text{Q}_2$  and (ii) peak broadening. The  $\text{Q}_2$  peaks decreased to a shoulder in Co-composites with 5 wt% and 10 wt% Co-loading. This suggests the presence of less geminal groups after formation of cobalt oxide species inside the pores. This can be attributed to the interaction of cobalt species with the oxygen of the surface silanol groups during calcination. The peak broadening however can be attributed to the paramagnetic properties of  $\text{Co}^{2+}$ . It is clear in the  $^{29}\text{Si}$  MAS NMR that by increasing the initial Co-loading from 5 wt% to 30 wt% the peaks became much broader. This can be evidence of incorporation of more  $\text{Co}^{2+}$  in the support. By increasing the Co-loading to 30 wt%, the spectrum became very broad such that the characteristic peaks of mesoporous silica could hardly be distinguished. However, a very low intense peak can be observed at -101 ppm ( $\text{Q}_3$ ). This suggests the existence of high amount of paramagnetic  $\text{Co}^{2+}$ .

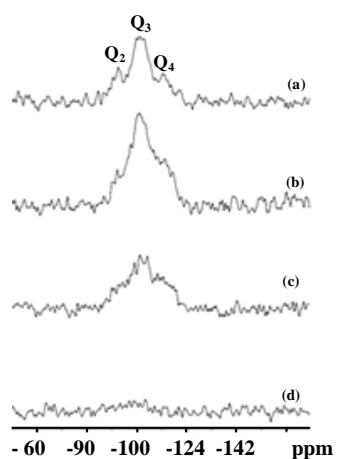


**Figure 1.**  $^{29}\text{Si}$  MAS NMR obtained from (a) SBA-15 and Co-composites with (b)  $\text{SCo}(\text{Cl})_5$ , (c)  $\text{SCo}(\text{Cl})_{10}$  and (d)  $\text{SCo}(\text{Cl})_{30}$

#### 4.4.2 References

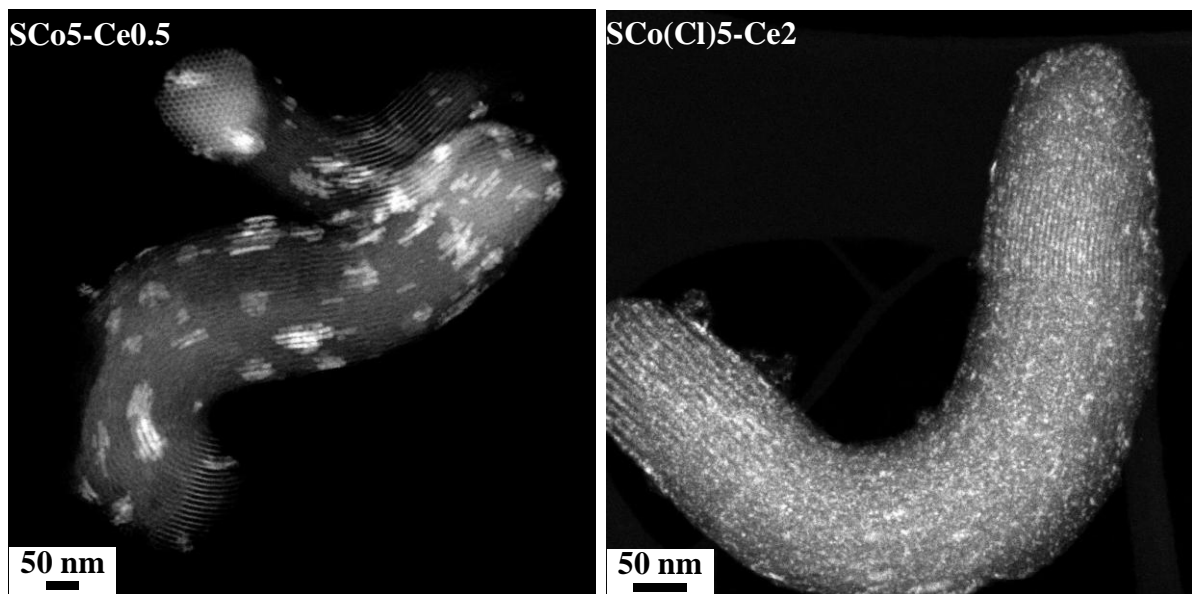
- [1] X.S. Zhao, G.Q. Lu, A.K. Whittaker, G.J. Millar, H.Y. Zhu, *J. Phys. Chem. B.* 101 (1997) 6525-6531.
- [2] M. Boutros, Z. Maoui, H. Sfihi, V. Viossat, A. Gédéon, F. Launay, *Micro. Meso. Mater.* 108 (2008) 247-257.
- [3] C.-M. Yang, B. Zibrowius, W. Schmidt, F. Schüth, *Chem. Mater.* 16 (2004) 2918-2925.

---

# Chapter 5

## Ce-doped Co-composites

---



## 5.1 Literature review

Cerium is among the fourteen lanthanides which, with scandium (Sc) and yttrium (Y), are known as the rare earth elements. Cerium is the most abundant rare earth element in the upper crust (64 ppm), it is even more abundant than tin (2.3 ppm) and copper (60 ppm) [1]. Cerium's abundance and its high catalytic activity for various reactions in different sectors of industry make its oxides one of the most interesting rare earth oxides industrially.

Cerium metal is thermodynamically unstable in the presence of oxygen. With its  $4f^2 5d^0 6s^2$  electron configuration it has two common oxidation states,  $Ce^{3+}$  and  $Ce^{4+}$ . Cerium (IV) is the only rare earth ion with an oxidation state higher than three that is stable in aqueous solution. Its high oxidation state makes it a strong oxidizing agent [2].

The rare earth oxides are generally thermally stable materials and can therefore be used in high temperature applications and cerium oxides are no exception. Ceria,  $CeO_2$ , is a nontoxic and highly stable oxide with the density of  $7.13 \text{ g cm}^{-3}$  and melting point of  $2600 \text{ }^\circ\text{C}$  [3]. Ceria crystallises in the fluorite structure with a face-centred cubic unit cell (space group  $Fm\bar{3}m$ , cell parameter  $0.5411 \text{ nm}$ ; see Figure 5.1).

In the perfect ceria unit cell, without oxygen deficiency, the oxygen ions ( $O^{2-}$ ) are tetrahedrally coordinated to cerium ions ( $Ce^{4+}$ ) and octahedrally coordinated to the surrounding oxygen ions (Figure 5.1). The oxygen ions exist in discrete layers.

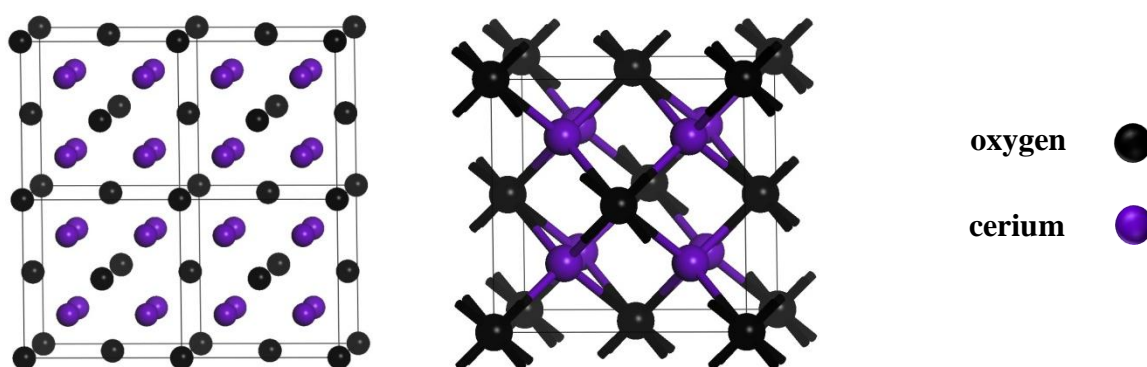


**Figure 5.1.** Ceria unit cell

The efficiency of the cerium oxides in catalytic applications is associated with the migration of the anion,  $O^{2-}$ , relatively freely through the lattice and also the ease of reducibility from  $Ce^{4+}$  to  $Ce^{3+}$ .

This reduction process results in release of oxygen and affects the lattice parameter and, in fact, the lattice parameter increases when  $Ce^{4+}$  reduces to  $Ce^{3+}$ , because the radius of  $Ce^{3+}$  is larger than that of  $Ce^{4+}$ . In order to maintain, neutrality, in the unit cell, for each two  $Ce^{4+}$

reduced one oxygen ion,  $O^{2-}$  should then leave the unit cell. This reduction process is reversible and its reversibility depends on the oxygen partial pressure and the temperature at which the reduction process occurs [4]. The ability of cerium ions to go through a redox cycle (Eq. 5.1) is generally referred to as the oxygen storage capacity (OSC) of ceria [3].



It is noteworthy that the fluorite oxide structure can be maintained even with a marked deviation from stoichiometry. This suggests that, even with a loss of substantial amounts of oxygen from the crystal lattice, the crystal structure of the  $CeO_2$  is preserved so that, in an oxidising environment, the existing sub-oxides can be readily re-oxidized [3].

### **5.1.1 Ceria applications**

#### **5.1.1.1 Ceria in the glass industry**

One of the main industrial applications of ceria, mainly in the form of  $CeO_2$  or  $CeO_{2-x}H_2O$ , is in the glass industry [5]. It is used as a polisher to accelerate the polishing process and also to improve the surface of the glass [6]. Ceria is also used as a decolorizer. At the melting temperature of the glass,  $CeO_2$  reduces to  $Ce_2O_3$  by releasing oxygen [7]. In the next step the  $Ce_2O_3$  re-oxidizes on the surface of the iron, which leads to decolorization of the iron in the glass.

Cerium and ceria in combination with other transition metal oxides can also be used to colour the glass. For instance, ceria and titania provide a beautiful yellow colour, ceria in combination with titania and manganese oxide also makes the glass yellow. The combination of ceria, titania and copper oxide colours the glass turquoise. The photo stability of pigments is also enhanced by the presence of cerium. This is because cerium compounds have low absorption in the visible region and do not affect its transmission.

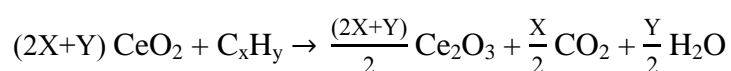
#### **5.1.1.2 Ceria in catalysis**

The catalytic activity of ceria and the mechanism(s) by which it is involved in catalytic processes are the subject of enormous interest [8]. It is also known that the catalytic performance of the transition metal/metal oxides increases if ceria is added as a promoter or used as a support [9-12]. Several factors are reported to be involved in this catalytic enhancement including, in particular, the OSC of the ceria. This is facilitated by the redox property of the cerium ions and the high mobility of the oxygen vacancies on the surface of

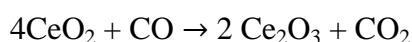
the catalyst as well as in the bulk. Some of the most extensively investigated reactions which are catalysed by ceria are briefly discussed below [13].

The “three-way catalyst” (TWC) is among the most important catalytic applications of ceria. This system, used widely in the automotive industry, simultaneously converts harmful emissions such as carbon monoxide and nitrogen oxides from fuel combustion to harmless, environmentally-acceptable gases [14-16]. The ceria provides oxygen buffering capacity; it is able to provide oxygen to some reactions and remove it from others. One way of representing the reactions involved is as follows:

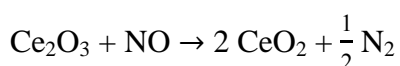
- Hydrocarbon combustion:



- Carbon monoxide oxidation:



- $\text{NO}_x$  reduction



It should be noted that effective TWCs also require the presence of one or more platinum group metals. However, the mediation (catalysis) afforded by ceria make the modern automotive exhaust treatment catalysts substantially more effective than those without ceria. The dispersion of the  $\text{CeO}_2$ , its particle size and the active surface area of the  $\text{CeO}_2$  particles have a substantial influence on the catalytic activity of the  $\text{CeO}_2$ , either bulk or supported.

#### **5.1.1.2.1 Cobalt-cerium mixed oxides in catalysis**

There is a reasonable body of literature on the use of cobalt and cerium in combination as catalysts. Most of these catalysts have been prepared by co-precipitation.

Cobalt-cerium mixed oxides were used for  $\text{N}_2\text{O}$  decomposition. These catalysts demonstrated higher catalytic performance relative to pure cobalt oxide and ceria separately [17]. The synergistic effect between cobalt and cerium was reported to improve the redox property of the metal mixed oxide and thus showed higher catalytic activity in nitrous oxide decomposition. The same catalytic behaviour was reported when cobalt-cerium mixed oxide catalysed soot oxidation [18].

Cobalt-cerium mixed oxides showed high thermal stability and catalytic performance in CO and n-alkane oxidation [19]. This was attributed to the higher dispersion and smaller crystal size of the  $\text{Co}_3\text{O}_4$  [20].

Cobalt-cerium mixed oxides were prepared and activated at different calcination temperatures to catalyse CO oxidation [21]. The composites prepared at the optimum calcination temperature showed higher catalytic performance and this was attributed to the total conversion of the cobalt precursor to  $\text{Co}_3\text{O}_4$ . At low calcination temperature only a small fraction of the cobalt precursor transformed into  $\text{Co}_3\text{O}_4$  nanoparticles. However, at very high temperatures large clusters were formed. These two phenomena led to a decrease in the catalytic performance of the composites.

Liotta et al. exploited the co-precipitation method to prepare a series of cobalt-cerium oxide with different Co:Ce atomic ratios. It was shown that when the Co:Ce atomic ratio was equal to 1, the catalytic activity of the composite was the same as that of pure  $\text{Co}_3\text{O}_4$  in propene oxidation. This was attributed to the textural properties of the mixed metal oxide catalyst [22]. It was also reported that when ceria was used as a catalyst for propene oxidation the active sites were electrophilic  $\text{O}_2^-$  and  $\text{O}^-$  species on the surface. However, in the case of cobalt-cerium oxide both the electrophilic oxygen species on the surface and the lattice oxygen (Mars and krevelen mechanism, see chapter 1, section 1.5.5) were reported to participate in the catalytic reaction.

The same group also compared the catalytic performance in methane oxidation of cobalt-cerium oxide containing 30 wt% cobalt with pure  $\text{Co}_3\text{O}_4$  and  $\text{CeO}_2$ . The better performance of the mixed catalyst was attributed to the improvement in morphological and redox properties of the cobalt-cerium oxide composites as well as to better dispersion of the  $\text{Co}_3\text{O}_4$  phase [23, 24].

The effect of Pd as a promoter on the catalytic performance of cobalt-cerium oxide composites in CO oxidation was investigated [25]. It was reported that  $\text{O}_2$  spillover was facilitated in the presence of Pd, thus improving the catalytic performance.

Mesoporous ceria similar to mesoporous transition metal oxides can be used as a support. Tsoncheva et al. reported preparing ceria, zirconia and magnesium oxide supported  $\text{Co}_3\text{O}_4$  via impregnation. Mesoporous ceria supported  $\text{Co}_3\text{O}_4$  demonstrated higher catalytic performance in methanol decomposition than SBA-15, MgO or  $\text{ZrO}_2$  supported  $\text{Co}_3\text{O}_4$  [12]. This high catalytic performance was attributed to the synergy between  $\text{Co}_3\text{O}_4$  and  $\text{CeO}_2$ , as well as the easier release of oxygen due to the presence of  $\text{CeO}_2$ .

Harrison et al. also prepared CeO<sub>2</sub> supported Co<sub>3</sub>O<sub>4</sub> via co-precipitation and impregnation [26]. The catalytic performance of these composites in diesel soot oxidation was compared with alumina, silica and tin (IV) oxide supported cobalt oxide. It was reported that ceria supported Co<sub>3</sub>O<sub>4</sub> had better catalytic activity and this was attributed to the presence of Co<sub>3</sub>O<sub>4</sub> as the dominant phase [26]. However in alumina, silica and tin (IV) oxide supported cobalt oxide the dominant phase was reported to be Co<sup>2+</sup> in strong interaction with the support. The strong metal support interaction was reported to be the main reason for poor catalytic activity when alumina, silica and tin (IV) oxide supported cobalt oxide were used as catalysts.

Some research groups have reported using ceria as a promoter to increase the performance of the catalyst. Qi et al. reported the effect of ceria and Pd addition on the catalytic performance of Al<sub>2</sub>O<sub>3</sub> supported Co<sub>3</sub>O<sub>4</sub> for benzene oxidation. It was shown that in the presence of the promoter the catalytic activity increased as the proportion of ceria in the composite increased. This was attributed to the better dispersion of cobalt oxide crystals on the support due to the presence of CeO<sub>2</sub> [27]. Mu et al. showed that the synergy between cerium and cobalt enhanced the catalytic performance of Co<sub>3</sub>O<sub>4</sub> supported on Ce containing SBA-15 in deep oxidation of benzene [28].

#### **5.1.1.2.2 Other mixed oxides systems containing ceria**

Copper-cerium mixed oxides are known to be promising materials in various catalytic applications such as NO reduction [29], hydrocarbon oxidation [30] and CO oxidation [31]. The high catalytic activity of these composites is generally attributed to synergistic effects between the two oxides. These include the presence of oxygen vacancies in CeO<sub>2</sub> and the facile redox interaction between the copper and cerium redox couple [8, 32]. Mesoporous CeO<sub>2</sub> was used as a support for CuO nanoparticles to catalyse CO oxidation. It was demonstrated that mesoporous CeO<sub>2</sub> as a support showed higher catalytic performance compared to nonporous analogues. This was attributed to the high dispersion of the active sites which results in high availability of the active sites for the reactants [31].

High surface area copper-cerium oxide was prepared using the surfactant-template method. This composite was shown to have promising catalytic activity in CO oxidation. The high dispersion of CuO entities was reported to be the main reason for high catalytic activity of this composite [33].

## 5.2 General overview

Since the catalytic performance of transition metal oxides is improved by the presence of the CeO<sub>2</sub> either as a dopant or support, the focus of this chapter has been to investigate the effect of ceria as a dopant for cobalt supported on SBA-15. The morphology, dispersion and catalytic activity a number of composite materials prepared in a variety of ways have been investigated in detail.

Chapter five comprises three manuscripts in which the impact of cerium on the dispersion and catalytic properties of supported cobalt oxide species were investigated.

Publication 1, ( section 5.4) focuses on the impact of cerium as a dopant on the dispersion, morphology and catalytic activity of SBA-15 supported cobalt prepared by the two-solvent method and using Co(NO<sub>3</sub>)<sub>2</sub>.6H<sub>2</sub>O (5 wt%), Ce(NO<sub>3</sub>)<sub>3</sub>.6H<sub>2</sub>O (0.5 wt%) as metal precursors. For comparison SBA-15 was separately loaded with Co(NO<sub>3</sub>)<sub>2</sub>.6H<sub>2</sub>O (5 wt%) or Ce(NO<sub>3</sub>)<sub>3</sub>.6H<sub>2</sub>O (5 wt% ) via the same method. In the cases of both the Ce-doped Co-composite and non-doped Co-composite, Co<sub>3</sub>O<sub>4</sub> patches were formed throughout the SBA-15. However, the Ce-doped Co-composites showed better dispersion and smaller sized Co<sub>3</sub>O<sub>4</sub> patches than the non-doped Co-composites. This Ce-doped Co-composite also showed higher catalytic activity in liquid phase oxidation of olefins and alcohols compared to the non-doped Co-composite. The synergistic effect between cobalt and cerium is possibly due to the improvement in the redox properties of the catalytic system in the presence of Ce<sup>3+</sup>/Ce<sup>4+</sup>. The higher dispersion and smaller size of Co<sub>3</sub>O<sub>4</sub> patches could also improve the catalytic activity of the Ce-doped Co-composites. This paper also investigates the effect of the support on the catalytic activity by comparing a neat Co-Ce oxide composite and a supported Ce-doped Co-composite that both have the same Co:Ce weight ratio. The neat Co-Ce oxide composite had negligible catalytic activity in oxidising 1-phenylethanol to its corresponding products and this was attributed to the low surface area of the composite.

Publication 2, (section 5.5) concerns the impact of Ce(NO<sub>3</sub>)<sub>3</sub>.6H<sub>2</sub>O (0.5 wt%) as a dopant on the crystallinity, dispersion and catalytic activity of the composites prepared from CoCl<sub>2</sub>.6H<sub>2</sub>O (5 wt%) as cobalt precursor, again via the two-solvent method. For comparison SBA-15 was separately loaded with CoCl<sub>2</sub>.6H<sub>2</sub>O (5 wt%) or Ce(NO<sub>3</sub>)<sub>3</sub>.6H<sub>2</sub>O (5 wt%) using the same method. It was found that addition of cerium increased the catalytic activity of the Co-composite in liquid phase oxidation reactions. This Ce-doped Co-composite showed higher catalytic activity than its analogous composite prepared from CoCl<sub>2</sub>.6H<sub>2</sub>O alone. It

was found that the addition of ceria did not overcome the issue of cobalt leakage into the reaction solution. It was also found that, upon adding cerium as a dopant, the crystallinity of cobalt oxide species did not appear to improve.

Publication 3, (section 5.6) concerns the effect of Co:Ce ratio on the morphology and catalytic activity of Ce-doped Co-composites prepared via the two-solvent method. Here SBA-15 was loaded with fixed amount of  $\text{CoCl}_2 \cdot 6\text{H}_2\text{O}$  (5 wt%) and various amounts of  $\text{Ce}(\text{NO}_3)_3 \cdot 6\text{H}_2\text{O}$  (0.5-2 wt%). All the composites showed a blue coloration. Cobalt oxide species were highly dispersed throughout the SBA-15, regardless of the amount of Ce-loading. With increasing Ce-loading more crystalline spherical  $\text{CeO}_2$  nanoparticles could be observed within the SBA-15 mesopores. These particles were also highly dispersed and, due to the Z-contrast, could be seen as bright spots in STEM images. The composites with 0.5 wt% and 1.5 wt% Ce-loading showed the highest catalytic activity. This irregular pattern of behaviour with increasing Ce-loading is not easy to explain and requires more investigation. However it was suggested that the extent by which ceria covers the surface of the supported cobalt oxide species can affect the synergistic effect between cobalt and cerium. It is hypothesized that certain Co:Ce weight ratios provide improved redox interactions between the cobalt and ceria oxide species and, thus, better catalytic activity.

### 5.3 References

- [1] T.J. Ahrens, *Global Earth Physics: A Handbook of Physical Constants I*, American Geophysical Union, Washington, D.C, 1995.
- [2] L. R. Morss, *Handbook on the Physics and Chemistry of Rare Earths*, Elsevier Science, New York, 1994.
- [3] j. Kaspar, M. Graziani, P. Fornasiero, *Handbook on the Physics and Chemistry of the Rare Earths*, Elsevier Science, 2000.
- [4] V. Perrichon, A. Laachir, G. Bergeret, R. Frety, L. Tournayan, O. Touret, *J. Chem. Soc. Faraday. Trans. 90* (1994) 773-781.
- [5] B.H. Kim, K.H. Lee, *J. Mater. Sci.* 29 (1994) 6592-6598.
- [6] L.M. Cook, *J. Non-Cryst. Solids.* 120 (1990) 152-171.
- [7] T.I. Veinberg, I.V. Pishch, *Glass and Ceramics, Optimum amount of glass decolorizers*, SpringerLink, 1968.
- [8] A. Trovarelli, *Catalysis by Ceria and Related Materials*, Imperial College Press, London, 2001.
- [9] C.E. Hori, A. Brenner, K.Y. Simon Ng, K.M. Rahmoeller, D. Belton, *Catal. Today.* 50 (1999) 299-308.
- [10] J.-Y. Luo, M. Meng, X. Li, X.-G. Li, Y.-Q. Zha, T.-D. Hu, Y.-N. Xie, J. Zhang, *J. Catal.* 254 (2008) 310-324.

- [11] L. Liotta, M. Ousmane, G. Di Carlo, G. Pantaleo, G. Deganello, A. Boreave, A. Giroir-Fendler, *Catal. Lett.* 127 (2009) 270-276.
- [12] T. Tsoncheva, L. Ivanova, C. Minchev, M. Fröba, J. *Colloid Interface Sci.* 333 (2009) 277-284.
- [13] G. Rao, Ranga, B. Mishra, Gopal, , *Bull. Catal. Soc. India.* 2 (2003) 122-134.
- [14] J. Kaspar, P. Fornasiero, N. Hickey, *Catal. Today.* 77 (2003) 419-449.
- [15] X.-D. Hou, Y.-Z. Wang, Y.-X. Zhao, *Catal. Lett.* 123 (2008) 321-326.
- [16] A. Garrido Pedrosa, M. Souza, J. Fernandes, D. Melo, A. Araujo, *Reac. Kinet. Catal. Lett.* 79 (2003) 391-396.
- [17] E. Iwanek, K. Krawczyk, J. Petryk, J.W. Sobczak, Z. Kaszukur, *Appl. Catal. B: Environ.* 106 (2011) 416-422.
- [18] M. Dhakad, T. Mitshuhashi, S. Rayalu, Pradip Doggali, S. Bakardjiva, J. Subrt, D. Fino, N.L. H. Haneda, *Catal. Today.* 132 (2008) 188-193.
- [19] M. Kang, M.W. Song, C.H. Lee, *Appl. Catal. A: Gen.* 251 (2003) 143-156.
- [20] S. Todorova, G. Kadinov, K. Tenchev, A. Caballero, J. Holgado, R. Pereñíguez, *Catal. Lett.* 129 (2009) 149-155.
- [21] J. Shao, P. Zhang, X. Tang, B. Zhang, W. Song, Y. Xu, W. Shen, *Chin. J. Catal.* 28 (2007) 163-169.
- [22] L.F. Liotta, M. Ousmane, G. Di Carlo, G. Pantaleo, G. Deganello, G. Marci, L. Retailleau, A. Giroir-Fendler, *Appl. Catal. A: Gen.* 347 (2008) 81-88.
- [23] L.F. Liotta, G. Di Carlo, G. Pantaleo, G. Deganello, *Appl. Catal. B: Environ.* 70 (2007) 314-322.
- [24] L.F. Liotta, G. Di Carlo, G. Pantaleo, A.M. Venezia, G. Deganello, *Appl. Catal. B: Environ.* 66 (2006) 217-227.
- [25] Z. Mu, J.J. Li, M.H. Duan, Z.P. Hao, S.Z. Qiao, *Catal. Commun.* 9 (2008) 1874-1877.
- [26] P.G. Harrison, I.K. Ball, W. Daniell, P. Lukinskas, M. Céspedes, E.E. Miró, M.A. Ulla, *Chem. Eng. J.* 95 (2003) 47-55.
- [27] S. Zuo, C. Qi, *Catal. Commun.* 15 (2011) 74-77.
- [28] Z. Mu, J.J. Li, H. Tian, Z.P. Hao, S.Z. Qiao, *Mater. Res. Bull.* 43 (2008) 2599-2606.
- [29] P. Bera, K.R. Priolkar, P.R. Sarode, M.S. Hegde, S. Emura, R. Kumashiro, N.P. Lalla, *Chem. Mater.* 14 (2002) 3591-3601.
- [30] A. Martínez-Arias, M. Fernández-García, A.B. Hungría, A. Iglesias-Juez, O. Gálvez, J.A. Anderson, J.C. Conesa, J. Soria, G. Munuera, *J. Catal.* 214 (2003) 261-272.
- [31] W. Shen, X. Dong, Y. Zhu, H. Chen, J. Shi, *Micro. Meso. Mater.* 85 (2005) 157-162.
- [32] Y. Li, Q. Fu, M. Flytzani-Stephanopoulos, *Appl. Catal. B: Environ.* 27 (2000) 179-191.
- [33] M.-F. Luo, J.-M. Ma, J.-Q. Lu, Y.-P. Song, Y.-J. Wang, *J. Catal.* 246 (2007) 52-59.

**Declaration for Thesis Chapter 5.4**

Effect of Ce-doping on the dispersion of Co<sub>3</sub>O<sub>4</sub> nanorods supported on SBA-15

**Declaration by candidate**

In the case of Chapter 3 the nature and extent of my contribution to the work was the following:

Nature of contribution	Extent of contribution (%)
Proposed original idea; prepared and analysed samples; identified major issues; developed interpretations; fully drafted papers and conclusions	80%

The following co-authors contributed to the work. Co-authors who are students at Monash University must also indicate the extent of their contribution in percentage terms:

Name	Nature of contribution	Extent of contribution (%) for student co-authors only
Gregory P. Knowles	Aided method development (catalyst characterisation), input to interpretation of results, input to manuscript revision	N/A
Alan L. Chaffee	Supervision, assisted interpretations of results, editorial assistance	N/A

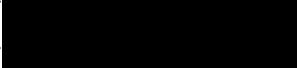
Candidate's Signature		Date 23.10.12
-----------------------	---	------------------

**Declaration by co-author:**

The undersigned hereby certify that:

- (1) the above declaration correctly reflects the nature and extent of the candidate's contribution to this work, and the nature of the contribution of each of the co-authors.
- (2) they meet the criteria for authorship in that they have participated in the conception, execution, or interpretation, of at least that part of the publication in their field of expertise;
- (3) they take public responsibility for their part of the publication, except for the responsible author who accepts overall responsibility for the publication;
- (4) there are no other authors of the publication according to these criteria;
- (5) potential conflicts of interest have been disclosed to (a) granting bodies, (b) the editor or publisher of journals or other publications, and (c) the head of the responsible academic unit; and
- (6) the original data are stored at the following location(s) and will be held for at least five years from the date indicated below:

Location(s)

Gregory P. Knowles		Date 22.10.12
Alan L. Chaffee		Date 22.10.12

## 5.4 Effect of Ce-doping on the dispersion of Co<sub>3</sub>O<sub>4</sub> nanorods supported on SBA-15

Jamileh Taghavimoghaddam, Gregory P. Knowles, Alan L. Chaffee

School of Chemistry, Monash University, Victoria 3800 Australia

### Abstract

SBA-15 supported cobalt oxide, cerium oxide and Ce-doped cobalt oxide composites were prepared via the two-solvent method using Co(NO<sub>3</sub>)<sub>2</sub>.6H<sub>2</sub>O and Ce(NO<sub>3</sub>)<sub>3</sub>.6H<sub>2</sub>O as metal precursors. The potential of Ce-doping to improve the dispersion of the Co<sub>3</sub>O<sub>4</sub> nanorods and catalytic performance of SBA-15 supported Co<sub>3</sub>O<sub>4</sub> in the tert-butylhydroperoxide oxidation of alcohols and olefins was investigated. A neat Co-Ce oxide mixture was separately prepared via a co-precipitation method for comparison to investigate the impact of a high surface area support on the catalytic activity of Ce-doped Co-composites. The Co:Ce weight ratio in the precursors for both neat and supported Ce-doped Co-composites was 10:1. All the composites were characterised by N<sub>2</sub> adsorption-desorption, XRD, FTIR, ICP-MS, TEM, HRTEM, SEM, STEM and elemental mapping. The catalytic performance of the composites was monitored by GC and GC-MS during the course of reaction. It was found that the use of cerium as a dopant improved the dispersion of the crystalline Co<sub>3</sub>O<sub>4</sub> nanorods in the support. The Ce-doped Co-composite also showed higher catalytic activity in the liquid phase oxidation reaction than either the supported Co-composite or Ce-composite. This can be attributed to the higher dispersion of Co<sub>3</sub>O<sub>4</sub> nanorods in the former composite and thus higher available surface area, and to the beneficial effect of Ce-doping on the redox properties of the catalyst. Neat Co-Ce demonstrated negligible catalytic activity, probably due to its much lower surface area than that of supported Ce-doped Co-composite.

**Keywords:** Supported Co<sub>3</sub>O<sub>4</sub>; Ceria; Dopant; Dispersion; Liquid phase oxidation; Two-solvent method

### 5.4.1 Introduction

Oxidation of organic substrates is a fundamental transformation in industry, as the corresponding oxidation products can often be valuable chemical intermediates. The use of heterogeneous catalysts for these oxidation reactions is of significant interest in order to improve the conversion of the reaction, selectivity of the products and recovery of the catalyst [1, 2]. Metal oxides, more specifically the transition metal oxides, are known to be important in catalytic processes. Many of these oxides can be relatively stable in more than

one oxidation state so that, they can facilitate oxidation-reduction or “redox” cycles. Among the transition metals, cobalt oxides, typically the spinel-structure  $\text{Co}_3\text{O}_4$ , have been shown to be particularly efficient catalysts in oxidation of hydrocarbons [3]. Spinel  $\text{Co}_3\text{O}_4$ , contains cobalt cations in two different oxidation states;  $\text{Co}^{2+}$  in tetrahedral and  $\text{Co}^{3+}$  in octahedral coordination [4].

The catalytic activity and selectivity of metal oxide nanoparticles strongly depends on their structural characteristics, specifically their size, dispersion and shape [5]. The size of the metal oxide nanoparticles is known to have a substantial impact on their catalytic performance since it affects the ‘active surface area’ [6, 7]. In the case of supported metal oxides, however, the type of the support plays a key role in determining the size and dispersion of the particles and therefore their catalytic activity [8-10]. The use of a high surface area support can enhance the dispersion of the active sites and thus the accessibility of active surface area to reactants [11]. This high accessibility also facilitates the adsorption and diffusion of reactant molecules, thereby increasing the conversion to product(s).

Ceria has been used as a promoter for various supported metal oxide catalysts [12, 13]. The oxygen storage capacity and the redox properties of  $\text{Ce}^{4+}/\text{Ce}^{3+}$  make ceria a desirable dopant for cobalt oxides [14]. Both supported and bulk ceria-doped Co-composites have been previously used as oxidation catalysts with better catalytic performance than non-doped analogues [12, 15]. It is also known that ceria as a dopant can not only improve the dispersion of the metal oxide particles, but also reduce the size of these particles [12]. This results in enhancement of the catalytic performance through the provision of higher active surface area [12]. Bulk ceria-doped  $\text{Co}_3\text{O}_4$  was tested for liquid phase oxidation of alcohols to the corresponding carbonyls [16]. It has also been reported that ceria-doped  $\text{Co}_3\text{O}_4$  showed better catalytic activity than either pure cobalt oxide or pure ceria. Todorova et al. reported that  $\text{SiO}_2$  supported  $\text{Co}_3\text{O}_4/\text{CeO}_2$  gave higher conversions for n-hexane and CO oxidation than either  $\text{SiO}_2$  supported  $\text{Co}_3\text{O}_4$  or  $\text{SiO}_2$  supported  $\text{CeO}_2$ . It was also shown that the sequence in which the cobalt and cerium precursors were added to the support affected the catalytic performance of the final products [17].

We previously reported the effect of the Co-loading on the dispersion and morphology of SBA-15 supported  $\text{Co}_3\text{O}_4$  particles. It was found that the composites with higher dispersion and smaller  $\text{Co}_3\text{O}_4$  particle size had better catalytic performance [18]. This was attributed to less pore blockage and better accessibility to active particles [19].

The present study concerns the effect of CeO<sub>2</sub> as a dopant on the dispersion and morphology of the Co<sub>3</sub>O<sub>4</sub> nanorods supported on SBA-15 as well as on the catalytic performance of the resulting composite. Co(NO<sub>3</sub>)<sub>2</sub>·6H<sub>2</sub>O and Ce(NO<sub>3</sub>)<sub>3</sub>·6H<sub>2</sub>O were used to prepare Ce-doped Co-composites via the two-solvent method [20]. SBA-15 was also separately loaded with Co(NO<sub>3</sub>)<sub>2</sub>·6H<sub>2</sub>O or Ce(NO<sub>3</sub>)<sub>3</sub>·6H<sub>2</sub>O individually via the same two-solvent method. A neat Co(NO<sub>3</sub>)<sub>2</sub>·6H<sub>2</sub>O/Ce(NO<sub>3</sub>)<sub>3</sub>·6H<sub>2</sub>O composite was also prepared via the co-precipitation method to study the effect of support on the catalytic performance of the composites with the same Co:Ce weight ratio. Morphological and chemical characterisation of the composites was carried out using various techniques such as X-ray diffraction (XRD), N<sub>2</sub> adsorption-desorption, temperature programmed reduction (TPR), Fourier transform infrared spectroscopy (FTIR), inductively coupled plasma-mass spectrometry (ICP-MS), scanning electron microscopy-electron (SEM), transmission electron microscopy (TEM), high resolution transmission electron microscopy (HRTEM), scanning transmission electron microscopy (STEM) and elemental mapping. Finally the composites were catalysed the oxidation of alcohols and olefins in the presence of tert-butylhydroperoxide (TBHP), and the products were identified by gas chromatography (GC) and gas chromatography-mass spectrometry (GC-MS).

## 5.4.2 Experimental

### 5.4.2.1 Catalyst preparation

SBA-15 was prepared using the method first described by Zhao and co-workers [21]. A supported Ce-doped Co-composite was synthesized using the two-solvent method [20] and Co(NO<sub>3</sub>)<sub>2</sub>·6H<sub>2</sub>O and Ce(NO<sub>3</sub>)<sub>3</sub>·6H<sub>2</sub>O. SBA-15 was first suspended in dry hexane (the hydrophobic solvent). The desired amounts of Co(NO<sub>3</sub>)<sub>2</sub>·6H<sub>2</sub>O and Ce(NO<sub>3</sub>)<sub>3</sub>·6H<sub>2</sub>O to obtain nominally 5 wt % and 0.5 wt % loading respectively, were dissolved in distilled water. The total amount of water used for both metal aqueous solutions corresponded to the pore volume of the mesoporous silica SBA-15, previously determined by N<sub>2</sub> adsorption-desorption. The aqueous solution of cobalt precursor was added to the hydrophobic solution and the mixture was stirred for 15 min. Cerium precursor aqueous solution was then added dropwise to the mixture while stirring for a further 15 min. The mixture was sonicated for 15 min and stirring was continued for a further 2 h. The solid was recovered by filtration and dried in air at room temperature overnight. Finally, the sample was calcined by heating in air at 2 °C min<sup>-1</sup>, then holding at 700 °C for 6 h [22]. This composite is referred to as SCo5-Ce0.5.

Non-doped Co-composite and Ce-composite were prepared separately with nominally 5 wt% Co or 5 wt% Ce, respectively, via the same two-solvent method. Here again the desired amount cobalt or cerium precursor was dissolved in water of volume equal to the pore volume of the SBA-15 and added dropwise to the hydrophobic mixture (SBA-15 dispersed in n-hexane). These composites are referred to as SCo5 and SCe5, respectively.

A neat Co-Ce composite (10:1 by wt) was synthesized via co-precipitation [16]. The required amounts of  $\text{Co}(\text{NO}_3)_2 \cdot 6\text{H}_2\text{O}$  and  $\text{Ce}(\text{NO}_3)_3 \cdot 6\text{H}_2\text{O}$  were dissolved in the minimum amount of deionised water. To this solution, aqueous ammonia (28 %) was added dropwise, with constant stirring, to obtain pH 10. The mixture was filtered and continuously washed with water so as to obtain a neutral filtrate. The precipitate was dried in air overnight at 110 °C, then ground and calcined by heating in air at 2 °C min<sup>-1</sup>, then holding at 350 °C for 6 h. This composite is referred to as Co-Ce.

#### 5.4.2.2 Characterization of materials structural morphology/chemsitry

*Low-angle and wide-angle XRD patterns* were obtained with a Bruker D8 Focus powder diffractometer using monochromatic  $\text{CuK}_\alpha$  source radiation ( $\lambda=1.5406 \text{ \AA}$ ) operated at 40 kV and 30 mA over the  $2\theta$  ranges of 0.4-4° and 15-80° respectively. Data in the  $2\theta$  range 0.4-4° were collected with a step size of 0.02° and a step time of 0.1° min<sup>-1</sup>. Data in the  $2\theta$  range 15-80° were collected with step size of 0.02° and step time of 1° min<sup>-1</sup>.

*N<sub>2</sub> adsorption-desorption isotherms* were obtained at -196 °C on a Coulter Omnisorb 360-CX gas sorption analyzer. Samples were outgassed under vacuum at 150 °C overnight prior to analysis. Pore volumes ( $P_v$ ) calculated from the desorption branch, BET surface areas over the relative pressure ( $p/p_0$ ) range 0.05-0.3, [21], and pore size distributions (PDS) using the BJH method [21] were calculated for each data set. The total pore volume of supported Ce-doped Co-composites was measured at relative pressure  $p/p_0 = 0.9$ , however the total pore volume of neat Co-Ce composite was measured at relative pressure  $p/p_0 = 0.99$ .

*FTIR* spectra were collected using a BIO-RAD FTS 40 spectrometer. The materials were diluted 1/300 in dry KBr, dried at 110 °C for 4-6 h, then pressed into pellets (under vacuum) immediately prior to analysis.

*ICP-MS* was carried out using a GBC OPTIMAS 9500 ICP-MS. All catalysts were digested in  $\text{HNO}_3$  and HF at 120 °C prior to measurement [23].

*TEM* and HRTEM images were collected using a JEOL 2011 transmission electron microscope equipped with a LaB<sub>6</sub> emitter (point resolution 0.21 nm) at an accelerating voltage of 200 kV.

*STEM* was carried out using a JEOL 2100F microscope equipped with a high angular annular dark field (HAADF) detector (camera length 10 cm and 0.5 nm probe) to collect elemental mapping profiles. A 50 mm JEOL Si(Li) electron dispersive x-ray EDX detector was used for elemental mapping.

*SEM* was carried out using a JEOL 7001F field emission gun scanning electron microscope.

*GC* was carried out on an Agilent 6850 gas chromatograph equipped with an flame ionization detector (FID) detector and a polar capillary column (BP20, 60 m × 0.25 mm). *GC-MS* was carried using an Agilent 5973 mass spectrometer (source conditions: EI, 70 eV, 200 °C) coupled to a 6890 series GC system.

### **5.4.2.3 Catalytic tests**

Liquid phase oxidation of organic substrates was performed in a round bottomed flask. In each test, 0.1g of catalyst was added to 20 mmol of substrate in 5 mL of acetonitrile. After reaching the desired temperature for the reaction (80-83 °C), the oxidant, TBHP, (24 mmol) was added dropwise over approximately 10 min. Reactions were carried out under reflux and monitored by GC, samples being taken every 4 h up to 24 h.

## **5.4.3 Results and discussion**

### **5.4.3.1 Characterization of supported catalysts**

#### **5.4.3.1.1 Low-angle X-ray Diffraction (XRD)**

Low-angle XRD patterns of pure SBA-15, SCo<sub>5</sub>, SCe<sub>5</sub> and SCo<sub>5</sub>-Ce<sub>0.5</sub> are shown in Fig. 1. The XRD pattern for pure SBA-15 exhibited three characteristic peaks at  $2\theta = 0.94^\circ$ ,  $1.52^\circ$  and  $1.78^\circ$ . These peaks were indexed to the (100), (110) and (200) diffractions of the two dimensional (2D) hexagonal mesostructure (space group p6mm) with  $d_{100}$  spacing of 9.8 nm [24, 25]. Similar XRD patterns were obtained for SCo<sub>5</sub>-Ce<sub>0.5</sub>, SCo<sub>5</sub> and SCe<sub>5</sub>, indicating that after Co and/or Ce loading the mesostructure of the support was preserved. However, the intensity of the main (100) peak decreased after Co and/or Ce loading when compared to the

pure SBA-15. This indicates that the mesoporosity in the composites was lower, probably because some pores had been filled by the metal oxides while others remained empty [26].

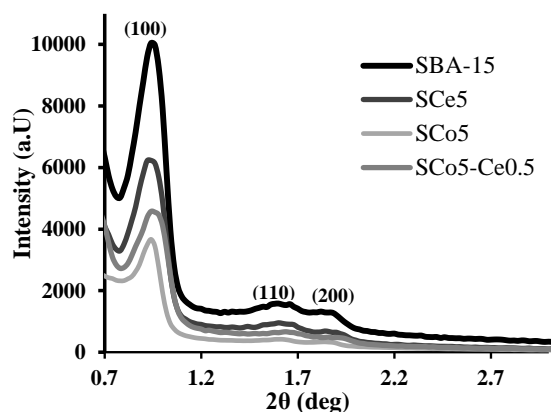


**Fig. 1** Low-angle XRD patterns of pure SBA-15 and all supported composites

#### 5.4.3.1.2 N<sub>2</sub> adsorption-desorption

Fig. 2 A presents the N<sub>2</sub> adsorption-desorption isotherms obtained for SBA-15 and all supported composites. The textural properties of the SBA-15 and all the composites, including the BET surface areas, pore diameters ( $P_d$ ), total pore volumes ( $P_v$ ) and micropore volumes ( $P_{vmic}$ ) are summarized in Table 1. The Co and/or Ce content are also included in Table 1. SBA-15 exhibits a type IV isotherm with H1 hysteresis according to the IUPAC classification [25]. The sharp inflection on adsorption branch of the isotherm between relative pressures ( $p/p_0$ ) 0.6-0.8 are characteristic of good quality SBA-15 and confirms the narrow PSD of the pure SBA-15 [27]. The adsorption at lower relative pressure  $p/p_0 < 0.3$  in SBA-15 is associated with the presence of micropores in the silica walls, which connect the cylindrical channels.

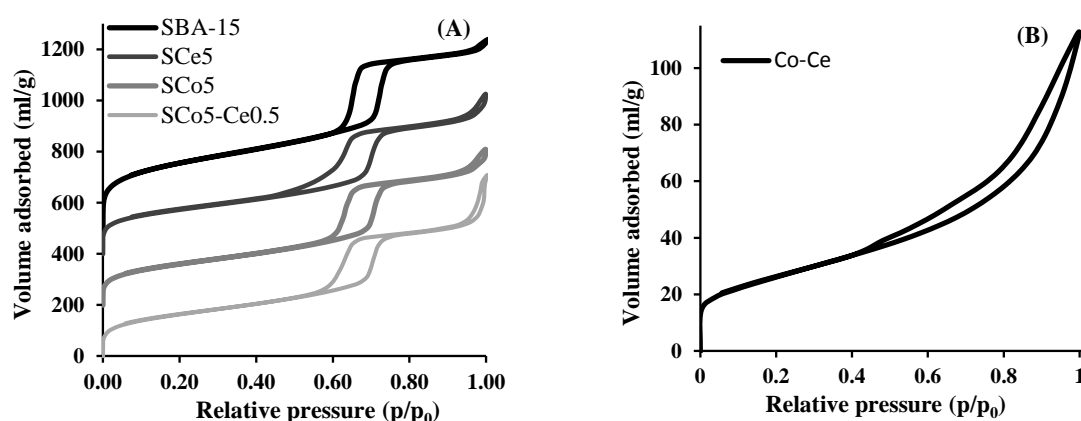


**Fig. 2** N<sub>2</sub> adsorption-desorption isotherm of (A) pure SBA-15 and all supported composites (to avoid overlapping of the isotherms they have been displaced) and (B) Co-Ce composite

After Co and/or Ce loading the general shape of the isotherms was nearly identical to that of pure SBA-15. This similarity confirms that the mesoporous structure of the support was

preserved after loading Co and/or Ce. However some changes in the isotherms were observed, such as the decrease in the volume of adsorbed N<sub>2</sub> both in the micropore and mesopore regions. In addition, the capillary condensation step of all supported composites occurred at a lower relative pressure than for pure SBA-15. This suggests the formation of Co and/or Ce oxide inside the mesopores [8, 28-30]. The slope of the capillary condensation for SCo5 and SCo5-Ce0.5 was not as sharp as that of pure SBA-15, indicating a relatively broader PSD for these two composites [31]. A shoulder was observed on the desorption branch of SCo5 at relative pressure (p/p<sub>0</sub>) 0.45, which can be attributed to the cavitation phenomenon, i.e., incomplete pore blockage [32].

Upon loading Co or Ce on SBA-15, SCo5 or SCo5-Ce0.5, the surface area, micropore and mesopore volume decreased significantly. However, essentially no decrease in surface area and micropore and mesopore volume for SCo5-Ce0.5 relative to SCo5 and SCo5 was observed. This is attributed to the presence of Co<sub>3</sub>O<sub>4</sub> nanorods inside the mesopores of SBA-15. From previous work, it is known that the loss of surface area and pore volume is only partially attributable to the pore filling by cobalt oxide, Co<sub>3</sub>O<sub>4</sub>, because the actual volume occupied by Co<sub>3</sub>O<sub>4</sub> is very low [19, 33]. In our samples the occupied volume related to cobalt oxide and cerium oxide in SCo5, SCo5-Ce0.5 and SCo5 was calculated to be 0.0116, 0.008 and 0.0118 cm<sup>3</sup>, respectively. This is based on the determined metal oxide concentrations and the known density of the spinel Co<sub>3</sub>O<sub>4</sub> and fluorite CeO<sub>2</sub> (assuming that the active patches are Co<sub>3</sub>O<sub>4</sub> and CeO<sub>2</sub>), which was 6.11 and 7.21 g cm<sup>-3</sup>, respectively. Thus, it is suggested that the formation of cobalt and/or cerium oxides within the SBA-15 mesopores blocked parts of the micropore and mesopore networks so that they became inaccessible to N<sub>2</sub> (chapter 3, publication 3, section 3.4.4)

The neat Co-Ce composite, by contrast, exhibited a type II isotherm (Fig. 2 B), which is characteristic of nonporous materials [34]. This composite possesses a relatively low surface area (91 m<sup>2</sup> g<sup>-1</sup>) and micropore and mesopore volumes compared to the supported composites.

**Table 1** Textural properties of SBA-15 and all

Sample	S <sub>BET</sub> (m <sup>2</sup> g <sup>-1</sup> )	P <sub>d</sub> (nm)	P <sub>v</sub> (cm <sup>3</sup> g <sup>-1</sup> ) <sup>a</sup>	P <sub>vmic</sub> (cm <sup>3</sup> g <sup>-1</sup> ) <sup>b</sup>	Co:Ce (wt %) <sup>c</sup>
SBA-15	946	6	1.1	0.36	0.0:0.0
SCo5	589	5.6	0.79	0.23	0.0:5.0
SCo5-Ce0.5	588	5.6	0.77	0.22	5.0:0.5
Co-Ce	91	-	0.17	0.02	10.0:1.0

a: Total pore volume, b: micropore volume and c: Co and Ce content measured by ICP-MS

Fig. 3 A shows the PSD of pure SBA-15 and all the composites. Pure SBA-15 showed a narrow PSD similar to those of SCo5 and SCo5-Ce0.5. However the PSD of SCo5 was broader than those of the other supported composites. A shoulder on the low diameter side of the main peak at 5.6 nm is consistent with the occurrence of partially blocked pores, as previously described [19, 35]. The Co-Ce composite also showed a very broad PSD and exhibited a preponderance of pores with diameters greater than 10 nm.

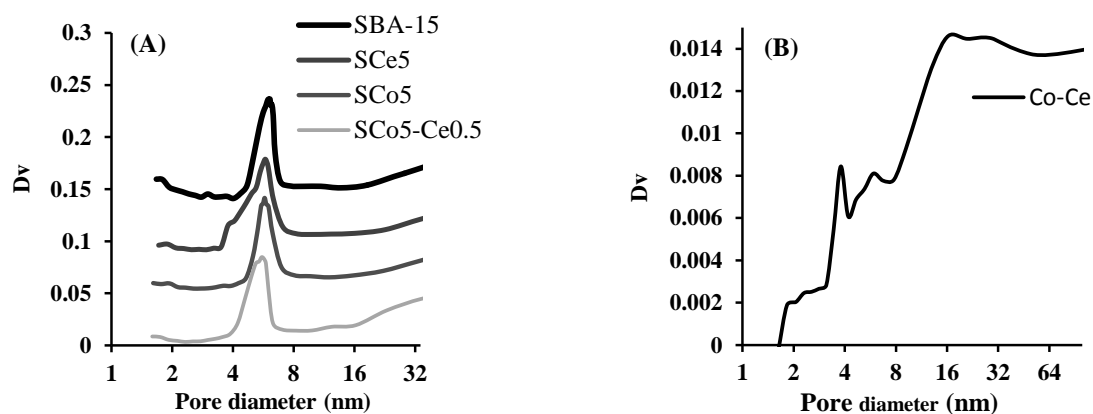


**Fig. 3** PSD of (A) SBA-15 and all supported composites and (B) Co-Ce composite

#### 5.4.3.1.3 Wide-angle X-ray Diffraction

Fig. 4 shows the X-ray diffraction patterns of the pure SBA-15, all supported and neat Co-Ce composites. No diffraction peaks were observed for the SBA-15 except for a broad peak at  $15^\circ < 2\theta < 30^\circ$  which is attributed to the amorphous silica [36-38]. This broad peak was common to all the supported composites.

The XRD pattern for neat Co-Ce composite showed diffractions at  $2\theta = 27.44^\circ, 32.02^\circ, 46.22^\circ$  and  $55^\circ$  corresponding to the (111), (200), (220) and (311) crystal planes of the fluorite structure of  $\text{CeO}_2$  (JCPDF file 00-034-0394) [15] as well as at  $2\theta = 36.56^\circ, 43.92^\circ, 55.44^\circ, 58.38^\circ$  and  $64.32^\circ$ , corresponding to the (311), (400), (422), (511) and (440) crystal planes of the spinel structure of  $\text{Co}_3\text{O}_4$  (JCPDF file 01-073-1701) [4, 18]. No diffraction peaks related to a mixed oxide phase were observed, suggesting that the  $\text{Co}_3\text{O}_4$  and  $\text{CeO}_2$  formed two separate phases.

The SCo5 XRD pattern showed weak diffraction peaks at  $2\theta = 27.47^\circ, 31.5^\circ, 46.2^\circ, 55.37^\circ, 77.05^\circ$  corresponding to the (111), (200), (220), (311), (331) crystal planes of the fluorite structure of  $\text{CeO}_2$  [15, 17]. The low intensity of the diffraction peaks in SCo5 suggests that either the particle size was very small or that the particles were highly dispersed throughout the support.

The XRD pattern of SCo5 exhibited the diffraction peaks for spinel  $\text{Co}_3\text{O}_4$  listed above. The average particle size was calculated to be 25 nm using the Scherrer equation [39]. This was larger than the pore diameter of SBA-15 determined by  $\text{N}_2$  adsorption-desorption and can be explained by the growth of  $\text{Co}_3\text{O}_4$  particles in adjacent connected pores, leading to the formation of crystalline  $\text{Co}_3\text{O}_4$  patches with an apparent particle size larger than the mesopore diameter [19].

For the Ce-doped Co-composite, SCo5-Ce0.5, the intensity of the diffraction peaks was less than that for the SCo5. The average particle size for this composite was calculated to be 10 nm, which is two and a half times smaller than for SCo5. This can be attributed to the presence of smaller  $\text{Co}_3\text{O}_4$  patches with better dispersion, which is in agreement with the TEM results (see section 5.4.3.1.4). It is noteworthy that no diffraction peaks corresponding to the fluorite  $\text{CeO}_2$  structure can be observed; this can be attributed to the low Ce-loading and/or its high dispersion throughout the support.

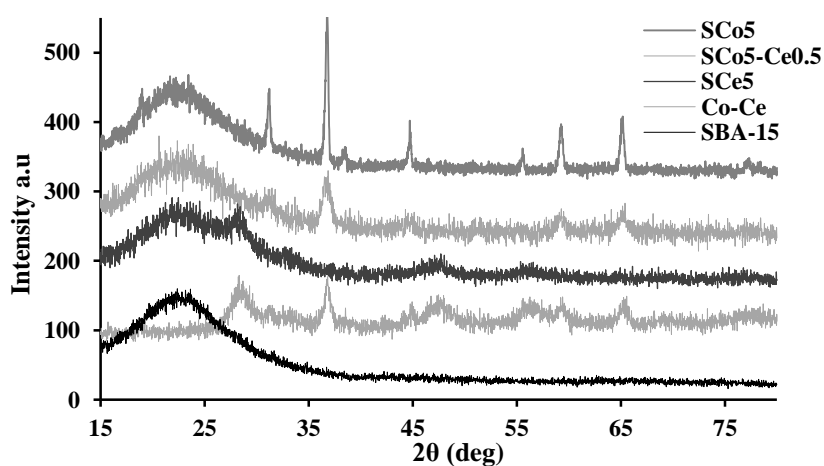
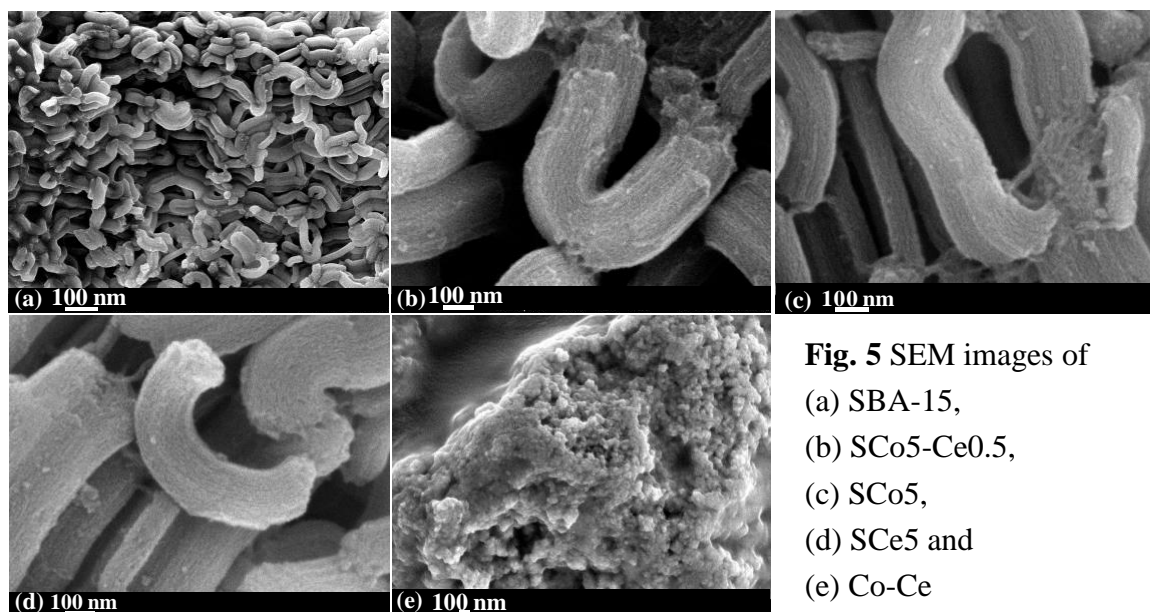


**Fig. 4** Wide-angle XRD patterns obtained for SBA-15 and all the composites

#### 5.4.3.1.4 Morphological investigation

Fig. 5 shows the SEM images of the pure SBA-15 and all the composites. SBA-15 consisted of rod-like particles with an average width and length of  $220 \pm 20$  nm and  $900 \pm 50$  nm respectively. Similar morphologies have been reported previously [40, 41]. The secondary aggregation of the particles from end to end or side to side resulted in a rope-like macrostructure. The surface of the SBA-15 particles exhibited uniform stripes that are consistent with the straight channels that are expected to be present. These stripes were also present on the surface of the supported composite particles, implying that the mesoporosity was preserved after loading cobalt and cerium. This is in agreement with  $\text{N}_2$  adsorption-desorption and low-angle XRD results.

The neat Co-Ce composite displayed an uneven surface and consists of crumb-like particles with a large degree of porosity. Fig. 5e demonstrates that the particles aggregated to form clusters with pores of sizes broadly consistent with the pore size distribution measured by N<sub>2</sub> desorption.



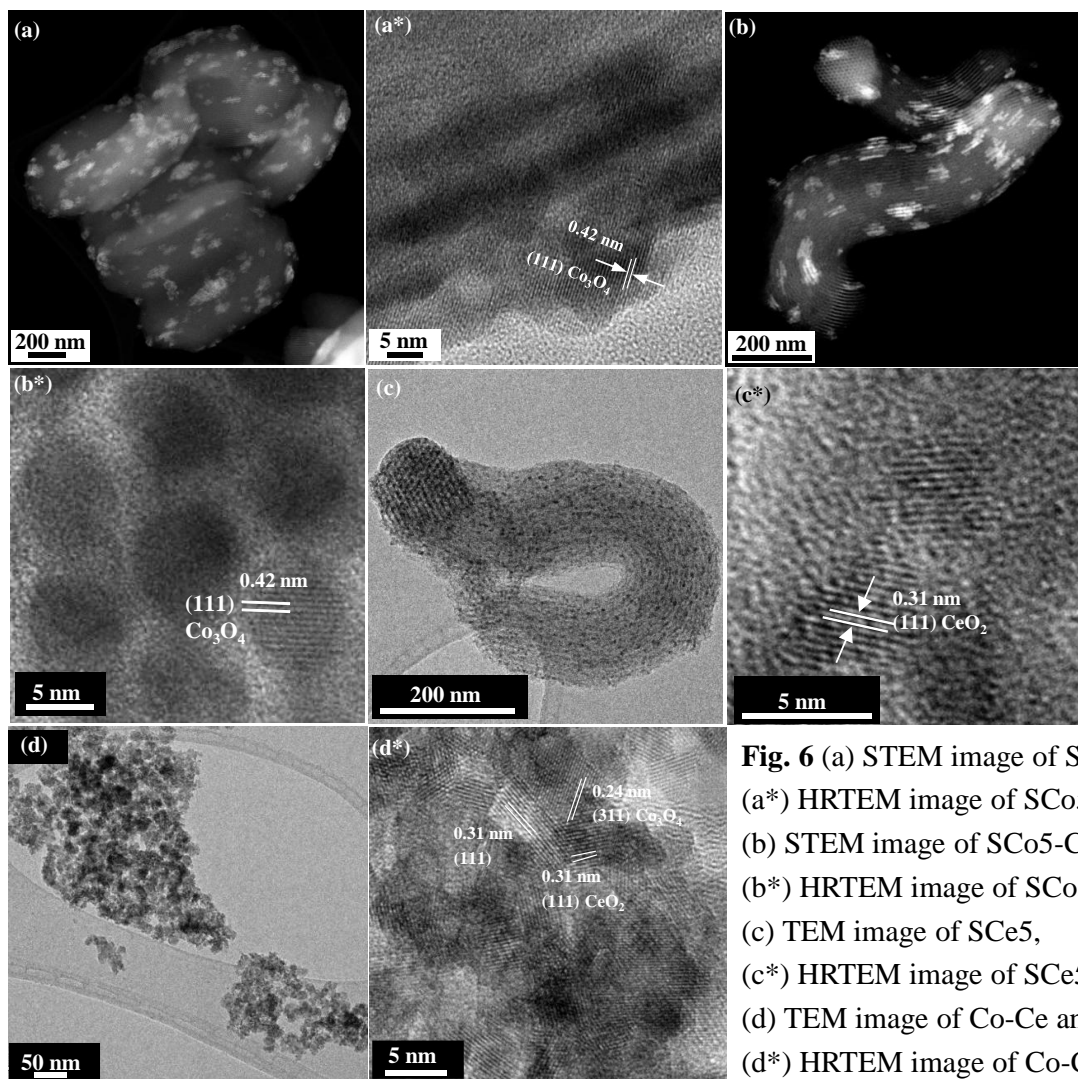
**Fig. 5** SEM images of  
 (a) SBA-15,  
 (b) SCo5-Ce0.5,  
 (c) SCo5,  
 (d) SCo5 and  
 (e) Co-Ce

Fig. 6 shows TEM images of all the composites. The presence of highly ordered channels in the supported composites clearly indicated the preservation of the SBA-15 mesoporous structure, which is in agreement with the results obtained from XRD, N<sub>2</sub> adsorption-desorption and SEM. The parallel channels of SBA-15 could also be observed after Co and/or Ce were loaded on the support.

In the case of SCo5 (Fig. 6 c and c\*) highly dispersed cerium oxide particles were observed throughout the SBA-15. These particles appeared as black dots due to the electronic density differences from the silica and were only seen inside the SBA-15 pores. The size of these particles was measured to be less than 5 nm. Since these particles were smaller than the pore diameter of the SBA-15, once formed on the internal surface of pore wall, they could have caused partial pore blockage. This is in agreement with the results obtained from N<sub>2</sub> adsorption-desorption. The parallel lattice fringes with 0.31 nm d-spacing corresponding to (111) planes in fluorite structure CeO<sub>2</sub> (JCPDF file 00-034-0394) could be observed in the HRTEM image.

In SCo5 spinel Co<sub>3</sub>O<sub>4</sub> patches were observed (Fig. 6 a and a\*) well dispersed throughout the SBA-15 [19]. Each patch was comprised of crystalline Co<sub>3</sub>O<sub>4</sub> nanorods connected to each other with small bridges through the micropores [38]. These patches formed in various sizes, with widths and lengths in the range of 50-100 nm and 75-200 nm respectively. The lattice

fringes of spinel  $\text{Co}_3\text{O}_4$  with 0.42 nm d-spacing corresponding to (111) planes (JCPDF file 01-073-1701) were observed in the HRTEM image. This confirmed the formation of crystalline  $\text{Co}_3\text{O}_4$  nanorods inside the pores of SBA-15. It is interesting that the dispersion behaviour of  $\text{Co}_3\text{O}_4$  observed in this work differs from that of  $\text{CeO}_2$  formed within the pores of the SBA-15. While  $\text{Co}_3\text{O}_4$  particles formed nanorods, which extended their growth via micropores to the adjacent mesopores upon calcination,  $\text{CeO}_2$  formed fine spherical particles within individual pores.



**Fig. 6** (a) STEM image of SCo5, (a\*) HRTEM image of SCo5, (b) STEM image of SCo5-Ce0.5, (b\*) HRTEM image of SCo5-Ce0.5, (c) TEM image of SCo5, (c\*) HRTEM image of SCo5, (d) TEM image of Co-Ce and (d\*) HRTEM image of Co-Ce

In the Ce-doped Co-composite the patches of  $\text{Co}_3\text{O}_4$  could still be observed throughout the support. However cerium addition had decreased the size of the patches and improved their dispersion. Here, most patches were comprised of just 2-3 adjacent nanorods such that the average widths and lengths of the patches were 15-25 nm and 40-60 nm respectively (Fig. 6 b). Some single rods were also observed in the channels of SBA-15. A similar phenomenon has been previously reported where conventional silica was used as support [17].

Fig. 6 d and d\* show the TEM and HRTEM images of the neat Co-Ce composite. In this work the size of the  $\text{Co}_3\text{O}_4$  clusters was measured to be approximately 20-50 nm, which suggests that  $\text{Co}_3\text{O}_4$  particles did not aggregate substantially during calcination. This can be attributed to the presence of  $\text{CeO}_2$  and its inhibition of  $\text{Co}_3\text{O}_4$  aggregation, as reported by Hou et al [12]. Sean et al. reported that for bulk  $\text{Co}_3\text{O}_4/\text{CeO}_2$ , the spaces between  $\text{Co}_3\text{O}_4$  particles were filled with  $\text{CeO}_2$ , and thus the aggregation of  $\text{Co}_3\text{O}_4$  particles at high temperature was prevented [42]. The HRTEM image exhibited the lattice fringes of both  $\text{Co}_3\text{O}_4$  and  $\text{CeO}_2$ , demonstrating that there was phase separation. Even with careful examination of various areas of the neat Co-Ce composite no mixed phase domains could be identified.

Fig. 7 shows the STEM images and elemental mapping profiles of SCo5 and SCo5-Ce0.5. Spinel  $\text{Co}_3\text{O}_4$  patches were observed for both SCo5 and SCo5-Ce0.5, but they were more evenly dispersed in the latter composite. This can be attributed to the presence of  $\text{CeO}_2$  as a dopant [17].  $\text{CeO}_2$  particles were also highly dispersed throughout the support and, in the case of SCo5-Ce0.5,  $\text{CeO}_2$  particles appeared to concentrate near where the  $\text{Co}_3\text{O}_4$  patches were located (Fig. 7 b white circles).

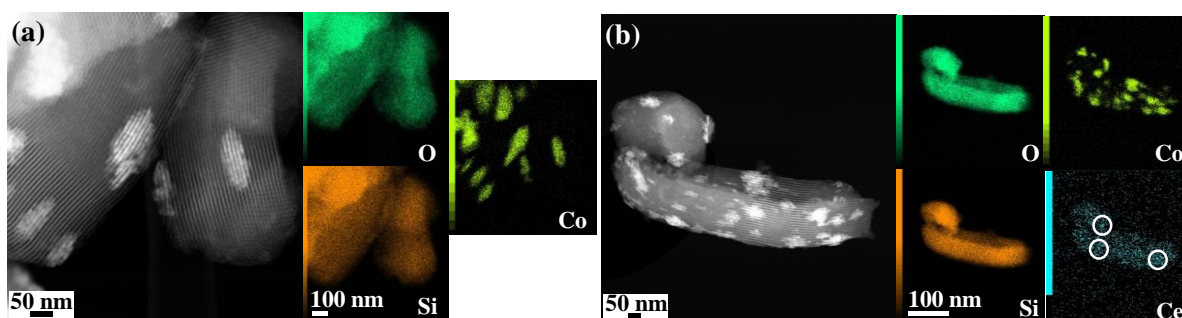


**Fig. 7** STEM images and elemental mapping profiles of (a) SCo5 and (b) SCo5-Ce0.5

#### 5.4.3.1.5 Fourier transform infrared spectroscopy

Fig. 8 shows the FTIR spectra of all the composites. The bands at  $470\text{ cm}^{-1}$ ,  $1081\text{ cm}^{-1}$  and  $808\text{ cm}^{-1}$  were due to asymmetric and symmetric Si-O-Si stretching vibrations respectively [43]. The broad band at around  $3400\text{ cm}^{-1}$  was due to the presence of surface  $-\text{OH}$  groups with a strong hydrogen bond interaction between them. The bending vibration of Si-OH was observed at around  $964\text{ cm}^{-1}$  [44]. The band at  $1630\text{ cm}^{-1}$  was assigned to the deformation modes of  $-\text{OH}$  bonds of the adsorbed water [45]. Spectra obtained for SCo5 and SCo5-Ce0.5 showed, in addition, absorbance peaks centred at  $690\text{ cm}^{-1}$  and  $580\text{ cm}^{-1}$  consistent with Co-O stretching vibrations (black arrows) [46-48]. The band at  $580\text{ cm}^{-1}$  is associated with  $\text{Co}^{3+}$ -O vibrations in octahedral positions of the spinel lattice while the band at around  $690\text{ cm}^{-1}$  is

attributed to  $\text{Co}^{2+}$ -O vibrations in tetrahedral positions. Cerium oxide did not show any bands in the scanned region [17].

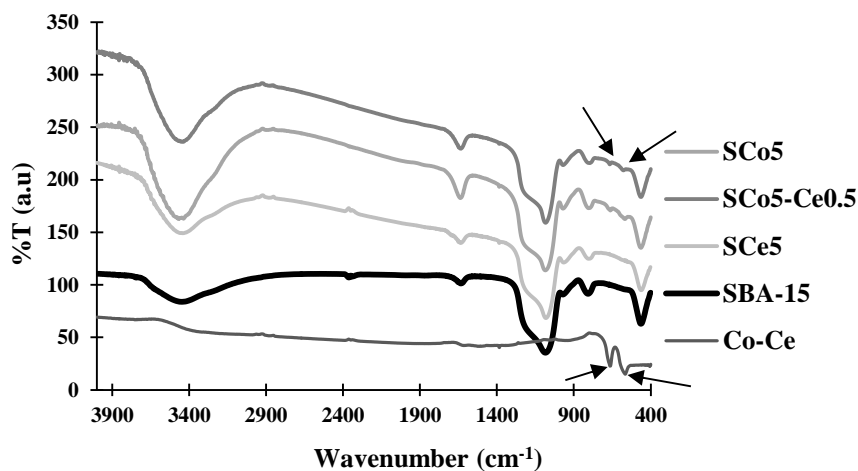


**Fig. 8** FT-IR spectra of SBA-15 and all the composites

#### 5.4.3.1.6 Catalyst evaluation

The catalytic performance of all the composites was evaluated in the oxidations of 1-phenylethanol, trans-2-hexene-1-ol, norbornene and cinnamyl alcohol in the presence of TBHP. The results are summarized in Table 2.

To compare the catalytic performance of SCo5-Ce0.5 with that of SCo5 and SCo5, 1-phenylethanol was used as the substrate. SCo5 and SCo5 showed similar catalytic activity for this oxidation (entries 2 and 3). However when SCo5-Ce0.5 was used as a catalyst, the reactivity doubled (entry 4). Cobalt oxide is generally known to be an effective catalyst for oxidation reactions, typically at high temperature in the gas phase, due to its high oxygen mobility [15, 49]. It was separately reported that the redox behaviour of  $\text{Co}^{2+}/\text{Co}^{3+}$  facilitates the catalytic reaction [19]. In addition, the high oxygen storage capacity of ceria as well as the redox behaviour of  $\text{Ce}^{3+}/\text{Ce}^{4+}$  was reported to further facilitate oxygen mobility in a series of bulk  $\text{Co}_3\text{O}_4/\text{CeO}_2$  composites. These properties were reported to improve the catalytic performance of  $\text{Co}_3\text{O}_4/\text{CeO}_2$  composites with certain Co:Ce ratio in low temperature propane oxidation [50]. Thus, it appears that, the synergistic effect between cobalt and cerium, which can be due to improvement of  $\text{Co}^{2+}/\text{Co}^{3+}$  redox property in the presence of  $\text{Ce}^{3+}/\text{Ce}^{4+}$ , which is well known in gas phase reactions [51], may also be the main reason for the higher catalytic activity of SCo5-Ce0.5 in this liquid phase system. Other groups have proposed that  $\text{CeO}_2$  can partially cover the surface of the supported metal oxide [52, 53] and the extent of this coverage was reported to play a crucial role in the catalytic activity of Ce-doped metal oxide composites [53]. In the present case it is suggested that in SCo5-Ce0.5 a  $\text{CeO}_2$  rich domain partially covered the surface of  $\text{Co}_3\text{O}_4$  to facilitate the synergistic effect between

cobalt and cerium. If the  $\text{CeO}_2$  were to fully cover the surface of the  $\text{Co}_3\text{O}_4$  species it might be expected that the catalytic behaviour would be less favourable, because there would then be less chance for both the  $\text{Co}^{2+}/\text{Co}^{3+}$  and the  $\text{Ce}^{3+}/\text{Ce}^{4+}$  to perform as catalytically active species and, therefore, the catalytic activity of SCo5-Ce0.5 might be expected to be similar to that of SCo5.

The higher dispersion of  $\text{Co}_3\text{O}_4$  nanorods can also be considered to be an important factor in improving the catalytic performance of SCo5-Ce0.5 relative to SCo5. This is because in heterogeneous catalysis the dispersion of the active species on the support is of significant importance in its catalytic performance [8, 53, 54]. The STEM, TEM images (section 5.4.3.1.4) and XRD patterns (section 5.4.3.1.3) clearly indicated the better dispersion and smaller size of the cobalt clusters in SCo5-Ce0.5 compared to SCo5.

SCo5-Ce0.5 was also evaluated for cyclohexanol oxidation (entry 5) and demonstrated better activity than SCo5 [19]. (Note that pure SBA-15 showed no activity for this reaction [19]). So these results underline the importance of the presence of both cobalt oxide,  $\text{Co}_3\text{O}_4$ , and cerium oxide,  $\text{CeO}_2$  for optimum catalytic performance. Trans-2-hexen-1-ol was also selectively catalysed to its corresponding epoxide in the presence of SCo5-Ce0.5 (entry 6). However cinnamyl alcohol was selectively oxidized to cinnamaldehyde (entry 8). It can be noted that cinnamaldehyde is essentially a dehydrated product of the corresponding epoxide which could have been formed as an intermediate. No further oxidation of the carbonyl groups to carboxylic groups was observed.

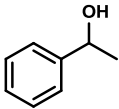
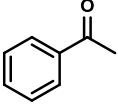
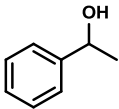
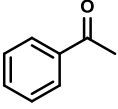
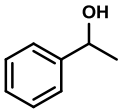
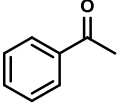
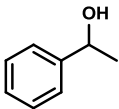
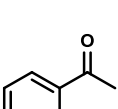
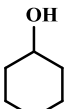
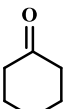
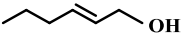
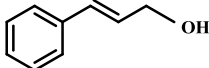
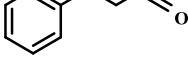
The total conversion of norbornene into norbornene oxide in the presence of SCo5-Ce0.5 was also observed (entry 7). The catalytic activity was higher for this substrate than for the other substrates used in this work, a feature which is attributed to the presence of an exposed double bond in the strained ring.

The recyclability of SCo5-Ce0.5 was tested for the 1-phenylethanol oxidation. This was done by simply separating the catalyst via filtration after the catalytic reaction, washing it several times with acetonitrile, drying it at 100 °C, then adding fresh substrate. SCo5-Ce0.5 could be used up to four times without significant change to its catalytic activity.

In order to investigate the impact of a high surface area support on catalytic performance of Ce-doped Co-composites, 1-phenylethanol oxidation was carried out in the presence of neat Co-Ce composite. Relatively low conversion was observed for this composite over the 24 h reaction period, which can be attributed to its relatively low surface area ( $91 \text{ m}^2 \text{ g}^{-1}$ ).

This result was as expected and validates the use of support to facilitate the dispersion of the catalytically active species and prevent their aggregation into large clusters.

**Table 2** Oxidation of organic substrates

Entry	Catalyst	Substrate	Time(h)	product	Conversion %
1	Co-Ce		4		6
			8		10
			12		13
			24		19
2	S <sub>Co5</sub>		4		12
			8		22
			12		31
			24		60
3	S <sub>Ce5</sub>		4		13
			8		25
			12		36
			100		62
4	S <sub>Co5-Ce0.5</sub>		4		28
			8		59
			12		87
			24		100
5	S <sub>Co5-Ce0.5</sub>		4		20
			8		33
			12		42
			24		63
6	S <sub>Co5-Ce0.5</sub>		4		14
			8		23
			12		31
			24		35
7	S <sub>Co5-Ce0.5</sub>		4		50
			8		90
			12		100
			24		100
8	S <sub>Co5</sub>		4		15
			8		19
			12		23
			24		40

**Reaction condition:** catalyst (0.1 g), substrate (20 mmol), TBHP (24 mmol), acetonitrile (5ml)

#### 5.4.4 Conclusion

SBA-15 supported Ce-doped Co-composite was prepared via the two-solvent method using  $\text{Co}(\text{NO}_3)_2 \cdot 6\text{H}_2\text{O}$  and  $\text{Ce}(\text{NO}_3)_3 \cdot 6\text{H}_2\text{O}$  as metal precursors. The morphological characterisation of this composite indicated better dispersion and smaller  $\text{Co}_3\text{O}_4$  patch size than that for the non-doped Co-composite. The catalytic performance of Ce-doped Co-composite was higher than that of either non-doped Co-composite or Ce-composite. This was attributed to the better dispersion of  $\text{Co}_3\text{O}_4$  species in the former composite, such that more active surface area was available for the reactants. In addition, the extent to which  $\text{CeO}_2$  as a dopant covered the surface of  $\text{Co}_3\text{O}_4$  species was suggested to have an impact on the synergistic effect between cobalt and cerium and thus improve the redox properties of the catalytic system.

The impact of the high surface area support was also investigated in this study for Ce-doped Co-composites and neat Co-Ce composite with the same Co:Ce weight ratio. The catalytic activity of neat Co-Ce composite was five times less than that of Ce-doped Co-composite in oxidation of 1-phenylethanol. This is attributed to the low surface area, and thus poor dispersion of active species, in neat Co-Ce composite.

#### 5.4.5 References

- [1] H. Ma, J. Xu, C. Chen, Q. Zhang, J. Ning, H. Miao, L. Zhou, X. Li, *Catal. Lett.* 113 (2007) 104-108.
- [2] I. Lopes, A. Davidson, C. Thomas, *Catal. Commun.* 8 (2007) 2105-2109.
- [3] B. Solsona, T.E. Davies, T. Garcia, I. Vázquez, A. Dejoz, S.H. Taylor, *Appl. Catal. B: Environ.* 84 (2008) 176-184.
- [4] C.-W. Tang, C.-B. Wang, S.-H. Chien, *Thermochim. Acta.* 473 (2008) 68-73.
- [5] J.P. den Breejen, P.B. Radstake, G.L. Bezemer, J.H. Bitter, V. Frøseth, A. Holmen, K.P.d. Jong, *J. Am. Chem. Soc.* 131 (2009) 7197-7203.
- [6] J. Zhu, K. Kailasam, A. Fischer, A. Thomas, *ACS Catal.* 1 (2011) 342-347.
- [7] R.A. Van Santen, *Accounts Chem. Res.* 42 (2008) 57-66.
- [8] Y. Wang, B. Hou, J. Chen, Y. Sun, *React. Kinet. Mech. Catal.* 102 (2011) 155-164.
- [9] S. Suvanto, T.A. Pakkanen, *J. Mol. Catal. A: Chem.* 164 (2000) 273-280.
- [10] T. Tsoncheva, L. Ivanova, C. Minchev, M. Fröba, *J. Colloid Interface Sci.* 333 (2009) 277-284.
- [11] X. Xu, J. Li, Z. Hao, W. Zhao, C. Hu, *Mater. Res. Bull.* 41 (2006) 406-413.
- [12] X.-D. Hou, Y.-Z. Wang, Y.-X. Zhao, *Catal. Lett.* 123 (2008) 321-326.
- [13] M. Kang, M.W. Song, C.H. Lee, *Appl. Catal. A: Gen.* 251 (2003) 143-156.
- [14] L. Wan, X. Cui, H. Chen, J. Shi, *Mater. Lett.* 64 (2010) 1379-1382.
- [15] A. Garrido Pedrosa, M. Souza, J. Fernandes, D. Melo, A. Araujo, *Reac. Kinet. Catal. Lett.* 79 (2003) 391-396.

- [16] S.S. Deshpande, R.V. Jayaram, *Catal. Commun.* 9 (2008) 186-193.
- [17] S. Todorova, G. Kadinov, K. Tenchev, A. Caballero, J. Holgado, R. Pereñíguez, *Catal. Lett.* 129 (2009) 149-155.
- [18] J. Taghavimoghaddam, G.P. Knowles, A.L. Chaffee, *Top. Catalysis.* 55 (2012) 571-579.
- [19] J. Taghavimoghaddam, G.P. Knowles, A.L. Chaffee, *J. Mol. Catal. A: Chem.* 358 (2012) 79-88.
- [20] F. Boubekr, A. Davidson, S. Casale, P. Massiani, *Micro. Meso. Mater.* 141 (2011) 157-166.
- [21] D. Zhao, Q. Huo, J. Feng, B.F. Chmelka, G.D. Stucky, *J. Am. Chem. Soc.* 120 (1998) 6024-6036.
- [22] G. Laugel, J. Arichi, P. Bernhardt, M. Molière, A. Kiennemann, F. Garin, B. Louis, *Comptes Rendus Chimie.* 12 (2009) 731-739.
- [23] P.F. Fulvio, S. Pikus, M. Jaroniec, *ACS Appl. Mater. Interfaces.* 2 (2009) 134-142.
- [24] Y. Wang, F. Zhang, Y. Wang, J. Ren, C. Li, X. Liu, Y. Guo, Y. Guo, G. Lu, *Mater. Chem. Phys.* 115 (2009) 649-655.
- [25] D. Zhao, J. Feng, Q. Huo, N. Melosh, G. H. Fredrickson, B. F. Chmelka, G.D. Stucky, *Science.* 279 (1998) 548.
- [26] R.M. Rioux, H. Song, J.D. Hoefelmeyer, P. Yang, G.A. Somorjai, *J. Phys. Chem. B.* 109 (2004) 2192-2202.
- [27] X. Liu, L. Li, Y. Du, Z. Guo, T.T. Ong, Y. Chen, S.C. Ng, Y. Yang, *J. Chromatogr. A.* 1216 (2009) 7767-7773.
- [28] C. Tao, J. Li, Y. Zhang, K.Y. Liew, *J. Mol. Catal. A: Chem.* 331 (2010) 50-57.
- [29] X. Ji, K.T. Lee, M. Monjauze, L.F. Nazar, *Chem. Commun.* (2008) 4288-4290.
- [30] C. Yang, Z. Wang, X. Zhou, X. Tian, Z. Pi, Y. Wang, *J. Porous Mater.* 18 (2011) 31-35.
- [31] J. Sauer, F. Marlow, B. Spliethoff, F. Schüth, *Chem. Mater.* 14 (2001) 217-224.
- [32] P. Van Der Voort, P.I. Ravikovitch, K.P. De Jong, A.V. Neimark, A.H. Janssen, M. Benjelloun, E. Van Bavel, P. Cool, B.M. Weckhuysen, E.F. Vansant, *Chem. Commun.* 9 (2002) 1010-1011.
- [33] J. van der Meer, I. Bardez, F. Bart, P.-A. Albouy, G. Wallez, A. Davidson, *Micro. Meso. Mater.* 118 (2009) 183-188.
- [34] K. Kaneko, *J. Membr. Sci.* 96 (1994) 59-89.
- [35] J. Morèrea, M.J. Tenorioa, M.J. Torralvob, C. Pandoa, J.A.R. Renuncioa, A. Cabañasa, *J. Supercrit. Fluids.* 56 (2011) 213-222.
- [36] M. Imperor-Clerc, D. Bazin, M. D. Appay, P. Beaunier, A. Davidson, *Chem. Mater.* 16 (2004) 1813-1821.
- [37] G. Laugel, J. Arichi, M. Molière, A. Kiennemann, F. Garin, B. Louis, *Catal. Today.* 138 (2008) 38-42.
- [38] F. Jiao, H. Frei, *Angew. Chem. Int. Ed.* 48 (2009) 1841-1844.
- [39] I. Lopes, N. El Hassan, H. Guerba, G. Wallez, A. Davidson, *Chem. Mater.* 18 (2006) 5826-5828.
- [40] D. Zhao, J. Sun, Q. Li, G.D. Stucky, *Chem. Mater.* 12 (2000) 275-279.
- [41] Q. Yan, Q. Liu, Q. Liu, *J. Am. Ceram. Soc.* 93 (2010) 2470-2472.

- [42] S.S.Y. Lin, D.H. Kim, S.Y. Ha, *Appl. Catal. A: Gen.* 355 (2009) 69-77.
- [43] Y.-q. Xu, G.-w. Zhou, C.-c. Wu, T.-d. Li, H.-b. Song, *Solid State Sci.* 13 (2011) 867-874.
- [44] I. Rivas, J. Alvarez, E. Pietri, M.J. Pérez-Zurita, M.R. Goldwasser, *Catal. Today.* 149 (2010) 388-393.
- [45] G.A. Eimer, S.G. Casuscelli, G.E. Ghione, M.E. Crivello, E.R. Herrero, *Appl. Catal. A: Gen.* 298 (2006) 232-242.
- [46] R. Al-Tuwirqi, A. Al-Ghamdia, N. Abdel Aal, A. Umarc, W.E. Mahmoud, *Superlattices Microst.* 49 (2011) 416-421.
- [47] M.S. Ghattas, *Micro. Meso. Mater.* 97 (2006) 107-113.
- [48] S.G. Christoskova, M. Stoyanova, M. Georgieva, D. Mehandjiev, *Mater. Chem. Phys.* 60 (1999) 39-43.
- [49] L.F. Liotta, G. Di Carlo, G. Pantaleo, G. Deganello, *Catal. Commun.* 6 (2005) 329-336.
- [50] L.F. Liotta, M. Ousmane, G. Di Carlo, G. Pantaleo, G. Deganello, G. Marci, L. Retailleau, A. Giroir-Fendler, *Appl. Catal. A: Gen.* 347 (2008) 81-88.
- [51] Z. Mu, J.J. Li, H. Tian, Z.P. Hao, S.Z. Qiao, *Mater. Res. Bull.* 43 (2008) 2599-2606.
- [52] G. Rao, Ranga, B. Mishra, Gopal, , *Bull. Catal. Soc. India.* 2 (2003) 122-134.
- [53] Q. Zhuang, Y. Qin, L. Chang, *Appl. Catal.* 70 (1991) 1-8.
- [54] A.M. Venezia, R. Murania, G. Pantaleo, V. La Parola, S. Scirè, G. Deganello, *Appl. Catal. A: Gen.* 353 (2009) 296-304.

**Monash University**

**Declaration for Thesis Chapter 5.5**

Effect of Ce-doping on the structure and redox properties of SBA-15 supported cobalt oxide species in catalytic oxidation reactions

**Declaration by candidate**

In the case of Chapter 3 the nature and extent of my contribution to the work was the following:

Nature of contribution	Extent of contribution (%)
Proposed original idea; prepared and analysed samples; identified major issues; developed interpretations; fully drafted papers and conclusions	80%

The following co-authors contributed to the work. Co-authors who are students at Monash University must also indicate the extent of their contribution in percentage terms:

Name	Nature of contribution	Extent of contribution (%) for student co-authors only
Alan L. Chaffee	Supervision, assisted interpretations of results, editorial assistance	N/A

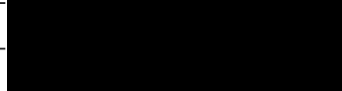
Candidate's Signature		Date 23.10.12
-----------------------	--	------------------

**Declaration by co-author**

The undersigned hereby certify that:

- (1) the above declaration correctly reflects the nature and extent of the candidate's contribution to this work, and the nature of the contribution of each of the co-authors.
- (2) they meet the criteria for authorship in that they have participated in the conception, execution, or interpretation, of at least that part of the publication in their field of expertise;
- (3) they take public responsibility for their part of the publication, except for the responsible author who accepts overall responsibility for the publication;
- (4) there are no other authors of the publication according to these criteria;
- (5) potential conflicts of interest have been disclosed to (a) granting bodies, (b) the editor or publisher of journals or other publications, and (c) the head of the responsible academic unit; and
- (6) the original data are stored at the following location(s) and will be held for at least five years from the date indicated below:

Location(s)

Alan L. Chaffee		22.10.12
-----------------	---	----------

## 5.5 Effect of Ce-doping on the structure and redox properties of the SBA-15 supported cobalt oxide species in catalytic oxidation reactions

Jamileh Taghavimoghaddam, Alan L. Chaffee

School of Chemistry, Monash University, Victoria 3800 Australia

### Abstract

The effect of CeO<sub>2</sub> as a dopant on the crystallisation and dispersion of cobalt oxide species supported on mesoporous silica SBA-15 was investigated. CoCl<sub>2</sub>·6H<sub>2</sub>O and Ce(NO<sub>3</sub>)<sub>3</sub>·6H<sub>2</sub>O were deposited on SBA-15 using the two-solvent method and subsequently calcined to obtain the composite material. CoCl<sub>2</sub>·6H<sub>2</sub>O and Ce(NO<sub>3</sub>)<sub>3</sub>·6H<sub>2</sub>O were also individually deposited on SBA-15 using the same procedure to compare the morphology, dispersion, crystallization, leakage and catalytic activity of the Ce-doped and non-doped Co-composite materials. All the composite materials were characterised by N<sub>2</sub> adsorption-desorption, XRD, FTIR, ICP-MS, TEM, HRTEM, SEM, STEM and elemental mapping. The elemental mapping profile of Ce-doped Co-composite demonstrates highly dispersed ceria and cobalt oxide species throughout the SBA-15. No trace of any mixed cerium-cobalt oxide phase was observed.

It was found that the Ce-doped composite exhibited better catalytic activity for the liquid phase oxidation of a series of small olefins and alcohols than did either pure ceria or pure cobalt oxide composites. This can be attributed to the synergistic effect between cobalt oxide and ceria that results from an improvement in the redox properties of Co<sup>2+</sup>/Co<sup>3+</sup>. However, the incorporation of ceria did not overcome the leakage of cobalt species into the reaction solution that occurred during the course of reaction.

**Keywords:** Supported cobalt oxide; Ceria; Dopant; Dispersion; Liquid phase oxidation; Two-solvent method.

### 5.5.1 Introduction

The catalytic oxidation of olefins and alcohols has received much attention in recent decades because the products are valuable intermediates in the chemical industry, particularly for petrochemicals and pharmaceuticals [1]. Conventionally, stoichiometric amount of oxidants such as chromium (VI) have been used to oxidized these substrates [2]. However, this approach is expensive, produces large amounts of heavy metal waste and usually uses chlorinated solvents, which are not considered environmentally friendly. Due to new

legislation the design of green catalytic processes for various oxidation reactions is of utmost importance. This involves designing processes which reduce or remove the need to use hazardous materials and minimize or eliminate generation of hazardous and undesirable by products [3, 4]. Transition metal oxides, particularly cobalt oxides, are attractive materials for mediating oxidation reactions because of their oxygen mobility [5] and ability to undergo repetitive oxidation-reduction, or, redox cycles [6].

It is a generally accepted concept that the surface area of the catalyst is one the key factors in determining its activity [7, 8]. It would be expected that as the active material's particle size decreases, the surface area increases, thereby providing more active surface area for interaction with the reactants.[9, 10]. One way to increase the surface area of a transition metal oxide is to deposit it on a high surface area support, for example a mesoporous silica such MCM-41 [11] or SBA-15 [12]. The high surface area of the support enhances the dispersion of the active species and the walls of the mesoporous silica prevent the aggregation of the metal oxide particles into large clusters [13, 14]. In this approach the channels of the support can also provide a 'reaction chamber' through which the reactant molecules can diffuse and interact with the active sites, thereby increasing the catalytic activity. Supported cobalt oxide has been reported to catalyse the liquid phase oxidation of alcohols and olefins [15-17], the deep oxidation of hydrocarbons [18], CO oxidation [19-22], styrene epoxidation [23, 24] and methane combustion [25, 26].

Ceria is well known for its redox properties ( $\text{Ce}^{4+}/\text{Ce}^{3+}$ ), its high oxygen storage capacity (HOSC) and its ability to make oxygen more available for oxidation processes [27]. It has been reported that the presence of cerium in different oxidation states, together with oxygen ions on its surface is critical to these properties [28]. Ceria has been used as a promoter for various supported metal catalysts [29, 30] and its effectiveness in this role has been attributed to properties such as: (a) high thermal and mechanical resistance [31], (b) HOSC [32, 33] and (c) ability to improve the dispersion of the principal catalytic metal or metal oxide entity [29].

Supported or bulk Ce-doped cobalt oxides have been used as catalysts for oxidation reactions [34]. Hou et al. reported that by doping small quantity of ceria into  $\text{Co}_3\text{O}_4$  smaller particles with higher surface area and dispersion were obtained. Their composite, compared to pure  $\text{Co}_3\text{O}_4$ , showed higher catalytic activity [29].  $\text{Co}_3\text{O}_4/\text{CeO}_2$  was tested for liquid phase oxidation of alcohols to the corresponding carbonyls [35]. It was reported that the  $\text{Co}_3\text{O}_4/\text{CeO}_2$  showed better catalytic activity than either pure  $\text{Co}_3\text{O}_4$  or  $\text{CeO}_2$ . Todorova et al. reported that supported  $\text{Co}_3\text{O}_4/\text{CeO}_2$  gave higher conversion for n-hexane and CO oxidation.

They also showed that the sequence in which the metal precursors were added to the support affected the catalytic properties of the catalysts [36].

We previously reported the effect of ceria as a promoter on the morphology, dispersion and catalytic activity of SBA-15 supported  $\text{Co}_3\text{O}_4$  prepared using  $\text{Co}(\text{NO}_3)_2 \cdot 6\text{H}_2\text{O}$  as a precursor (chapter 5, publication 1, section 5.4) It was found that ceria, as a promoter, improved the dispersion of the  $\text{Co}_3\text{O}_4$  throughout the support. The Ce-doped Co-composite comprised both  $\text{Co}_3\text{O}_4$  single rods and  $\text{Co}_3\text{O}_4$  patches. These patches were composed of 2-3 nanorods in adjacent pores of SBA-15. By comparison,  $\text{Co}_3\text{O}_4$  patches on the non-doped composite were composed of 4-7 nanorods in adjacent pores. The Ce-doped Co-composite demonstrated higher catalytic activity than the non-doped composite. This was attributed to the higher dispersion of the catalytically active particles and/or a synergistic effect between  $\text{Co}_3\text{O}_4$  and  $\text{CeO}_2$  due to the improvement of  $\text{Co}^{2+}/\text{Co}^{3+}$  redox properties, in the presence of  $\text{Ce}^{3+}/\text{Ce}^{4+}$ .

We have recently reported the results of our study in which  $\text{CoCl}_2 \cdot 6\text{H}_2\text{O}$  was deposited on SBA-15 using various preparation methods (chapter 4, publication 2, section 4.3). These composites showed higher catalytic activity than those prepared with  $\text{Co}(\text{NO}_3)_2 \cdot 6\text{H}_2\text{O}$  as metal precursor [16]. It was found that the cobalt oxide phase, using  $\text{CoCl}_2 \cdot 6\text{H}_2\text{O}$  as precursor, was highly dispersed and amorphous; however, some leakage of cobalt was observed from these composites, causing them to behave more as a mixed 'heterogeneous-homogeneous' catalytic system rather than a straight forward heterogeneous system. It has been reported that the addition of dopant reduced the amount of leakage in ceria-zirconia-copper oxide composites [37]. Hence, the purpose of this study is to investigate the impact of ceria as a dopant on the dispersion, crystallinity, leakage and catalytic activity of SBA-15 supported cobalt oxide composite. Here  $\text{CoCl}_2 \cdot 6\text{H}_2\text{O}$  and  $\text{Ce}(\text{NO}_3)_3 \cdot 6\text{H}_2\text{O}$  were used to prepared SBA-15 supported cobalt oxide, ceria and Ce-doped cobalt oxide composites via the two-solvent method. The composite materials were characterized by X-ray diffraction (XRD),  $\text{N}_2$  adsorption-desorption, fourier transform infrared (FTIR), inductively coupled plasma-mass spectrometry (ICP-MS), scanning electron microscopy (SEM), transmission electron microscopy (TEM), high resolution transmission electron microscopy (HRTEM) scanning transmission electron microscopy (STEM) and elemental mapping. The catalytic activity of all composites was monitored by gas chromatography (GC) and gas chromatography-mass spectrometry (GC-MS) during the course of reaction by withdrawing samples every 4 h up to 24 h.

## 5.5.2 Experimental

### 5.5.2.1 Synthesis of the SBA-15 support

Mesoporous silica SBA-15 was prepared using the method first described by Zhao and co-workers [38]. Ce-doped Co-composite was synthesized using the two-solvent method [39] with  $\text{CoCl}_2 \cdot 6\text{H}_2\text{O}$  and  $\text{Ce}(\text{NO}_3)_3 \cdot 6\text{H}_2\text{O}$  as metal precursors. SBA-15 was first suspended in dry hexane (the hydrophobic solvent). The desired amounts of  $\text{CoCl}_2 \cdot 6\text{H}_2\text{O}$  and  $\text{Ce}(\text{NO}_3)_3 \cdot 6\text{H}_2\text{O}$  to obtain nominally 5 wt% and 0.5 wt% loadings respectively were separately dissolved in distilled water. The total amount of water used for the addition of both metal aqueous solutions corresponded to the pore volume of the mesoporous silica SBA-15 previously determined by  $\text{N}_2$  adsorption-desorption.

The cobalt aqueous solution was first added dropwise to the hydrophobic solution and the mixture stirred for a 15 min. Next the cerium aqueous solution was added in the same manner to the mixture, stirred for further 15 min, followed by 15 min sonication. The mixture was stirred for a further 2 h. The solid was then recovered by filtration and dried in air at room temperature overnight. Finally, the samples were calcined by heating in air at  $2\text{ }^\circ\text{C min}^{-1}$ , then holding at  $700\text{ }^\circ\text{C}$  for 6 h [40]. This composite is referred to as SCo(Cl)5-Ce0.5.

Supported cobalt oxides and ceria (without doping) were prepared separately via the two-solvent method to achieve 5 wt% Co and 5 wt% Ce loadings, respectively. These composites are referred to as SCo(Cl)5 and SCo5.

### 5.5.2.2 Characterization techniques

*Low-angle XRD* patterns were obtained with a Bruker D8 Focus powder diffractometer operated at 40 kV and 30 mA over a  $2\theta$  range of  $0.4\text{--}4^\circ$  using a monochromatic  $\text{CuK}_\alpha$  source radiation ( $\lambda=1.5406\text{ \AA}$ ). Data were collected with a step size of  $0.02^\circ$  and a step time of  $0.1^\circ\text{ min}^{-1}$ .

*$\text{N}_2$  adsorption/desorption isotherms* were obtained at  $-196\text{ }^\circ\text{C}$  on a Coulter Omnisorb 360-CX gas sorption analyzer. Samples were outgassed at  $150\text{ }^\circ\text{C}$  overnight prior to analysis. Pore volume, BET surface area [41], and the pore size distribution (PDS) as giving by the BJH method [38] were calculated for each data set.

*FTIR* spectra were collected via a BIO-RAD FTS 40 spectrometer. The materials were diluted 1/300 in KBr, dried at  $110\text{ }^\circ\text{C}$  for 4-6 h, then pressed into pellets under vacuum prior to analysis.

*ICP-MS* was carried out using a GBC OPTIMAS 9500 ICP-MS. Prior to measurement all catalysts were digested in HNO<sub>3</sub> and HF at 120 °C [42].

*TEM* and HRTEM were carried out using a JEOL 2011 transmission electron microscope equipped with a LaB<sub>6</sub> emitter (point resolution 0.21 nm). An accelerating voltage of 200 kV was used for this study.

*STEM* was carried out on a JEOL 2100F microscope equipped with a high angular annular dark field (HAADF) detector (camera length 10 cm and 0.5 nm probe). The electron dispersive X-ray spectroscopy (EDX) detector was a 50 mm JEOL Si(Li) used for elemental mapping.

*SEM* was carried out using a JEOL 7001F field emission gun scanning electron microscope.

*GC* was carried out on a Varian 3700 gas chromatograph equipped with an FID detector, a 30 m polar capillary column (SGE 30QC5/BP20 1.0 $\mu$ , ID 0.53 mm) and an Agilent EZChrom Elite (version 3.2.1) data system. *GC-MS* was carried out on an Agilent 5973 Network MS coupled to a 6890 series GC system (source conditions: EI, 70 eV, 200 °C).

### 5.5.2.3 Catalytic tests

Liquid phase oxidation of organic substrates was performed in a round bottomed flask. In each test, 0.1g of catalyst was added to acetonitrile (5mL) containing substrate (20 mmol). After reaching the desired temperature for the reaction (80-83 °C) the oxidant, tert-butylhydroperoxide, TBHP, (24 mmol) was then added dropwise over approximately 10 min. Reactions were carried out under reflux and monitored by GC, withdrawing samples every 4 h up to 24 h.

## 5.5.3 Results and discussion

### 5.5.3.1 Characterization of supported catalysts

#### 5.5.3.1.1 Low-angle XRD

Fig. 1 shows the low-angle XRD patterns of pure SBA-15 and all the composites materials. The XRD patterns have been displaced to assist in distinguishing the peaks. The XRD pattern obtained from pure SBA-15 exhibited three characteristic peaks at  $2\theta = 0.92^\circ$ ,  $1.54^\circ$  and  $1.78^\circ$ . These peaks were indexed to the (100), (110) and (200) diffractions of the two dimensional (2D) hexagonal mesostructure (space group  $p6mm$ ) [41, 43] with a  $d_{100}$

spacing of 9.6 nm. Similar XRD patterns that were obtained from SCo5, SCo(Cl)5 and SCo(Cl)5-Ce0.5, indicating that after cobalt and/or cerium loading the mesostructure of the support was preserved. However, the intensity of the main peak (100) decreased in SCo5 compared to pure SBA-15. This suggests that the degree of mesoporosity in this composite decreased due to the presence of cerium oxide particles inside some pores while a small fraction of pores were empty [44]. The decrease in the intensity of (100) peak was not as great for SCo(Cl)5 and SCo(Cl)5-Ce0.5, suggesting that the cobalt and cerium oxide particles were relatively better dispersed throughout the SBA-15 so that the changes in the structure of the support were too small to be detected.

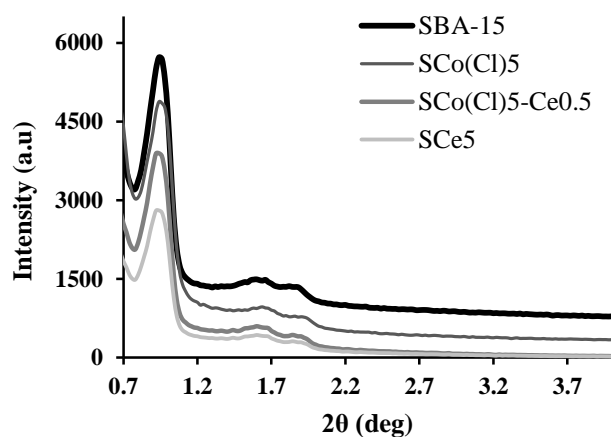


**Fig. 1** Low-angle XRD patterns of SBA-15 and all the composites

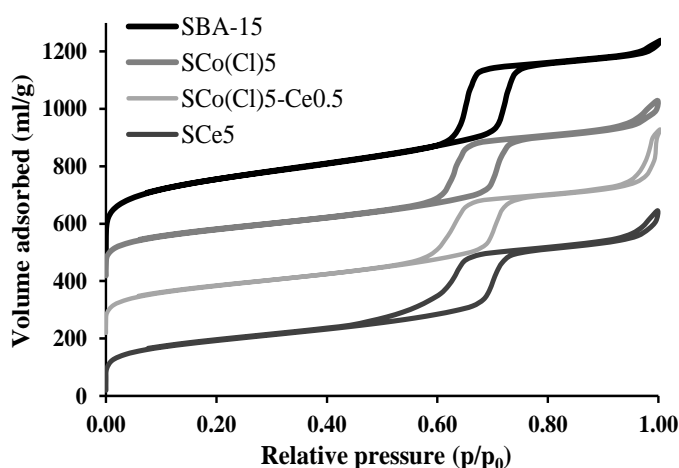
### 5.5.3.1.2 N<sub>2</sub> adsorption-desorption

Fig. 2 illustrates the N<sub>2</sub> adsorption-desorption isotherms of SBA-15 and all the composite materials. The corresponding textural properties are summarized in Table 1. SBA-15 exhibited a type IV isotherm with H1 hysteresis following the IUPAC classification [41]. The adsorption at lower relative pressure  $p/p_0 < 0.25$  in SBA-15 is associated with the presence of micropores in the walls, which connect the cylindrical mesopores [45]. A sharp inflection at relative pressure ( $p/p_0$ ) in the range 0.6-0.8 was also observed for this isotherm and was attributed to the capillary condensation of N<sub>2</sub> in the mesopores. This is characteristic of good quality SBA-15 with 2D cylindrical channels [41]. The sharpness of the hysteresis loop is attributed to the narrow PSD for pure SBA-15 [46].

The shape of the isotherms of all the composites was nearly identical to that of SBA-15. This similarity suggests that the integrity of the support, SBA-15, was preserved after loading cobalt and cerium. The capillary condensation step for all the composite materials occurred at a lower relative pressure than for SBA-15. The slope of the capillary condensation part of the isotherms of these composite materials was not as high as that of pure SBA-15. This indicates

a broader PSD for the composite materials relative to pure SBA-15. This was more pronounced for SCo5 than for SCo(Cl)5 and SCo(Cl)5-Ce0.5, suggesting the PSD of SCo5 was broader than those of the latter composites.

In addition, a shoulder was observed on the desorption branch of SCo5. This suggests partial pore blockage in this composite and is referred to as the “cavitation phenomenon” [47]. The data suggest that for this sample the cerium oxide particles have grown against the silica walls such that some of the pore volume was only accessible via a narrow pore neck. As a result during desorption, though N<sub>2</sub> first desorbed from empty pores at the relative pressure  $p/p_0=0.6$ , partially blocked pores showed delayed N<sub>2</sub> desorption until the vapour pressure was reduced to  $p/p_0=0.45$  [48].



**Fig. 2** N<sub>2</sub> adsorption-desorption isotherm of SBA-15 and all the composite materials

**Table 1** Textural properties of SBA-15 and metal composites

Sample	$S_{BET}(m^2/g)^a$	$P_d(nm)^b$	$P_v(cm^3/g)^c$	$P_{vm}(cm^3/g)^d$	Co:Ce (wt %)
SBA-15	946	6	1.1	0.36	0.0:0.0
SCo5	589	5.6	0.79	0.23	0.0:5.0
SCo(Cl)5	560	5.6	0.77	0.22	5.0:0.0
SCo(Cl)5-Ce0.5	548	5.7	0.77	0.21	5.0:0.5

a: Surface area, b: average pore diameter, c: total pore volume and d: micropore volume

A substantial loss in the surface area of the composite materials as well as the decrease in both average pore diameter and pore volume relative to pure SBA-15 suggested that the metal oxide particles were formed inside the pores of SBA-15. In addition, the decrease in volume of adsorbed N<sub>2</sub> at relative pressure  $p/p_0 < 0.25$  (micropore volume,  $P_{vm}$ ) after metal (cobalt and/or cerium loading) suggests that a fraction of micropores were also blocked due to the presence of either cobalt or cerium oxide inside the mesopores [49-52].

### 5.5.3.1.3 Scanning electron microscopy

Fig. 3 shows the SEM images of SBA-15, SCo(Cl)5-Ce0.5 and SCe5. The rope-like macrostructure of SBA-15 was comprised of rod-like structural unit particles, aggregated to form the SBA-15 macrostructure [53]. The individual particles of SBA-15 prepared in this study were typically  $900 \pm 50$  nm long and  $220 \pm 20$  nm wide [17]. The overall morphology of SBA-15 was common to all the composite materials. On the surface of the individual particles, parallel stripes were observed, which are attributed to the uniform array of hexagonal channels of the support. This further suggests that the mesostructure of the support was preserved after loading cobalt and/or cerium. This supports the deduction from the  $N_2$  adsorption-desorption and XRD results that the mesostructure of the support was preserved after loading cobalt and/or cerium.

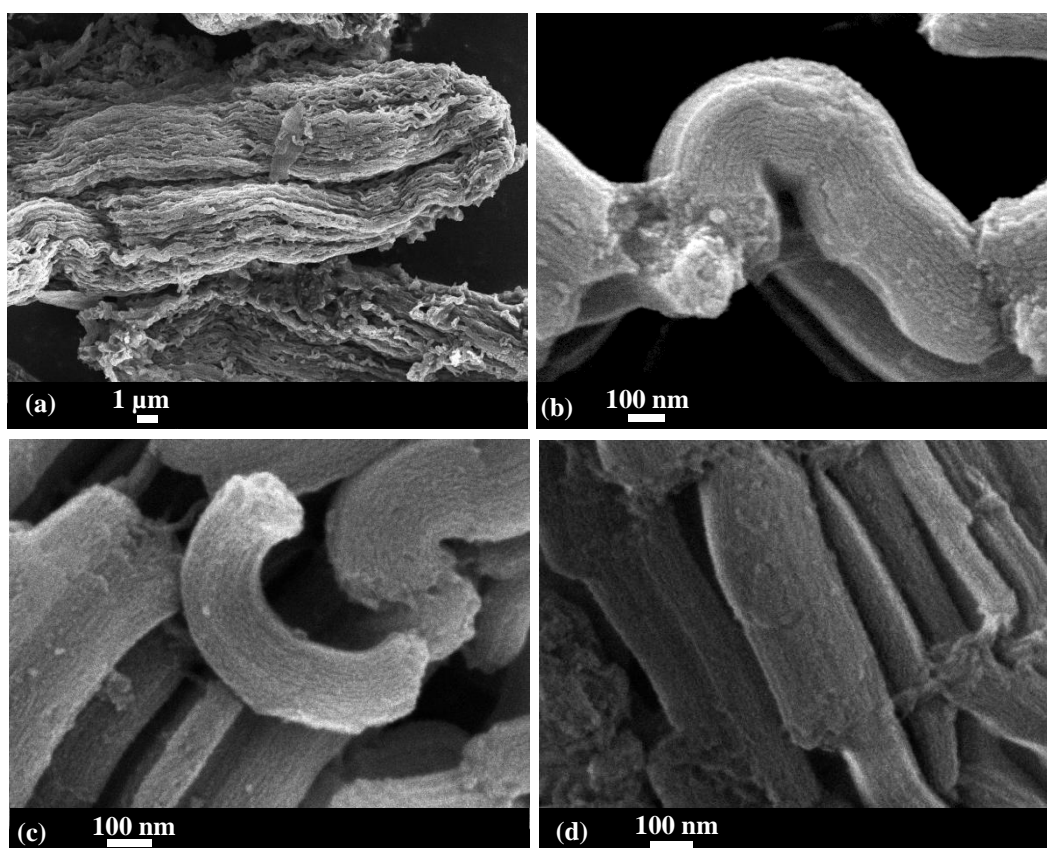


**Fig. 3** SEM images of (a) SBA-15, (b) SCo(Cl)5, (c) SCe5 and (d) SCo(Cl)5-Ce0.5

### 5.5.3.1.4 Transmission electron microscopy

Fig. 4 shows the TEM images of SCo(Cl)5-Ce0.5 and SCe5. Both composite materials showed the highly ordered parallel channels with the electron beam perpendicular to the channels, and a well-ordered honeycomb structure when the electron beam was parallel to the channels (Fig. 4 a and b dotted circles) [16, 39]. For SCo(Cl)5-Ce0.5 composite, not much

contrast was observed between the support and cobalt and/or cerium oxide species. This was not the case when  $\text{Co}(\text{NO}_3)_2 \cdot 6\text{H}_2\text{O}$  and  $\text{Ce}(\text{NO}_3)_3 \cdot 6\text{H}_2\text{O}$  were used as metal precursors, where highly dispersed patches of  $\text{Co}_3\text{O}_4$  as well as single nanorods of  $\text{Co}_3\text{O}_4$  were observed throughout the SBA-15 (chapter 5, publication 1, section 5.4).

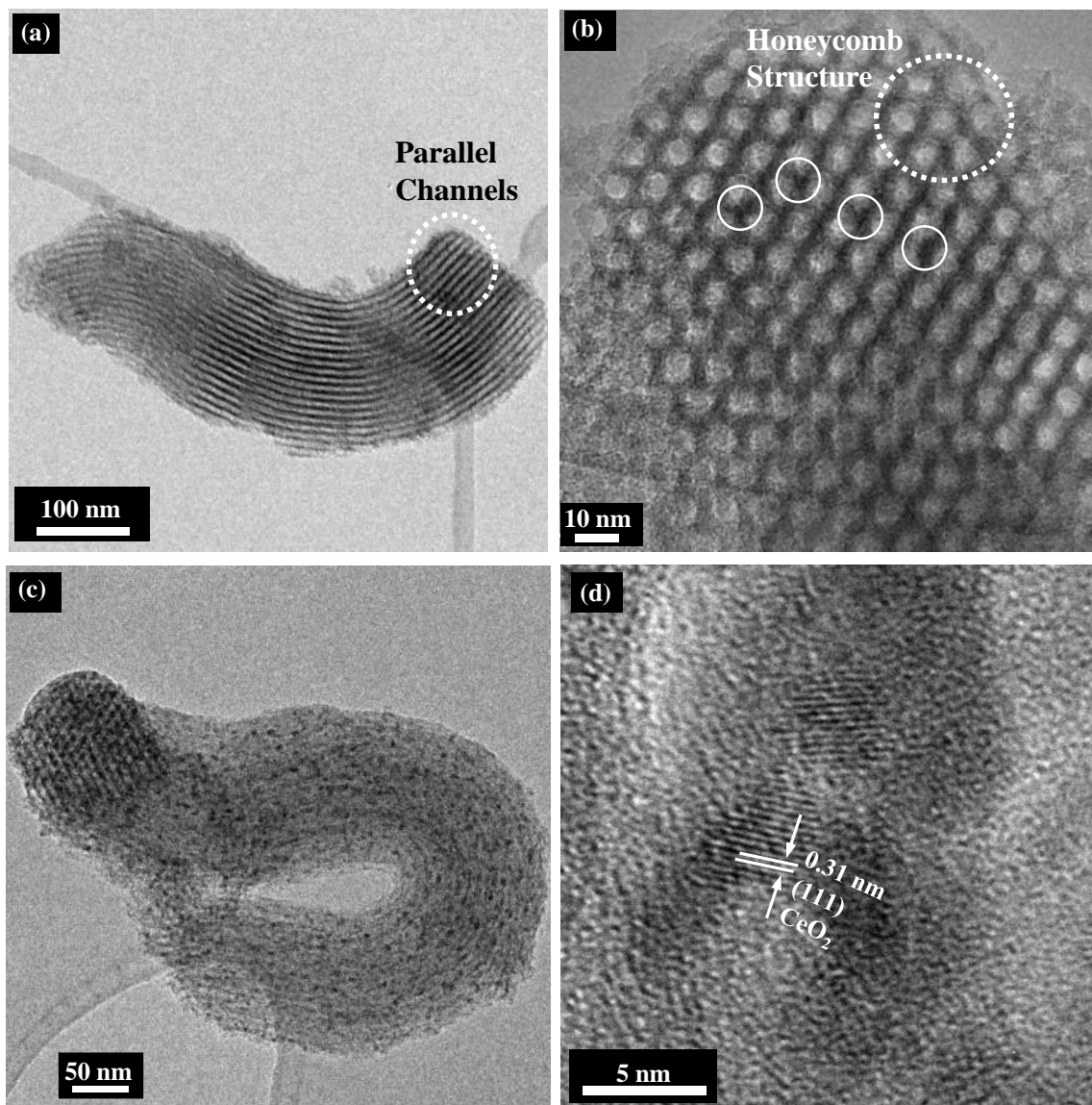


**Fig. 4** TEM images of (a, b)  $\text{SCo}(\text{Cl})_5\text{-Ce}_{0.5}$  and (c, d)  $\text{SCo}_5$

Here it seems that the crystallization of cobalt oxide species inside the mesopores was prevented due to the high decomposition temperature, normally above  $500\text{ }^\circ\text{C}$ , of the counter ion ( $\text{Cl}^-$ ) (chapter 4, publication 1, section 4.2). In our previous study of SBA-15 supported  $\text{CoCl}_2 \cdot 6\text{H}_2\text{O}$ , it was speculated that cobalt oxide species were formed which interact with the support;  $\text{Co}^{2+}$  was tetrahedrally co-ordinated to the oxygen of the silica wall (chapter 4, publication 2, section 4.3). Comparing  $\text{SCo}(\text{Cl})_5\text{-Ce}_{0.5}$  with the non-doped Co-composite previously reported (chapter 4, publication 2, section 4.3), gave no indication that the

addition of  $\text{Ce}(\text{NO}_3)_3 \cdot 6\text{H}_2\text{O}$  improved the crystallization of the cobalt oxide species. Some darker spots were observed, mainly on the walls of the SBA-15, which can be attributed to the cobalt oxide species on the internal side of the walls (white circles Fig. 4b). No lattice fringes could be observed at higher magnification and this can be attributed to the interaction between Si-OH groups and  $\text{Co}^{2+}$  resulting in formation of an amorphous Si-O-Co phase [54] so that no crystalline Co phases were formed. The decrease of the surface area and pore volume of SCo(Cl)5-Ce0.5 also suggested that cobalt oxide species were formed inside the pores (section 5.5.3.1.2).

Fig. 4c and d show the SCo5 composite, in which the spherical cerium oxide particles were highly dispersed throughout the SBA-15. The size of the particles were about 5 nm and the parallel lattice fringes with 0.31 nm d-spacing, corresponding to the (111) planes in fluorite  $\text{CeO}_2$  (JCPDF file 00-034-0394), were observed in HRTEM image.

Fig. 5 shows the STEM images and elemental mapping profiles of SCo(Cl)5-Ce0.5. The high dispersion of both the cobalt oxide species and ceria on SBA-15 was evident from the profiles. The somewhat higher contrast for cobalt relative to cerium is attributed to its higher concentration. No separate phase belonging to cobalt rich or cerium rich species was observed.

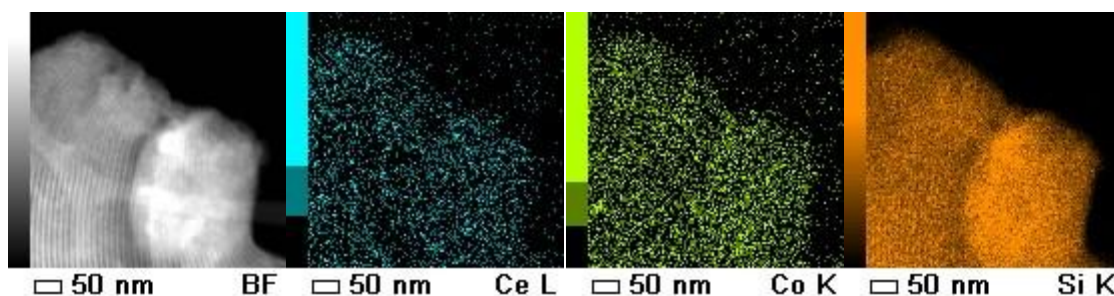


**Fig. 5** STEM images and elemental mapping profiles of SCo(Cl)5-Ce0.5

#### 5.5.3.1.5 Fourier transform infrared spectroscopy

Fig. 6 shows the FT-IR spectra of SBA-15 and all the composite materials. The bands at about  $470\text{ cm}^{-1}$ ,  $1081\text{ cm}^{-1}$  and  $808\text{ cm}^{-1}$  common to all composites were assigned to Si-O-Si stretching vibrations respectively [55]. The bending vibrations of Si-OH were observed at around  $964\text{ cm}^{-1}$  [56]. The band at  $1630\text{ cm}^{-1}$  was assigned to the deformation modes of -OH bonds of adsorbed water [57]. Two peaks were registered for all samples containing cobalt. These bands, at around  $690$  and  $580\text{ cm}^{-1}$  were attributed to the stretching vibrations of Co-O bonds mostly in a spinel structure [36, 58-60]. It was reported previously that small fraction

of the  $\text{CoCl}_2 \cdot 6\text{H}_2\text{O}$  transformed into spinel  $\text{Co}_3\text{O}_4$ , while the remaining cobalt was in amorphous cobalt silicate form (chapter 4, publication 2, section 4.3). The Si-O-Co vibration was reported to occur at  $1029\text{ cm}^{-1}$  [61], but in this work it could overlap with the Si-O-Si band and so not be distinguishable. No characteristic peaks could be observed for S-Ce in the studied region [36].

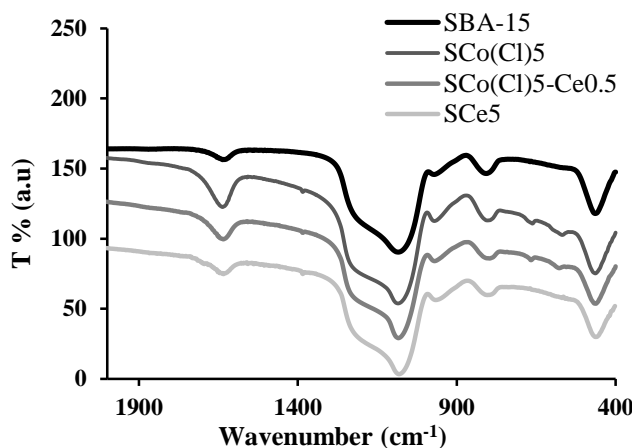


**Fig. 6** FT-IR Spectra of SBA-15 and all the composite materials

#### 5.5.3.1.6 Catalyst evaluation

The catalytic activity of the composite materials was evaluated for the oxidation of a series of organic substrates in the presence of TBHP. Table 2 summarises the results of oxidation reactions using  $\text{SCo}(\text{Cl})_5$ ,  $\text{SCe}_5$  and  $\text{SCo}(\text{Cl})_5\text{-Ce}_{0.5}$  as catalysts. It is clear that the catalytic activity for oxidation of 1-phenylethanol was increased nearly by a factor of two after introducing cerium as a dopant (entry 2 and 3). This can be attributed to the synergistic effect between cobalt and cerium resulting an improvement in the redox properties of the cobalt ions brought about by close interaction with  $\text{Ce}^{3+}/\text{Ce}^{4+}$  [62].

The  $\text{SCe}_5$  catalyst was examined with only one substrate, 1-phenylethanol (entry 1), and exhibited a considerably lower activity than did  $\text{SCo}(\text{Cl})_5$  or  $\text{SCo}(\text{Cl})_5\text{-Ce}_{0.5}$ . This composite showed a high dispersion of spherical ceria particles throughout the SBA-15, but no reduction peak characteristic of ceria ( $\text{Ce}^{4+}$  to  $\text{Ce}^{3+}$  or  $\text{Ce}^{3+}$  to metallic Ce) was observed in temperature programmed reduction profile, TPR, of this sample (see supporting information, section 5.5.6). The irreducibility of the ceria particles suggests that the two-solvent method resulted in strong interaction between ceria and the SBA-15 support in the resulting composite and, this maybe one reason for the poor catalytic activity of  $\text{SCe}_5$ . The relatively poor catalytic activity of supported ceria catalysts is already known for catalysts prepared by other methods [36].

Norbornene showed the highest catalytic activity among all substrates when  $\text{SCo}(\text{Cl})_5\text{-Ce}_{0.5}$  was used as the catalyst (entry 7). Benzyl alcohol was the next most reactive substrate (entry 6). These substrates also showed the highest catalytic activity when oxidized by SBA-15 supported  $\text{Co}_3\text{O}_4$  [17] and Ce-doped SBA-15 supported  $\text{Co}_3\text{O}_4$  (chapter 5, publication 1, section 5.4). The exposed double bond in the strained ring of norbornene and the inherent reactivity of benzylic hydrogen (and associated stability of the benzylic radical) explain the high catalytic activity of these two substrates [17].

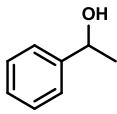
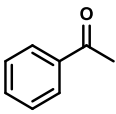
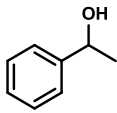
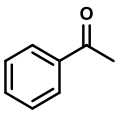
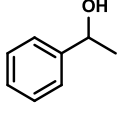
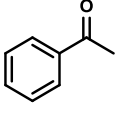
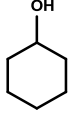
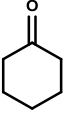
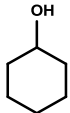
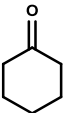
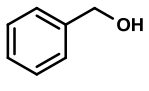
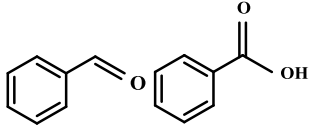
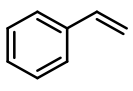
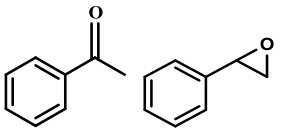
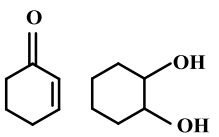
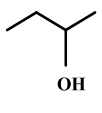
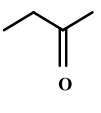
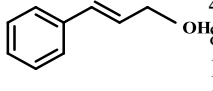
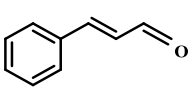
Cyclohexene was oxidised to 1,2 cyclohexanediol and 2-cyclohexene-1-one during the course of reaction (entry 9). The selectivity with respect to 1,2 cyclohexanediol, the more highly oxidised product, increased as the reaction proceeded. After 24 h the total conversion to the products was 83 % while the GC results showed that more than half of the TBHP was still in the reaction mixture. It is noteworthy that though equimolar quantities of TBHP and substrate were combined at the beginning of the reaction, the consumption of TBHP was not sufficient to produce the product mixture obtained after 24 h of reaction. The same phenomenon was reported previously for catalysts prepared from  $\text{Co}(\text{NO}_3)_2 \cdot 6\text{H}_2\text{O}$  as metal precursor. In that case it was proposed that oxygen (from air) participated in the reaction as a co-oxidant [17]. Here, it is thought that the same explanation applies and that the oxidation of cyclohexene occurred at least partially via a parallel reaction that was only initiated by TBHP.

Styrene was also oxidised to acetophenone and styrene oxide (entry 8). If the TBHP was the only oxidant in the catalytic reaction, no further conversion to the products would be expected after 12 h as all the TBHP added would have had to be consumed to obtain the conversion found after 12 h of reaction. However conversion increased up to 24 h, which again suggested the participation of atmospheric oxygen in the reaction through a parallel mechanism.

Isopropanol and 2-butanol (entries 10 and 11) were oxidised to the corresponding ketones with promising results. In these cases the GC results demonstrated that the TBHP was the main oxidant in the reactions and that the stoichiometric amount of TBHP was used to oxidise the substrates to the products.

Cinnamyl alcohol (entry 12) was selectively oxidized to cinnamaldehyde. This can be attributed to the conjugation of the double bond with the benzyl ring which facilitates the rearrangement and dehydration of the potential epoxide intermediate to cinnamaldehyde as a final product.

**Table 2** Oxidation of organic substrate

Entry	Catalyst	Substrate	Time (h)	Product	%Conversion( ) <sup>a</sup>
1	SCe5		4		13
			8		25
			12		36
			24		62
2	SCo(Cl)5		4		27
			8		45
			12		60
			24		96
3	SCo(Cl)5-Ce0.5		4		53
			8		89
			12		100
			24		100
4	SCo(Cl)5		4		21
			8		32
			12		43
			24		62
5	SCo(Cl)5-Ce0.5		4		32
			8		51
			12		65
			24		87
6	SCo(Cl)5-Ce0.5		4		56 (50:50)
			8		80 (30:70)
			12		100 (5:95)
			24		100 (0:100)
7	SCo(Cl)5-Ce0.5		4		70
			8		100
			12		100
			24		100
8	SCo(Cl)5-Ce0.5		4		25 (34:66)
			8		43 (28:72)
			12		57 (33:77)
			24		93 (16:84)
9	SCo(Cl)5-Ce0.5		4		30 (48:52)
			8		52 (40:60)
			12		70 (36:64)
			24		83 (20:80)
10	SCo(Cl)5-Ce0.5		4		28
			8		46
			12		59
			24		80
11	SCo(Cl)5-Ce0.5		4		23
			8		40
			12		50
			24		63
12	SCo(Cl)5-Ce0.5		4		25
			8		36
			12		44
			24		64

<sup>a</sup>: presents ratio of the two isomer products generates during the course of reaction

To check the catalyst stability, the solid composite SCo(Cl)5-Ce0.5 was separated from the reaction mixture used to oxidize 1-phenylethanol after 4 h of reaction (while the mixture was still hot). The reactivity of the solution, without solid catalyst, was monitored every 4 h up to 24 h. Although the catalytic activity was reduced relative to the reaction with solid catalyst, the solution did still show some activity. ICP-MS analysis indicated that approximately 10 % of the original amount of the cobalt had leaked into the reaction solution after 4h. This phenomenon also occurred in the absence of the dopant (chapter 4, publication 2, section 4.3) and suggests that the addition of ceria did not improve the cobalt leakage. So, again, it appears that this catalytic system might more appropriately be described as a mixed ‘heterogeneous-homogeneous’ system.

#### 5.5.4 Conclusion

The effect of adding Ce(NO<sub>3</sub>)<sub>3</sub>·6H<sub>2</sub>O as a dopant to SBA-15 supported CoCl<sub>2</sub>·6H<sub>2</sub>O was investigated using the two-solvent method of catalyst preparation. The catalytic activity of the Ce-doped Co-composite was evaluated for liquid phase oxidation of a series of organic substrates in the presence of TBHP. The Ce-doped Co-composite demonstrated higher catalytic activity compared to its non-doped analogue, and both were superior to SBA-15 and supported CeO<sub>2</sub>. The improved activity is attributed to the synergistic effect between ceria and cobalt oxide species, which comes about as a result of improvement of the cobalt ion (Co<sup>2+</sup>/Co<sup>3+</sup>) redox properties in the presence of Ce<sup>3+</sup>/Ce<sup>4+</sup>. Addition of ceria, as a dopant, did not improve the crystallisation of cobalt oxide species on the surface of SBA-15. The addition of ceria also did not improve the leakage of cobalt into solution which occurred during the course of the reaction. SBA-15 supported CeO<sub>2</sub> showed poor catalytic activity, which is attributed to the strong interaction between the fine spherical CeO<sub>2</sub> particles and the support.

#### 5.5.5 References

- [1] J.M. Thomas, R. Raja, G. Sankar, R.G. Bell, *Nature*. 398 (1999) 227-230.
- [2] S.V. Ley, A. Madin, *Comprehensive Organic Synthesis*, Pergamon, Oxford, 1991.
- [3] M. Ziolek, *Catal. Today*. 90 (2004) 145-150.
- [4] R.A. Sheldon, I.W.C.E. Arends, G.-J. ten Brink, A. Dijksman, *Acc. Chem. Res.* 35 (2002) 774-781.
- [5] J. Jansson, A.E.C. Palmqvist, E. Fridell, M. Skoglundh, L. Österlund, P. Thormählen, V. Langer, *J. Catal.* 211 (2002) 387-397.
- [6] A. Alvarez, S. Ivanova, M.A. Centeno, J.A. Odriozola, *Appl. Catal. A: Gen.* 431-432 (2012) 9-17.

- [7] S. Todorova, G. Kadinov, K. Tenchev, Y. Kalvachev, V. Kostov-Kytin, *J. Mater. Sci.* 42 (2007) 3315-3320.
- [8] J. Chen, Y. Zhang, L. Tan, Y. Zhang, *Ind. Eng. Chem. Res.* 50 (2011) 4212-4215.
- [9] J.P. den Breejen, P.B. Radstake, G.L. Bezemer, J.H. Bitter, V. Frøseth, A. Holmen, K.P.d. Jong, *J. Am. Chem. Soc.* 131 (2009) 7197-7203.
- [10] A. Martinez, C. López, F. Márquez, I. Diaz, *J. Catal.* 220 (2003) 486-499.
- [11] S. Vetrivel, A. Pandurangan, *J. Mol. Catal. A: Chem.* 227 (2005) 269-278.
- [12] Á. Szegedi, M. Popova, C. Minchev, *J. Mater. Sci.* 44 (2009) 6710-6716.
- [13] X. Xu, J. Li, Z. Hao, W. Zhao, C. Hu, *Mater. Res. Bull.* 41 (2006) 406-413.
- [14] Z. Zhang, S. Dai, D.A. Blom, J. Shen, *Chem. Mater.* 14 (2002) 965-968.
- [15] J. Zhu, K. Kailasam, A. Fischer, A. Thomas, *ACS Catal.* 1 (2011) 342-347.
- [16] J. Taghavimoghaddam, G.P. Knowles, A.L. Chaffee, *J. Mol. Catal. A: Chem.* 358 (2012) 79-88.
- [17] J. Taghavimoghaddam, G.P. Knowles, A.L. Chaffee, *Top. Catalysis.* 55 (2012) 571-579.
- [18] R.S. Drago, K. Jurczyk, D.J. Singh, V. Young, *Appl. Catal. B: Environ.* 6 (1995) 155-168.
- [19] I. Lopes, A. Davidson, C. Thomas, *Catal. Commun.* 8 (2007) 2105-2109.
- [20] J.-Y. Luo, M. Meng, X. Li, X.-G. Li, Y.-Q. Zha, T.-D. Hu, Y.-N. Xie, J. Zhang, *J. Catal.* 254 (2008) 310-324.
- [21] S. Sun, Q. Gao, H. Wang, J. Zhu, H. Guo, *Appl. Catal. B: Environ.* 97 (2010) 284-291.
- [22] T. Garcia, S. Agouram, J.F. Sánchez-Royo, R. Murillo, A.M. Mastral, A. Aranda, I. Vázquez, A. Dejoz, B. Solsona, *Appl. Catal. A: Gen.* 386 (2010) 16-27.
- [23] Q. Tang, Q. Zhang, H. Wu, Y. Wang, *J. Catal.* 230 (2005) 384-397.
- [24] H.J. Zhan, Q.H. Xia, X.H. Lu, Q. Zhang, H.X. Yuan, K.X. Su, X.T. Ma, *Catal. Commun.* 8 (2007) 1472-1478.
- [25] G. Laugel, J. Arichi, M. Molière, A. Kiennemann, F. Garin, B. Louis, *Catal. Today.* 138 (2008) 38-42.
- [26] G. Laugel, J. Arichi, H. Guerba, M. Molière, A. Kiennemann, F. Garin, B. Louis, *Catal. Lett.* 125 (2008) 14-21.
- [27] L. Wan, X. Cui, H. Chen, J. Shi, *Mater. Lett.* 64 (2010) 1379-1382.
- [28] C. Li, Q. Xin, *J. Phys. Chem.* 96 (1992) 7714-7718.
- [29] X.-D. Hou, Y.-Z. Wang, Y.-X. Zhao, *Catal. Lett.* 123 (2008) 321-326.
- [30] M. Kang, M.W. Song, C.H. Lee, *Appl. Catal. A: Gen.* 251 (2003) 143-156.
- [31] X.Q. Cao, R. Vassen, D. Stoeber, *J. Eur. Ceram. Soc.* 24 (2004) 1-10.
- [32] J. Kaspar, P. Fornasiero, N. Hickey, *Catal. Today.* 77 (2003) 419-449.
- [33] P. Fornasiero, R. Dimonte, G.R. Rao, J. Kaspar, S. Meriani, A. Trovarelli, M. Graziani, *J. Catal.* 151 (1995) 168-177.
- [34] A. Garrido Pedrosa, M. Souza, J. Fernandes, D. Melo, A. Araujo, *Reac. Kinet. Catal. Lett.* 79 (2003) 391-396.
- [35] S.S. Deshpande, R.V. Jayaram, *Catal. Commun.* 9 (2008) 186-193.
- [36] S. Todorova, G. Kadinov, K. Tenchev, A. Caballero, J. Holgado, R. Pereñíguez, *Catal. Lett.* 129 (2009) 149-155.

- [37] C. de Leitenburg, D. Goi, A. Primavera, A. Trovarelli, G. Dolcetti, *Appl. Catal. B: Environ.* 11 (1996) L29-L35.
- [38] D. Zhao, Q. Huo, J. Feng, B.F. Chmelka, G.D. Stucky, *J. Am. Chem. Soc.* 120 (1998) 6024-6036.
- [39] F. Boubekr, A. Davidson, S. Casale, P. Massiani, *Micro. Meso. Mater.* 141 (2011) 157-166.
- [40] G. Laugel, J. Arichi, P. Bernhardt, M. Molière, A. Kiennemann, F. Garin, B. Louis, *Comptes Rendus Chimie.* 12 (2009) 731-739.
- [41] D. Zhao, J. Feng, Q. Huo, N. Melosh, G. H. Fredrickson, B. F. Chmelka, G.D. Stucky, *Science.* 279 (1998) 548.
- [42] P.F. Fulvio, S. Pikus, M. Jaroniec, *ACS Appl. Mater. Interfaces.* 2 (2009) 134-142.
- [43] Y. Wang, F. Zhang, Y. Wang, J. Ren, C. Li, X. Liu, Y. Guo, Y. Guo, G. Lu, *Mater. Chem. Phys.* 115 (2009) 649-655.
- [44] R.M. Rioux, H. Song, J.D. Hoefelmeyer, P. Yang, G.A. Somorjai, *J. Phys. Chem. B.* 109 (2004) 2192-2202.
- [45] R. Ryoo, C.H. Ko, M. Kruk, V. Antochshuk, M. Jaroniec, *J. Phys. Chem. B.* 104 (2000) 11465-11471.
- [46] X. Liu, L. Li, Y. Du, Z. Guo, T.T. Ong, Y. Chen, S.C. Ng, Y. Yang, *J. Chromatogr. A.* 1216 (2009) 7767-7773.
- [47] A.H. Janssen, C.M. Yang, Y. Wang, F. Schüth, A.J. Koster, K.P. de Jong, *J. Phys. Chem. B.* 107 (2003) 10552-10556.
- [48] P. Van Der Voort, P.I. Ravikovitch, K.P. De Jong, M. Benjelloun, E. Van Bavel, A.H. Janssen, A.V. Neimark, B.M. Weckhuysen, E.F. Vansant, *J. Phys. Chem. B.* 106 (2002) 5873-5877.
- [49] C. Tao, J. Li, Y. Zhang, K.Y. Liew, *J. Mol. Catal. A: Chem.* 331 (2010) 50-57.
- [50] Z. Mu, J.J. Li, M.H. Duan, Z.P. Hao, S.Z. Qiao, *Catal. Commun.* 9 (2008) 1874-1877.
- [51] C. Yang, Z. Wang, X. Zhou, X. Tian, Z. Pi, Y. Wang, *J. Porous Mater.* 18 (2011) 31-35.
- [52] Y. Wang, B. Hou, J. Chen, Y. Sun, *React. Kinet. Mech. Catal.* 102 (2011) 155-164.
- [53] Q. Yan, Q. Liu, Q. Liu, *J. Am. Ceram. Soc.* 93 (2010) 2470-2472.
- [54] M. Stoia, M. Stefanescu, T. Dippong, O. Stefanescu, P. Barvinschi, *J. Sol-Gel Sci. Technol.* 54 (2010) 49-56.
- [55] Y.-q. Xu, G.-w. Zhou, C.-c. Wu, T.-d. Li, H.-b. Song, *Solid State Sci.* 13 (2011) 867-874.
- [56] I. Rivas, J. Alvarez, E. Pietri, M.J. Pérez-Zurita, M.R. Goldwasser, *Catal. Today.* 149 (2010) 388-393.
- [57] G.A. Eimer, S.G. Casuscelli, G.E. Ghione, M.E. Crivello, E.R. Herrero, *Appl. Catal. A: Gen.* 298 (2006) 232-242.
- [58] M.S. Ghattas, *Micro. Meso. Mater.* 97 (2006) 107-113.
- [59] S.G. Christoskova, M. Stoyanova, M. Georgieva, D. Mehandjiev, *Mater. Chem. Phys.* 60 (1999) 39-43.
- [60] R. Al-Tuwirqi, A. Al-Ghamdia, N. Abdel Aal, A. Umair, W.E. Mahmoud, *Superlattices Microst.* 49 (2011) 416-421.
- [61] H. Cui, M. Zayat, D. Levy, *J. Sol-Gel Sci. Technol.* 40 (2006) 83-87.
- [62] Z. Mu, J.J. Li, H. Tian, Z.P. Hao, S.Z. Qiao, *Mater. Res. Bull.* 43 (2008) 2599-2606.



### 5.5.6 Supportin information

## Ceria as a dopant enhances the redox properties of the SBA-15 supported cobalt oxide species

Jamileh Taghavimoghaddam, Alan L. Chaffee

School of Chemistry, Monash University, Victoria 3800 Australia

*Temperature programmed reduction (TPR)* experiments were carried out with a Setaram Thermogravimetric Analyser (TAG24). Typically 10 mg of calcined catalyst was flushed with high purity argon (Ar) at 150 °C for 2 h, to drive off moisture, and then cooled to 20 °C. Next, the flow was switched to 10% H<sub>2</sub>/Ar and the temperature raised at 5 °C min<sup>-1</sup> to 1100 °C, where it was held for 20 min under 10% H<sub>2</sub>/Ar, and then 20 min under Ar. The gas flow rate over the sample was maintained at 70 cm<sup>3</sup> min<sup>-1</sup>. The weights of the samples both before and after analysis were also separately measured with an analytical balance.

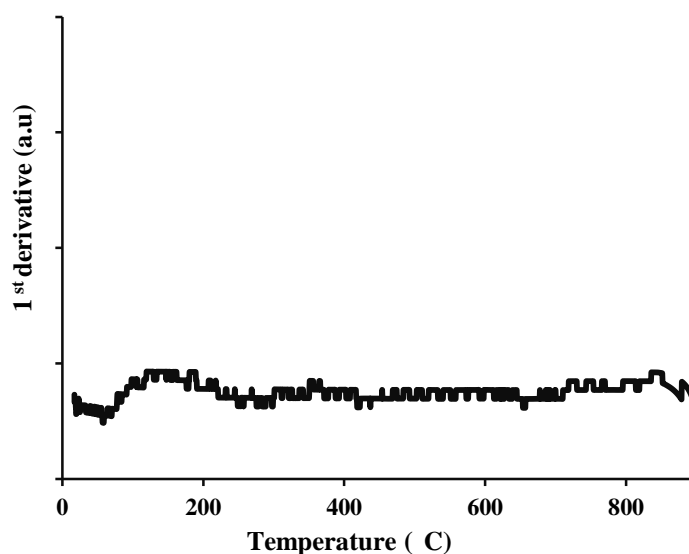


Fig. S1 TPR profile of SCe5

**Declaration for Thesis Chapter 5.6**

The impact of Co:Ce ratio on the dispersion and catalytic activity of cobalt-cerium oxides supported on SBA-15

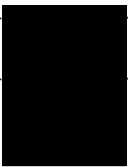
**Declaration by candidate**

In the case of Chapter 3 the nature and extent of my contribution to the work was the following:

Nature of contribution	Extent of contribution (%)
Proposed original idea; prepared and analysed samples; identified major issues; developed interpretations; fully drafted papers and conclusions	80%

The following co-authors contributed to the work. Co-authors who are students at Monash University must also indicate the extent of their contribution in percentage terms:

Name	Nature of contribution	Extent of contribution (%) for student co-authors only
Gregory P. Knowles	Aided method development (catalyst characterisation), input to interpretation of results,	N/A
Alan L. Chaffee	Supervision, assisted interpretations of results, editorial assistance	N/A

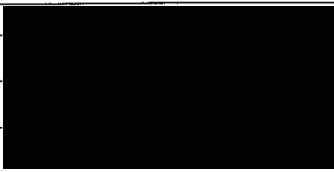
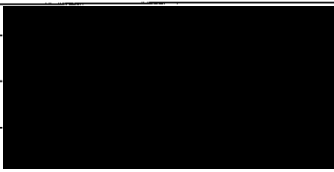
Candidate's Signature		Date 23.10.12
-----------------------	--	------------------

**Declaration by co-authors**

The undersigned hereby certify that:

- (1) the above declaration correctly reflects the nature and extent of the candidate's contribution to this work, and the nature of the contribution of each of the co-authors.
- (2) they meet the criteria for authorship in that they have participated in the conception, execution, or interpretation, of at least that part of the publication in their field of expertise;
- (3) they take public responsibility for their part of the publication, except for the responsible author who accepts overall responsibility for the publication;
- (4) there are no other authors of the publication according to these criteria;
- (5) potential conflicts of interest have been disclosed to (a) granting bodies, (b) the editor or publisher of journals or other publications, and (c) the head of the responsible academic unit; and
- (6) the original data are stored at the following location(s) and will be held for at least five years from the date indicated below:

Location(s) :

Gregory P. Knowles		Date 22.10.12
Alan L. Chaffee		Date 22.10.12

## 5.6 The impact Co:Ce ratio on the dispersion and catalytic activity of cobalt-cerium oxide supported on SBA-15

Jamileh Taghavimoghaddam, Gregory P. Knowles and Alan L. Chaffee

School of Chemistry, Monash University, Victoria 3800 Australia

### Abstract

The effect of the Co:Ce ratio on the morphology, dispersion and catalytic activity of supported cobalt-cerium oxide (SCo(Cl)-Ce) composites was investigated. SBA-15 was loaded with a fixed amount of cobalt ( $\text{CoCl}_2 \cdot 6\text{H}_2\text{O}$ , 5 wt%) and various amounts of cerium ( $\text{Ce}(\text{NO}_3)_3 \cdot 6\text{H}_2\text{O}$ , 0.5-2 wt%) by the two-solvent method. Regardless of the amount of dopant, a blue coloration was observed for all the composites. The dominant phase in these composites, as previously reported, was amorphous  $\text{Co}_2\text{SiO}_4$ . This is in agreement with the blue coloration of the composites. The SCo(Cl)-Ce composites were characterised using XRD,  $\text{N}_2$  adsorption-desorption, ICP-MS, TEM, HRTEM, STEM and TPR. Fine spots were observed in both TEM and STEM images which can be attributed to the presence of  $\text{CeO}_2$ . HRTEM images also showed the lattice fringes of cubic  $\text{CeO}_2$ . Catalytic activity of these composites was evaluated for liquid phase oxidation of a series of organic substrates and the progress of the catalytic reaction was monitored by GC and GC-MS. A synergistic effect was clearly observed when ceria was added as a dopant, but no clear relationship between the Co:Ce ratio and catalytic activity of the composites could be established

**Keywords:** Supported cobalt-cerium oxide, oxidation reaction, Co-Ce composite, Heterogeneous catalyst

### 5.6.1 Introduction

Rare earth oxides have been widely studied as promoters to improve the catalytic activity of a wide range of metal oxide-based catalysts [1]. Among rare earth oxides, cerium oxide, typically  $\text{CeO}_2$ , has been used as a structural and electronic promoter in heterogeneous catalysts. The presence of  $\text{CeO}_2$  as a promoter has been demonstrated to influence secondary processes, which affect the catalytic activity of the transition metal oxides. These secondary processes are related to ceria's oxygen storage/release capacity, a feature which is associated with its  $\text{Ce}^{4+}/\text{Ce}^{3+}$  redox properties [2]. The inclusion of ceria has also been reported to result

in an improvement to the dispersion of supported transition metal oxides [3, 4] (chapter 5, publication 5.1). It can also improve the thermal stability of the supported metal oxides [2].

Cobalt-cerium oxide composites have been used as catalysts for a wide range of reactions such as methanol oxidation [5], methane combustion [6], propane oxidation [7], diesel soot oxidation [8], benzene oxidation [9], CO oxidation and n-hexane oxidation [10, 11]. The effect of ceria as a promoter on the morphology, dispersion and catalytic activity of SBA-15 supported  $\text{Co}_3\text{O}_4$  has been previously reported by our group (chapter 5, publication 1, section 5.4). When  $\text{Co}(\text{NO}_3)_2 \cdot 6\text{H}_2\text{O}$  was used as the precursor, it was observed that the addition of a small amount of ceria increased the dispersion of  $\text{Co}_3\text{O}_4$  and hence improved the catalytic activity. In this case, the  $\text{Co}_3\text{O}_4$  occurred as patches of adjacent nanorods, which were formed when SBA-15 mesopore channels were filled with  $\text{Co}_3\text{O}_4$ .

Larachi et al. investigated the effect of Mn:Ce ratio in a series of manganese-ceria mixed oxide. They reported that the surface area of the composites as well as the percentage of phenol conversion had a volcano relationship with Mn:Ce ratio [12]. Several other groups also reported a similar behaviour when manganese-ceria mixed oxides catalysed wet phenol oxidation [13, 14]. XPS analyses demonstrated the coexistence of  $\text{Ce}^{3+}$  and  $\text{Ce}^{4+}$  on the surface of the manganese-ceria mixed metal oxide, but  $\text{Ce}^{4+}$  was the predominant species [12]. It was suggested that electron transfer from Ce to Mn decreased the proportion of  $\text{Ce}^{3+}$  on the surface and increased the catalytic activity of composites with certain Mn:Ce ratios [12].

This study addresses the effect of Co:Ce ratio on the morphology and catalytic activity of Ce-doped Co-composites prepared by the two-solvent method, using  $\text{CoCl}_2 \cdot 6\text{H}_2\text{O}$  and  $\text{Ce}(\text{NO}_3)_3 \cdot 6\text{H}_2\text{O}$  as metal precursors. The activity of the composites was evaluated in the liquid phase oxidation of cyclohexanol, 1-phenylethanol, benzyl alcohol and norbornene in the presence of tert-butylhydroperoxide (TBHP).

## 5.6.2 Experimental

### 5.6.2.1 Synthesis of the SBA-15 and supported mixed oxide catalyst support

SBA-15 was prepared using the method first described by Zhao and co-workers [15]. The template was removed via calcination by heating in air at  $1\text{ }^\circ\text{C min}^{-1}$  up to  $550\text{ }^\circ\text{C}$  for 6 h and then cooled down to room temperature. Ce-doped Co-composites,  $(\text{S}(\text{Co}(\text{Cl})\text{X})\text{Ce Y})$ , where S, X and Y represent support, nominal Co and Ce-loading based on weight percentage), were synthesized using the “two-solvent” method [16]. SBA-15 was first suspended in dry n-

hexane. The hydrophobic mixture was stirred for approximately 15 min prior to the addition of Co and Ce aqueous solutions containing the desired amount of  $\text{CoCl}_2 \cdot 6\text{H}_2\text{O}$  or  $\text{Ce}(\text{NO}_3)_3 \cdot 6\text{H}_2\text{O}$ . For each preparation, the Co aqueous solution was added first, in a dropwise manner, to the hydrophobic solution, followed by 15 min stirring. The Ce aqueous solution was then added to the mixture in a similar manner. The mixture was sonicated for 15 min and then stirred for 2 h. The solid was then recovered by filtration and air-dried at ambient temperature. Finally, the samples were calcined by heating in air at  $2\text{ }^\circ\text{C min}^{-1}$ , then holding at  $700\text{ }^\circ\text{C}$  for 6 h. The supported mixed oxides in this study are referred to as SCo(Cl)5-Ce0.5, SCo(Cl)5-Ce1, SCo(Cl)5-Ce1.5, SCo(Cl)5-Ce2. For comparison SBA-15 was separately loaded with  $\text{CoCl}_2 \cdot 6\text{H}_2\text{O}$  (5 wt%) or  $\text{Ce}(\text{NO}_3)_3 \cdot 6\text{H}_2\text{O}$  (5 wt%) via the two-solvent method. These composites are referred to as SCo(Cl)5 and SCe5.

### 5.6.2.2 Characterization techniques

*Low-angle X-ray diffraction (XRD) patterns* were obtained with a Bruker D8 Focus powder diffractometer with monochromatic  $\text{CuK}_\alpha$  source radiation ( $\lambda=1.5406\text{ \AA}$ ) operated at 40 kV and 30 mA over  $2\theta$  ranges of  $0.4\text{-}4^\circ$ . Data were collected with a step size of  $0.02^\circ$  and a step time of  $0.1\text{ }^\circ\text{ min}^{-1}$ .

*$\text{N}_2$  adsorption/desorption isotherms* were obtained at  $-196\text{ }^\circ\text{C}$  on a Coulter Omnisorb 360-CX gas sorption analyzer. Samples were outgassed at  $150\text{ }^\circ\text{C}$  overnight prior to analysis. Pore volume, BET surface area, [17] and the pore size distribution (BJH method) [15] were calculated for each data set.

*Fourier transform infrared (FTIR) spectra* were collected from a BIO-RAD FTS 40 spectrometer. The materials were diluted 1/300 in dry KBr, then pressed into pellets (under vacuum) immediately prior to analysis.

*Temperature programmed reduction (TPR) experiments* were carried out with a Setaram Thermogravimetric Analyser (TAG24). Typically 10 mg of calcined catalyst was flushed with high purity argon (Ar) at  $150\text{ }^\circ\text{C}$  for 2 h, to drive off moisture, and then cooled to  $20\text{ }^\circ\text{C}$ . Next, the flow was switched to 10%  $\text{H}_2/\text{Ar}$  and the temperature raised at  $5\text{ }^\circ\text{C min}^{-1}$  to  $1100\text{ }^\circ\text{C}$ , where it was held for 20 min under 10%  $\text{H}_2/\text{Ar}$ , and then 20 min under Ar. The gas flow rate over the sample was maintained at  $70\text{ cm}^3\text{ min}^{-1}$ . The weights of the samples both before and after analysis were also separately measured with an analytical balance.

*Inductively coupled plasma-mass spectrometry (ICP-MS)* was carried out using a GBC OPTIMAS 9500 ICP-MS. Prior to measurement all catalysts were digested with HNO<sub>3</sub> and HF at 120 °C [18].

*Transmission electron microscopy (TEM)* and high resolution transmission electron microscopy (HRTEM) were carried out using a JEOL 2011 transmission electron microscope equipped with a LaB<sub>6</sub> emitter (point resolution 0.21 nm). An accelerating voltage of 200kV was used for this study.

*Scanning Transmission Electron Microscopy (STEM)* was carried out using a JEOL 2100F microscope equipped with a high angular annular dark field (HAADF) detector (camera length 10 cm and 0.5 nm probe). The electron dispersive X-ray spectroscopy (EDX) detector was a 50 mm JEOL Si(Li) used for elemental mapping.

*Gas chromatography (GC)* was carried out on a Varian 3700 gas chromatograph equipped with an FID detector, a 30 m polar capillary column (SGE 30QC5/BP20 1.0μ, ID 0.53 mm) and an Agilent EZChrom Elite (version 3.2.1) data system. *Gas chromatography-mass spectrometry (GC-MS)* was carried out on an Agilent 5973 Network MS coupled to a 6890 series GC system (source conditions: EI, 70 eV, 200 °C).

### **5.6.2.3 Catalytic tests**

Liquid phase oxidation of various organic substrates was performed in round bottomed flasks. In each test, 0.1g of catalyst (contains 5 mg cobalt and 0.5-2 mg cerium) was added to acetonitrile (5 mL) containing the organic substrate (20 mmol). The oxidant, TBHP, (24 mmol) was then added dropwise over approximately 10 minutes. Reactions were carried out under reflux and monitored by GC, withdrawing samples every 4 h up to 24 h.

## **5.6.3 Results and discussion**

### **5.6.3.1 Characterization of supported mixed oxides catalysts**

#### **5.6.3.1.1 X-ray diffraction (XRD)**

Fig. 1 displays low-angle XRD patterns obtained from SBA-15, SCo5, SCo(Cl)5 and all the SCo(Cl)-Ce oxide composites. The diffraction patterns have been displaced to be able to distinguish the peaks easier. All samples exhibit three well-resolved diffraction peaks at 0.94°, 1.56° and 1.84° which can be indexed to the planes (100), (110) and (200), characteristic of highly ordered mesoporous silica SBA-15 [16]. The  $d_{100}$  spacing between

(100) planes for SBA-15 was calculated to be 9.39 nm. The cell parameter ( $a_0$ ), which corresponds to the distance between two pores ( $a_0 = 2d_{100} / \sqrt{3}$ ) was 10.85 nm [19]. It can be seen that the mesoporous structure in all the composites was preserved after loading both Co and Ce.

However, the intensity of the (100) peak decreased with increasing Ce-loading. This can be attributed to the presence of cerium oxide species, partially filling the pores, which in turn reduced the apparent degree of periodicity in the composites relative to that of the SBA-15. As the Co-loading was the same in all composites, the decrease in periodicity can be attributed to the presence of more cerium oxide. In addition, a slight shift towards higher  $2\theta$  was observed for all the composites relative to SBA-15. This suggests that the SBA-15 mesoporous structure experienced some further shrinkage as it was calcined (a second time) to convert the metal precursors to their oxide forms (chapter 4, publication 2, section 4.3).

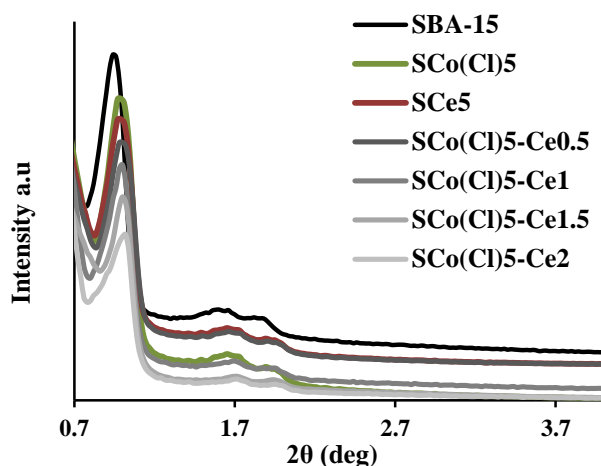


**Fig. 1** Low-angle XRD patterns of SBA-15 and SCo(Cl)-Ce composites

#### 5.1.1.1.1 $N_2$ adsorption-desorption

Fig. 2 shows the  $N_2$  adsorption-desorption isotherms of SBA-15 and SCo-Ce oxide composites. The isotherms have been displaced to avoid overlapping. For comparison the isotherms of SCe5 and SCo(Cl)5 are also included. SBA-15 exhibited a type IV isotherm with H1 hysteresis loop according to IUPAC classification [20]. There was a sharp inflection at relative pressure ( $p/p_0$ ) in the range 0.6-0.8, corresponding to multilayer  $N_2$  filling of the mesoporous channels. As seen in Fig. 2, all the SCo(Cl)-Ce oxide composites had similar isotherms to that of SBA-15. This indicates the preservation of the mesoporous system. However, the capillary condensation region for SCo(Cl)-Ce oxide composites was shifted to lower relative pressure compared to that of SBA-15, suggesting the formation of metal oxide species inside the pores [16]. It is also noteworthy that the slopes of the capillary condensation region of the SCo(Cl)-Ce oxide composite isotherms were not as high as the

corresponding slope of the SBA-15 isotherm, indicative of broader PSD relative to that of SBA-15 [21].

The hysteresis loop of the S<sub>Ce</sub>5 isotherms was quite different to that of isotherms of SCo(Cl)-Ce oxide composites or SCo(Cl)5. A two-step N<sub>2</sub> desorption was observed on the desorption branch of the isotherms of this composite. This can be attributed to the formation of isolated particles inside the mesopores, which partially blocked the pores, such that they behaved like ink bottle mesopores [22]. The hysteresis loop of these pores closed at around relative pressure  $p/p_0=0.4$  [23] (chapter 3, publication 3, section 3.4). The PSD of this composite, S<sub>Ce</sub>5, was broader than those of either SCo(Cl)-Ce or S<sub>Ce</sub>5 (Fig. 3). This is in agreement with the shape of the isotherm and the possibility of the presence of partially blocked pores [23]. The PSD of SCo(Cl)-Ce oxide composites became progressively broader as the Ce-loading increased to 1 wt% and beyond.

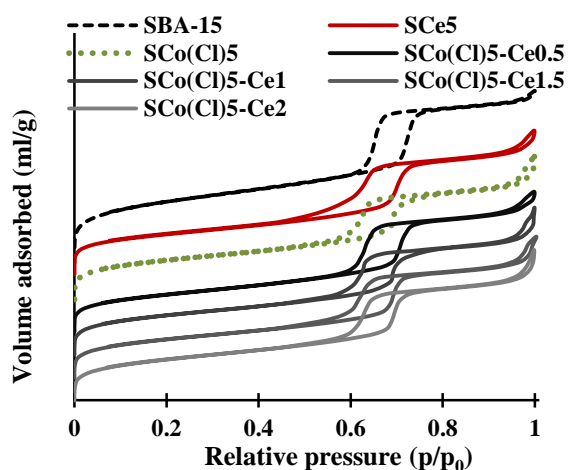


**Fig. 2** N<sub>2</sub> adsorption-desorption isotherms SBA-15 and all the composites

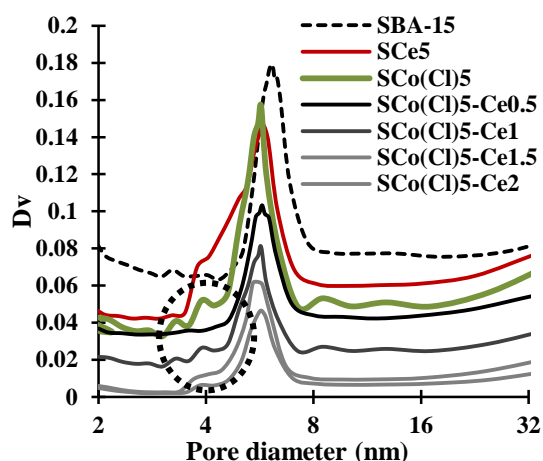


**Fig. 3** PSD of SBA-15 and all the composites

**Table 1** Textural parameters of parent SBA-15 and catalysts

Sample	$S_{BET}(m^2 g^{-1})$	$D_p$ (nm)	$V_{Micro}(cm^3 g^{-1})^a$	$V_T (cm^3 g^{-1})^b$	Co:Ce (wt %) <sup>c</sup>
SBA-15	946	6.16	0.35	1.06	-
SCo(Cl)5	560	5.7	0.22	0.79	5.0:0.0
S <sub>Ce</sub> 5	589	5.50	0.23	0.79	0.0:5.0
SCo(Cl)5-Ce0.5	556	5.74	0.17	0.79	5.0:0.5
SCo(Cl)5-Ce1	582	5.70	0.19	0.75	5.0:1.0
SCo5(Cl)-Ce1.5	564	5.75	0.19	0.75	5.0:1.5
SCo(Cl)5-Ce2	611	5.71	0.21	0.79	5.0:2.0

a: micropore volume, b: total pore volume c: actual Co and Ce content from ICP-MS

The calculated textural parameters from these isotherms, including BET surface area, average pore diameter and micropore volume and total pore volume as well as the Co and Ce contents for each composite, determined by ICP-MS, are summarized in Table 1. It is clear that upon loading Co and/or Ce on SBA-15 the surface area and micropore and mesopore volumes decreased noticeably. This can be attributed to the formation of cobalt oxide and/or cerium oxide species inside the pores of the support, SBA-15.

### 5.6.3.1.2 Transmission electron microscopy

Fig. 4 shows the morphology of SBA-15 and all SCo(Cl)-Ce oxide composites with different amounts of Ce as dopant. It can be seen that the integrity of the SBA-15 channels was preserved after both Co and Ce were loaded on the support. The parallel channels and the highly ordered honeycomb structure (Fig. 4a white circle) of the support could be clearly observed with the electron beam perpendicular and parallel to the channels, respectively [16].

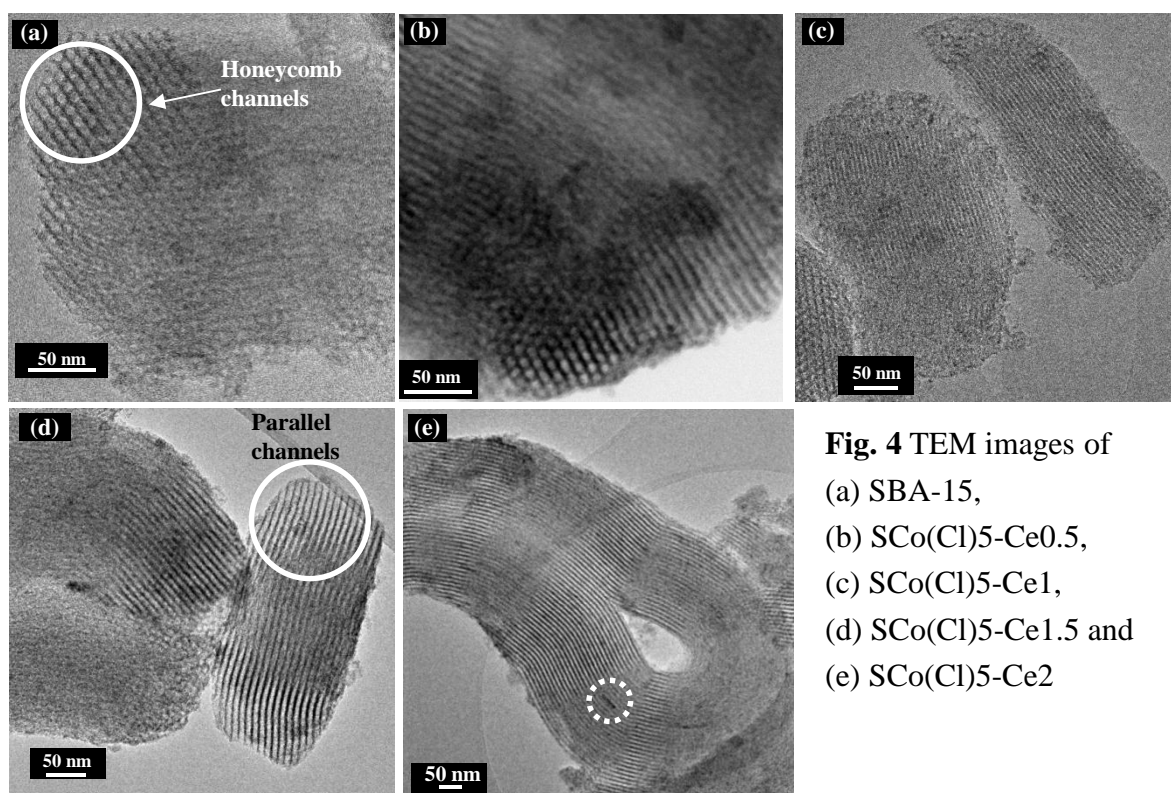
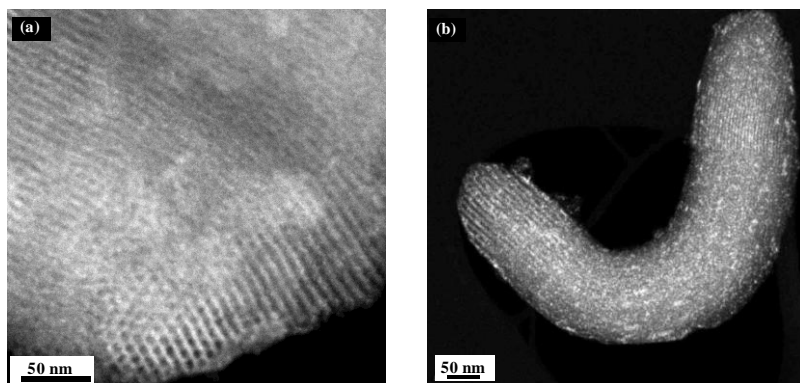


**Fig. 4** TEM images of (a) SBA-15, (b) SCo(Cl)5-Ce0.5, (c) SCo(Cl)5-Ce1, (d) SCo(Cl)5-Ce1.5 and (e) SCo(Cl)5-Ce2

In TEM images of all SCo(Cl)-Ce oxide composites dark spots which were highly dispersed throughout the support could be observed. Some of these spots were very small and it is speculated that they may have corresponded to cobalt oxide particles located inside micropores rather than in the mesopores. Yuranov et al. reported the presence of dark spots in the framework of SBA-15, similar to those observed in this work, and attributed them to the

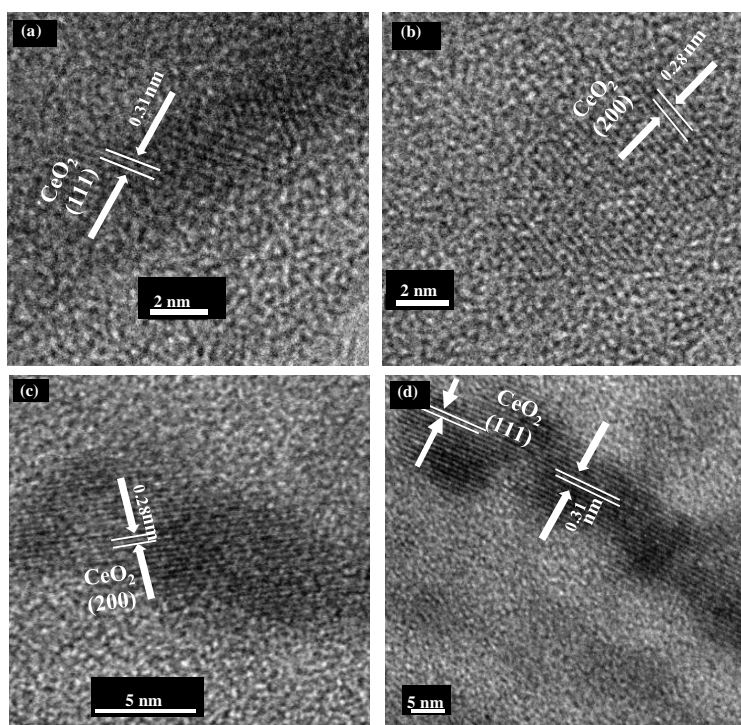
presence of Pd nanoparticles in the micropores of SBA-15 [24]. By increasing the Ce-loading more dark spots with average size less than 5 nm could be observed.

Fig. 5 shows STEM images of selected composites. Because of the high Z-contrast, the metal oxides would be expected to appear as bright spots, and indeed bright spots are evenly dispersed throughout the support. The number of bright spots increased noticeably when the Ce-loading was increased from 0.5 wt% to 2 wt%. Since the Co-loading remained the same, bright spots can be attributed to the cerium oxide species.



**Fig. 5** STEM images of  
(a) SCo(Cl)5-Ce0.5,  
(b) SCo(Cl)5-Ce1

Fig. 6 displays HRTEM images of selected composites. Both SCo(Cl)5-Ce1 and SCo(Cl)5-Ce2 (HRTEM image, Fig. 6d, taken from the area within the dotted circle in Fig. 4e) exhibit crystal lattice fringes with d spacings of 0.31 and 0.28 nm, which can be attributed to (111) and (200) planes of cubic CeO<sub>2</sub> (JCPDF file 00-034-0394), respectively. This also suggests that the dark spots were due to the presence of crystalline CeO<sub>2</sub>.



**Fig. 6** HRTEM images of  
(a, b) SCo(Cl)5-Ce1 and  
(c, d) SCo(Cl)5-Ce2

### 5.6.3.1.3 Temperature programmed reduction

Fig. 7 displays the TPR profiles of the SCo(Cl)-Ce oxide composites. Generally the reduction behavior of supported metal oxide composites is more complicated than that of bulk metal oxides. This is attributed to the large number of extra factors which can have an effect such as the size of the metal oxide particles [25], the H<sub>2</sub> diffusion rate within the pores, strong metal-support interaction (SMSI) [26, 27], the presence of promoters which can facilitate H<sub>2</sub> spill over [4, 28] and the extent of pore blockage.

In our previous study SBA-15 supported cobalt oxide species, prepared using CoCl<sub>2</sub>.6H<sub>2</sub>O (5 wt%) via the two-solvent method, exhibited single step reduction with a peak centered at 319 °C (chapter 4, publication 2, section 4.3). It was also reported earlier by Bi et al. that SBA-15 supported ceria showed two reduction peaks, at 500 °C and 830 °C [29]. The first reduction peak was attributed to the Ce<sup>4+</sup> on the surface and the second one to the Ce<sup>4+</sup> in the bulk of the CeO<sub>2</sub> [11].

In order to study the reduction behavior of SCo5, this composite was reduced under the same condition as SCo(Cl)-Ce oxide composites. No peak(s) related to the above-mentioned ceria reduction could be observed. This is possibly due to the preparation method and associated nature of the ceria particles. The previous report concerned SBA-15 supported CeO<sub>2</sub> prepared via impregnation, which resulted in the formation of large crystalline clusters of CeO<sub>2</sub> both on the external and internal surfaces of SBA-15 [29]. However, the formation of fine spherical CeO<sub>2</sub> particles in SCo5 was recently reported by our group (chapter 5, publication 1, section 5.4). It seems likely that these Ce species might have had strong interactions with the support which inhibited their reduction.

Upon adding ceria (0.5 wt%) as a dopant a slight shift to higher temperature (327 °C) relative to the non-doped Co-composite was observed in the reduction peak (chapter 4, publication 2, section 4.3). A similar increase in the reduction temperature of Ce-doped Co-composite was observed by Todorova et al. when comparing the Ce-doped and non-doped composites [11]. By increasing the amount of dopant the reduction temperature was progressively shifted to higher temperature. The increase of the reduction temperature can be attributed to the oxygen release capacity of ceria. Since ceria tends to favor release of oxygen from its surface, as its concentration increases, it becomes increasingly difficult for the cobalt to be reduced [11, 30]. When the amount of dopant increased to 2 wt% (SCo(Cl)5-Ce2) not

only did the reduction peak shift to higher temperature, but the intensity of the peak also decreased, suggesting that some of the Co was no longer able to be reduced.

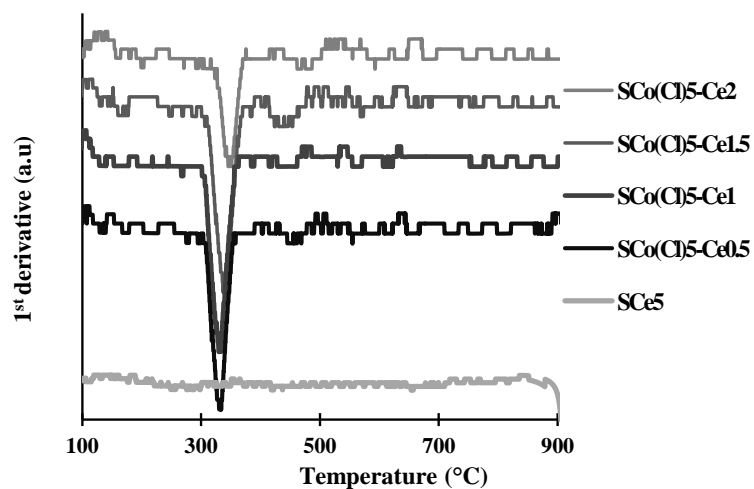


**Fig. 7** TPR profiles of SCo(Cl)-Ce oxide composite and SCo5

#### 5.6.3.1.4 Catalyst evaluation

SCo(Cl)-Ce oxide composites were used as catalysts to investigate the effect of Co:Ce ratio on the catalytic activity of the composites in liquid phase oxidation reactions and the results are summarized in Table 2.

It was previously shown that by adding a small amount of cerium (0.5 wt%) to either SBA-15 supported  $\text{Co}_3\text{O}_4$  (prepared using  $\text{Co}(\text{NO}_3)_2 \cdot 6\text{H}_2\text{O}$ , chapter 5, publication 1, section 5.4) or to SBA-15 supported cobalt oxide species (prepared using  $\text{CoCl}_2 \cdot 6\text{H}_2\text{O}$ , chapter 5, publication 2, section 5.5) the catalytic activity in liquid phase oxidation reactions increased. This was attributed to the synergistic effect between cobalt oxide and ceria, which occurs due to an improvement in the redox properties of  $\text{Co}^{2+}/\text{Co}^{3+}$  in the presence of  $\text{Ce}^{3+}/\text{Ce}^{4+}$ . In the case of ceria-doped SBA-15 supported  $\text{Co}_3\text{O}_4$  the dispersion of  $\text{Co}_3\text{O}_4$  nanorod/patches was also increased (chapter 5, publication 1 and 2, section 5.4 and 5.5). However, the SBA-15 supported ceria, SCo5, showed lower catalytic activity than either SCo(Cl)5, or the Ce-doped Co-composites (chapter 5, publication 1, section 5.4). Rosynek also reported that the catalytic activity of ceria in gas phase oxidation reactions was 10-100 times less than that of a transition metal oxide [31].

In this study, the effect of Co:Ce ratio on catalytic activity of SCo(Cl)-Ce oxide composites provided interesting results (Fig. 8a). It can be seen that that the activity behaved in an irregular manner as the Ce-content varied. For all substrates, the highest catalytic activities were obtained with the SCo(Cl)5-Ce0.5 and SCo(Cl)5-Ce1.5 composites. The composite with intermediate Ce-content, SCo(Cl)5-Ce1.0, and the composite with the highest

Ce-content, SCo(Cl)5-Ce2.0, both provided lower activity. It is noted that these composite formulations were prepared and their catalytic activities determined in replicate experiments, to confirm the validity of the reported data and trends.

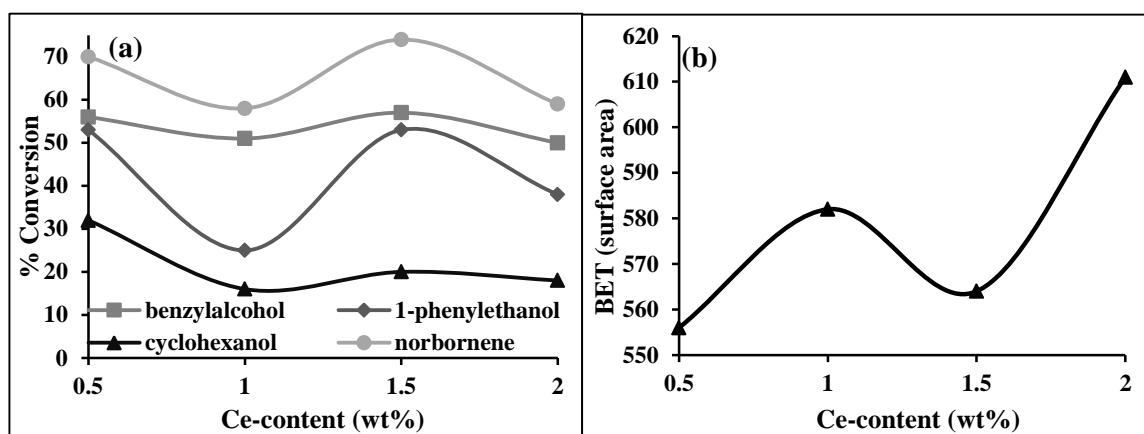


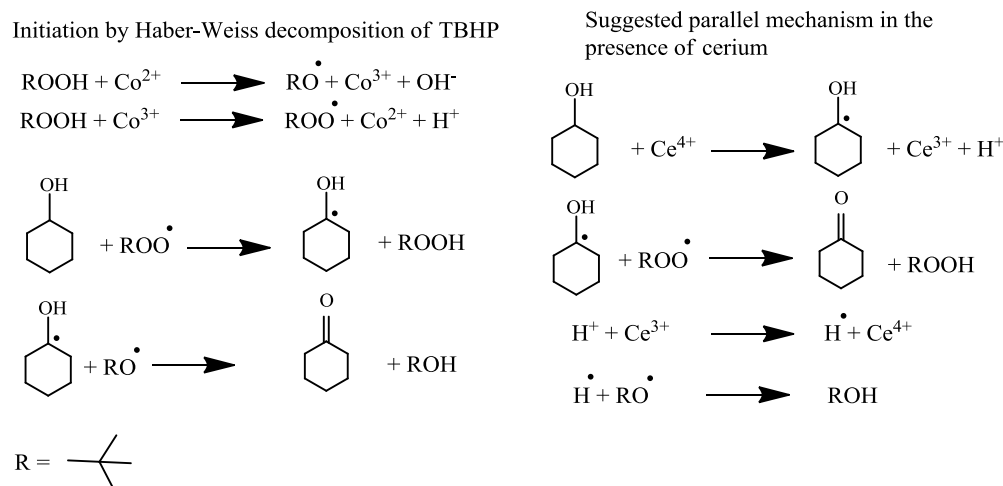
**Fig. 8** (a) Conversion percentage of organic substrates as a function of Ce-content in composites after 4 h of reaction and (b) BET surface area as a function of Ce-content in composites

An explanation for this irregular behavior is not easy to suggest. As seen in Fig. 8b, the two composites with the highest activity also had the lowest surface areas. Therefore it does not appear that surface area was the principal determinant of catalytic activity. Instead it is suggested that the catalytic activity of these composites was determined by the nature of the active cobalt sites and their interaction with ceria. In particular, it is hypothesized that ceria in SCo(Cl)5-Ce0.5 and SCo(Cl)5-Ce1.5 composites may have interacted with the surface of the cobalt oxide species more effectively such that the surface of the cobalt oxide species was partially covered with a ceria-rich phase. As a result the boundary formed between fine ceria particles and cobalt oxide species would be more extensive.

This hypothesis was suggested in part by the comments by Zhaung et al., who reported that when ceria is used as a dopant for supported nickel oxide the catalytic activity for steam reforming improved [32]. Zhaung et al, suggested that ceria, as a promoter, can partially cover the surface of the metal oxide and facilitate the interaction with reactants [32]. Wang and Qin reported the presence of  $Ce^{3+}$  on the surface of Ce-doped supported nickel oxide and attributed the presence of these species to the redox properties of ceria [33]. In a study of catalytic wet oxidation, Larachi et al also observed  $Ce^{3+}$  on the surface of composites with various Ce:Mn ratios and similarly attributed this to the redox behavior of ceria [12]. However, their results indicated that, the predominant form of ceria on the surface was  $Ce^{4+}$ . It was suggested that the lower abundance of  $Ce^{3+}$  on the surface was a result of electron

transfer from Ce to Mn. In any case, they reported that it was the availability of mixed oxidation states, or redox behavior that facilitated the catalytic activity [12].

In the light of these prior studies, it appears that it is likely to be the redox properties of ceria and the impact that this has on the supported cobalt oxide that brings about the synergistic effect. The ceria may be responsible for either stabilization of the active intermediates, improvement of  $\text{Co}^{2+}/\text{Co}^{3+}$  redox properties or better interaction between active intermediates.

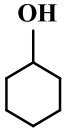
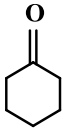
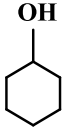
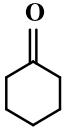
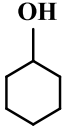
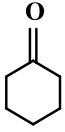
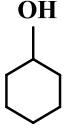
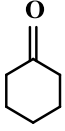
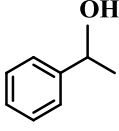
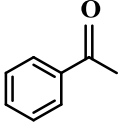
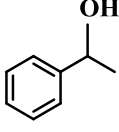
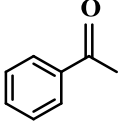
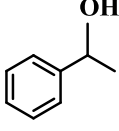
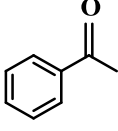
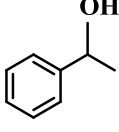
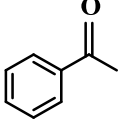
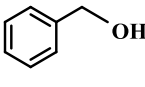
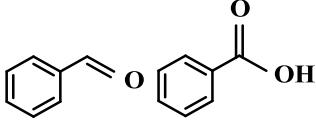
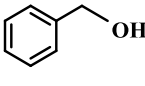
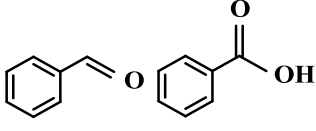
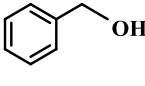
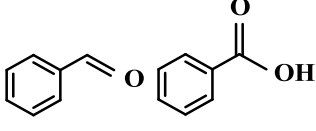


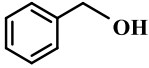
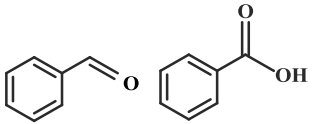
**Fig. 9** Suggested mechanism of involvement of ceria as a dopant in catalytic reactions

A proposed mechanism, shown in Fig. 9, suggests that the redox properties of ceria may facilitate the formation of cyclohexanol radical. The active radicals can then enter the mechanistic cycle, thereby, enhancing the reactivity.

If this hypothesis is correct, it remains unclear why the composites with 1 wt% and 2 wt% Ce-loading exhibited lower activities. Perhaps, in these two composites the nature of the interaction between ceria as a promoter and cobalt oxide species was different or less extensive. Further surface analyses, by XPS will be necessary to provide a better understanding of this phenomenon.

**Table 2** Oxidation of organic substrates

Catalysts	Substrate	Reaction time(h)	Product	Conversion % ( ) <sup>a</sup>
S <sub>2</sub> Co(Cl) <sub>5</sub> -Ce <sub>0.5</sub>		4		32
		8		51
		12		65
		24		87
S <sub>2</sub> Co(Cl) <sub>5</sub> -Ce <sub>1</sub>		4		16
		8		30
		12		42
		24		75
S <sub>2</sub> Co(Cl) <sub>5</sub> -Ce <sub>1.5</sub>		4		20
		8		38
		12		50
		24		75
S <sub>2</sub> Co(Cl) <sub>5</sub> -Ce <sub>2</sub>		4		18
		8		34
		12		46
		24		74
S <sub>2</sub> Co(Cl) <sub>5</sub> -Ce <sub>0.5</sub>		4		53
		8		89
		12		100
		24		100
S <sub>2</sub> Co(Cl) <sub>5</sub> -Ce <sub>1</sub>		4		25
		8		45
		12		60
		24		85
S <sub>2</sub> Co(Cl) <sub>5</sub> -Ce <sub>1.5</sub>		4		53
		8		91
		12		100
		24		100
S <sub>2</sub> Co(Cl) <sub>5</sub> -Ce <sub>2</sub>		4		38
		8		68
		12		75
		24		100
S <sub>2</sub> Co(Cl) <sub>5</sub> -Ce <sub>0.5</sub>		4		56 (50:50)
		8		80 (30:70)
		12		100 (5:95)
		24		100 (0:100)
S <sub>2</sub> Co(Cl) <sub>5</sub> -Ce <sub>1</sub>		4		51 (55:45)
		8		81 (28:72)
		12		100 (9:91)
		24		100 (0:100)
S <sub>2</sub> Co(Cl) <sub>5</sub> -Ce <sub>1.5</sub>		4		57 (50:50)
		8		85 (32:68)
		12		100 (3:97)
		24		100 (0:100)

Catalysts	Substrate	Reaction time(h)	Product	Conversion % ( ) <sup>a</sup>
S <sub>Co</sub> (Cl) <sub>5</sub> -Ce <sub>2</sub>		4		50 (55:45)
		8		79 (27:73)
		12		100 (9:91)
		24		100 (0:100)
S <sub>Co</sub> (Cl) <sub>5</sub> -Ce <sub>0.5</sub>		4		70
		8		100
		12		100
		24		100
S <sub>Co</sub> (Cl) <sub>5</sub> -Ce <sub>1</sub>		4		58
		8		100
		12		100
		24		100
S <sub>Co</sub> (Cl) <sub>5</sub> -Ce <sub>1.5</sub>		4		74
		8		100
		12		100
		24		100
S <sub>Co</sub> (Cl) <sub>5</sub> -Ce <sub>2</sub>		4		59
		8		100
		12		100
		24		100

<sup>a</sup>: presents ratio of the isomer products generates during the course of reaction

#### 5.6.4 Conclusion

The effect of the Co:Ce ratio on the morphology, metal dispersion and catalytic activity of a series of S<sub>Co</sub>(Cl)-Ce oxide composites prepared via the two-solvent method using CoCl<sub>2</sub>.6H<sub>2</sub>O (5 wt%) and Ce(NO<sub>3</sub>)<sub>3</sub>.6H<sub>2</sub>O (0.5-2 wt%) was addressed. The integrity and mesoporosity of the original SBA-15 was preserved in all the product composites. TEM and STEM images demonstrated that by increasing the amount of Ce as a dopant, more dark spots (TEM) and light spots (STEM) were formed evenly throughout the support. Lattice fringes of cubic CeO<sub>2</sub> were observed in HRTEM images. There was a clear synergistic effect for these mixed catalysts; however, neither the surface area nor the Co:Ce (bulk) ratio of the composites could be correlated with catalytic activity. It is suggested that the synergistic effect may be the result of the dispersed cobalt oxides species being partially covered by a ceria rich species. However, this remains to be validated.

#### 5.6.5 References

- [1] A. Trovarelli, C. de Leitenburg, M. Boaro, G. Dolcetti, *Catal. Today*. 50 (1999) 353-367.
- [2] A. Trovarelli, *Catal. Rev.* 38 (1996) 439-520.
- [3] M.M. Natile, A. Glisenti, *Chem. Mater.* 17 (2005) 3403-3414.

- [4] J.-Y. Luo, M. Meng, X. Li, X.-G. Li, Y.-Q. Zha, T.-D. Hu, Y.-N. Xie, J. Zhang, *J. Catal.* 254 (2008) 310-324.
- [5] T. Ataloglou, C. Fountzoula, K. Bourikas, J. Vakros, A. Lycourghiotis, C. Kordulis, *Appl. Catal. A: Gen.* 288 (2005) 1-9.
- [6] L.F. Liotta, G. Di Carlo, G. Pantaleo, A.M. Venezia, G. Deganello, *Appl. Catal. B: Environ.* 66 (2006) 217-227.
- [7] L.F. Liotta, M. Ousmane, G. Di Carlo, G. Pantaleo, G. Deganello, G. Marci, L. Retailleau, A. Giroir-Fendler, *Appl. Catal. A: Gen.* 347 (2008) 81-88.
- [8] P.G. Harrison, I.K. Ball, W. Daniell, P. Lukinskas, M. Céspedes, E.E. Miró, M.A. Ulla, *Chem. Eng. J.* 95 (2003) 47-55.
- [9] Z. Mu, J.J. Li, H. Tian, Z.P. Hao, S.Z. Qiao, *Mater. Res. Bull.* 43 (2008) 2599-2606.
- [10] J. Shao, P. Zhang, X. Tang, B. Zhang, W. Song, Y. Xu, W. Shen, *Chin. J. Catal.* 28 (2007) 163-169.
- [11] S. Todorova, G. Kadinov, K. Tenchev, A. Caballero, J. Holgado, R. Pereñíguez, *Catal. Lett.* 129 (2009) 149-155.
- [12] F. Larachi, *Top. Catalysis.* 33 (2005) 109-134.
- [13] F. Arena, G. Trunfio, J. Negro, L. Spadaro, *Appl. Catal. B: Environ.* 85 (2008) 40-47.
- [14] H. Chen, A. Sayari, A. Adnot, F.ç. Larachi, *Appl. Catal. B: Environ.* 32 (2001) 195-204.
- [15] D. Zhao, Q. Huo, J. Feng, B.F. Chmelka, G.D. Stucky, *J. Am. Chem. Soc.* 120 (1998) 6024-6036.
- [16] J. Taghavimoghaddam, G.P. Knowles, A.L. Chaffee, *J. Mol. Catal. A: Chem.* 358 (2012) 79-88.
- [17] D. Zhao, J. Feng, Q. Huo, N. Melosh, G. H. Fredrickson, B. F. Chmelka, G.D. Stucky, *Science.* 279 (1998) 548.
- [18] P.F. Fulvio, S. Pikus, M. Jaroniec, *ACS Appl. Mater. Interfaces.* 2 (2009) 134-142.
- [19] C.-M. Yang, H.-A. Lin, B. Zibrowius, B. Spliethoff, F. Schuth, S.-C. Liou, M.-W. Chu, C.-H. Chen, *Chem. Mater.* 19 (2007) 3205-3211.
- [20] K. Kaneko, *J. Membr. Sci.* 96 (1994) 59-89.
- [21] C.-Y. Liu, C.-F. Chen, J.-P. Leu, *Sensor. Actuat. B: Chem.* 137 (2009) 700-703.
- [22] Z. Mu, J.J. Li, Z.P. Hao, S.Z. Qiao, *Micro. Meso. Mater.* 113 (2008) 72-80.
- [23] J. Sauer, F. Marlow, B. Spliethoff, F. Schüth, *Chem. Mater.* 14 (2001) 217-224.
- [24] I. Yuranov, L. Kiwi-Minsker, P. Buffat, A. Renken, *Chem. Mater.* 16 (2004) 760-761.
- [25] H. Li, S. Wang, F. Ling, J. Li, *J. Mol. Catal. A: Chem.* 244 (2006) 33-40.
- [26] Z. Mu, J.J. Li, M.H. Duan, Z.P. Hao, S.Z. Qiao, *Catal. Commun.* 9 (2008) 1874-1877.
- [27] Q. Tang, Q. Zhang, P. Wang, Y. Wang, H. Wan, *Chem. Mater.* 16 (2004) 1967-1976.
- [28] S. Zuo, C. Qi, *Catal. Commun.* 15 (2011) 74-77.
- [29] Y. Bi, W. Zhang, H. Xu, W. Li, *Catal. Lett.* 119 (2007) 126-133.
- [30] X.-D. Hou, Y.-Z. Wang, Y.-X. Zhao, *Catal. Lett.* 123 (2008) 321-326.
- [31] M.P. Rosynek, *Catal. Rev.* 16 (1977) 111-154.
- [32] Q. Zhuang, Y. Qin, L. Chang, *Appl. Catal.* 70 (1991) 1-8.
- [33] X. Wang, Y. Qin, *Proc 3rd China-Japan-USA Symposium on Catalysis, Xiamen, China, 1987.*



---

# Chapter 6

## Conclusion and future work

## 6.1 Concluding remarks

The objectives of this study were to investigate the impact of cobalt precursor, cobalt loading, preparation method and cerium as a dopant on the morphology and dispersion of the catalytically active species supported on SBA-15. The catalytic activity of the resulting Co-composites was evaluated in liquid phase oxidation reactions of a series of organic substrates in the presence of TBHP. Three series of Co-composites were prepared in which  $\text{Co}(\text{NO}_3)_2 \cdot 6\text{H}_2\text{O}$  and  $\text{CoCl}_2 \cdot 6\text{H}_2\text{O}$  were used as cobalt precursors and  $\text{Ce}(\text{NO}_3)_3 \cdot 6\text{H}_2\text{O}$  as cerium precursor. The relatively recently devised ‘two-solvent’ method was used to prepare most of the Co-composites, but this was compared with conventional wet impregnation and adsorption methods.

### 6.1.1 SBA-15 supported $\text{Co}_3\text{O}_4$ nanorods

The first section of this study (Chapter 3) focused on the impact of Co-loading and preparation method when SBA-15 was loaded with  $\text{Co}(\text{NO}_3)_2 \cdot \text{H}_2\text{O}$ . Here 1 wt%, 5 wt%, 10 wt% and 30 wt% cobalt were loaded on SBA-15 via the two-solvent method. These composites are referred to as SCo-1, SCo-5, SCo-10 and SCo-30. A Co-composite with 5 wt% (nominal) Co-loading was also prepared via adsorption and is designated SCo-5-A (with actual loading 1 wt%). Wet impregnation was also employed to deposit 1 wt% and 5 wt% cobalt on SBA-15 and these Co-composites are referred to as SCo-1-I and SCo-5-I.

The mesoporous structure of SBA-15 was preserved regardless of the preparation method even at a Co-loading as high as 30 wt%. This was demonstrated by low-angle XRD, SEM and TEM analyses. A dark brown coloration was observed for all composites, with the intensity proportional to the Co-loading. Formation of crystalline  $\text{Co}_3\text{O}_4$  was confirmed by wide-angle XRD and the presence of  $\text{Co}^{2+}$  in tetrahedral and  $\text{Co}^{3+}$  in octahedral sites of the spinel structure was shown by DR UV-vis and FT-IR analyses.  $\text{N}_2$  adsorption-desorption analyses suggested that  $\text{Co}_3\text{O}_4$  species were formed inside the pores of SBA-15, which caused pore blockage to various extents for all the Co-composites. The pore blockage was shown to be proportional to the Co-loading in the series prepared by the two-solvent method.

TEM, STEM images and elemental mapping profiles showed the formation of the  $\text{Co}_3\text{O}_4$  patches throughout the SBA-15 for all Co-composites prepared using  $\text{Co}(\text{NO}_3)_2 \cdot \text{H}_2\text{O}$  as precursor. These patches were comprised of nanorods which had grown in adjacent mesopores and appeared to be interconnected via ‘bridges’ that filled what were originally the micropores of the SBA-15. For the series of composites prepared by the two-solvent

method, the  $\text{Co}_3\text{O}_4$  patches were formed predominantly inside the pores of the SBA-15, incorporating nearly all the cobalt available. The size of these patches was proportional to the Co-loading and, in the case of SCo-30, the length of the patches exceeded 400 nm. For the composite prepared via adsorption the patches were also formed to a large extent inside the pores of the SBA-15, but not all the cobalt in the solution was incorporated. The actual low concentration of the cobalt in this composite (1% Co) resulted in the formation of small patches similar to those of SCo-1. However, for the Co-composites prepared via impregnation,  $\text{Co}_3\text{O}_4$  patches were found both on the external and internal surface of SBA-15, with all the available cobalt incorporated. In these composites some  $\text{Co}_3\text{O}_4$  patches were observed to form at the apertures of the pores, causing noticeable pore blockage.

The catalytic activity of the series of Co-composites prepared by the two-solvent method in liquid phase oxidation reactions was found to be in reverse proportion to the Co-loading as follows: SCo-1>SCo-5>SCo-10>SCo-30. The higher catalytic activity of SCo-1 was attributed to its higher surface area, lesser pore blockage and better dispersion of cobalt. Despite the lower amount of cobalt present, the catalytically active species were more available to interact with the organic substrates. SCo-5-A and SCo-1 contained a similar amount of cobalt, yet the catalytic activity of SCo-5-A was slightly lower. This was attributed to differences in the preparation method, which resulted in the presence of some partially blocked pores in SCo-1. Thus, a greater number of active Co-species were accessible to the organic substrates in SCo-1. SCo-5-I showed slightly higher catalytic activity than SCo-30; this is attributed to the significant level of complete pore blockage in SCo-30 which made much of the cobalt completely inaccessible to the reactants. Recycling tests on SCo-5 and SCo-1 showed that these catalysts could be used up to four times without significant change in their catalytic activity. Thus, the results presented here indicate that the two-solvent method is an effective technique to facilitate the high dispersion of  $\text{Co}_3\text{O}_4$  species throughout the support compared to the more conventional techniques. However, only small amounts of cobalt could be added profitably, since it was also demonstrated that, as the amount of cobalt increased, the pores became blocked and this limited the accessibility to catalytically active sites. The leak test on SCo-5 confirmed that active cobalt species did not leak into the solution during the reaction. This indicated that the catalytic system was strictly heterogeneous.

A mechanistic pathway for liquid phase oxidation of benzyl alcohol was suggested based on the results collected from GC and GC-MS. This substrate was oxidized first to

benzaldehyde and then on to benzoic acid. However the amount of TBHP added as an oxidant was not stoichiometrically sufficient to facilitate this 'double oxidation'. In addition after the completion of the catalytic reaction, with 100 % conversion to benzoic acid, TBHP was still present in the reaction mixture. This suggested that oxidation was mediated by air and that TBHP acted mainly as an initiator of the catalytic reaction.

### **6.1.2 SBA-15 supported highly dispersed cobalt oxide species**

In this section (Chapter 4) the precursor  $\text{CoCl}_2 \cdot 6\text{H}_2\text{O}$  was used. SBA-15 was loaded with various amounts of  $\text{CoCl}_2 \cdot 6\text{H}_2\text{O}$  via the two-solvent method, adsorption and conventional wet impregnation. The series prepared by the two-solvent method are referred to as SCo(Cl)5, SCo(Cl)10, SCo(Cl)20, SCo(Cl)30 and SCo(Cl)40, with 5 wt%, 10 wt%, 20 wt%, 30 wt% and 40 wt% Co-loading, respectively. To investigate the effect of the calcination step on the morphology of the Co-composite with 30 wt% Co-loading, part of the sample was separated before calcination and is referred to as SCo(Cl)30-BC. When adsorption and impregnation were used as a means of preparation the composites are designated SCo(Cl)5-A and SCo(Cl)5-I, respectively. A blue coloration with intensity proportional to the Co-loading was observed for all the Co-composite products, regardless of preparation method. This was the first obvious physical difference between this series of Co-composites and the series prepared from  $\text{Co}(\text{NO}_3)_2 \cdot 6\text{H}_2\text{O}$ .

Low-angle XRD demonstrated that the mesoporous structure of SBA-15 was preserved at Co-loadings below 30 wt %. However, when the Co-loading was increased to 30 wt% or beyond, the Co-composites underwent a morphological transformation such that no characteristic peaks could be observed for these composites in low-angle XRD patterns. The SEM and TEM images showed that the highly ordered channels of the support had collapsed, and the periodic structure (hexagonal array of mesopores) within the particles was destroyed. The general shape of the original particles did not change significantly, but a new intraparticulate morphology appeared as a continuous surface with cavities approximately 20-30 nm in diameter. This morphological transformation occurred during the calcination step, since the mesoporosity was observed to be preserved in SCo(Cl)30-BC.  $\text{N}_2$  adsorption-desorption analyses exhibited a progressive decrease in the surface area and pore volume of Co-composites as the Co-loading was increased from 5 wt% to below 30 wt%. This suggested the formation of cobalt oxide species inside the pores of the support. However this trend was disrupted for the Co-composites which underwent the morphological transformation, SCo(Cl)30 and SCo(Cl)40. A substantial reduction in the surface area and

pore volume was observed for these composites (in agreement with the results obtained from low-angle XRD, SEM and TEM).

For all the catalysts prepared with  $\text{CoCl}_2 \cdot 6\text{H}_2\text{O}$  as precursor, the cobalt oxide species were observed to form a highly dispersed amorphous phase. Elemental mapping profiles showed high dispersion of cobalt throughout the composite, even for those cases in which the morphological transformation had occurred. This is quite different to what was observed for Co-composites prepared from  $\text{Co}(\text{NO}_3)_2 \cdot 6\text{H}_2\text{O}$ , where the cobalt was present as a crystalline cobalt oxide phase ( $\text{Co}_3\text{O}_4$ ) which formed into patches displaying a different dispersion behaviour. Using  $\text{CoCl}_2 \cdot 6\text{H}_2\text{O}$  as precursor, it appears that some interactions are able to develop between the oxygen of the silica support and the product cobalt entities.

The DR UV-vis and XPS analyses indicated that  $\text{Co}^{2+}$  in tetrahedral co-ordination was the dominant species and this is concordant with the blue coloration observed for these Co-composites. It is suggested that before the calcination step,  $\text{Cl}^-$ , superficial  $\text{H}_2\text{O}$  and  $\text{O}^-$  of the silica wall all had the potential to interact with the  $\text{Co}^{2+}$ . However, during the calcination step, due to decomposition and evaporation of the first two ligands, the oxygen of the silica walls remained as the only available ligand for  $\text{Co}^{2+}$ . Lattice fringes corresponding to  $\text{Co}_2\text{SiO}_4$  were observed in HRTEM images, which further supported the significance of this interaction.

The catalytic activity of this series of Co-composites was evaluated for the liquid phase oxidation of cyclohexanol, using TBHP as an oxidant. It was shown that the catalytic activity in the absence of either solid catalyst or TBHP was negligible. Negligible conversion was also observed when pure SBA-15 was used as a solid catalyst. The composite with the lowest Co-loading, SCo(Cl)5-A, showed the highest catalytic activity. This high catalytic activity was observed, for this series again, for the composite with the highest surface area, least pore blockage and, thus, highest availability of active Co species to the oxidation substrates. Amongst the series prepared via the two-solvent method, SCo(Cl)5 was the most active composite. However, the activities of SCo(Cl)10 and SCo(Cl)30 were quite similar. Since SCo(Cl)30 had undergone the morphological transformation, it was the accessibility of the active cobalt species, rather than the change in the surface area, that is considered to offer the main reason for the relative similarity in catalytic behaviour of these two composites. The catalytic activity of SCo(Cl)5-I was also similar to that of SCo(Cl)10 and SCo(Cl)30. Closer examination of the reaction system using the composite SCo(Cl)5 indicated there was some leakage of cobalt into the liquid phase of the reaction mixture. After separation of the liquid

and solid phases, the solution was shown to retain catalytic activity. Thus the catalysts prepared using this precursor, might better be thought of as a mixed heterogeneous-homogeneous system. These series of Co-composites showed higher catalytic activity than those prepared from  $\text{Co}(\text{NO}_3)_2 \cdot 6\text{H}_2\text{O}$ . This can be attributed either to the higher dispersion of the cobalt oxide active species and/or to leakage of cobalt into the solutions for the series prepared from  $\text{CoCl}_2 \cdot 6\text{H}_2\text{O}$ .

From comparison of the results of these first two sections, it can be concluded that the nature of the cobalt precursor significantly affects the physical and chemical properties of the resulting Co-composites, as well as their dispersion and catalytic behaviour.

### 6.1.3 Ce-doped Co-composites

The third section of this thesis concentrated on the effect of cerium, as a dopant or promoter, on the morphology, dispersion and catalytic activity of the SBA-15 supported cobalt oxide species. Here  $\text{Ce}(\text{NO}_3)_3 \cdot 6\text{H}_2\text{O}$  was used as cerium precursor and  $\text{Co}(\text{NO}_3)_2 \cdot 6\text{H}_2\text{O}$  or  $\text{CoCl}_2 \cdot 6\text{H}_2\text{O}$  were used as cobalt precursors. Ce-doped SBA-15 supported  $\text{Co}_3\text{O}_4$ , SCo5-Ce0.5, was prepared by loading SBA-15 with 5 wt% of  $\text{Co}(\text{NO}_3)_2 \cdot 6\text{H}_2\text{O}$  and 0.5 wt%  $\text{Ce}(\text{NO}_3)_3 \cdot 6\text{H}_2\text{O}$  via the two-solvent method. Neat Co-Ce oxide, Co-Ce, was also prepared using  $\text{Co}(\text{NO}_3)_2 \cdot 6\text{H}_2\text{O}$  and  $\text{Ce}(\text{NO}_3)_3 \cdot 6\text{H}_2\text{O}$  via co-precipitation to investigate the effect of the high surface area support on the catalytic activity of the Ce-doped Co-composites. SBA-15 was separately loaded with 5 wt%  $\text{Ce}(\text{NO}_3)_3 \cdot 6\text{H}_2\text{O}$  (SCe5) or 5 wt%  $\text{Co}(\text{NO}_3)_2 \cdot 6\text{H}_2\text{O}$  (SCo5) via the two-solvent method to assist in investigating the differences between the doped and non-doped Co-composites.

Low-angle XRD demonstrated that the mesoporosity of all the supported composites, either doped or non-doped, was preserved. Wide-angle XRD patterns of SCe5 and SCo5-Ce0.5 demonstrated the presence of crystalline  $\text{CeO}_2$  and  $\text{Co}_3\text{O}_4$ , species, respectively. Comparison of the XRD patterns of SCo5-Ce0.5 and SCo5 indicated that the intensity of the  $\text{Co}_3\text{O}_4$  characteristic peaks was reduced in the former composite. In addition, the TEM and STEM images for SCo5-Ce0.5 showed the presence of  $\text{Co}_3\text{O}_4$  single nanorods as well as  $\text{Co}_3\text{O}_4$  patches which were less extensive than those of SCo5. The TEM images of SCe5 displayed fine spherical  $\text{CeO}_2$  particles with average size less than 5 nm, which were evenly dispersed throughout the support. The HRTEM images showed lattice fringes corresponding to  $\text{CeO}_2$  and  $\text{Co}_3\text{O}_4$ , in SCe5 and SCo5-Ce0.5 composites, respectively. It was clear that upon adding cerium as a dopant the dispersion of  $\text{Co}_3\text{O}_4$  species improved while the size of aggregates (patches) decreased. This was consistent with the wide-angle XRD results. For the

Co-Ce composite the lattice fringes of  $\text{CeO}_2$  and  $\text{Co}_3\text{O}_4$  were also observed in HRTEM images. However, wide-angle XRD patterns did not show any diffraction peaks related to a mixed cobalt-cerium oxide.

The catalytic activity of SCo5-Ce0.5, SCo5, SCo5 and Co-Ce was investigated for the liquid phase oxidation of a series of organic substrates in the presence of TBHP. Among the supported catalysts the highest catalytic activity was observed for SCo5-Ce0.5, which can be at least partially attributed to the higher dispersion of the  $\text{Co}_3\text{O}_4$  patches. The apparent synergistic effect between the cobalt and cerium may also be partly attributable to improved redox properties mediated by the cerium in this mixed metal system. Negligible catalytic activity was observed for the Co-Ce composite, emphasizing the importance of the high surface area support in improving the catalytic activity of the cerium-doped cobalt oxide species.

A separate series of samples was prepared by loading SBA-15 with  $\text{CoCl}_2 \cdot 6\text{H}_2\text{O}$  (5 wt%) and  $\text{Ce}(\text{NO}_3)_3 \cdot 6\text{H}_2\text{O}$  (0.5-2 wt%) as cobalt and cerium precursors, respectively, via the two-solvent method. These Ce-doped Co-composites are referred to as SCo(Cl)5-CeX, where S represents SBA-15, Co(Cl):  $\text{CoCl}_2 \cdot 6\text{H}_2\text{O}$ , Ce:  $\text{Ce}(\text{NO}_3)_3 \cdot 6\text{H}_2\text{O}$  and X: Ce wt%. This work had two main objectives: (i) investigation of the effect of cerium as a dopant on the crystallinity, dispersion and catalytic activity of the Ce-doped Co-composites prepared from  $\text{CoCl}_2 \cdot 6\text{H}_2\text{O}$  and (ii) investigation of the impact of Co:Ce ratio on the morphology of the active species and thus their catalytic activity.

Regardless of the amount of dopant (cerium) added, low-angle XRD demonstrated the preservation of the mesoporosity in the resultant Ce-doped Co-composites. As the amount of Ce-loading increased the number of fine dark spots (in TEM images) or bright spots (in STEM images), attributed to  $\text{CeO}_2$  species, progressively increased. When the amount of cerium as a dopant reached 1 wt% the lattice fringes of  $\text{CeO}_2$  could be observed by HRTEM. However, no lattice fringes related to cobalt oxide species could be observed. Thus the addition of cerium did not improve the crystallinity of cobalt oxide species.

Elemental mapping profiles showed that both cobalt and cerium were highly dispersed throughout the composites in all cases so that there was no indication that the addition of ceria improved the dispersion of cobalt species. However the catalytic activity of the SCo(Cl)5-Ce0.5 was observed to be higher than that of either SCo(Cl)5 or SCo5. This is attributed to an improvement in the cobalt redox properties mediated by the cerium in what can be described as a synergistic effect. Among the Ce-doped Co-composites prepared with

different amounts of Ce-loading the relationship between activity and cerium concentration was irregular such that SCo(Cl)5-Ce0.5 and SCo(Cl)5-Ce1.5 demonstrated the highest catalytic activities. It was suggested that at certain Co:Ce ratios the resulting ceria phase may have more effectively covered the surface of the cobalt oxide species such that synergy (improved redox behaviour) was increased.

In the light of the results obtained in this section it can be concluded that Ce-doped composites have higher catalytic activity than non-doped composites. In the case of composites prepared with nitrate precursor, cerium obviously improved the dispersion of the active species. However, the results also suggested that there is a synergistic effect between cobalt and cerium, due to improved redox properties, and that this improves the catalytic activity in the mixed metal systems.

## 6.2 Future work

There are many opportunities to follow up on aspects of the work reported here. Some prospects for future work are identified below:

1- In the current work, mesoporous silica SBA-15 was chosen as a support and the resulting  $\text{Co}_3\text{O}_4$  particles (from  $\text{Co}(\text{NO}_3)_2 \cdot 6\text{H}_2\text{O}$  using the two-solvent method) formed dispersed patches throughout the support. The patch-like morphology of the  $\text{Co}_3\text{O}_4$  particles was attributed to the presence of the micropores in the SBA-15 framework which interconnected the mesopores. Therefore it would be interesting to investigate the morphology and dispersion of  $\text{Co}_3\text{O}_4$  particles on mesoporous silica that does not have micropores), using the same precursor and preparation method. Suitable mesoporous silica type would be MCM-41.

2- In this thesis SBA-15 supported  $\text{Co}_3\text{O}_4$  composites with the highest Co-loading (30 wt%), prepared using  $\text{Co}(\text{NO}_3)_2 \cdot 6\text{H}_2\text{O}$  via the two-solvent method, showed the lowest catalytic activity. This was attributed to pore blockage and accessibility limitations to the active species by the reactants. In this Co-composite most of the  $\text{Co}_3\text{O}_4$  was bounded by the silica wall and therefore not available for the catalytic interaction. It would be interesting to investigate the catalytic activity of these Co-composites after the removal of SBA-15. It might be expected that upon SBA-15 removal (using HF or NaOH as etching reagents) a greater proportion of  $\text{Co}_3\text{O}_4$  surface would be available to the reactants, and this might result in improvement of catalytic activity.

3- In the current work two series of Co-composites were prepared via the two-solvent method, using  $\text{Co}(\text{NO}_3)_2 \cdot 6\text{H}_2\text{O}$  or  $\text{CoCl}_2 \cdot 6\text{H}_2\text{O}$  as cobalt precursor. The resulting Co-composites exhibited different physical, chemical and dispersion behaviours. A suggested experiment is to premix the desired amount of both metal precursors and then add this mixture to the hydrophobic solution (SBA-15 dispersed in n-hexane) and investigate the morphology and dispersion of the resulting mixed precursor Co-composites. It is unknown whether this would result in mixture of the different types of cobalt dispersion observed when the two precursors are used independently or in some other phenomena.

4- Further investigation using X-ray photoelectron spectroscopy (XPS) is required to achieve a better understanding on the surface chemistry of Ce-doped Co-composites. It is expected that this would shed light on the nature and concentration of the oxide species on the surface of Ce-doped Co-composites and how this varies with Co:Ce ratio.

5- In this thesis the use of  $\text{Ce}(\text{NO}_3)_3 \cdot 6\text{H}_2\text{O}$  (0.5 wt%) as a dopant with  $\text{Co}(\text{NO}_3)_2 \cdot 6\text{H}_2\text{O}$  (5 wt%) as cobalt precursor led to improvement in dispersion of the  $\text{Co}_3\text{O}_4$  patches and a reduction in the size of these patches. It would be interesting to investigate the impact of Co:Ce ratio on dispersion and catalytic activity for a series of Co-composites prepared with different amount of cerium from these precursors. Variation of the sequence in which the metal precursors are added is also worth studying.

6- In the current study two series of Co-composites were prepared, via the two-solvent method using either  $\text{Co}(\text{NO}_3)_2 \cdot 6\text{H}_2\text{O}$  or  $\text{CoCl}_2 \cdot 6\text{H}_2\text{O}$ , with different dispersion behaviour. It would be interesting to investigate the catalytic activity of these composites in other reactions, for example in the Fischer-Tropsch synthesis (FTs). Cobalt-based heterogeneous catalysts are well known to be effective in the FTs but it is reduced forms of cobalt, rather than oxidised forms that are active. As a result it would be interesting to investigate the availability, reducibility and activity of the cobalt active species in a similar series of composites with various Co-loadings and prepared from different precursors for the FTs.

## Jamileh (Shah) Taghavi Moghaddam

Email: [REDACTED]

### Core Competencies

- Excellent material characterisation skills.
- Excellent synthetic skills.
- Strong skills in time management and problem solving.
- Ability to work independently and as part of a team.
- Capable of working under tight deadlines.
- Thorough, organised with excellent attention to detail.

### Instrumental Skills

- Powder X-ray Diffraction (XRD).
- X-ray Photoelectron Spectroscopy (XPS) at the Australian Synchrotron.
- Transmission Electron Microscopy (TEM), High Resolution Transmission Electron Microscopy (HRTEM).
- Scanning Transmission Electron Microscopy (STEM) and elemental mapping.
- Thermogravimetric Analysis (TGA)/Differential Thermal Analysis (DTA)/Temperature Programmed Reduction (TPR).
- Solution Inductively Coupled Plasma-Mass Spectrometry (ICP-MS).
- UV-Vis and Diffuse Reflectance UV-Vis Spectrophotometry.
- Nitrogen Physisorption.
- Proximate Analysis.
- Gas Chromatography (GC), Gas Chromatography-Mass Spectrometry (GC-MS) and Fourier Transform-Infrared Spectroscopy (FT-IR).

### Qualifications

- **PhD.** in Material Science.

**Intitute name:** Monash University, Melbourne, Australia.

**Thesis title:** Mesoporous silica SBA-15 supported cobalt oxide: An investigation of the structure, morphology and catalytic activity of various composites.

**Duration:** April 2009 - October 2012.

- **MS.** in Inorganic Chemistry

**Intitute name:** Alzahra University, Tehran, Iran.

**Thesis title:** Heterogenization of biomimetic complexes using natural clays and mesoporous silica MCM-41 as catalytic active sites.

**Duration:** 2001- 2003.

- **BS.** in Applied Chemistry

**Intitute name:** Azad University (Central Branch), Tehran, Iran.

**Duration:** 1996 - 2000.

### **Career History**

- **Feb 2012 to present:**

**Job title:** Senior undergraduate Laboratory assistant.

**Intitute name:** School of Chemistry, Monash University.

**Responsibility included:** Preparing 2<sup>nd</sup> and 3<sup>rd</sup> Year Laboratory chemicals, maintaing the laboratory instruments, purchasing the required chemicals and training both demonstrators and students to use new instruments.

- **Jan 2011 - Dec 2012:**

**Job title:** 1<sup>st</sup> Year Chemistry Laboratory demostrator.

**Intitute name:** School of Chemistry, Monash University.

**Responsibility included:** Teaching 1<sup>st</sup> Year Chemistry students, familiarising students with writing scientic reports and marking students reports.

- **2003 - 2009**

**Job title:** Research assistant.

**Intitute name:** Feed-Machine Company.

**Responsibility included:** Assisting the project manager in developing techniques on anti-corrosion coating, being in charge of quality control of products and the final packaging process.

- **2002 - 2003**

**Job title:** Sales manager.

**Intitute name:** Ronaghy Dental Company.

**Responsibility included:** Supervising sales team, negotiating and providing technical information for potential customers.

- **2001- 2002**

**Job title:** Sales manager assistant.

**Intitute name:** Ronaghy Dental Company.

**Responsibility included:** Processing the cliens' enquiries, providing customers with quotes, processing the invoices and maintaing sales data in relevent spreadsheet.

### **List of publications and conferences are attached**

## Referees

- Prof Alan Chaffee, School of Chemistry, Monash University.

Email: [REDACTED], Tel: [REDACTED]

- Prof Douglas Macfarlane, School of Chemistry, Monash University.

Email: [REDACTED], Tel: [REDACTED]

- Mr. Bruce Dobney, Senior Undergraduate Laboratory manager, Monash University.

Email: [REDACTED], Tel: [REDACTED]

## **Selected publications**

- F. Farzaneh, J. Taghavi, R. Malakooti, M. Ghandi

Immobilized vitamin B12 within nanoreactors of MCM-41 as a selective catalyst for oxidation of organic substrates.

### **J. Mol. Catal. A: Chem 244 (2006) 252-257**

- Jamileh Taghavimoghaddam, Gregory P. Knowles, Alan L. Chaffee

Preparation and characterization of mesoporous silica supported cobalt oxide as a catalyst for the oxidation of cyclohexanol.

### **J. Mol. Catal. A: Chem 358 (2012) 79-88**

- Jamileh Taghavimoghaddam, Gregory P. Knowles, Alan L. Chaffee

Mesoporous silica SBA-15 supported  $\text{Co}_3\text{O}_4$  nanorods as efficient liquid phase oxidative catalyst.

### **Top. Catal 55 (2012) 7-10**

- Jamileh Taghavimoghaddam, Gregory P. Knowles, Alan L. Chaffee

Impact of low cobalt loading on the morphology and dispersion of the crystalline  $\text{Co}_3\text{O}_4$  patches supported on SBA-15.

### **J. Mol. Catal. A: Chem (submitted)**

- Jamileh Taghavimoghaddam, Tim Williams, Alan L. Chaffee

Cobalt precursor impact on the dispersion and morphological development of SBA-15 supported cobalt oxide species.

### **J. Micro. Meso. Mater (submitted)**

- Jamileh Taghavimoghaddam, Gregory P. Knowles, Alan L. Chaffee

SBA-15 supported cobalt oxide species: Preparation, morphology and catalytic activity.

### **Appl. Catal. A: Gen (final draft)**

- Jamileh Taghavimoghaddam, Gregory P. Knowles, Alan L. Chaffee

Evenly dispersed cobalt oxide species: Morphology and chemical investigation.

### **Catal. Today (in preparation)**

- Jamileh Taghavimoghaddam, Gregory P. Knowles, Alan L. Chaffee

Effect of Ce-doped on the dispersion of  $\text{Co}_3\text{O}_4$  nanorods supported on SBA-15.

### **ACS Catalysis (submitted)**

- Jamileh Taghavimoghaddam, Alan L. Chaffee

Ce-doped enhances the redox properties of SBA-15 supported cobalt oxide species.

### **J. catal. (final draft)**

- Jamileh Taghavimoghaddam, Gregory P. Knowles, Alan L. Chaffee

Compositional effect of supported cobalt-cerium oxide composites in liquid phase oxidation reactions.

### **Top. Catal. (final draft)**

- Jamileh Taghavimoghaddam, Gregory P. Knowles, Alan L. Chaffee

Supported cobalt oxide: Preparation and application for liquid phase oxidation of cyclohexanol.

**Am. Chem. Soc. Div Petro Chem, Prepr 57 (2012) 263-264**

### **Conferences**

- Jamileh Taghavimoghaddam, Alan L. Chaffee

“Immobilization of vitamin B12 on ionic liquid grafted mesoporous silica SBA-15”

ARCI conventional/IUPAC RACI Symposium - Nanoparticle Synthesis & Application

**Oral presentation, July 2010**

- Jamileh Taghavimoghaddam, Gregory P. Knowles, Alan L. Chaffee

“Preparation and characterization of mesoporous silica supported cobalt oxide catalysts for the oxidation of organic substrates”

Green Chemistry 2011 Innovation, 3<sup>rd</sup> Asia-Oceania Conference on Green and sustainable Chemistry

**Poster, December 2011**

- Jamileh Taghavimoghaddam, Gregory P. Knowles, Alan L. Chaffee

“Supported cobalt oxide: Preparation and application for liquid phase oxidation of cyclohexanol”

American Chemical Society (ACS) Division Petroleum

**Oral presentation, March 2012**

- Jamileh Taghavimoghaddam, Gregory P. Knowles, Alan L. Chaffee

“Morphological investigation on cobalt oxide species supported on mesoporous silica SBA-15”

ACMM-22, 22<sup>nd</sup> Australian Conference on Microscopy and Microanalysis

**Oral presentation, Feb 2012**

- Jamileh Taghavimoghaddam, Gregory P. Knowles, Alan L. Chaffee

“Supported cobalt oxide with low Co-content: Preparation and application for liquid phase oxidation of cyclohexanol”

The 24<sup>th</sup> Organic Reactions Catalysis Society (ORCS) Conference

**Oral presentation, April 2012**